Advances in Information Entropy

Lead Guest Editor: Bin Wang
Guest Editors: Naixue Xiong and Fengming Xin

Advances in Information Entropy

Advances in Information Entropy

Lead Guest Editor: Bin Wang
Guest Editors: Naixue Xiong and Fengming Xin

Contents

Editorial

Advances in Information Entropy

Bin Wang ⓘ,[1] **Naixue Xiong** ⓘ,[2] **and Fengming Xin** ⓘ[3]

[1]*Hebei Provincial Collaborative Innovation Center of Transportation Power Grid Intelligent Integration Technology and Equipment, School of Electrical and Electronic Engineering, Shijiazhuang Tiedao University, Shijiazhuang, China*
[2]*Department of Mathematics and Computer Science, Northeastern State University, Tahlequah, OK, USA*
[3]*School of Computer and Communication Engineering, Northeastern University at Qinhuangdao, Qinhuangdao, China*

Correspondence should be addressed to Bin Wang; wangbinneu@qq.com

Entropy comes from thermodynamics in physics. It is one of the state parameters of matter to describe the degradation of energy. It generally refers to a measure of the state of some material systems. With the development of statistical physics and information theory, the essence of entropy is gradually explained, that is, the degree of internal chaos of a system. It has important applications in many fields, such as cybernetics, probability theory, life science, and astrophysics. In information theory, entropy gives a measure of the amount of information in an event drawn from a distribution. In the information world, the higher the entropy is, the more information can be transmitted. The lower the entropy is, the less information can be transmitted. Information entropy is always a useful tool to deal with the information quantity contained in the information and random variables. Information entropy also measures the complexity of a system. Information entropy is widely used in signal processing, system analysis, and other related fields.

This special issue includes 11 high-quality peer-reviewed papers that deal with different aspects of information entropy problems. These papers contain some new, novel, and innovative techniques and ideas. The aim of this special issue is to bring together original research and review articles highlighting the recent advances in this field. We hope that this special issue provides a platform to outline the continuing efforts to understand this field.

In the paper entitled "Anti-Interference Heartbeat Measurement Based on a Miniaturized Doppler Radar Sensor," the authors propose a novel algorithm to solve the sudden and unexpected interference. Firstly, the one-dimensional signal detected by the sensor is divided into segments to form a two-dimensional data matrix. In both the intrasegment and intersegment domains of the data matrix, a robust algorithm is employed to suppress unwanted interference, which significantly improves the robustness of demodulation. Experiments show the effectiveness of the proposed algorithm, based on which weak heartbeat signal hidden in the interference can be well extracted.

In the paper entitled "Use Python Data Analysis to Gain Insights from Airbnb Hosts," the author uses Python and its external data processing package to conduct an in-depth analysis machine study of Airbnb review data. The first part is for all hosts (super and nonsuper hosts). The second part suggestions are for nonsuper hosts to improve and super hosts to maintain. In the future, the author will build on this to further optimize the design.

In the paper entitled "Study on Announcement Effect of Stock Repurchase from the Perspective of Configuration Analysis," the authors take the stock repurchase cases in 2018-2019 after the promulgation of the New Company Law as the research object and use qualitative comparative analysis methods and the PSO-ICA-GARCH model to analyze 240 stock repurchase cases in the Chinese securities market from 2018 to 2019, and through the study of five types of 7 paths of high and nonhigh CAR stock repurchase announcement effects. The next step is to further optimize the model to make the analysis more accurate and effective.

In the paper entitled "The Statistical Analysis of Multidimensional Psychological Characteristics and User Feedback

Willingness," the authors study the influence of multidimensional psychological characteristics on users' feedback intention by using several statistical analysis methods based on information theory. The results show that both personality traits and cognitive styles can have a significant impact on feedback motivation factors and also show that self-efficacy may be the only evident feedback motivation to encourage useful feedback information. The results show that the willing users with extraversion trait are more likely be motivated by self-efficacy and thus have evident feedback willingness.

In the paper entitled "Asymptotic Behavior of Solution for Functional Evolution Equations with Stepanov Forcing Terms," through the use of the measure theory, evolution family, "Acquistapace–Terreni" condition, and Hölder inequality, the core objective of this work is to seek to analyze whether there is unique μ-pseudo almost periodic solution to a functional evolution equation with Stepanov forcing terms in a Banach space. Certain adequate conditions are derived guaranteeing there is unique μ-pseudo almost periodic solution to the equation by Lipschitz condition and contraction mapping principle.

In the paper entitled "ECG Signal Detection and Classification of Heart Rhythm Diseases Based on ResNet and LSTM," based on the ResNet34 network, three-layer stacked long-term and short-term memory networks are added, and the Mish function is used as the activation function. The final improved model can obtain the context dependence of the feature and retain the negative information in the ECG signal. Comparing the results of the ResNet34 model and ResNet-18 model on the same test dataset, the improved model in this paper has a better classification and recognition effect on ECG signals as a whole, which can identify atrial fibrillation diseases more effectively.

In the paper entitled "Research on Spectrum Feature Identification of Indoor Multimodal Communication Signal," the authors solve the problem of large signal acquisition error caused by radio wave multipath effect in indoor environment. Firstly, the signal source carried on the motion platform is collected for spectrum signal, and the signal processed by wavelet threshold denoising algorithms extracted and stored for spectrum feature extraction. Then, after data training and identification, the signal source is input into the system in random mode for identification. The experimental results show that the improved fuzzy clustering algorithm (FCA) is 12.7% higher than the spectrum envelope extraction method (SEEM) in the recognition rate of spectrum characteristics of different modes of signal source.

In the paper entitled "Multiperson Target Dynamic Tracking Method for Athlete Training Based on Wireless Body Area Network," aiming at the problems of large tracking error and long tracking time in traditional multiperson target dynamic tracking methods, a new method based on wireless body area network for athlete training multiperson target dynamic tracking is proposed. Experimental results show that this method can accurately measure the similarity of target features, with small tracking error and short tracking time. The minimum tracking error is only 0.11 frame.

In the paper entitled "Characterizations and Entropy Measures of the Exponentiated Generalized Frechet Geometric Distribution," some characterizations and entropy measures of the exponentiated generalized Fréchet geometric (EGFG) distribution are studied. Firstly, characterizations of the EGFG distribution based on five different approaches are discussed. The submodels for the EGFG distribution with their characterization expressions formed on the ratio of two truncated moments are also presented. Secondly, four different entropy measures are considered and expressed analytically via the incomplete gamma function. The behavior of all these entropy measures is discussed by performing a numerical study.

In the paper entitled "A Cloud Computing-Based Intelligent Forecasting Method for Cross-Border E-Commerce Logistics Costs," aiming at the problems of poor forecasting effect and low accuracy and low efficiency in current cross-border e-commerce logistics cost prediction methods, a cloud computing-based intelligent method for cross-border e-commerce logistics cost prediction is proposed. The experimental results show that the cross-border e-commerce logistics cost prediction effect of the proposed method is good, and it can effectively improve the accuracy and efficiency of cross-border e-commerce logistics cost prediction.

In the paper entitled "HRM-An Intelligent Helmet Recognition Model in Complex Scenes," the authors present an intelligent helmet recognition model in complex scenes based on YOLOv5s. The experimental results show that in the project, the average accuracy of helmet detection reaches 92.82%. Compared with SSD, YOLOv3, and YOLOv5s, the average accuracy of this algorithm is improved by 6.89%, 8.28%, and 2.44% and has a strong generalization ability in dense scenes and small target scenes, which meets the accuracy requirements of helmet wearing detection in engineering applications.

Conflicts of Interest

The editors declare that they have no conflicts of interest regarding the publication of this Special Issue.

Acknowledgments

Bin Wang
Naixue Xiong
Fengming Xin

Research Article

HRM: An Intelligent Helmet Recognition Model in Complex Scenes

Panbo He ⓘ,[1] Chunxue Wu ⓘ,[1] Rami Yared,[2] and Yuanhao Ma[3]

[1]*School of Optical-Electrical and Computer Engineering, University of Shanghai for Science and Technology, Shanghai 200093, China*
[2]*School of Computer Science, Arab International University, Damascus 999099, Syria*
[3]*College of Information Engineering, Shanghai Maritime University, Shanghai 201306, China*

Correspondence should be addressed to Chunxue Wu; wcx@usst.edu.cn

This paper presents an intelligent helmet recognition model in complex scenes based on YOLOv5. Firstly, in construction site projects, consider that the photograph which needs to be identified has numerous problems. For example, helmet's pixels are too tiny to detect, or a large number of workers makes helmets appear densely. A SE-Net channel attention module is added in different parts of the network layer of the model, so that the improved model can pay more attention to the global variables and increase the detection performance of small target information and dense target information. In addition, this paper constructs a helmet data set based on projects and adds training samples of dense targets and long-range small targets. Finally, the modified mosaic data enhancement reduces the influence of redundant background on the model and improves the recognition accuracy of the tiny target. The experimental results show that in the project, the average accuracy of helmet detection reaches 92.82%. Compared with SSD, YOLOv3, and YOLOv5, the average accuracy of this algorithm is improved by 6.89%, 8.28%, and 2.44% and has strong generalization ability in dense scenes and small target scenes, which meets the accuracy requirements of helmet wearing detection in engineering applications.

1. Introduction

The working environment of the construction site is complex and full of danger, and the workers are very vulnerable to injury in the process of work. Therefore, it is essential for workers on the construction site to wear safety protection equipment. In actual work, manual supervision is usually used to judge whether workers wear safety helmets. Therefore, there are problems such as wide operation ranges of constructors and failure to track and manage all workers in time at the construction site [1–5]. Automatic monitoring based on video stream is conducive to on-site real-time monitoring.

Traditional target detection usually adopts manual feature selection and designs and trains classifiers according to specific detection objects. This method has strong subjectivity, complex design process, and poor generalization ability and has great limitations in engineering application.

Therefore, many researchers are committed to the possibility of combining a domain model with an actual construction site scene. In 2015, Redmon et al. [6] proposed a one-stage detection model YOLO (You Only Look Once), which abstracted the detection task as a regression problem for the first time. In 2016, Liu et al. [7] proposed an SSD (single shot multibox detector) detection algorithm and introduced a multiscale detection method, which can effectively detect groups of small targets. In 2018, Redmon and Farhadi [8] further proposed You Only Look Once version 3. The model uses the Feature Pyramid Network (FPN) method to integrate three feature maps of different sizes for detection tasks, which significantly improves the detection effect of small-size targets. In 2020, Bochkovskiy et al. [9] proposed YOLOv4 (You Only Look Once version 4). The model selects CSP (Cross Stage Partial) darknet-53 as the backbone network and uses PAnet (path aggregation network) method to replace the FPN algorithm in the YOLOv3 network,

which greatly improves the detection accuracy of the model. In 2020, Usman et al. [10] proposed YOLOv5 (You Only Look Once version 5), which adds a focus structure to the backbone network to achieve the best balance between speed and accuracy.

Nowadays, a large number of scholars have carried out a series of related research on helmet detection. In 2016, Rubaiyat et al. and Silva et al. [11–14] combined the frequency domain information in the image with the Histogram of Orientation Gradients (HOG) algorithm to detect the human body and then used the Circle Hough Transform (CHT) to detect the helmet. In 2017, Li [15] uses a visual background extractor (Vibe) algorithm to locate the human body, then used the convex algorithm to detect the head, and finally combined the HOG algorithm and SVM to realize the helmet wearing detection. In 2018, Hao and Jza [16] proposed a hybrid descriptor composed of Local Binary Patterns (LBP), Color Histograms (CH), and Hu Moment Invariants (HMI) to extract helmet features and then constructed Hierarchical Support Vector Machine (H-SVM) to classify helmets. Due to the complex environment, the detection accuracy of helmet wearing is low at this stage, which does not meet the monitoring requirements of the actual production environment.

In this paper, we use two kinds of targets, construction workers wearing safety helmets and construction workers without safety helmets, which are taken as the detection tasks. A total of 26491 pictures are collected from the online collection and operation site for preprocessing, the safety helmet detection data set is constructed, and the YOLOv5 network model is selected as the basic model. The main contributions of this paper are as follows:

(1) A helmet data set based on an engineering project is constructed, and the training samples of dense targets and long-range small targets are added. The data-enhanced mosaic is optimized to reduce useless boundary information and improve the robustness of the model

(2) After the C3 module of the YOLOv5 backbone network and neck layer, the SE-Net channel attention module is introduced to collect global information in the feature extraction stage to improve the effect of small target helmet detection

(3) By introducing pixel IoU, the problem of an inaccurate positioning frame is solved, and the sensitivity of loss value to the processing dimension frame is improved

The experimental results show that the mean average precision (mAP) of the optimized model algorithm is significantly improved to meet the detection requirements in the construction scene.

2. Materials and Methods

2.1. Principle of the YOLOv5 Algorithm.
The YOLOv5 network structure is divided into input, backbone, neck, and prediction according to the processing stages, as shown in

Figure 1. The input part completes basic processing tasks such as data enhancement, adaptive picture scaling, and anchor box calculation. As the backbone network, the backbone mainly uses CSP structure to extract the main information in the input samples for subsequent stages. The neck part uses FPN and pan structure and uses the information extracted from the backbone part to strengthen feature fusion. The prediction section makes a prediction and calculates the GIOU_Loss value such as loss (see Figure 1).

2.2. SE-Net Attention Module.
An attention mechanism comes from the way the human brain processes visual information. By rapidly observing the global information of the image, human beings find out the candidate area that needs to be focused, that is, the location of the focus, and will focus on this area to extract more detailed information of the target [17]. Because of its powerful and effective expression, it has been widely used in deep learning, especially in deep-seated high-performance networks [18] (see Figure 2).

Firstly, for the feature map with channel number C, each channel contains different feature information. During feature extraction, the convolution layer mainly calculates the feature information of adjacent positions of each feature map without considering the correlation mapping between channel information [19]. Because the image resolution of small target helmet is low and the pixel value and channel characteristic information are limited, it is necessary to strengthen the training of relevant channel characteristic information in the training process. References [20–26] fully demonstrate that the attention module of the SE-Net channel can optimize the learning of specific categories of feature information in a deep-seated network. And the module is also a plug and play module, which is usually applied behind the convolution module. Therefore, we add the SE-Net channel attention module behind the C3 module of the neck detection layer of the YOLOv5 network; that is, after the detection layers of different scales, we add the SE-Net module, respectively, by establishing feature mapping relationship between channels; the network makes full use of these global information and gives higher weight to the channel feature information of small targets. So as to better fit the relevant characteristic information between small target channels, ignore and suppress useless information, and finally make the model focus on training the specific category of small target helmet.

2.3. Loss Function Improved.
The types of loss functions commonly used in YOLO series algorithms are GIoU, DIoU, and CIoU. The evolution from GIoU to CIoU makes the regression loss more accurate and the target frame regression more stable. However, it is found that the above three types of loss functions will cause the problem of an inaccurate positioning frame for targets with a high aspect ratio and dense targets; in order to solve this problem, the pixel IoU (PIoU) function [27] is introduced.

By introducing a rotation parameter, the loss function can frame the target more compactly. In order to accurately calculate the target intersection union ratio, the loss function calculates the target IoU by pixel counting, which makes the
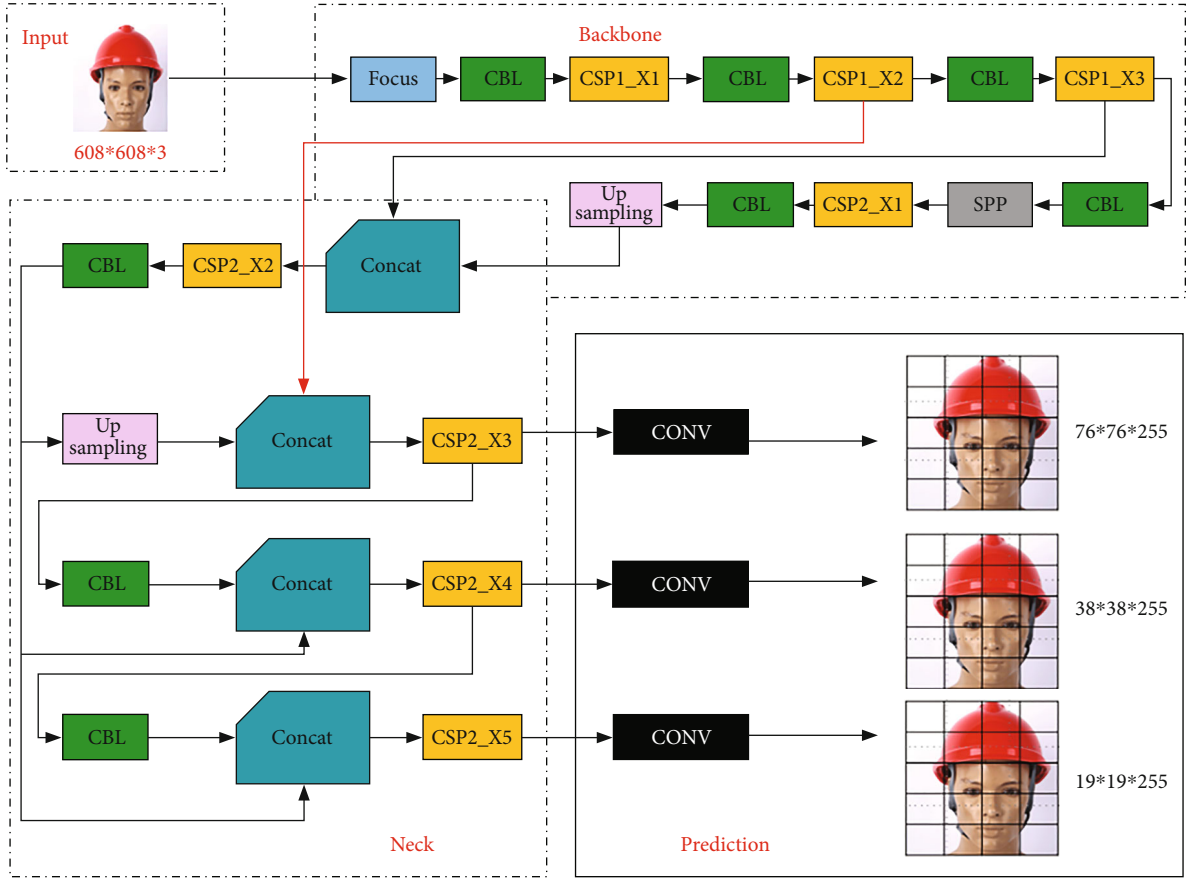
FIGURE 1: Basic framework of the YOLOv5 network structure, including input, backbone, neck, and prediction.
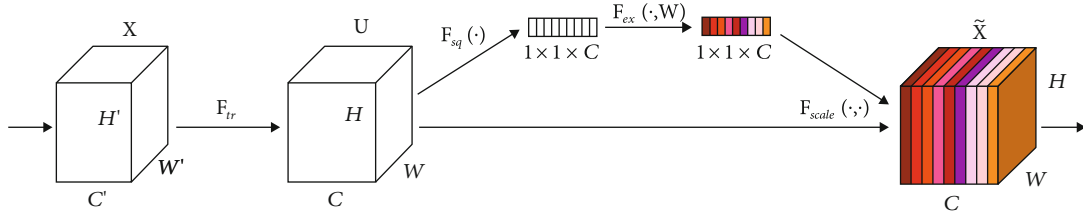
FIGURE 2: SE-Net structure diagram. F_{sq} is the squeeze, F_{ex} is the excitation, and F_{scale} is the scale.

loss value sensitive to the size, position, and rotation of the processing label box. The calculation formula of PIoU loss is

$$L_{\mathrm{PIoU}} = -\left(\frac{1}{|M|}\right) \sum_{(b,b^`) \in M} \ln F_{\mathrm{PIoU}}\left(b, b^`\right). \qquad (1)$$

In the formula, M is the set of all positive samples and $|M|$ is the number of positive samples. b is the ground truth, and $b^`$ is the target box. The calculation formula of the PIoU function is

$$F_{\mathrm{PIoU}}\left(b, b^`\right) = \frac{S_{b \cap b^`}}{S_{b \cup b^`}}. \qquad (2)$$

In the formula, $S_{b \cap b^`}$ and $S_{b \cup b^`}$, respectively, represent the number of pixels in the intersection of target b and target frame $b^`$ and the number of pixels in the union after being processed by the loss function kernel function.

2.4. Network Layer Adds SE-Net. In the small target detection task, with the gradual increase in the number of network layers, the collectable small target feature information is also gradually weakened, so it is easy to cause false detection and missed detection of small targets by the network model. The SE attention module itself uses the global average pool and other frequency components to enhance the features in the feature map, so that the network can strengthen the easy view learning of the target features in the training process. However, at this stage, no research

(a)

(b)
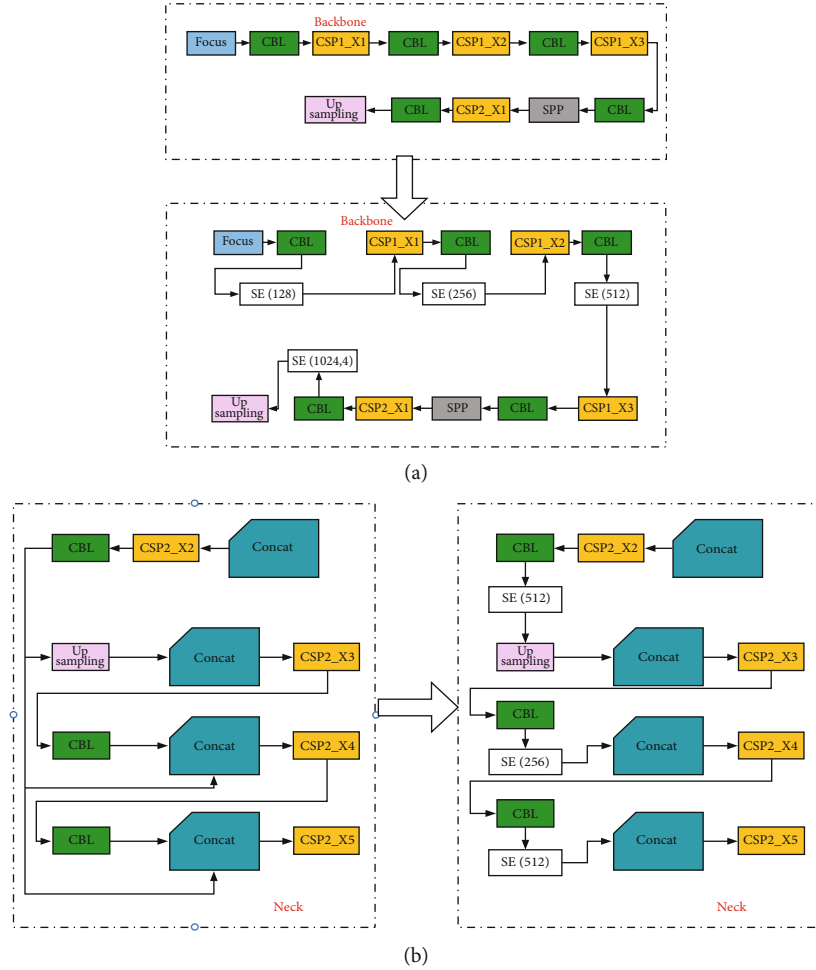
FIGURE 3: (a) Adding SE-Net in the YOLOv5 backbone layer. (b) Adding SE-Net in the YOLOv5 neck part. SE (128) means that this layer's input size is 128.

shows that the SE attention mechanism module should integrate which location of the network can effectively improve the detection efficiency.

Inspired by References [28–33], this paper integrates the SE attention module into different positions of the network model and studies the detection results. According to the structure of the YOLOv5 network model, the SE attention module is fused in the backbone network and neck of YOLOV5. Since the SE module performs feature enhancement in important channels and spatial locations, the SE attention module is fused to each feature fusion area in the above two parts, respectively, resulting in two new network models based on the YOLOv5 algorithm: SE-backbone and SE-neck. Figure 3 shows the specific location of the SE attention module fusion network.

The experimental comparison of adding the SE attention module in two different positions is shown in Table 1. It can be concluded that after the SE-Net module is integrated into the backbone network of YOLOv5, the detection accuracy of small targets is significantly improved, which can effectively improve the detection effect of the network on small target objects, and the mean average precision (mAP) is increased by 3.3 percentage points. After the SE-Net module is inte-

TABLE 1: Ablation results.

Name	P%	R%	mAP%
YOLOv5	91.613	91.494	89.813
SE-backbone	93.433	94.087	91.104
SE-neck	94.37	93.858	90.729
SE-neck+mosaic	95.023	93.522	91.761
SE-backbone+mosaic	95.518	94.776	92.827

grated into the neck module of YOLOv5, the performance of the model is not improved; on the contrary, the map is also reduced. This paper holds that the reason why the SE-Net module is fused to different positions in the model to produce different experimental results is that although the semantic information in the backbone network is not rich, it still implies the texture information and contour information that are easy to be ignored in the middle and low layers of the target. The fusion of the SE-Net module in the backbone network can better fuse the spatial features and channel features of small targets in the feature map, so as to enhance the feature information. In the deeper neck and

(a)

(b)
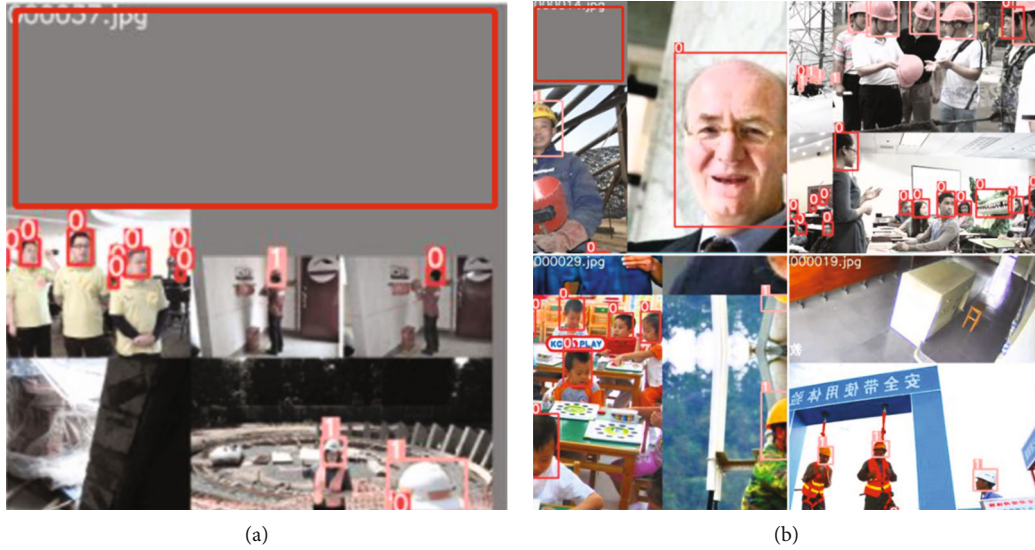
FIGURE 4: Compare two mosaics: (a) having huge blank filling; (b) improved picture having much small area of blank filling.

(a)

(b)

FIGURE 5: Improved mosaic result: a blocked helmet is detected in (b).

prediction module of the network, because its feature map has richer semantic features, a smaller feature map, and a huge receptive field, the SE net module has difficulty distinguishing important spatial features and channel features.

2.5. Mosaic Improvements. Mosaic, the data enhancement method in the YOLOv5 algorithm, is very practical. The basic principle is to randomly select four pictures: first cut them randomly, then splice them on one picture clockwise, and finally scale them to the set input size, which is introduced into the model as a new sample. This enriches the background of targets, increases the number of small targets, and achieves the balance between targets of different scales [34].

The data set in this paper is divided into two categories: helmet and head. The total amount of data is also relatively small compared with the coco data set, with only more than 20000 pieces. Due to the particularity of safety helmet pictures on the construction site, the targets to be identified are often not in the center of the picture. Random cutting has a high probability to cut the targets, so that there is only background in the input picture samples, and this will make the spliced pictures have more black-and-white boundaries,

which will lead to a large amount of useless feature information in model training and affect the convergence speed of the model [35].

Different from the coco data set, most of the images in the data set in this paper come from the frames taken from the video stream, and the size of the images is consistent with that of the pixels. Therefore, according to the characteristics of the data set, this paper improves the mosaic data enhancement method. Firstly, the number of mosaics is changed from 4 to 16, and then, the judgment conditions are added to ensure as little useless area as possible, and these filled black-and-white boundaries are at the edge of the image. As shown in the figure, the optimized original mosaic has a large area of blank filling, and the improved picture has a small area of blank filling (see Figure 4).

The performance comparison of the two methods is shown in Table 1. It can be seen that the accuracy of the improved model remains basically unchanged, but the recall and average accuracy of the improved model are increased by 2.08% and 1.71%, respectively.

The comparison of test results is shown in Figure 5. Figure 5(a) is the original model test diagram, and Figure 5(b) is the improved model test effect diagram.

(a)

(b)

(c)

(d)

(e)

(f)

(g)

(h)
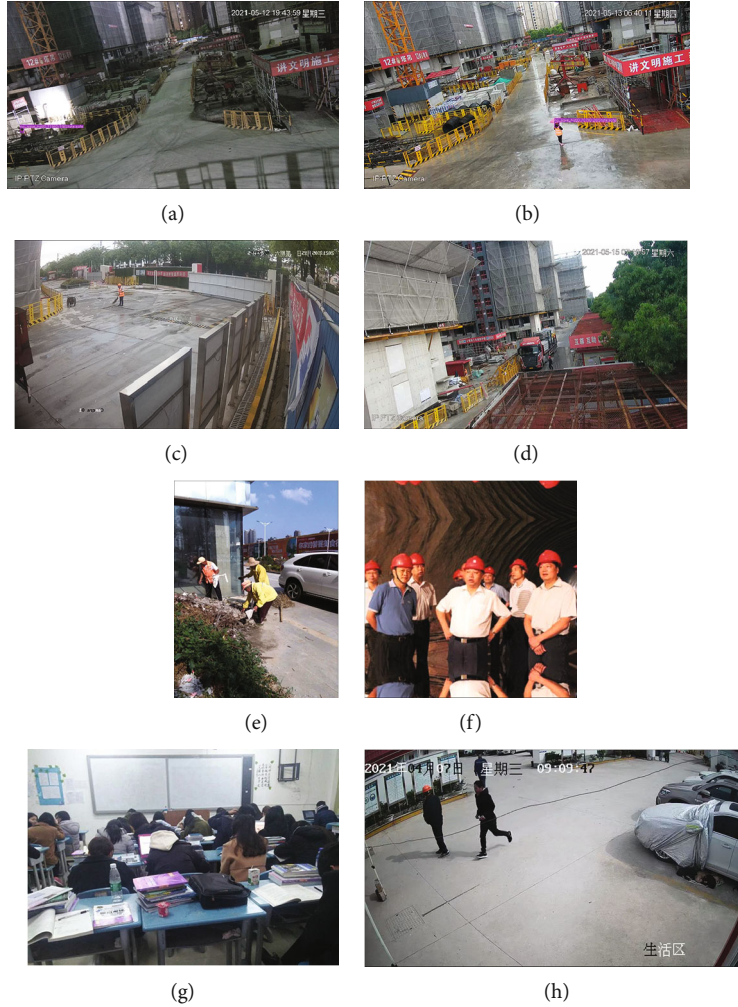
Figure 6: Helmet sample: (a) dark light; (b) small targets; (c, d) real environment; (e) interference term; (f) dense term; (g) dense interference term; (h) helmet and without helmet.

Figure 5 shows the helmet image of densely occluded small targets. It can be seen from the observation that compared with the original model, the improved model detects the targets wearing safety helmets. It shows that the improved model has strong robustness in these scenarios (see Figure 5).

3. Results and Discussion

3.1. Data and Training Setting. The results and discussion may be presented separately or in one combined section and may optionally be divided into headed subsections.

The main source of open-source helmet data set on the network is SHWD (Safety Helmet Wearing Dataset) [36], and most scenes are monitoring images of students in class. The data set deviates greatly from the standard site scene data set. Therefore, this paper expands the data set. The images mainly come from the site video stream frame cutting and handheld device shooting. The data collected include two types: workers wearing safety helmets and workers not wearing safety helmets in different site environments. In order to increase the diversity and robustness of

Table 2: Data set.

Type	Picture number	Box number
Hat	13428	45969
Head	14815	220453
Sum	26491	266422

the training set, some baseball caps, hard hats, and other data are added to increase the generalization ability of the model (see Figure 6).

The data set finally obtained in this paper has a total of 26491 pictures, of which the specific information of the targets wearing and not wearing helmets in this data set is shown in Table 2. The data set contains a variety of construction scenes, which can fully reflect the real construction scenes.

This paper is based on Linux, Ubuntu 18.04, and GeForce 3090 with 24 GPU video memory, the CUDA version is 11.2, and pytorch is selected as the framework. The data set is randomly divided into a training set, verification set, and test set according to the ratio of 8 : 1 : 1, batch size = 32, epoch = 300, and LR = 0.01.

(a)
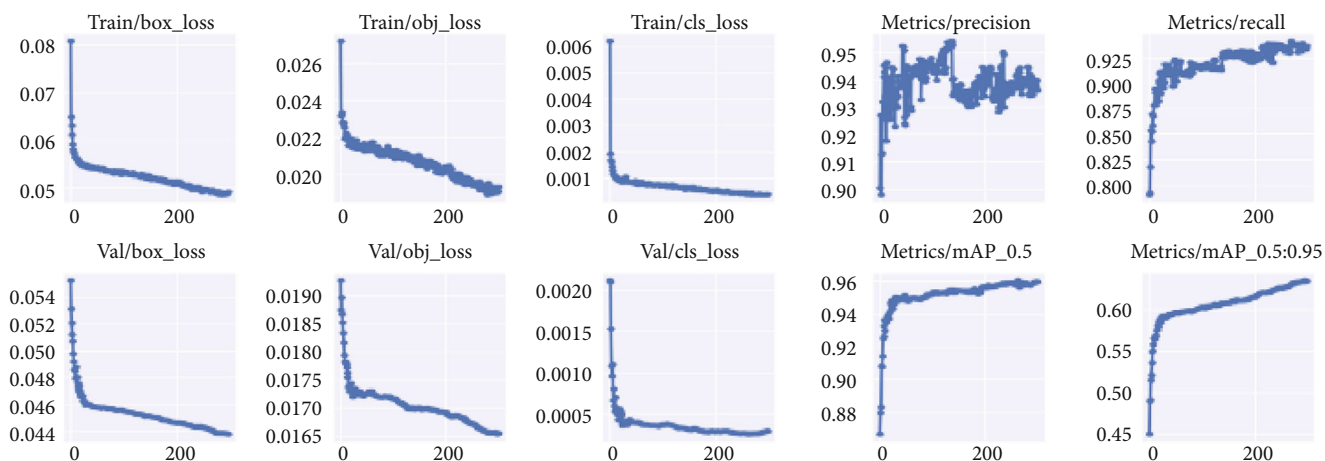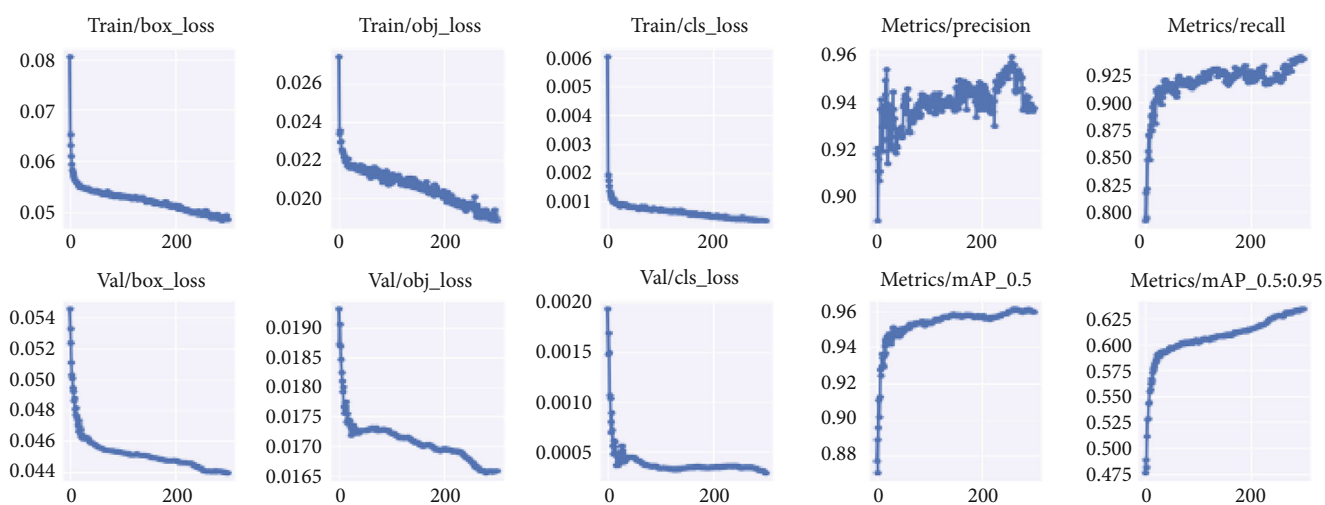
(b)

Figure 7: Model training loss diagram: (a) origin YOLOv5; (b) our model.
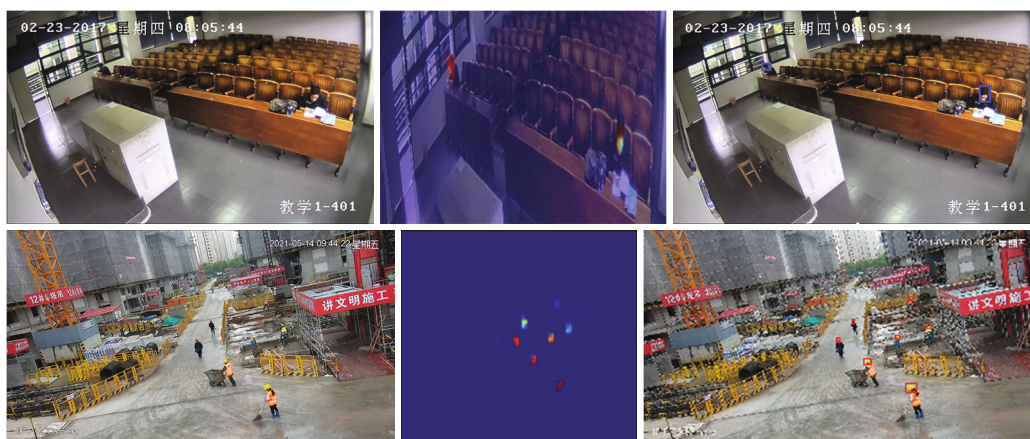
Figure 8: Characteristic thermodynamic diagram. Our model can capture small and dense targets.

FIGURE 9: Detection pictures. Use for different work environments. Good at detecting small and dense targets.

TABLE 3: Comparison of results of multiple detection models.

Name	mAP (%)	Speed (s)	Params (M)
SSD	85.39	0.11/picture	570.4
YOLOv3	84	0.06/picture	340.7
YOLOv5	89.84	0.03/picture	269.8
Ours	92.82	0.04/picture	266.1

3.2. Experimental Results. The model training loss diagram is compared as follows (see Figure 7), and the thermal diagram of our model is printed. It can be seen that the optimized model can put forward the characteristics of small goals and secret script goals (see Figure 8).

It can be seen from the figure that our model can capture the long-distance recognition targets in the image according to the characteristics of the pictures taken by the camera. The midpicture describes the feature map of the original figure. It can be concluded that our model well distinguishes between foreground and background and increases the feature capture of small and microtargets.

From the measured results of some site pictures, it can be seen that the optimized model in this paper improves the detection effect of small targets and dense targets and is suitable for many different actual scenes (see Figure 9).

At the same time, this paper also compares the optimized model with the mainstream target detection model. The results are shown in Table 3.

The experimental results show that this algorithm can effectively improve the detection accuracy of safety helmets and construction workers without safety helmets. The average detection accuracy of this algorithm for construction workers wearing safety helmets is 94.77%, and the mean average precision (mAP) is 92.82%, which is much higher than those of the YOLOv5 and SSD. Compared with SSD, YOLOv3, and original YOLOv5, this algorithm has a certain improvement in accuracy and mAP. This shows that this algorithm performs well in the accuracy of helmet wearing detection and can meet the accuracy requirements of helmet detection in complex working environment.

4. Conclusions

In order to improve the shortcomings of existing helmet algorithms in dense target and small target scenarios, a YOLOv5 algorithm is proposed in this paper. Through the SE-Net attention module and improved data enhancement method, the detection effect of the model for small target helmets is improved, the loss function is optimized, and the generalization ability of the model in dense scenes is increased. Through comparative experiments, compared with the original YOLOv5 model, the improved model reduces the missing detection of helmet and improves the classification confidence score. The experimental results show that this algorithm can obtain better detection accuracy and basically meet the accuracy requirements of helmet wearing detection in complex construction scenes.

Data Availability

The data set includes corresponding pictures and labels, and the file size is 2 GB. Data used to support the findings of this study are available from the corresponding author upon request.

Conflicts of Interest

The authors declare that there are no known competing financial interests or personal relationships that could have appeared to influence the work reported in this paper.

Acknowledgments

References

[1] J. Li, Y. F. Bai, and J. L. He, "Design and implementation of embedded video surveillance system based on human detection," *Applied Mechanics & Materials*, vol. 513-517, pp. 4535–4538, 2014.

[2] Z. Wang, T. Li, N. Xiong, and Y. Pan, "Erratum to: a novel dynamic network data replication scheme based on historical access record and proactive deletion," *Journal of Supercomputing*, vol. 62, no. 1, p. 616, 2012.

[3] W. Guo, N. Xiong, A. V. Vasilakos, G. Chen, and H. Cheng, "Multi-source temporal data aggregation in wireless sensor networks," *Wireless Personal Communications*, vol. 56, no. 3, pp. 359–370, 2011.

[4] J. Yin, W. Lo, S. Deng, Y. Li, Z. Wu, and N. Xiong, "Colbar: a collaborative location-based regularization framework for QoS prediction," *Information Sciences*, vol. 265, pp. 68–84, 2014.

[5] Z. Wan, N. Xiong, N. Ghani, A. V. Vasilakos, and L. Zhou, "Adaptive unequal protection for wireless video transmission over IEEE 802.11e networks," *Multimedia Tools & Applications*, vol. 72, no. 1, pp. 541–571, 2014.

[6] J. Redmon, S. Divvala, R. Girshick, and A. Farhadi, "You Only Look Once: unified, real-time object detection," in *Proceedings of the IEEE conference on computer vision and pattern recognition*, Las Vegas, NV, USA, 2016.

[7] W. Liu, D. Anguelov, D. Erhan et al., *SSD: single shot multi box detector*, Springer, Cham, 2016.

[8] J. Redmon and A. Farhadi, "YOLOv3: an incremental improvement," 2018, https://arxiv.org/abs/1804.02767.

[9] A. Bochkovskiy, C. Y. Wang, and H. Liao, "YOLOv4: optimal speed and accuracy of object detection," 2020, https://arxiv.org/abs/2004.10934.

[10] S. M. Usman, G. R. Jocher, S. T. Dye, W. F. McDonough, and J. G. Learned, "AGM2015: Antineutrino Global Map 2015," *Scientific reports*, vol. 5, no. 1, article ???, 2015.

[11] A. H. Rubaiyat, T. T. Toma, M. Kalantari-Khandani et al., "Automatic detection of helmet uses for construction safety," in *IEEE/WIC/ACM, International Conference on Web Intelligence Workshops*, Omaha, NE, USA, 2017.

[12] R. Silva, K. Aires, and R. Veras, "Helmet detection on motorcyclists using image descriptors and classifiers," *2014 27th SIBGRAPI Conference on Graphics, Patterns and Images*, pp. , 2014141–148, 2014.

[13] Y. Qu and N. Xiong, "RFH: a resilient, fault-tolerant and high-efficient replication algorithm for distributed cloud storage," in *2012 41st International Conference on Parallel Processing*, Pittsburgh, PA, USA, 2012.

[14] M. Wu, L. Tan, and N. Xiong, "A structure fidelity approach for big data collection in wireless sensor networks," *Sensors*, vol. 15, no. 1, pp. 248–273, 2015.

[15] Q. R. Li, *A Research and Implementation of Safety-Helmet Video Detection System Based on Human Body Recognition*, University of Electronic Science and Technology of China, 2017.

[16] W. A. Hao and B. Jza, "An intelligent vision-based approach for helmet identification for work safety," *Computers in Industry*, vol. 100, pp. 267–277, 2018.

[17] X. Tang, B. Zhong, J. Peng, B. Hao, and J. Li, "Multi-scale channel importance sorting and spatial attention mechanism for retinal vessels segmentation," *Applied Soft Computing*, vol. 93, p. 106353, 2020.

[18] G. Zhang, J. Yang, Y. Zheng, Y. Wang, Y. Wu, and S. Chen, "Hybrid-attention guided network with multiple resolution features for person re-identification," *Information Sciences*, vol. 578, pp. 525–538, 2021.

[19] W. H. Chen, J. He, and G. Liu, "Convolutional neural network with attention mechanism for hyperspectral image classification," *Laser & Optoelectronics Progress*, vol. 59, article 0411002, 2022.

[20] Z. Y. Zou, S. Y. Gai, F. P. Da, and L. L, "An occluded pedestrian detection algorithm based on attention mechanism," *Acta Optica Sinica*, vol. 41, pp. 149–157, 2021.

[21] J. Hu, L. Shen, and G. Sun, "Squeeze-and-excitation networks," *IEEE Transactions on Pattern Analysis and Machine Intelligence*, p. 99, 2017.

[22] R. He, N. Xiong, L. T. Yang, and J. H. Park, "Using multi-modal semantic association rules to fuse keywords and visual features automatically for web image retrieval," *Information Fusion*, vol. 12, no. 3, pp. 223–230, 2011.

[23] Q. Zhang, C. Zhou, Y. C. Tian, N. Xiong, Y. Qin, and B. Hu, "A fuzzy probability Bayesian network approach for dynamic cybersecurity risk assessment in industrial control systems," *IEEE Transactions on Industrial Informatics*, vol. 14, pp. 2497–2506, 2017.

[24] S. Huang, A. Liu, S. Zhang, T. Wang, and N. N. Xiong, "BD-VTE: a novel baseline data based verifiable trust evaluation scheme for smart network systems," *IEEE Transactions on Network Science and Engineering*, vol. 8, pp. 2087–2105, 2021.

[25] H. Li, J. Liu, K. Wu, Z. Yang, R. W. Liu, and N. Xiong, "Spatio-temporal vessel trajectory clustering based on data mapping and density," *IEEE Access*, vol. 6, pp. 58939–58954, 2018.

[26] Y. Yao, N. Xiong, J. H. Park, L. Ma, and J. Liu, "Privacy-preserving max/min query in two-tiered wireless sensor networks," *Computers & Mathematics with Applications*, vol. 65, no. 9, pp. 1318–1325, 2013.

[27] Z. Cao, M. Shao, L. Xu, S. Mu, and H. Qu, "MaskHunter: real-time object detection of face masks during the COVID-19 pandemic," *IET Image Processing*, vol. 14, p. 10223, 2020.

[28] Z. Zhang, X. Zhang, C. Peng, X. Xue, and J. Sun, "ExFuse: enhancing feature fusion for semantic segmentation," in *European Conference on Computer Vision Springer*, Cham, 2018.

[29] S. Chaib, H. Liu, Y. Gu, and H. Yao, "Deep feature fusion for VHR remote sensing scene classification," *IEEE Transactions on Geoscience and Remote Sensing*, vol. 55, no. 8, pp. 4775–4784, 2017.

[30] G. Ghiasi, T. Y. Lin, and Q. V. Le, "NAS-FPN: learning scalable feature pyramid architecture for object detection," in *2019 IEEE/CVF Conference on Computer Vision and Pattern Recognition (CVPR)*, Long Beach, CA, USA, 2019.

[31] F. Xia, R. Hao, J. Li, N. Xiong, L. T. Yang, and Y. Zhang, "Adaptive GTS allocation in IEEE 802.15.4 for real-time wireless sensor networks," *Journal of Systems Architecture*, vol. 59, no. 10, pp. 1231–1242, 2013.

[32] K. Gao, F. Han, P. Dong, N. Xiong, and R. Du, "Connected vehicle as a mobile sensor for real time queue length at signalized intersections," *Sensors*, vol. 19, no. 9, p. 2059, 2019.

[33] Y. Lu, S. Wu, Z. Fang, N. Xiong, S. Yoon, and D. S. Park, "Exploring finger vein based personal authentication for secure IoT," *Future Generation Computer Systems*, vol. 77, pp. 149–160, 2017.

[34] L. Chengyue, Y. Jianmin, and L. Zhixian, "Object detection method based on improved YOLO lightweight network," *Laser & Optoelectronics Progress*, vol. 57, no. 14, p. 141003, 2020.

[35] A. Gautier, R. Roussel, C. Lange et al., "Effects of genetic susceptibility for type 2 diabetes on the evolution of glucose homeostasis traits before and after diabetes diagnosis," *Diabetes*, vol. 60, no. 10, pp. 2654–2663, 2011.

[36] D. Peng, Z. Sun, Z. Chen, Z. Cai, L. Xie, and L. Jin, "Detecting heads using feature refine net and cascaded multi-scale architecture," in *2018 24th International Conference on Pattern Recognition (ICPR)*, Beijing, China, 2018.

Research Article

A Cloud Computing-Based Intelligent Forecasting Method for Cross-Border E-Commerce Logistics Costs

Yanting Li [ID]

Information Center of Chengyi University College, Jimei University, Xiamen, Fujian 361021, China

Correspondence should be addressed to Yanting Li; liyanting@jmu.edu.cn

Aiming at the problems of poor forecasting effect and low accuracy and low efficiency in current cross-border e-commerce logistics cost prediction methods, a cloud computing-based intelligent method for cross-border e-commerce logistics cost prediction is proposed. Analyze cloud computing concepts, characteristics, and service models, study cloud computing-related technologies, and train BP neural network algorithms based on BP neural network principles. The BP neural network structure is obtained by determining the number of neurons in the input layer, the number of neurons in the hidden layer, the number of neurons in the output layer, and the activation function of the neural network. Normalize the input data samples of the input layer, and select the initial weight, threshold, and learning rate parameters of the BP neural network to determine the momentum coefficient. This paper uses neural network model combined with Spark cloud computing platform to realize the intelligent prediction of cross-border e-commerce logistics cost. This method has good predictive ability. After a large amount of data input and output relationship training, it has obtained the most suitable model for prediction. The experimental results show that the cross-border e-commerce logistics cost prediction effect of the proposed method is good, and it can effectively improve the accuracy and efficiency of cross-border e-commerce logistics cost prediction.

1. Introduction

As a new form of foreign trade, cross-border e-commerce shows strong vitality in the environment of relatively weak import and export market [1]. Cross-border e-commerce plays a very important role in the mode of economic growth, taking a new road to industrialization, realizing the optimal allocation of resources, and enhancing international competitiveness. The development of cross-border e-commerce can promote industrialization through informatization, change the mode of economic growth, and take a new road to industrialization. In addition, accelerating the development of cross-border e-commerce is conducive to grasping the development opportunities brought by economic globalization, coping with the challenges brought by economic globalization, and improving international prestige. In the environment of fierce development momentum of cross-border e-commerce industry, cross-border logistics, as an indispensable and important link in the operation of cross-border e-commerce, has attracted much attention

[2]. Cross-border logistics transportation is a necessary condition and basic guarantee for the development of cross-border e-commerce enterprises [3]. Therefore, it is very important to effectively control the transportation cost of cross-border e-commerce enterprise logistics. The prediction of cross-border e-commerce logistics cost is helpful to more effectively integrate logistics resources and formulate logistics development planning.

At present, scholars in related fields have studied cost prediction and achieved some theoretical results. Reference [4] proposed the difference between cost-benefit results and prediction of road widening. The cost-benefit analysis of road investment involves a model that takes saving travel time as the main cost-benefit. The cost-benefit result of traffic flow road widening predicted using the variable demand model based on SATURN software. Predicting faster traffic speed is the input of an economic model used to compare investment benefits and costs, and the resulting benefit-cost ratio proves the rationality of the investment. This method has certain validity. Reference [5] proposed a

research on the logistics cost optimization of the offshore oil service industry based on the offshore oil service cost model. The logistics cost of offshore oil service industry refers to the currency performance of various offshore operations and resources consumed in the space movement or time occupation of offshore engineering equipment. It is the sum of human, material, and financial resources expended in various activities of marine engineering equipment during the physical movement. Based on the characteristics of offshore oil service industry, this paper optimizes the logistics cost of offshore oil service industry from the three aspects of accounting method, system perspective, and macro level. Innovative and basic research has been conducted on the formation mechanism, forecasting, and optimization strategies of CNOOC service logistics costs. This method has certain feasibility. However, the above methods still have the problems of poor prediction effect, accuracy, and efficiency.

To solve the above problems, an intelligent prediction method of cross-border e-commerce logistics cost based on cloud computing is proposed. Using BP neural network algorithm, determine the structure of BP neural network, normalize the data samples, select the learning parameters of BP neural network, determine the momentum coefficient, and complete the training of BP neural network. Using cloud computing technology, Spark cloud computing platform and BP neural network algorithm are combined to realize the intelligent prediction of cross-border e-commerce logistics cost. The cross-border e-commerce logistics cost intelligent prediction effect of this method is good and can effectively improve the accuracy and efficiency of cross-border e-commerce logistics cost intelligent prediction.

The research innovations of this article are as follows:

(1) An intelligent method for cross-border e-commerce logistics cost prediction based on cloud computing is proposed

(2) Analyze cloud computing concepts, characteristics, and service models, study cloud computing-related technologies, and propose training BP neural network algorithms based on BP neural network principles

(3) This article uses neural network model combined with Spark cloud computing platform to realize the intelligent prediction of cross-border e-commerce logistics costs

2. Cloud Computing Technology

2.1. Cloud Computing Concepts and Characteristics.
Cloud computing is an Internet-based computing method. In this way, shared software and hardware resources and information can be provided to computers and other devices on demand [6]. Cloud computing is a computing mode that integrates large-scale computing, storage, applications, and other decentralized computing resources to work together and provides users with infrastructure, platforms, software, applications, and other services through the Internet. The characteristics of cloud computing are summarized as follows:

(1) Ultralarge scale: cloud computing service providers have large-scale server groups. Google has more than 1 million cloud computing servers, and every cloud computing service provider such as Amazon, IBM, and Microsoft has at least several hundred thousand. The server "cloud" can give users advanced computing power

(2) Virtualization: the biggest feature of the cloud computing platform at the current stage of development is to rely on a series of technologies such as virtualization to realize the virtualized control, management, scheduling, and application of hardware resources. Users can use network resources provided by cloud service providers through virtual platforms, but they can complete complex calculations that cannot be solved by local computers

(3) Scalable: in the cloud computing system, the number of servers can be expanded at any time, and more computing resources can enhance the processing capacity of cloud computing

(4) On-demand service: in cloud computing applications, users can purchase cloud services according to their own needs

(5) High reliability: the application runs on the server side, the calculation is processed by the server side, and the generated data is also stored on the server side. When a server has a problem, the task will continue to run by other servers, ensuring the normal progress of applications and calculations, users do not need to back up, and the data is automatically restored and saved on the server

(6) Low cost: the operation of "cloud" enables enterprises to reduce the high operating costs of data centers, and cloud service providers charge according to user needs

2.2. Cloud Computing Service Model.
Cloud computing has three service models, Software as a Service (SaaS), Platform as a Service (PaaS), and Infrastructure as a Service (IaaS). The cloud computing service model is shown in Figure 1.

2.2.1. Software as a Service (SaaS).
SaaS provides access to complete programs as a service. SaaS service providers uniformly deploy application service software on the server and divide and price the application service software according to specifications. Users can pay service fees through the Internet to enjoy application software services. The quantity and use time of application software can be customized according to user needs.

2.2.2. Platform as a Service (PaaS).
PaaS is a basic platform service used to generate various applications. PaaS service providers can provide basic platform services to users. Users
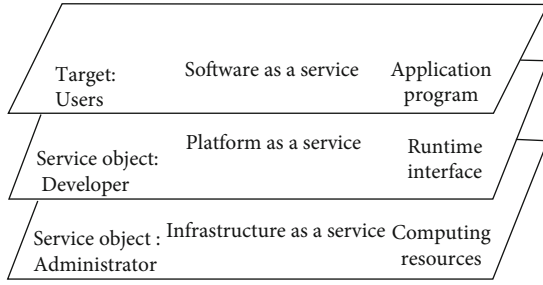
FIGURE 1: Cloud computing service model.

can purchase platform services from PaaS providers according to their own R&D needs to customize the R&D platform.

2.2.3. Infrastructure as a Service (IaaS). IaaS is an infrastructure service that provides a workplace for publishing, running, and processing virtual machines and storage space. IaaS service providers provide services to users based on the granularity of virtual resources. IaaS provides the possibility of real-time scalability of computing resources and on-demand storage devices.

2.3. Cloud Computing-Related Technologies

2.3.1. Hadoop Cloud Computing Platform. Hadoop is a distributed system basic framework developed by Apache Software Foundation, which allows users to ignore the underlying details when developing programs and focus on the development of programming models [7]. Hadoop includes three main components: distributed file system (Hadoop Distributed File System, HDFS), MapReduce programming framework, and distributed database HBase.

(1) HDFS. HDFS is designed and inspired by Google's file system GFS (Google File System, GFS) and is highly fault-tolerant. HDFS is a reliable and fault-tolerant file system suitable for low-cost storage of large-scale data. The organization structure of HDFS is shown in Figure 2.

The files in HDFS are written once and read multiple times, and the system does not need to be deployed on expensive and stable hardware devices. HDFS adopts the master/slave architecture, which can realize applications that optimize the throughput of large amounts of data. The HDFS cluster includes a NameNode node and several Data-Node nodes. These two types of nodes have different responsibilities, but they cooperate with each other to complete their different tasks through work in different modes.

(2) MapReduce Programming Framework. MapReduce is a programming model proposed by Google for parallel operations on large-scale data sets [8]. A MapReduce job contains a large number of Map and Reduce operation pairs. Map operations generally perform data operations similar to filtering, sorting, and data conversion. Reduce operations are generally used to complete data aggregation operations. The MapReduce workflow is shown in Figure 3.
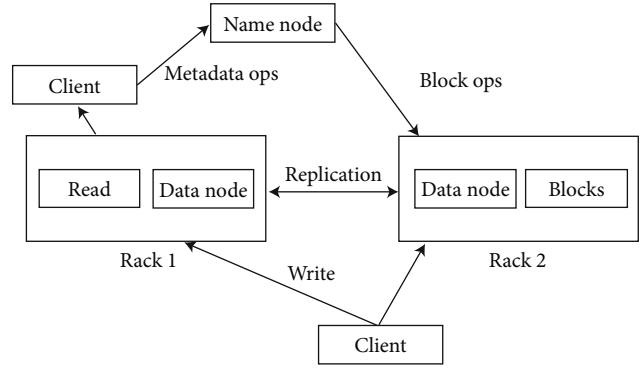
FIGURE 2: Organizational structure of HDFS.

According to the characteristics of the task, the data processing process is generally divided into two stages: Map and Reduce: in the Map stage, the Map task reads input file blocks, analyzes the data in parallel, and saves the processed intermediate results in the Map task node. In the Reduce phase, the Reduce task reads and merges the intermediate execution results of multiple Map tasks. Both Map tasks and Reduce tasks can be executed in parallel, which can speed up the overall processing speed by increasing the number of computing nodes. The parameters required for cross-border e-commerce smart cost prediction include e-commerce cost, e-commerce price, and e-commerce quantity.

(3) HBase Distributed Database. HBase Distributed Database is an open source implementation of Google Big-table, which imitates and provides all the functions of the Big-table database based on the Google file system. The HBase data model is a sorted, multidimensional, sparse, long-term mapping table stored on the hard disk. HBase is mainly used to store unstructured and semistructured loose data.

2.3.2. Spark Cloud Computing Platform. Spark is a general parallel computing framework developed by UC Berkeley AMP Lab based on the MapReduce computing framework [9]. Based on the advantages of MapReduce, it saves the intermediate results of tasks directly in memory. The running architecture of Spark is shown in Figure 4.

The task control node (Driver Program) sends the partitioned task set to the cluster's running job task node (Worker Node) through the cluster resource management service (Cluster Manager) and executes the corresponding process (Executor) on each node.

RDD is the core of Spark and the foundation of the entire Spark architecture. All operations of Spark are implemented on the basis of RDD. RDD is a data collection that has a good fault tolerance mechanism and can be executed in parallel. RDD can be created from an existing data set in memory through the parallelize function, or from a file through the textFile function. At the same time, RDD provides transformations and actions to operate on RDD data sets. The conversion can be converted from an existing RDD to a new RDD by functions such as map, filter, and join. The action is to transfer the running result on the
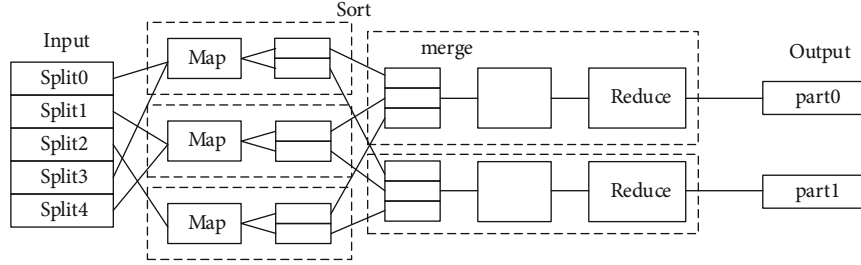
FIGURE 3: MapReduce work flow chart.
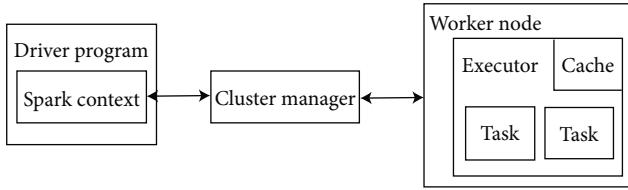
FIGURE 4: Spark running architecture diagram.

RDD data set back to the driver or write it to the storage system, such as reduce, count, saveAsTextFile, and other functional operations.

3. BP Neural Network

3.1. Principle of BP Neural Network. BP neural network is the abbreviation of error back propagation neural network. It is composed of an input layer, one or more hidden layers, and an output layer, and each layer is composed of a certain number of neurons [10]. These neurons are interrelated, and the neurons in adjacent layers are connected with each other, but there is no connection between the neurons in each layer. Such connection constitutes a hierarchical neural network system. The topology of BP neural network is shown in Figure 5.

When the BP neural network obtains an input signal, the signal is transmitted and calculated from the input layer neuron to the hidden layer neuron and then transmitted from the hidden layer neuron to the output layer neuron, and finally, the prediction result is output by the output layer neuron. This is a process of state update layer by layer and a forward propagation process of the network. If there is an error between the output budget result and the actual expected value, the network system will transfer the obtained error from the output layer to the input layer layer by layer, and in the transmission process, modify the connection weights of each layer, redistribute the network weights, and reduce the error until a satisfactory result is obtained. This process is called network back propagation process. The above process is repeated until the error meets the training error requirements, or the training reaches the maximum number of training steps, and the learning is completed. Once the BP neural network is learned, the prediction system only carries out forward propagation, and there is no back propagation of error. To sum up, the learning process
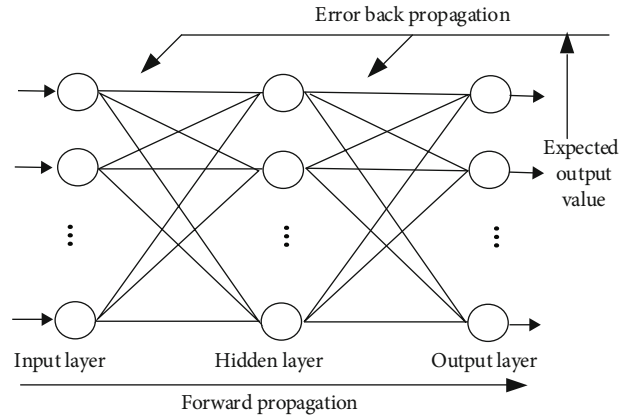
FIGURE 5: Topology of BP neural network.

of BP neural network is the process of continuously adjusting the connection weight of each layer.

3.2. Mathematical Description of BP Neural Network Algorithm. BP neural network algorithm is an artificial neural network suitable for multilayer neural network under tutor training. Its convergence law is carried out through the steepest gradient descent method. The following is a mathematical description of the artificial neural network:

Assuming an artificial network with a total of L layers and n nodes, the nodes of each layer except the input node can only obtain information from the neural network of the previous layer. In the same way, each layer of nodes outside the output node only transmits information to its next layer of nodes, and the activation function of each node of the neural network is set to Sigmoid type [11]. In order to make the whole process easier to understand, suppose that the output layer of the entire neural network has only one node y. Now suppose that (x_k, y_k), $k = 1, 2, \cdots, N$ is the training data, o_i is the output of the node i, and o_{ik} is the output of the node i corresponding to the (x_k, y_k) sample. When the input of the j unit of the l layer is the k sample, the calculation formula for the input of node j is

$$\text{net}_{ij}^l = \sum_j w_{ij}^l o_{jk}^{l-1}, \tag{1}$$

$$o_{jk}^l = f\left(\text{net}_{jk}^l\right), \tag{2}$$

where o_{jk}^l represents the l layer, when the k sample is input, the output of the j unit node. The calculation method of the error function is

$$E_k = \frac{1}{2} \sum_l (y_{lk} - \bar{y}_{lk})^2, \tag{3}$$

where $\bar{y}_{lk}$ is the actual output of unit j. The calculation formula of the total error is

$$E = \frac{1}{2N} \sum_{k=1}^{N} E_k. \tag{4}$$

Definition:

$$\delta_{jk}^l = \frac{\partial E_k}{\partial \text{net}_{jk}^l}. \tag{5}$$

Then:

$$\frac{\partial E_k}{\partial w_{ij}^l} = \frac{\partial E_k}{\partial \text{net}_{jk}^l} \frac{\partial \text{net}_{jk}^l}{\partial w_{ij}^l} = \frac{\partial E_k}{\partial \text{net}_{jk}^l} o_{jk}^{l-1} = \delta_{jk}^l o_{jk}^{l-1}. \tag{6}$$

Then, there are

$$\begin{cases} \delta_{jk}^l = \sum_m \delta_{mk}^{l+1} w_{mj}^{l+1} f'\left(\text{net}_{jk}^l\right), \\ \dfrac{\partial E_k}{\partial w_{ij}^l} = \delta_{jk}^l o_{jk}^{l-1}. \end{cases} \tag{7}$$

The specific steps of the BP neural network algorithm are as follows:

(1) Initialize the weight of neural network

(2) The error of repeated iteration meets the following requirements:

$$E = \frac{1}{2N} \sum_{k=1}^{N} E_k < \varepsilon \tag{8}$$

where ε represents the preset accuracy.

During the $k = 1$ to N process:

Positive direction: o_{jk}^{l-1}, net_{jk}^l, and $\bar{y}_{lk}$ of each layer are calculated according to the calculation

Reverse: Calculate the δ_{jk}^l of each unit from 2 to L-2

Update weight:

$$w_{ij} = w_{ij} - \mu \frac{\partial E}{\partial w_{ij}}, \quad \mu > 0 \tag{9}$$

(3) The algorithm ends

In the training process, the sample is given randomly when needed. In addition, the momentum and learning effi-

ciency of the neural network need to be changed according to the number of iterations.

4. Theories Related to Cross-Border E-Commerce Logistics Costs

4.1. Concept and Characteristics of Cross-Border E-Commerce. Cross-border e-commerce refers to the use of existing industrial platforms and resource advantages to explore specific cross-border e-commerce comprehensive service system and basic information standards and interface specifications such as online customs clearance, inspection and quarantine, tax rebate, and foreign exchange settlement involved in cross-border e-commerce import and export. Realize the standardized information flow between customs, national inspection, national taxation, foreign management, and other departments and e-commerce enterprises and logistics supporting enterprises [12]. Cross-border e-commerce is a global, paperless, and direct international trade activity. Transaction subjects in different customs territories reach a transaction agreement on the e-commerce platform, make payment and settlement through various financial payment institutions at home and abroad, and then send goods to consumers through cross-border logistics to complete the transaction.

Cross-border e-commerce is a new trade mode relying on the Internet and cross-border logistics. Compared with traditional export e-commerce, it can meet customer needs more quickly and conveniently and has the following characteristics:

(1) Openness and globality: cross-border e-commerce is different from the traditional form of foreign trade. The information of e-commerce enterprises can be displayed on the web page, which increases more trade opportunities for foreign trade enterprises and saves a lot of human and material resources. At the same time, without the limitation of time and place, it has flourished all over the world

(2) Multilateralization: multilateralization is reflected in that when e-commerce enterprises and customers reach a transaction agreement, they may use the transaction platform of country A to reach transaction and use the payment platform of country B to make payment, and the logistics institutions of country C carry out logistics delivery according to the requirements of orders. The characteristics of cross-border e-commerce multilateralization are very obvious

(3) Directness: cross-border e-commerce enterprises can display the specific information of commodities through the network service platform and update them at any time. Customers can directly query the products they need on the network service platform, conduct commodity transactions through the service platform, and complete the signing of purchase and sales contracts. It is direct and different from traditional foreign trade

(4) Low cost: the e-commerce activities carried out by cross-border e-commerce enterprises are completed on their own web pages or network service platforms, and the delivery of commodity ownership is completed online, which greatly reduces the time cost and labor cost and improves the work efficiency

4.2. Concept and Classification of Logistics Cost. Logistics cost refers to the monetary performance of materialized labor and live labor consumed in enterprise logistics activities [13]. It includes the summation of human, material, and financial resources consumed in the process of transportation, storage, packaging, loading and unloading, circulation and processing, logistics information, and logistics management, as well as the working capital occupation cost, inventory risk cost, and inventory insurance cost related to inventory. Among them, logistics transportation cost is a part of logistics cost. Logistics transportation costs mainly include labor costs, such as transportation personnel wages and benefits; operating expenses, such as fuel cost of operating vehicles, depreciation, and highway transportation management fee; and other expenses, such as travel expenses.

Logistics transportation costs can be classified into several categories:

(1) According to different transportation modes, logistics transportation cost can be divided into road transportation cost, railway transportation cost, water transportation cost, air transportation cost, and pipeline transportation cost

(2) According to the cost characteristics, logistics transportation cost can be divided into fixed transportation cost and variable transportation cost. Fixed transportation cost refers to the cost that does not change with the change of transportation volume and transportation mileage. Variable transportation cost changes with the change of transportation volume and transportation mileage

(3) According to different goods delivery batches, the logistics transportation cost can be divided into vehicle transportation cost and LCL transportation cost. Vehicle transportation cost refers to the freight calculated and charged according to the freight rate of the vehicle. LCL transportation cost refers to the freight charged according to the freight rate of LCL transportation when the goods are delivered sporadically, and the goods are less than the full vehicle and the whole batch tonnage, and the goods are calculated according to the actual weight

(4) According to cost concealment, logistics transportation cost can be divided into explicit transportation cost and implicit transportation cost. Explicit transportation cost refers to the actual expenditure that can be seen in the transportation process, including the monetary performance of various materialized labor and live labor consumed in the transportation process. Implicit transportation cost is relative to explicit transportation cost. It is hidden, difficult to avoid, and difficult to quantify. It mainly includes the increased cost of empty vehicle without cargo, the increased cost of convective transportation, the increased cost of circuitous transportation, the increased cost of repeated transportation, the increased cost of over distance transportation, and the increased cost of improper selection of transportation capacity

5. Spark-Based BP Neural Network Cross-Border E-Commerce Logistics Cost Intelligent Prediction Method

This research is oriented to the logistics cost of cross-border e-commerce, using BP neural network, combined with the Spark cloud computing platform, to predict the logistics cost of cross-border e-commerce.

5.1. Determine the Network Structure. The important premise of using BP neural network for prediction is to determine a reasonable network structure. Whether the network structure is reasonable or not directly affects the accuracy of the prediction results [14]. When constructing the BP neural network structure, the principles of reducing system scale, reducing system complexity, and shortening learning time should be followed. By determining the number of neurons in the input layer, the number of neurons in the hidden layer, the number of neurons in the output layer, and the activation function of the neural network, a reasonable neural network structure is obtained.

5.1.1. Determination of the Number of Neurons in the Input Layer. The number of input neurons in the BP neural network is determined according to the problem to be solved and the way the data is expressed, which refers to the number of factors that affect the output result. The number of neurons in the output layer of the BP neural network of the cross-border e-commerce logistics cost is the number of factors that affect the cross-border e-commerce logistics cost.

5.1.2. Determination of the Number of neurons in the Hidden Layer. In the BP neural network, neurons in the hidden layer play a role in extracting and storing the internal laws of the sample. The system assigns several weight parameters to each hidden layer neuron to enhance the mapping function of the neural network. Moreover, the number of hidden layer neurons directly affects the nonlinear performance of the network and also determines the complexity of the problem to be solved. The basic steps for determining the number of hidden layer nodes are as follows:

By determining the value range of the number of hidden layer nodes, the number of hidden layer nodes is determined after many training processes, the original sample data is input, the network is studied, the error is compared, and the number of nodes is adjusted repeatedly to reduce the error and determine the best number. Generally, for the

three-layer forward network, the number of hidden layer neurons is

$$N < \sum_{i=0}^{n} C_i^j, \tag{10}$$

where N represents the number of samples, j represents the number of neurons in the hidden layer, and n represents the number of neurons in the input layer. If $i > j$, $C_i^j = 0$; in the selection formula of the number of neurons in the hidden layer j, there are mainly two forms, namely,

$$j = \sqrt{n + m} + \alpha, \tag{11}$$

$$j = \log_2 n, \tag{12}$$

where m represents the number of neurons in the input layer and α represents a constant from 1 to 10.

5.1.3. Determination of the Number of Neurons in the Output Layer. Similar to the neurons in the input layer, output neurons are the purpose of prediction, and the number of neurons is determined by the type of prediction result. The result of cross-border e-commerce logistics cost prediction is the freight cost, so the number of neurons in the output layer is 1.

5.1.4. Determination of Neuron Activation Function. In the construction of the BP neural network, in order to facilitate the learning of the input signal and converge the input signal, the tansig function of the tangent form of the sigmoid function is selected as the activation of the hidden layer neuron function. In order to make the output of the entire network can take any value, the linear function Purelin is used as the transfer function of the neurons in the output layer.

5.2. Learning Sample Preprocessing. The number of samples in the input layer of the BP neural network determines the eigenvalues of the network. The more samples input in the input layer, the more eigenvalues that the BP neural network needs to recognize. In order to avoid the loss of indicators with fewer values or the system prematurely falling into the saturation zone due to these differences, the data samples input by the input layer need to be normalized. Considering the characteristics of cross-border e-commerce logistics cost drivers and their impact on the results of cross-border e-commerce logistics cost prediction, the most commonly used data sample preprocessing method is calculated as

$$Y_i = \begin{cases} 1, x_{\min} \leq x_i, \\ \dfrac{(x_i - x_{\min})}{(x_{\max} - x_{\min})}, x_{\min} < x_i < x_{\max}, \\ 0, x_i \leq x_{\max}, \end{cases} \tag{13}$$

where Y_i represents the normalized result of data i, x_i represents the actual value of data i, and $x_{\max}$ and $x_{\min}$ represent the maximum and minimum values of the group of data, respectively.

5.3. Selection of Learning Parameters. The learning parameters of the BP neural network include initial weights, thresholds, and learning rate. The following specifically introduces the selection method of learning parameters.

5.3.1. Determination of Initial Weight and Threshold. The initial weight and threshold of BP neural network directly affect the learning results of neural network. The size of initial weight and threshold is related to the convergence of output value in the learning process, whether it can reach the local minimum and the convergence speed of computer network. The basic requirement for the selection of the initial position is that after the initial weight input is accumulated, it can ensure that the output value of each trivial element is close to zero. Based on the above principles, the initial weight and threshold are generally selected randomly between $[-1, 1]$.

5.3.2. The Determination of the Learning Rate. The network learning rate determines the amount of change of the weight and the threshold generated in each cycle [15]; the relationship between the weight and the threshold and the learning rate is

$$\Delta \omega_{ij} = -\lambda \frac{\partial E_k}{\partial \omega_{ij}} (0 < \lambda < 1),$$

$$\Delta \theta_i = \lambda \delta_i (0 < \lambda < 1), \tag{14}$$

$$\delta_i = -\frac{\partial E_k}{\partial a_i},$$

where $\Delta \omega_{ij}$ represents the change in connection weights, $\Delta \theta_i$ represents the threshold change, δ_i represents the network error correction, a_i represents the network input value, and λ represents the learning rate.

5.4. Determination of Momentum Coefficient. The momentum term reflects the influence of the last weight change on momentum through the momentum coefficient. The value range of the momentum coefficient is $[0, 1]$. When the momentum constant is 0, the weight change is obtained according to the gradient. When the momentum constant is 1, the new weight change is equal to the last weight change. After introducing momentum, the iterative relationship that connects the weight and the threshold is

$$\omega_{ij}(n + 1) = \omega_{ij}(n) + \Delta \omega_{ij} + \rho \left[\omega_{ij}(n) - \omega_{ij}(n - 1)\right],$$

$$\theta_i(n + 1) = \theta_i(n) + \Delta \theta_i + \rho[\theta_i(n) - \theta_i(n - 1)], \tag{15}$$

where $\rho[\omega_{ij}(n) - \omega_{ij}(n - 1)]$ represents the momentum term and ρ represents the momentum factor.

5.5. Distributed BP Neural Network Parallel Computing. When carrying out cross-border e-commerce logistics cost prediction, it is necessary to train massive amounts of data to make the training results meet the requirements.

Therefore, this article combines the Spark cloud computing platform with BP neural network and uses the advantages of both to predict the logistics cost of cross-border e-commerce.

The BP neural network algorithm needs to be trained under multiple nodes. The calculation method of the final predicted value of $\bar{x}$ is

$$\bar{x} = \sum_{i=1}^{n} w_i x_i, \tag{16}$$

where x_i represents the predicted value of the i node and w_i represents the weight of the i node. The standard error of each node is expressed as

$$E = \frac{1}{2}(t - \bar{y})^2, \tag{17}$$

where t represents the target value of each input training set of the BP neural network. Implementation steps of cross-border e-commerce logistics cost prediction algorithm under Spark platform are as follows:

(1) Obtain massive data for cross-border e-commerce logistics cost prediction from the distributed file system of the Spark platform. The Map Partition function in Spark divides the prediction data set into ψ parts, where ψ is the number of Spark nodes

(2) The predicted result is obtained by running the designed BP neural network algorithm in the Map function of each node, which is equivalent to ψ neural networks

(3) Finally, through the Reduce function, the predicted values of ψ nodes are subjected to weight decision to obtain the final predicted value

Through the above steps, the intelligent forecast of cross-border e-commerce logistics costs is realized.

6. Experimental Analysis

6.1. Experimental Environment and Data. In order to verify the effectiveness of the cloud computing-based intelligent prediction method for cross-border e-commerce logistics costs, the experiment built a Spark platform composed of 9 nodes, and each node's machine configuration is Intel (R) Core (TM) i7-3537U CPU@ 2.50 GHz, 8 GB RAM, 160 G hard disk space, and 100 Mbit/s network bandwidth. Spark version is 1.0.2. This article uses the ubuntu12.04 system, the JDK1.7.0_55 version is used in the experiment, and SSH is installed to ensure the communication between the nodes. In this experiment, the system is debugged through a stand-alone pseudodistribution, and a fully distributed environment built with 9 nodes is used during the performance test. Taking a cross-border e-commerce logistics enterprise as an example, the cross-border e-commerce logistics cost samples are preprocessed by using cluster analysis method, combining qualitative and quantitative

methods, comprehensively considering the characteristics of cross-border e-commerce logistics cost drivers and their impact on the prediction results of cross-border e-commerce logistics cost. The input samples of the prediction model are divided into two parts: training samples and prediction samples. The training samples are used to determine the optimal weights and thresholds of the BP neural network model, and then, the optimized parameters are substituted into the BP neural network, and the prediction samples are input to obtain the prediction results.

6.2. Cross-Border E-Commerce Logistics Cost Prediction and Evaluation Indicators. In this paper, the prediction effect, prediction accuracy, and prediction efficiency are used as evaluation indexes. The predicted cost is compared with the actual predicted cost to measure the prediction effect. The more consistent the predicted cost is with the actual predicted cost, the better the prediction effect is. The root mean square (RMSE) of the prediction accuracy is used to measure the prediction accuracy. The smaller the RMSE value, the higher the prediction accuracy. RMSE is the main performance index to measure the advantages and disadvantages of cross-border e-commerce logistics cost prediction algorithm. The calculation formula is

$$\text{RMSE} = \frac{\sqrt{\sum_{i=1}^{n}\left(P_{mi} - P_{pi}\right)^2}}{\sqrt{n}} \times 100\%, \tag{18}$$

where n is the number of samples, P_{mi} is the actual cost at time i, and P_{pi} is the predicted cost at time i. Use the time taken to predict the cost to measure the forecasting efficiency. The shorter the forecasting time, the higher the forecasting efficiency.

6.3. Comparison of the Effect of Cross-Border E-Commerce Logistics Cost Prediction. In order to verify the prediction effect of the proposed method, the method of reference [4] and the method of reference [5] are used to compare with the proposed method, and the comparison results of cross-border e-commerce logistics cost prediction results of different methods are shown in Figure 6.

It can be seen from Figure 6 that the results of cross-border e-commerce logistics cost predictions based on the method of reference [4] and the method of reference [5] are quite different from the actual cross-border e-commerce logistics cost prediction results. The cross-border e-commerce logistics cost prediction results of the proposed method are more consistent with the actual cross-border e-commerce logistics cost prediction results. It can be seen that, compared with the method of reference [4] and the method of reference [5], the proposed method has a better effect of predicting the cost of cross-border e-commerce logistics.

6.4. Comparison of the Efficiency of Cross-Border E-Commerce Logistics Cost Prediction. To further verify the prediction efficiency of the proposed method, the method of reference [4], the method of reference [5], and the proposed method are used to compare, and the comparison
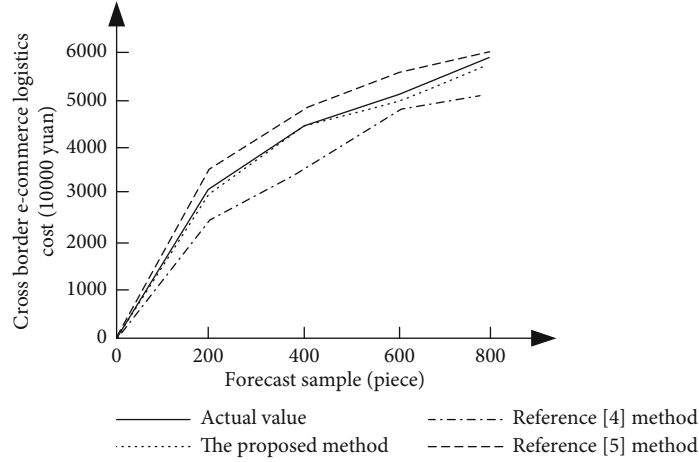
FIGURE 6: Comparison results of cross-border e-commerce logistics cost prediction results with different methods.

results of cross-border e-commerce logistics cost prediction time of different methods are shown in Figure 7.

It can be seen from Figure 7 that with the increase of the number of prediction samples, the prediction time of cross-border e-commerce logistics cost of different methods increases. When the number of prediction samples is 800, the cross-border e-commerce logistics cost prediction time of the method of reference [4] is 44.5 s, and the cross-border e-commerce logistics cost prediction time of the method of reference [5] is 55 s, while the cross-border e-commerce logistics cost prediction time of the proposed method is only 22.5 s. It can be seen that, compared with the method of reference [4] and the method of reference [5], the cross-border e-commerce logistics cost prediction time of the proposed method is shorter, and it can effectively improve the efficiency of cross-border e-commerce logistics cost prediction. Figures 6 and 7 compare the method in this paper with the traditional method. It can be seen through simulation that the method in this paper has good predictive ability, higher accuracy, and better fault tolerance.

6.5. Comparison of the Accuracy of Cross-Border E-Commerce Logistics Cost Prediction. On this basis, the prediction accuracy of the proposed method is further verified. The method of reference [4], the method of reference [5], and the proposed method are compared, respectively, and the RMSE values of cross-border e-commerce logistics cost prediction of different methods are obtained. The comparison results are shown in Table 1.

According to the data in Table 1, with the increase of the number of prediction samples, the RMSE value of cross-border e-commerce logistics cost prediction by different methods increases. When the number of prediction samples is 800, the RMSE value of cross-border e-commerce logistics cost prediction of the method of reference [4] is 21.47%, and the RMSE value of cross-border e-commerce logistics cost prediction of the method of reference [5] is 23.32%, while the RMSE value of cross-border e-commerce logistics cost prediction of the proposed method is only 13.65%. Therefore, compared with the methods of reference [4] and the methods of reference [5], the RMSE value of cross-border

FIGURE 7: Comparison results of different methods of cross-border e-commerce logistics cost forecast time.

TABLE 1: Comparison results of the RMSE value of cross-border e-commerce logistics cost forecast by different methods.

Predicted sample quantity (piece)	The proposed method (%)	The method of reference [4] (%)	The method of reference [5] (%)
200	3.34	7.98	9.76
400	6.18	12.87	15.83
600	10.97	17.79	20.66
800	13.65	21.47	23.32

e-commerce logistics cost prediction of the proposed method is smaller and the prediction accuracy of cross-border e-commerce logistics cost is higher.

7. Conclusion

The intelligent forecasting method of cross-border e-commerce logistics cost based on cloud computing proposed

in this paper gives full play to the advantages of cloud computing technology. The BP neural network algorithm is used to train a large number of input and output relationships for parameters in logistics. The intelligent prediction of cross-border e-commerce logistics cost has a good effect, which can effectively improve the accuracy and efficiency of cross-border e-commerce logistics cost intelligent prediction. However, in the process of intelligent cross-border e-commerce logistics cost prediction, because the BP neural network needs to normalize the samples before inputting the samples, there is a problem of selecting decimal places and there are certain errors. Therefore, in the following research, it is necessary to further consider the choice of decimal places to improve the calculation accuracy of the BP neural network, thereby improving the accuracy of the prediction results.

Data Availability

The data used to support the findings of this study are available from the corresponding author upon request.

Conflicts of Interest

The author declares that he has no conflict of interest.

Acknowledgments

References

[1] Y. Zhao, "Influencing factors of cross-border e-commerce trade between China and "belt and road" coastal and inland countries," *Journal of Coastal Research*, vol. 103, no. sp1, p. 70, 2020.

[2] X. Li, X. Zhao, and D. Bai, "Marine transport efficiency evaluation of cross-border logistics based on AHP-TOPSIS method," *Journal of Coastal Research*, vol. 110, pp. 2112–2119, 2020.

[3] X. Chen, "Marine transport efficiency evaluation of cross-border e-commerce logistics based on analytic hierarchy process," *Journal of Coastal Research*, vol. 94, no. sp1, p. 682, 2019.

[4] D. Metz, "Economic benefits of road widening: discrepancy between outturn and forecast," *Transportation Research Part A Policy and Practice*, vol. 147, no. 1, pp. 312–319, 2021.

[5] H. Wang and Z. Zhao, "Study on logistics cost optimization of offshore oil service industry based on offshore oil service cost model," *Journal of Coastal Research*, vol. 98, no. sp1, p. 171, 2019.

[6] M. N. Jahantigh, A. M. Rahmani, N. J. Navimirour, and A. Rezaee, "Integration of internet of things and cloud computing: a systematic survey," *IET Communications*, vol. 14, no. 2, pp. 165–176, 2020.

[7] W. G. Choi and S. Park, "A write-friendly approach to manage namespace of Hadoop distributed file system by utilizing nonvolatile memory," *The Journal of Supercomputing*, vol. 75, no. 10, pp. 6632–6662, 2019.

[8] N. Maleki, A. M. Rahmani, and M. Conti, "Map reduce: an infrastructure review and research insights," *The Journal of Supercomputing*, vol. 75, no. 10, pp. 6934–7002, 2019.

[9] L. Yin, L. Qin, Z. Jiang, and X. Xu, "A fast parallel attribute reduction algorithm using Apache Spark," *Knowledge-Based Systems*, vol. 212, article 106582, 2021.

[10] S. Liu, P. Reviriego, and F. Lombardi, "Selective neuron recomputation (SNRC) for error-tolerant neural networks," *IEEE Transactions on Computers*, vol. 99, 2021.

[11] Y. Ying, N. Zhang, P. Shan, L. Miao, P. Sun, and S. Peng, "Improving squeeze-and-excitation block with parametric sigmoid," *Applied Intelligence*, vol. 51, no. 10, pp. 7427–7439, 2021.

[12] B. Li, "Export effect of trade facilitation in Asian "belt and road" coastal countries on China's cross-border e-commerce," *Journal of Coastal Research*, vol. 104, p. 104, 2020.

[13] P. Gui and S. Na, "Empirical study on the application of activity-based cost model in marine third-party logistics cost management," *Journal of Coastal Research*, vol. 98, p. 195, 2019.

[14] Q. Ma, "BP neural network short-term traffic flow prediction based on improved particle swarm optimization," *Computer Simulation*, vol. 36, no. 4, pp. 94–98, 2019.

[15] L. Wen, X. Li, and L. Gao, "A new reinforcement learning based learning rate scheduler for convolutional neural network in fault classification," *IEEE Transactions on Industrial Electronics*, vol. 99, 2020.

Research Article

Characterizations and Entropy Measures of the Exponentiated Generalized Frechet Geometric Distribution

Naz Saud,[1] Aqsa Rafique,[1] Muhammad Ijaz,[2] Naila Amjad,[1] Mahmoud El-Morshedy [3,4] and Syed Habib Shah[5]

[1]*Lahore College for Women University, Lahore, Pakistan*
[2]*The University of Haripur, Haripur 22630, Pakistan*
[3]*Department of Mathematics, College of Science and Humanities in Al-Kharj, Prince Sattam bin Abdulaziz University, Al-Kharj 11942, Saudi Arabia*
[4]*Department of Mathematics, Faculty of Science, Mansoura University, Mansoura 35516, Egypt*
[5]*Institute of Numerical Sciences, Kohat University of Science and Technology, Kohat, KPK, Pakistan*

Correspondence should be addressed to Mahmoud El-Morshedy; mah_elmorshedy@mans.edu.eg

Some characterizations and entropy measures of the Exponentiated Generalized Fréchet Geometric (EGFG) distribution are studied in this paper. Firstly, characterizations of the EGFG distribution based on five different approaches are discussed. The submodels for the EGFG distribution with their characterization expressions formed on the ratio of two truncated moments are also presented. Secondly, four different entropy measures are considered and expressed analytically via the incomplete gamma function. The behavior of all these entropy measures is discussed by performing a numerical study.

1. Introduction

Characterization is a distributional property of statistics that determines the associated stochastic model. In designing a stochastic model for a particular modeling problem, it is crucial to validate whether the specified probability distribution fulfills the underlying conditions by its characterization before a specified probability model is used to fit data applications. Thus, it will rely on the characterization of the chosen distribution. It plays an essential role in different fields of mathematical and statistical sciences.

Although in several statistical applications, an increase in the number of parameters gives a more appropriate model, and a smaller number of parameters (without affecting the model suitability) is mathematically more attractive in characterization complications. Over the years, many researchers have studied the different techniques of characterization of continuous probability distributions such as Glänzel [1]; Glänzel [2]; Hamedani [3]; Hamedani [4];

Hamedani [5]; Hamedani and Ahsanullah [6]; Hamedani [7]; Bhatti et al. [8]; and Rafique and Saud [9]. Consequently, numerous characterization techniques have been studied in this paper.

Entropy is used to measure the amount of uncertainty, randomness, and disorderness in the system. These essential mathematical techniques are used to evaluate the uncertainty of the stochastic variable. To be more specific, the distribution of a random variable is related to some level of uncertainty, which is quantified by entropy.

In any stochastic process, the probability distribution varies over time; hence, it is clear that the entropy or uncertainty of a probability distribution changes over time as well. It becomes knowing how the uncertainty changes over time. The application of entropy measures is useful in many branches of science and disciplines. Several examples from different areas where different entropy concepts were used, e.g., topological entropy, Kolmogorov–Sinai entropy, topological order, can be found in the following references

proposed by Caneco et al. [10], Rocha and Aleixo [11], and Rocha and Carvalho [12].

The essential references in this regard are briefly presented below. Shannon [13] introduced the concept of entropy. Cho et al. [14] estimated the entropy of a Weibull distribution under generalized progressive hybrid censoring. The comparison of different entropy measures was discussed by Dey et al. [15]. Basit et al. [16] studied the entropy measures for weighted and truncated weighted exponential distributions. The entropy measures for the uncertainty quantification of stochastic processes were investigated by Namdari and Li [17], while Ijaz et al. [18] compared different

entropy measures for Lomax distribution using relative loss approach.

This present work deals with the characterization and entropy measures of the univariate continuous distribution named as "Exponentiated Generalized Fréchet Geometric (EGFG) distribution." The EGFG distribution was proposed by Rafique and Saud [19]. They studied the mathematical properties of the suggested model and also provided its application study.

The probability density function (*pdf*) and cumulative distribution function (*cdf*) of the Exponentiated Generalized Fréchet Geometric distribution with parameters η, κ, ϕ, δ, and $\tau \in (0, 1)$ are defined, respectively, as follows:

$$f(y; \underline{\theta}) = \frac{(1-\tau)\kappa\delta\phi\eta^{\phi}y^{-(\phi+1)}e^{-(\eta/y)^{\phi}}\left(1-e^{-(\eta/y)^{\phi}}\right)^{\kappa-1}\left[1-\left(1-e^{-(\eta/y)^{\phi}}\right)^{\kappa}\right]^{\delta-1}}{\left(1-\tau\left(1-\left[1-\left(1-e^{-(\eta/y)^{\phi}}\right)^{\kappa}\right]^{\delta}\right)\right)^{2}}, \quad y \geq 0, \eta, \kappa, \phi, \delta > 0, \ \tau \in (0, 1), \tag{1}$$

and

$$F(y; \underline{\theta}) = 1 - \frac{(1-\tau)\left(1-\left[1-\left(1-e^{-(\eta/y)^{\phi}}\right)^{\kappa}\right]^{\delta}\right)}{1-\tau\left(1-\left[1-\left(1-e^{-(\eta/y)^{\phi}}\right)^{\kappa}\right]^{\delta}\right)}. \tag{2}$$

$\theta \subseteq \mathbb{R}^{5}$ given by $\underline{\theta} = \left\{(\eta, \kappa, \phi, \delta, \tau) \in \mathbb{R}^{5}\right\}$ [19].

2. Structural Properties

According to Rafique and Saud [19], the hazard rate, reverse hazard rate, and survival function of the EGFG are defined, respectively, by

$$h(y) = \frac{\kappa\delta\phi\eta^{\phi}y^{-(\phi+1)}e^{-(\eta/y)^{\phi}}\left(1-e^{-(\eta/y)^{\phi}}\right)^{\kappa-1}\left[1-\left(1-e^{-(\eta/y)^{\phi}}\right)^{\kappa}\right]^{\delta-1}}{\left(1-\tau\left(1-\left[1-\left(1-e^{-(\eta/y)^{\phi}}\right)^{\kappa}\right]^{\delta}\right)\right)\left(1-\left[1-\left(1-e^{-(\eta/y)^{\phi}}\right)^{\kappa}\right]^{\delta}\right)}, \tag{3}$$

$$r(y) = \frac{(1-\tau)\kappa\delta\phi\eta^{\phi}y^{-(\phi+1)}e^{-(\eta/y)^{\phi}}\left(1-e^{-(\eta/y)^{\phi}}\right)^{\kappa-1}\left[1-\left(1-e^{-(\eta/y)^{\phi}}\right)^{\kappa}\right]^{\delta-1}\left(1-\tau\left(1-\left[1-\left(1-e^{-(\eta/y)^{\phi}}\right)^{\kappa}\right]^{\delta}\right)\right)^{-1}}{\left[1-\tau\left(1-\left[1-\left(1-e^{-(\eta/y)^{\phi}}\right)^{\kappa}\right]^{\delta}\right)-(1-\tau)\left(1-\left[1-\left(1-e^{-(\eta/y)^{\phi}}\right)^{\kappa}\right]^{\delta}\right)\right]}, \tag{4}$$

$$S(y) = \frac{(1-\tau)\left(1-\left[1-\left(1-e^{-(\eta/y)^{\phi}}\right)^{\kappa}\right]^{\delta}\right)}{1-\tau\left(1-\left[1-\left(1-e^{-(\eta/y)^{\phi}}\right)^{\kappa}\right]^{\delta}\right)}. \tag{5}$$

The mills ratio and elasticity function of any probability distribution can be defined as

$$m(y) = \frac{1 - F(y)}{f(y)},$$

(6)

$$e(y) = yr(y).$$

[20] The mills ratio and elasticity function of the EGFG distribution are given by

$$m(y) = \frac{\left(1 - \tau\left(1 - \left[1 - \left(1 - e^{-(\eta/y)^\phi}\right)^\kappa\right]^\delta\right)\right)\left(1 - \left[1 - \left(1 - e^{-(\eta/y)^\phi}\right)^\kappa\right]^\delta\right)}{\kappa\delta\phi\eta^\phi y^{-(\phi+1)} e^{-(\eta/y)^\phi}\left(1 - e^{-(\eta/y)^\phi}\right)^{\kappa-1}\left[1 - \left(1 - e^{-(\eta/y)^\phi}\right)^\kappa\right]^{\delta-1}},$$

(7)

$$e(y) = \frac{(1-\tau)\kappa\delta\phi\eta^\phi y^{-\phi} e^{-(\eta/y)^\phi}\left(1 - e^{-(\eta/y)^\phi}\right)^{\kappa-1}\left[1 - \left(1 - e^{-(\eta/y)^\phi}\right)^\kappa\right]^{\delta-1}\left(1 - \tau\left(1 - \left[1 - \left(1 - e^{-(\eta/y)^\phi}\right)^\kappa\right]^\delta\right)\right)^{-1}}{\left[1 - \tau\left(1 - \left[1 - \left(1 - e^{-(\eta/y)^\phi}\right)^\kappa\right]^\delta\right) - (1-\tau)\left(1 - \left[1 - \left(1 - e^{-(\eta/y)^\phi}\right)^\kappa\right]^\delta\right)\right]}.$$

(8)

3. Materials and Methods

3.1. Characterization via Ratio of Two Truncated Moments.
The EGFG distribution is characterized through ratio of two truncated moments. Glanzel [21] stated that this characterization is stable in the sense of weak convergence.

Proposition 1. *Suppose* $Y: \Omega \longrightarrow (0, \infty)$ *be a continuous random variable with probability density function defined in equation (1) and let*

$$k_1(y) = 1,$$

(9)

$$k_2(y) = k_1(y)\left\{\frac{(1-\tau)\left(1 - \left[1 - \left(1 - e^{-(\eta/y)^\phi}\right)^\kappa\right]^\delta\right)}{1 - \tau\left(1 - \left[1 - \left(1 - e^{-(\eta/y)^\phi}\right)^\kappa\right]^\delta\right)}\right\}, \quad y > 0,$$

(10)

and then, the function Σ *which is presented in theorem (Glänzel [1, 2]) has the following expression:*

$$\Sigma(y) = \frac{1}{2}\left\{\frac{(1-\tau)\left(1 - \left[1 - \left(1 - e^{-(\eta/y)^\phi}\right)^\kappa\right]^\delta\right)}{1 - \tau\left(1 - \left[1 - \left(1 - e^{-(\eta/y)^\phi}\right)^\kappa\right]^\delta\right)}\right\}, \quad y > 0.$$

(11)

Proof. Suppose Y has *pdf* in equation (1), then

$$(1 - F(y))E(k_1|Y \geq y) = \left\{\frac{(1-\tau)\left(1 - \left[1 - \left(1 - e^{-(\eta/y)^\phi}\right)^\kappa\right]^\delta\right)}{1 - \tau\left(1 - \left[1 - \left(1 - e^{-(\eta/y)^\phi}\right)^\kappa\right]^\delta\right)}\right\}, \quad y > 0,$$

(12)

$$(1 - F(y))E(k_2|Y \geq y) = \frac{1}{2}\left\{\frac{(1-\tau)\left(1 - \left[1 - \left(1 - e^{-(\eta/y)^\phi}\right)^\kappa\right]^\delta\right)}{1 - \tau\left(1 - \left[1 - \left(1 - e^{-(\eta/y)^\phi}\right)^\kappa\right]^\delta\right)}\right\}^2,$$

and so

$$\Sigma(y) = \frac{(1-F(y))E(k_2|Y \geq y)}{(1-F(y))E(k_1|Y \geq y)} = \frac{1}{2}\left\{\frac{(1-\tau)\left(1-\left[1-\left(1-e^{-(\eta/y)^{\phi}}\right)^{\kappa}\right]^{\delta}\right)}{1-\tau\left(1-\left[1-\left(1-e^{-(\eta/y)^{\phi}}\right)^{\kappa}\right]^{\delta}\right)}\right\}, \tag{13}$$

$$\Sigma'(y) = -\frac{1}{2}\frac{(1-\tau)\kappa\delta\phi\eta^{\phi}y^{-\phi}e^{-(\eta/y)^{\phi}}\left(1-e^{-(\eta/y)^{\phi}}\right)^{\kappa-1}\left[1-\left(1-e^{-(\eta/y)^{\phi}}\right)^{\kappa}\right]^{\delta-1}}{\left(1-\tau\left(1-\left[1-\left(1-e^{-(\eta/y)^{\phi}}\right)^{\kappa}\right]^{\delta}\right)\right)^2}. \tag{14}$$

As

$$\Sigma(y)k_1(y) - k_2(y) = -\frac{k_1(y)}{2}\left\{\frac{(1-\tau)\left(1-\left[1-\left(1-e^{-(\eta/y)^{\phi}}\right)^{\kappa}\right]^{\delta}\right)}{1-\tau\left(1-\left[1-\left(1-e^{-(\eta/y)^{\phi}}\right)^{\kappa}\right]^{\delta}\right)}\right\} \neq 0, \quad \forall y, \tag{15}$$

the proof is as follows:

Conversely, if Σ is defined as above, then

$$s'(y) = \frac{\Sigma'(y)k_1(y)}{\Sigma(y)k_1(y) - k_2(y)} = \frac{\Sigma'(y)k_1(y)}{-(1/2)k_2(y)},$$

$$s'(y) = \frac{\kappa\delta\phi\eta^{\phi}y^{-(\phi+1)}e^{-(\eta/y)^{\phi}}\left(1-e^{-(\eta/y)^{\phi}}\right)^{\kappa-1}\left[1-\left(1-e^{-(\eta/y)^{\phi}}\right)^{\kappa}\right]^{\delta-1}}{\left(1-\tau\left(1-\left[1-\left(1-e^{-(\eta/y)^{\phi}}\right)^{\kappa}\right]^{\delta}\right)\right)\left(1-\left[1-\left(1-e^{-(\eta/y)^{\phi}}\right)^{\kappa}\right]^{\delta}\right)}, \tag{16}$$

and hence,

$$s(y) = -\ln\left\{\frac{(1-\tau)\left(1-\left[1-\left(1-e^{-(\eta/y)^{\phi}}\right)^{\kappa}\right]^{\delta}\right)}{1-\tau\left(1-\left[1-\left(1-e^{-(\eta/y)^{\phi}}\right)^{\kappa}\right]^{\delta}\right)}\right\}, \tag{17}$$

and

$$e^{-s(y)} = \frac{(1-\tau)\left(1-\left[1-\left(1-e^{-(\eta/y)^{\phi}}\right)^{\kappa}\right]^{\delta}\right)}{1-\tau\left(1-\left[1-\left(1-e^{-(\eta/y)^{\phi}}\right)^{\kappa}\right]^{\delta}\right)}, \quad y > 0. \tag{18}$$

Therefore, in the light of theorem, given in Glänzel [1] and Glanzel [21], Y has *pdf* in equation (1).

Corollary 1. *Suppose that the continuous random $Y: \Omega \longrightarrow (0, \infty)$ and let $k_1(y)$ as given in proposition equation (1). The pdf of Y in equation (1) provided functions $k_2(y)$ and Σ defined in the theorem (Glänzel [1]). The theorem is based on truncated moments specified in the ratio form.*

$$\frac{\Sigma'(y)k_1(y)}{\Sigma(y)k_1(y) - k_2(y)} = \frac{\kappa\delta\phi\eta^{\phi}y^{-(\phi+1)}e^{-(\eta/y)^{\phi}}\left(1-e^{-(\eta/y)^{\phi}}\right)^{\kappa-1}\left[1-\left(1-e^{-(\eta/y)^{\phi}}\right)^{\kappa}\right]^{\delta-1}}{\left(1-\tau\left(1-\left[1-\left(1-e^{-(\eta/y)^{\phi}}\right)^{\kappa}\right]^{\delta}\right)\right)\left(1-\left[1-\left(1-e^{-(\eta/y)^{\phi}}\right)^{\kappa}\right]^{\delta}\right)}. \tag{19}$$

Remark 1. The solution of the equation in corollary equation (1) is

$$\Sigma(y) = \frac{1 - \tau\left(1 - \left[1 - \left(1 - e^{-(\eta/y)^\phi}\right)^\kappa\right]^\delta\right)}{(1 - \tau)\left(1 - \left[1 - \left(1 - e^{-(\eta/y)^\phi}\right)^\kappa\right]^\delta\right)}$$

$$\int\left\{\frac{-g(y)(1 - \tau)\kappa\delta\phi\eta^\phi y^{-\phi}e^{-(\eta/y)^\phi}\left(1 - e^{-(\eta/y)^\phi}\right)^{\kappa-1}\left[1 - \left(1 - e^{-(\eta/y)^\phi}\right)^\kappa\right]^{\delta-1}}{\left(1 - \tau\left(1 - \left[1 - \left(1 - e^{-(\eta/y)^\phi}\right)^\kappa\right]^\delta\right)\right)^2}\right\}dy + D,$$

$$(20)$$

where D is the constant.

3.1.1. Special Cases of the Exponentiated Generalized Fréchet Geometric Distribution.

The expressions of $k_1(y)$, $k_2(y)$, and $\Sigma(y)$ to characterize the submodels of the EGFG distribution are given as follows:

(1) Generalized Fréchet Geometric Distribution. Putting $\kappa = 1$, suppose that

$$k_1(y) = 1,$$

$$k_2(y) = k_1(y)\frac{(1 - \tau)\left(1 - e^{-\delta(\eta/y)^\phi}\right)}{1 - \tau\left(1 - e^{-\delta(\eta/y)^\phi}\right)}, \quad y \geq 0, \quad (21)$$

so that Y follows GFG distribution if and only if the function Σ obtained in Proposition 1 has the following expression:

$$\Sigma(y) = \frac{1}{2}\frac{(1 - \tau)\left(1 - e^{-\delta(\eta/y)^\phi}\right)}{1 - \tau\left(1 - e^{-\delta(\eta/y)^\phi}\right)}. \quad (22)$$

(2) Fréchet Geometric Distribution. For $\kappa = \delta = 1$, let

$$k_1(y) = 1,$$

$$k_2(y) = k_1(y)\frac{(1 - \tau)\left(1 - e^{-(\eta/y)^\phi}\right)}{1 - \tau\left(1 - e^{-(\eta/y)^\phi}\right)}, \quad y \geq 0, \quad (23)$$

and if Σ obtained in Proposition 1 has the expression, then Y follows Fréchet Geometric distribution as follows:

$$\Sigma(y) = \frac{1}{2}\frac{(1 - \tau)\left(1 - e^{-(\eta/y)^\phi}\right)}{1 - \tau\left(1 - e^{-(\eta/y)^\phi}\right)}. \quad (24)$$

(3) Inverse Rayleigh Geometric Distribution. With $\kappa = 1$, $\delta = 1$, and $\phi = 2$, we get

$$k_1(y) = 1,$$

$$k_2(y) = k_1(y)\frac{(1 - \tau)\left(1 - e^{-(\eta/y)^2}\right)}{1 - \tau\left(1 - e^{-(\eta/y)^2}\right)}, \quad y \geq 0, \quad (25)$$

and then, r.v. Y follows IRG distribution if the function Σ has the following expression:

$$\Sigma(y) = \frac{1}{2}\frac{(1 - \tau)\left(1 - e^{-(\eta/y)^2}\right)}{1 - \tau\left(1 - e^{-(\eta/y)^2}\right)}. \quad (26)$$

(4) Inverse Exponential Distribution. For $\kappa = \delta = \phi = 1$, we have

$$k_1(y) = 1,$$

$$k_2(y) = k_1(y)\frac{(1 - \tau)\left(1 - e^{-(\eta/y)^1}\right)}{1 - \tau\left(1 - e^{-(\eta/y)^1}\right)}, \quad y \geq 0, \quad (27)$$

and

$$\Sigma(y) = \frac{1}{2}\frac{(1 - \tau)\left(1 - e^{-(\eta/y)^1}\right)}{1 - \tau\left(1 - e^{-(\eta/y)^1}\right)}. \quad (28)$$

3.2. Characterization of EGFG under Hazard Rate Function.

In this subsection, the characterization of the EGFG distribution is obtained by hazard rate function.

Definition 1. Suppose the absolutely continuous random variable "Y" with $pdf f(y)$ and $cdf F(y)$. The hazard function to F is symbolized as h_F and is obtained by

$$h_F(y) = \frac{f(y)}{1 - F(y)}, \quad y \in \text{Supp} \quad F, \quad (29)$$

where F represents twice "differentiable distribution function." The hazard function satisfies the following differential equation:

$$\frac{h_F'(y)}{h_F(y)} - h_F(y) = \frac{f'(y)}{f(y)} = \sigma(y), \qquad (30)$$

where $\sigma(y)$ is an appropriate integrable function. The purpose here is to define a differential equation that has a simple form as possible and a nontrivial form as in equation (30). However, in some continuous distributions, this may be impossible.

Proposition 2. Let the random variable $Y: \Omega \in (0, \infty)$ follows the EGFG distribution. The density function of "Y" is equation (1) if and only if its hazard rate function $h_F(y)$ satisfies the following differential equation:

$$h_F'(y) - (-\phi - 1)y^{-1}h_F(y) = \tau^2 \left[\kappa\delta\phi\eta^\phi y^{-(\phi+1)} e^{-(\eta/y)^\phi} \left(1 - e^{-(\eta/y)^\phi}\right)^{\kappa-1} \left[1 - \left(1 - e^{-(\eta/y)^\phi}\right)^\kappa\right]^{\delta-1}\right]^2$$

$$\frac{\left(1 - \tau\left(1 - \left[1 - \left(1 - e^{-(\eta/y)^\phi}\right)^\kappa\right]^\delta\right)\right)^{-1}}{\tau\left(1 - \left[1 - \left(1 - e^{-(\eta/y)^\phi}\right)^\kappa\right]^\delta\right)} \left[(\tau\delta)^{-1}(\delta - 1)\left[1 - \left(1 - e^{-(\eta/y)^\phi}\right)^\kappa\right]^{-\delta} +\right.$$

$$\frac{\phi\eta^\phi y^{-(\phi+1)} - (\kappa - 1)\phi\eta^\phi y^{-(\phi+1)} e^{-(\eta/y)^\phi}\left(1 - e^{-(\eta/y)^\phi}\right)^{-1}}{\tau\left[\kappa\delta\phi\eta^\phi y^{-(\phi+1)} e^{-(\eta/y)^\phi}\left(1 - e^{-(\eta/y)^\phi}\right)^{\kappa-1}\left[1 - \left(1 - e^{-(\eta/y)^\phi}\right)^\kappa\right]^{\delta-1}\right]} - \qquad (31)$$

$$2\left(1 - \tau\left(1 - \left[1 - \left(1 - e^{-(\eta/y)^\phi}\right)^\kappa\right]^\delta\right)\right)^{-1} + \frac{\left(1 - \tau\left(1 - \left[1 - \left(1 - e^{-(\eta/y)^\phi}\right)^\kappa\right]^\delta\right)\right)^{-1}}{\tau\left(1 - \left[1 - \left(1 - e^{-(\eta/y)^\phi}\right)^\kappa\right]^\delta\right)}\right].$$

Proof. If the r.v Y has the *hrf* given in equation (3), then

$$h_F'(y) = \tau^2 \left[\kappa\delta\phi\eta^\phi y^{-(\phi+1)} e^{-(\eta/y)^\phi}\left(1 - e^{-(\eta/y)^\phi}\right)^{\kappa-1}\left[1 - \left(1 - e^{-(\eta/y)^\phi}\right)^\kappa\right]^{\delta-1}\right]^2$$

$$\frac{\left(1 - \tau\left(1 - \left[1 - \left(1 - e^{-(\eta/y)^\phi}\right)^\kappa\right]^\delta\right)\right)^{-1}}{\tau\left(1 - \left[1 - \left(1 - e^{-(\eta/y)^\phi}\right)^\kappa\right]^\delta\right)} \left[(\tau\delta)^{-1}(\delta - 1)\left[1 - \left(1 - e^{-(\eta/y)^\phi}\right)^\kappa\right]^{-\delta} +\right.$$

$$\frac{-(\phi + 1)y^{-1} + \phi\eta^\phi y^{-(\phi+1)} - (\kappa - 1)\phi\eta^\phi y^{-(\phi+1)} e^{-(\eta/y)^\phi}\left(1 - e^{-(\eta/y)^\phi}\right)^{-1}}{\tau\left[\kappa\delta\phi\eta^\phi y^{-(\phi+1)} e^{-(\eta/y)^\phi}\left(1 - e^{-(\eta/y)^\phi}\right)^{\kappa-1}\left[1 - \left(1 - e^{-(\eta/y)^\phi}\right)^\kappa\right]^{\delta-1}\right]}$$

$$-2\left(1 - \tau\left(1 - \left[1 - \left(1 - e^{-(\eta/y)^\phi}\right)^\kappa\right]^\delta\right)\right)^{-1} + \frac{\left(1 - \tau\left(1 - \left[1 - \left(1 - e^{-(\eta/y)^\phi}\right)^\kappa\right]^\delta\right)\right)^{-1}}{\tau\left(1 - \left[1 - \left(1 - e^{-(\eta/y)^\phi}\right)^\kappa\right]^\delta\right)}\right],$$

$$h_F'(y) - (-\phi - 1)y^{-1}h_F(y) = \tau^2 \left[\kappa\delta\phi\eta^\phi y^{-(\phi+1)} e^{-(\eta/y)^\phi}\left(1 - e^{-(\eta/y)^\phi}\right)^{\kappa-1}\left[1 - \left(1 - e^{-(\eta/y)^\phi}\right)^\kappa\right]^{\delta-1}\right]^2$$

$$\frac{\left(1-\tau\left(1-\left[1-\left(1-e^{-(\eta/y)^{\phi}}\right)^{\kappa}\right]^{\delta}\right)\right)^{-1}}{\tau\left(1-\left[1-\left(1-e^{-(\eta/y)^{\phi}}\right)^{\kappa}\right]^{\delta}\right)}\left[(\tau\delta)^{-1}(\delta-1)\left[1-\left(1-e^{-(\eta/y)^{\phi}}\right)^{\kappa}\right]^{-\delta}+\right.$$

$$\frac{\phi\eta^{\phi}y^{-(\phi+1)}-(\kappa-1)\phi\eta^{\phi}y^{-(\phi+1)}e^{-(\eta/y)^{\phi}}\left(1-e^{-(\eta/y)^{\phi}}\right)^{-1}}{\tau\left[\kappa\delta\phi\eta^{\phi}y^{-(\phi+1)}e^{-(\eta/y)^{\phi}}\left(1-e^{-(\eta/y)^{\phi}}\right)^{\kappa-1}\left[1-\left(1-e^{-(\eta/y)^{\phi}}\right)^{\kappa}\right]^{\delta-1}\right]}$$

$$\left.-2\left(1-\tau\left(1-\left[1-\left(1-e^{-(\eta/y)^{\phi}}\right)^{\kappa}\right]^{\delta}\right)\right)^{-1}+\frac{\left(1-\tau\left(1-\left[1-\left(1-e^{-(\eta/y)^{\phi}}\right)^{\kappa}\right]^{\delta}\right)\right)^{-1}}{\tau\left(1-\left[1-\left(1-e^{-(\eta/y)^{\phi}}\right)^{\kappa}\right]^{\delta}\right)}\right],$$

$$\frac{d}{dy}\left[y^{\phi+1}h_F(y)\right]=\frac{d}{dy}\left[\frac{\kappa\delta\phi\eta^{\phi}e^{-(\eta/y)^{\phi}}\left(1-e^{-(\eta/y)^{\phi}}\right)^{\kappa-1}\left[1-\left(1-e^{-(\eta/y)^{\phi}}\right)^{\kappa}\right]^{\delta-1}}{\left(1-\tau\left(1-\left[1-\left(1-e^{-(\eta/y)^{\phi}}\right)^{\kappa}\right]^{\delta}\right)\right)\left(1-\left[1-\left(1-e^{-(\eta/y)^{\phi}}\right)^{\kappa}\right]^{\delta}\right)}\right], \tag{32}$$

and simplification results in equation (3).

3.3. Characterization of EGFG under Reverse Hazard Rate Function.
In this subsection, the EGFG distribution is characterized via the reverse hazard rate function.

Definition 2. Suppose the absolutely continuous random variable "Y" with *pdf* equation (1) and *cdf* equation (2). The reverse hazard rate function to F is symbolized as r_F and is given by

$$r_F(y)=\frac{f(y)}{F(y)}, \quad y\in\mathrm{Supp}F, \tag{33}$$

where F represents the twice "differentiable distribution function." The reverse hazard function satisfies the following differential equation:

$$\frac{f'(y)}{f(y)}=\frac{r_F'(y)}{r_F(y)}+r_F(y). \tag{34}$$

Proposition 3. Let the random variable $Y:\Omega\in(0,\infty)$ follows the EGFG distribution. The density function of Y is equation (1) if and only if its reverse hazard function $r_F(y)$ satisfies the following differential equation:

$$r_F'(y)-(-\phi-1)y^{-1}r_F(y)=\tau^2\left[\kappa\delta\phi\eta^{\phi}y^{-(\phi+1)}e^{-(\eta/y)^{\phi}}\left(1-e^{-(\eta/y)^{\phi}}\right)^{\kappa-1}\left[1-\left(1-e^{-(\eta/y)^{\phi}}\right)^{\kappa}\right]^{\delta-1}\right]^2$$

$$\tau(1-\tau)-\frac{\tau\left(1-\left[1-\left(1-e^{-(\eta/y)^{\phi}}\right)^{\kappa}\right]^{\delta}\right)}{\left(1-\tau\left(1-\left[1-\left(1-e^{-(\eta/y)^{\phi}}\right)^{\kappa}\right]^{\delta}\right)\right)}\left[(\tau\delta)^{-1}(\delta-1)\left[1-\left(1-e^{-(\eta/y)^{\phi}}\right)^{\kappa}\right]^{-\delta}+\right.$$

$$\frac{+\phi\eta^{\phi}y^{-(\phi+1)}-(\kappa-1)\phi\eta^{\phi}y^{-(\phi+1)}e^{-(\eta/y)^{\phi}}\left(1-e^{-(\eta/y)^{\phi}}\right)^{-1}}{\tau\left[\kappa\delta\phi\eta^{\phi}y^{-(\phi+1)}e^{-(\eta/y)^{\phi}}\left(1-e^{-(\eta/y)^{\phi}}\right)^{\kappa-1}\left[1-\left(1-e^{-(\eta/y)^{\phi}}\right)^{\kappa}\right]^{\delta-1}\right]}$$

$$-2\left(1-\tau\left(1-\left[1-\left(1-e^{-(\eta/y)^\phi}\right)^\kappa\right]^\delta\right)\right)^{-1}$$

$$-\frac{\left(\left(1-\tau\left(1-\left[1-\left(1-e^{-(\eta/y)^\phi}\right)^\kappa\right]^\delta\right)\right)^{-2}\Big/\tau\left(1-\left[1-\left(1-e^{-(\eta/y)^\phi}\right)^\kappa\right]^\delta\right)\right)\right]}{\tau(1-\tau)-\left(1-\tau\left(1-\left[1-\left(1-e^{-(\eta/y)^\phi}\right)^\kappa\right]^\delta\right)\right)}. \tag{35}$$

Proof. If the r.v Y has density function in equation (1), then surely equation (35) holds.

$$r_F'(y)=\tau^2\left[\kappa\delta\phi\eta^\phi y^{-(\phi+1)}e^{-(\eta/y)^\phi}\left(1-e^{-(\eta/y)^\phi}\right)^{\kappa-1}\left[1-\left(1-e^{-(\eta/y)^\phi}\right)^\kappa\right]^{\delta-1}\right]^2$$

$$\tau(1-\tau)-\frac{\tau\left(1-\left[1-\left(1-e^{-(\eta/y)^\phi}\right)^\kappa\right]^\delta\right)}{\left(1-\tau\left(1-\left[1-\left(1-e^{-(\eta/y)^\phi}\right)^\kappa\right]^\delta\right)\right)}\left[(\tau\delta)^{-1}(\delta-1)\left[1-\left(1-e^{-(\eta/y)^\phi}\right)^\kappa\right]^{-\delta}+\right.$$

$$\frac{-(\phi+1)y^{-1}+\phi\eta^\phi y^{-(\phi+1)}-(\kappa-1)\phi\eta^\phi y^{-(\phi+1)}e^{-(\eta/y)^\phi}\left(1-e^{-(\eta/y)^\phi}\right)^{-1}}{\tau\left[\kappa\delta\phi\eta^\phi y^{-(\phi+1)}e^{-(\eta/y)^\phi}\left(1-e^{-(\eta/y)^\phi}\right)^{\kappa-1}\left[1-\left(1-e^{-(\eta/y)^\phi}\right)^\kappa\right]^{\delta-1}\right]}$$

$$-2\left(1-\tau\left(1-\left[1-\left(1-e^{-(\eta/y)^\phi}\right)^\kappa\right]^\delta\right)\right)^{-1}$$

$$-\frac{\left(\left(1-\tau\left(1-\left[1-\left(1-e^{-(\eta/y)^\phi}\right)^\kappa\right]^\delta\right)\right)^{-2}\Big/\tau\left(1-\left[1-\left(1-e^{-(\eta/y)^\phi}\right)^\kappa\right]^\delta\right)\right)\right]}{\tau(1-\tau)-\left(1-\tau\left(1-\left[1-\left(1-e^{-(\eta/y)^\phi}\right)^\kappa\right]^\delta\right)\right)}$$

$$r_F'(y)-(-\phi-1)y^{-1}r_F(y)=\tau^2\left[\kappa\delta\phi\eta^\phi y^{-(\phi+1)}e^{-(\eta/y)^\phi}\left(1-e^{-(\eta/y)^\phi}\right)^{\kappa-1}\left[1-\left(1-e^{-(\eta/y)^\phi}\right)^\kappa\right]^{\delta-1}\right]^2$$

$$\tau(1-\tau)-\frac{\tau\left(1-\left[1-\left(1-e^{-(\eta/y)^\phi}\right)^\kappa\right]^\delta\right)}{\left(1-\tau\left(1-\left[1-\left(1-e^{-(\eta/y)^\phi}\right)^\kappa\right]^\delta\right)\right)}\left[(\tau^{-1}\delta)(\delta-1)\left[1-\left(1-e^{-(\eta/y)^\phi}\right)^\kappa\right]^{-\delta}+\right.$$

$$\frac{+\phi\eta^\phi y^{-(\phi+1)}-(\kappa-1)\phi\eta^\phi y^{-(\phi+1)}e^{-(\eta/y)^\phi}\left(1-e^{-(\eta/y)^\phi}\right)^{-1}}{\tau\left[\kappa\delta\phi\eta^\phi y^{-(\phi+1)}e^{-(\eta/y)^\phi}\left(1-e^{-(\eta/y)^\phi}\right)^{\kappa-1}\left[1-\left(1-e^{-(\eta/y)^\phi}\right)^\kappa\right]^{\delta-1}\right]}$$

$$-2\left(1-\tau\left(1-\left[1-\left(1-e^{-(\eta/y)^\phi}\right)^\kappa\right]^\delta\right)\right)^{-1}$$

$$-\frac{\left(\left(1-\tau\left(1-\left[1-\left(1-e^{-(\eta/y)^\phi}\right)^\kappa\right]^\delta\right)\right)^{-2}/\tau\left(1-\left[1-\left(1-e^{-(\eta/y)^\phi}\right)^\kappa\right]^\delta\right)\right)}{\tau(1-\tau)-\left(1-\tau\left(1-\left[1-\left(1-e^{-(\eta/y)^\phi}\right)^\kappa\right]^\delta\right)\right)},$$

$$\frac{d}{dy}\left[y^{(\phi+1)}r(y)\right]=$$

$$\frac{d}{dy}\left[\frac{(1-\tau)\kappa\delta\phi\eta^\phi e^{-(\eta/y)^\phi}\left(1-e^{-(\eta/y)^\phi}\right)^{\kappa-1}\left[1-\left(1-e^{-(\eta/y)^\phi}\right)^\kappa\right]^{\delta-1}\left(1-\tau\left(1-\left[1-\left(1-e^{-(\eta/y)^\phi}\right)^\kappa\right]^\delta\right)\right)^{-1}}{\left[1-\tau\left(1-\left[1-\left(1-e^{-(\eta/y)^\phi}\right)^\kappa\right]^\delta\right)\right]-(1-\tau)\left(1-\left[1-\left(1-e^{-(\eta/y)^\phi}\right)^\kappa\right]^\delta\right)}\right],$$

$$(36)$$

and simplification results in equation (4).

3.4. Characterization of EGFG under Mills Ratio. In this subsection, the EGFG distribution is characterized via mills ratio.

Definition 3. Suppose the absolutely continuous random variable "Y" with *pdf* $f(y)$ and *cdf* $F(y)$. The mills ratio to F is symbolized as m_F and is obtained by

$$m_F(y)=\frac{1-F(y)}{f(y)},\quad y\in\text{Supp}F,\qquad(37)$$

where F represents the twice "differentiable distribution function." The mills ratio satisfies the following differential equation:

$$\frac{f'(y)}{f(y)}=\sigma(y)=-\left[\frac{m_F'(y)}{m_F(y)}+\frac{1}{m_F(y)}\right],\qquad(38)$$

where $\sigma(y)$ is an appropriate integrable function.

Proposition 4. *Let the random variable $Y:\Omega\in(0,\infty)$ follows the EGFG distribution. The density function of Y is equation (1) if and only if its mills ratio $m_F(y)$ defined in equation (7) satisfies the following differential equation:*

$$y^{-(\phi+1)}m'(y)-(\phi+1)y^{-(\phi+2)}m(y)=-y^{-(\phi+1)}\frac{\left(1-\left[1-\left(1-e^{-(\eta/y)^\phi}\right)^\kappa\right]^\delta\right)}{\left(1-\tau\left(1-\left[1-\left(1-e^{-(\eta/y)^\phi}\right)^\kappa\right]^\delta\right)\right)^{-1}}$$

$$\left[-2\left(1-\tau\left(1-\left[1-\left(1-e^{-\left(\frac{\eta}{y}\right)^\phi}\right)^\kappa\right]^\delta\right)\right)^{-1}+\left(\tau^{-1}\delta\right)(\delta-1)\left[1-\left(1-e^{-(\eta/y)^\phi}\right)^\kappa\right]^{-\delta}+\right.$$

$$\left.\frac{\phi\eta^\phi y^{-(\phi+1)}-(\kappa-1)\phi\eta^\phi y^{-(\phi+1)}e^{-(\eta/y)^\phi}\left(1-e^{-(\eta/y)^\phi}\right)^{-1}}{\tau\left[\kappa\delta\phi\eta^\phi y^{-(\phi+1)}e^{-(\eta/y)^\phi}\left(1-e^{-(\eta/y)^\phi}\right)^{\kappa-1}\left[1-\left(1-e^{-(\eta/y)^\phi}\right)^\kappa\right]^{\delta-1}\right]}\right]-y^{-(\phi+1)}.$$

$$(39)$$

Proof. If the r.v Y has density function equation (1), then surely equation (7) holds.

$$m'(y) = -\frac{\left(1-\left[1-\left(1-e^{-(\eta/y)^\phi}\right)^\kappa\right]^\delta\right)}{\left(1-\tau\left(1-\left[1-\left(1-e^{-(\eta/y)^\phi}\right)^\kappa\right]^\delta\right)\right)^{-1}}$$

$$\left[-2\left(1-\tau\left(1-\left[1-\left(1-e^{-(\eta/y)^\phi}\right)^\kappa\right]^\delta\right)\right)^{-1}+\left(\tau^{-1}\delta\right)(\delta-1)\left[1-\left(1-e^{-(\eta/y)^\phi}\right)^\kappa\right]^{-\delta}+\right.$$

$$\left.\frac{-(\phi+1)y^{-1}+\phi\eta^\phi y^{-(\phi+1)}-(\kappa-1)\phi\eta^\phi y^{-(\phi+1)}e^{-(\eta/y)^\phi}\left(1-e^{-(\eta/y)^\phi}\right)^{-1}}{\tau\left[\kappa\delta\phi\eta^\phi y^{-(\phi+1)}e^{-(\eta/y)^\phi}\left(1-e^{-(\eta/y)^\phi}\right)^{\kappa-1}\left[1-\left(1-e^{-(\eta/y)^\phi}\right)^\kappa\right]^{\delta-1}\right]}\right]-1,$$

$$y^{-(\phi+1)}m'(y)-(\phi+1)y^{-(\phi+2)}m(y) = -y^{-(\phi+1)}\frac{\left(1-\left[1-\left(1-e^{-(\eta/y)^\phi}\right)^\kappa\right]^\delta\right)}{\left(1-\tau\left(1-\left[1-\left(1-e^{-(\eta/y)^\phi}\right)^\kappa\right]^\delta\right)\right)^{-1}}$$

$$\left[-2\left(1-\tau\left(1-\left[1-\left(1-e^{-(\eta/y)^\phi}\right)^\kappa\right]^\delta\right)\right)^{-1}+\left(\tau^{-1}\delta\right)(\delta-1)\left[1-\left(1-e^{-(\eta/y)^\phi}\right)^\kappa\right]^{-\delta}+\right.$$

$$\left.\frac{\phi\eta^\phi y^{-(\phi+1)}-(\kappa-1)\phi\eta^\phi y^{-(\phi+1)}e^{-(\eta/y)^\phi}\left(1-e^{-(\eta/y)^\phi}\right)^{-1}}{\tau\left[\kappa\delta\phi\eta^\phi y^{-(\phi+1)}e^{-(\eta/y)^\phi}\left(1-e^{-(\eta/y)^\phi}\right)^{\kappa-1}\left[1-\left(1-e^{-(\eta/y)^\phi}\right)^\kappa\right]^{\delta-1}\right]}\right]-y^{-(\phi+1)},$$

$$\frac{d}{dy}\left[m_F(y)y^{-(\phi+1)}\right] = \frac{d}{dy}\left[\frac{\left(1-\tau\left(1-\left[1-\left(1-e^{-(\eta/y)^\phi}\right)^\kappa\right]^\delta\right)\right)\left(1-\left[1-\left(1-e^{-(\eta/y)^\phi}\right)^\kappa\right]^\delta\right)}{\kappa\delta\phi\eta^\phi e^{-(\eta/y)^\phi}\left(1-e^{-(\eta/y)^\phi}\right)^{\kappa-1}\left[1-\left(1-e^{-(\eta/y)^\phi}\right)^\kappa\right]^{\delta-1}}\right],$$

(40)

and simplification results in equation (7). □

3.5. Characterization of EGFG under Elasticity Function.

In this subsection, the EGFG distribution is characterized through the elasticity function.

Definition 4. Suppose the absolutely continuous random variable "Y" with *pdf* $f(y)$ and *cdf* $F(y)$. The elasticity function to F is symbolized as e_F and is obtained by

$$e_F(y) = \frac{yf(y)}{F(y)}, \quad y \in \mathrm{Supp}F,$$ (41)

where F represents the twice "differentiable distribution function." The elasticity function satisfies the following equation:

$$\frac{f'(y)}{f(y)} = \frac{e_F'(y)}{e_F(y)} + \frac{e_F(y)}{Y} - \frac{1}{Y}.$$ (42)

Proposition 5. *Let the random variable $Y: \Omega \in (0, \infty)$ follows the EGFG distribution. The density function of Y is equation (1) if and only if its elasticity function $e_F(y)$ satisfies the following differential equation:*

$$e_F'(y) - y^{-1}e_F(y) = y\tau^2 \left[\kappa\delta\phi\eta^\phi y^{-(\phi+1)} e^{-(\eta/y)^\phi} \left(1 - e^{-(\eta/y)^\phi}\right)^{\kappa-1} \left[1 - \left(1 - e^{-(\eta/y)^\phi}\right)^\kappa\right]^{\delta-1} \right]^2$$

$$\tau(1-\tau) - \frac{\tau\left(1 - \left[1 - \left(1 - e^{-(\eta/y)^\phi}\right)^\kappa\right]^\delta\right)}{\left(1 - \tau\left(1 - \left[1 - \left(1 - e^{-(\eta/y)^\phi}\right)^\kappa\right]^\delta\right)\right)} \left[(\tau^{-1}\delta)(\delta-1)\left[1 - \left(1 - e^{-(\eta/y)^\phi}\right)^\kappa\right]^{-\delta} +\right.$$

$$\frac{-(\phi+1)y^{-1} + \phi\eta^\phi y^{-(\phi+1)} - (\kappa-1)\phi\eta^\phi y^{-(\phi+1)} e^{-(\eta/y)^\phi} \left(1 - e^{-(\eta/y)^\phi}\right)^{-1}}{\tau\left[\kappa\delta\phi\eta^\phi y^{-(\phi+1)} e^{-(\eta/y)^\phi} \left(1 - e^{-(\eta/y)^\phi}\right)^{\kappa-1} \left[1 - \left(1 - e^{-(\eta/y)^\phi}\right)^\kappa\right]^{\delta-1}\right]}$$ (43)

$$- 2y\left(1 - \tau\left(1 - \left[1 - \left(1 - e^{-(\eta/y)^\phi}\right)^\kappa\right]^\delta\right)\right)^{-1}$$

$$- y\frac{\left(\left(1 - \tau\left(1 - \left[1 - \left(1 - e^{-(\eta/y)^\phi}\right)^\kappa\right]^\delta\right)\right)^{-2} /\tau\left(1 - \left[1 - \left(1 - e^{-(\eta/y)^\phi}\right)^\kappa\right]^\delta\right)\right)}{\tau(1-\tau) - \left(1 - \tau\left(1 - \left[1 - \left(1 - e^{-(\eta/y)^\phi}\right)^\kappa\right]^\delta\right)\right)}.$$

Proof. If the r.v Y has density function equation (1), then surely equation (43) holds.

$$e_F'(y) = y\tau^2 \left[\kappa\delta\phi\eta^\phi y^{-(\phi+1)} e^{-(\eta/y)^\phi} \left(1 - e^{-(\eta/y)^\phi}\right)^{\kappa-1} \left[1 - \left(1 - e^{-(\eta/y)^\phi}\right)^\kappa\right]^{\delta-1} \right]^2$$

$$\tau(1-\tau) - \frac{\tau\left(1 - \left[1 - \left(1 - e^{-(\eta/y)^\phi}\right)^\kappa\right]^\delta\right)}{\left(1 - \tau\left(1 - \left[1 - \left(1 - e^{-(\eta/y)^\phi}\right)^\kappa\right]^\delta\right)\right)} \left[(\tau^{-1}\delta)(\delta-1)\left[1 - \left(1 - e^{-(\eta/y)^\phi}\right)^\kappa\right]^{-\delta} +\right.$$

$$\frac{-(\phi+1)y^{-1} + \phi\eta^\phi y^{-(\phi+1)} - (\kappa-1)\phi\eta^\phi y^{-(\phi+1)} e^{-(\eta/y)^\phi} \left(1 - e^{-(\eta/y)^\phi}\right)^{-1}}{\tau\left[\kappa\delta\phi\eta^\phi y^{-(\phi+1)} e^{-(\eta/y)^\phi} \left(1 - e^{-(\eta/y)^\phi}\right)^{\kappa-1} \left[1 - \left(1 - e^{-(\eta/y)^\phi}\right)^\kappa\right]^{\delta-1}\right]}$$

$$- 2y\left(1 - \tau\left(1 - \left[1 - \left(1 - e^{-(\eta/y)^\phi}\right)^\kappa\right]^\delta\right)\right)^{-1}$$

$$- y\frac{\left(\left(1 - \tau\left(1 - \left[1 - \left(1 - e^{-(\eta/y)^\phi}\right)^\kappa\right]^\delta\right)\right)^{-2} /\tau\left(1 - \left[1 - \left(1 - e^{-(\eta/y)^\phi}\right)^\kappa\right]^\delta\right)\right)}{\tau(1-\tau) - \left(1 - \tau\left(1 - \left[1 - \left(1 - e^{-(\eta/y)^\phi}\right)^\kappa\right]^\delta\right)\right)} +$$

$$(1-\tau)\kappa\delta\phi\eta^\phi y^{-(\phi+1)} e^{-(\eta/y)^\phi} \left(1 - e^{-(\eta/y)^\phi}\right)^{\kappa-1} \left[1 - \left(1 - e^{-(\eta/y)^\phi}\right)^\kappa\right]^{\delta-1}$$

$$\frac{\left(1 - \tau\left(1 - \left[1 - \left(1 - e^{-(\eta/y)^\phi}\right)^\kappa\right]^\delta\right)\right)^{-1}}{\left[1 - \tau\left(1 - \left[1 - \left(1 - e^{-(\eta/y)^\phi}\right)^\kappa\right]^\delta\right) - (1-\tau)\left(1 - \left[1 - \left(1 - e^{-(\eta/y)^\phi}\right)^\kappa\right]^\delta\right)\right]},$$

$$e_F'(y) - y^{-1}e_F(y) = y\tau^2\left[\kappa\delta\phi\eta^\phi y^{-(\phi+1)}e^{-(\eta/y)^\phi}\left(1 - e^{-(\eta/y)^\phi}\right)^{\kappa-1}\left[1 - \left(1 - e^{-(\eta/y)^\phi}\right)^\kappa\right]^{\delta-1}\right]^2$$

$$\tau(1-\tau) - \frac{\tau\left(1 - \left[1 - \left(1 - e^{-(\eta/y)^\phi}\right)^\kappa\right]^\delta\right)}{\left(1 - \tau\left(1 - \left[1 - \left(1 - e^{-(\eta/y)^\phi}\right)^\kappa\right]^\delta\right)\right)}\left[(\tau^{-1}\delta)(\delta-1)\left[1 - \left(1 - e^{-(\eta/y)^\phi}\right)^\kappa\right]^{-\delta} +\right.$$

$$\frac{-(\phi+1)y^{-1} + \phi\eta^\phi y^{-(\phi+1)} - (\kappa-1)\phi\eta^\phi y^{-(\phi+1)}e^{-(\eta/y)^\phi}\left(1 - e^{-(\eta/y)^\phi}\right)^{-1}}{\tau\left[\kappa\delta\phi\eta^\phi y^{-(\phi+1)}e^{-(\eta/y)^\phi}\left(1 - e^{-(\eta/y)^\phi}\right)^{\kappa-1}\left[1 - \left(1 - e^{-(\eta/y)^\phi}\right)^\kappa\right]^{\delta-1}\right]}$$

$$-2y\left(1 - \tau\left(1 - \left[1 - \left(1 - e^{-(\eta/y)^\phi}\right)^\kappa\right]^\delta\right)\right)^{-1}$$

$$-y\frac{\left(\left(1 - \tau\left(1 - \left[1 - \left(1 - e^{-(\eta/y)^\phi}\right)^\kappa\right]^\delta\right)\right)^{-2}/\tau\left(1 - \left[1 - \left(1 - e^{-(\eta/y)^\phi}\right)^\kappa\right]^\delta\right)\right)\right]}{\tau(1-\tau) - \left(1 - \tau\left(1 - \left[1 - \left(1 - e^{-(\eta/y)^\phi}\right)^\kappa\right]^\delta\right)\right)}. \tag{44}$$

Now, the result is as follows: conversely if equation (43) holds, then

$$e_F(y) = \frac{(1-\tau)\kappa\delta\phi\eta^\phi y^{-(\phi)}e^{-(\eta/y)^\phi}\left(1 - e^{-(\eta/y)^\phi}\right)^{\kappa-1}\left[1 - \left(1 - e^{-(\eta/y)^\phi}\right)^\kappa\right]^{\delta-1}\left(1 - \tau\left(1 - \left[1 - \left(1 - e^{-(\eta/y)^\phi}\right)^\kappa\right]^\delta\right)\right)^{-1}}{\left[1 - \tau\left(1 - \left[1 - \left(1 - e^{-(\eta/y)^\phi}\right)^\kappa\right]^\delta\right) - (1-\tau)\left(1 - \left[1 - \left(1 - e^{-(\eta/y)^\phi}\right)^\kappa\right]^\delta\right)\right]}, \tag{45}$$

which is the elasticity function of the EGFG distribution.

4. Entropy of the Exponentiated Generalized Fréchet Geometric Distribution

Entropy measures have a strength of prediction. Different studies of time series may influence the predictive capacity of entropy measures. According to Liang et al. [22], time series analysis affects many entropy methods. Different entropy methods for measuring the complexity of time series were studied by Chen et al. [23]. According to Yin and Shang [24], entropy is a useful tool for examining time series because it does not include any constraints on the probability distribution. Solís-Montufar et al. [25] stated that several entropy measures can be used for complex time series. Its value may be positive, negative, or zero. A higher value shows randomness, while zero shows the certainty of information.

4.1. An Integral Result. The following results indicate that some integrals, including the density of the EGFG distribution, may be defined in terms of the incomplete gamma function.

Proposition 6. Let $\omega > 0$, $f(y, \underline{\theta})$, be specified by equation (1) and

$$I_\omega(\underline{\theta}) = \int_0^\infty f(y; \underline{\theta})^\omega \, dy. \tag{46}$$

Then, $I_\omega(\underline{\theta})$ exists if and only if $\min(\underline{\theta}) > \max(1 - (1/\omega), 0)$, and it is defined as

$$I_\omega(\underline{\theta}) = \frac{1}{\phi}\left((\omega + k)^{(1/\phi)}\eta\right)^{-\omega(\phi+1)-1}Y_{mkji}\Gamma \tag{47}$$

$$\left(\frac{1}{\phi}\{\omega(\phi+1)-1\}\right),$$

where $Y_{mkji} = \sum_{m=0}^{\infty}\sum_{k=0}^{\infty}\sum_{i=0}^{\infty}\sum_{j=0}^{\infty}\left(s + b - 1 \ b - 1\right)\tau^m \left((1 - \tau)\kappa\delta\phi\eta^\phi\right)^\omega (-1)^{i+j+k}\begin{pmatrix}\kappa(\omega + j) - \omega \\ k\end{pmatrix}\left(\delta(i + \omega) - \omega \right.$ $\left. j\right)\begin{pmatrix} m \\ i \end{pmatrix}$.

Proof. Owing to equation (1), we have

$$I_\omega(\underline{\theta}) = \int_0^\infty \frac{\left((1 - \tau)\kappa\delta\phi\eta^\phi\right)^\omega y^{-\omega(\phi+1)}e^{-\omega(\eta/y)^\phi}\left(1 - e^{-(\eta/y)^\phi}\right)^{\omega(\kappa-1)}\left[1 - \left(1 - e^{-(\eta/y)^\phi}\right)^\kappa\right]^{\omega(\delta-1)}}{\left(1 - \tau\left(1 - \left[1 - \left(1 - e^{-(\eta/y)^\phi}\right)^\kappa\right]^\delta\right)\right)^{-2\omega}}\,\mathrm{d}y. \tag{48}$$

For any positive real number b and for $|w| < 1$, we have the binomial and generalized binomial expansion:

$$(1 - w)^{b-1} = \sum_{s=0}^{\infty}\begin{pmatrix} b - 1 \\ s \end{pmatrix}(-1)^s w^s, \tag{49}$$

$$(1 - w)^{-b} = \sum_{s=0}^{\infty}\begin{pmatrix} s + b - 1 \\ b - 1 \end{pmatrix}w^s. \tag{50}$$

Applying equations (50) and (49), we get

$$I_\omega(\underline{\theta}) = Y_{mkji}\int_0^\infty y^{-\omega(\phi+1)}e^{-(\omega+k)(\eta/y)^\phi}\,\mathrm{d}y,$$

$$= \frac{1}{\phi}\left((\omega + k)^{(1/\phi)}\eta\right)^{-\omega(\phi+1)-1}Y_{mkji}\Gamma \tag{51}$$

$$\left(\frac{1}{\phi}\{\omega(\phi + 1) - 1\}\right).$$

In this study, the interest of Proposition 6 is that $I_\omega(\underline{\theta})$ is the major ingredient in the definitions of various entropy measures of the EGFG distribution as derived in the next part.

4.2. Various Entropy Measures.
In this subsection, some important entropy measures are studied using different techniques. The literature contains many entropies that are defined in Table 1 for the general distribution with $pdf f(k; \theta)$. Suppose that $\omega > 0$ and $\omega \neq 0$ as basic assumptions in this general case.

From Table 2, we see that the integral $\int_{-\infty}^{\infty} f(k; \theta)^\omega \, \mathrm{d}k$ is central to obtain the considered entropy measures. Now, we study the entropy measures of the EGFG distribution based on Proposition 6.

4.2.1. Rényi Entropy.
Based on Table 2, equation (1), and Proposition 6, the Rényi entropy of the EGFG distribution can be defined as

$$R_\omega(\theta) = \frac{1}{1 - \omega}\log[I_\omega(\theta)],$$

$$= \frac{1}{1 - \omega}\log$$

$$\left[\frac{1}{\phi}\left((\omega + k)^{(1/\phi)}\eta\right)^{-\omega(\phi+1)+1}Y_{mkji}\Gamma\left(\frac{1}{\phi}\{\omega(\phi + 1) - 1\}\right)\right]. \tag{52}$$

4.2.2. Havrda and Charvát Entropy.
From Table 2, equation (1), and Proposition 6, the Havrda and Charvát entropy of the EGFG distribution is specified by

$$HC_\omega(\theta) = \frac{1}{2^{1-\omega} - 1}\left[I_\omega(\theta) - 1\right],$$

$$= \frac{1}{2^{1-\omega} - 1}\left[\frac{1}{\phi}\left((\omega + k)^{(1/\phi)}\eta\right)^{-\omega(\phi+1)+1}Y_{mkji}\Gamma\left(\frac{1}{\phi}\{\omega(\phi + 1) - 1\}\right) - 1\right]. \tag{53}$$

4.2.3. Arimoto Entropy.
Again, from Table 2, equation (1), and Proposition 6, the Arimoto entropy of the EGFG distribution is expressed by

TABLE 1: Submodels from the exponentiated generalized fréchet geometric (EGFG) distribution.

Sr.No.	γ	ϕ	κ	δ	τ	Models	$p\,df$
1	$\eta > 0$	$\phi > 0$	$\kappa = 1$	$\delta > 0$	$0 < \tau < 1$	GFG	$\dfrac{(1-\tau)\delta\phi\eta^\phi y^{-(\phi+1)}e^{-\delta(\eta/y)^\phi}}{(1-\tau(1-e^{-\delta(\eta/y)^\phi}))^2}$
2	$\eta > 0$	$\phi > 0$	$\kappa = 1$	$\delta = 1$	$0 < \tau < 1$	FG	$\dfrac{(1-\tau)\phi\eta^\phi y^{-(\phi+1)}e^{-(\eta/y)^\phi}}{(1-\tau(1-e^{-(\eta/y)^\phi}))^2}$
3	$\eta > 0$	$\phi = 2$	$\kappa = 1$	$\delta = 1$	$0 < \tau < 1$	IRG	$\dfrac{2(1-\tau)\eta^2 y^{-(2+1)}e^{-(\eta/y)^2}}{(1-\tau(1-e^{-(\eta/y)^2}))^2}$
4	$\eta > 0$	$\phi = 1$	$\kappa = 1$	$\delta = 1$	$0 < \tau < 1$	IEG	$\dfrac{(1-\tau)\delta\eta y^{-2}e^{-\delta(\eta/y)}}{(1-\tau(1-e^{-\delta(\eta/y)}))^2}$

TABLE 2: Important entropy measures of a distribution with $pdf\,f(k;\theta)$ at ω.

Name of the entropy	Reference	Notation	Expression
Rényi	Rényi [26]	$R_\omega(\theta)$	$(1/1-\omega)\log\left[\int_{-\infty}^{\infty} f(k;\theta)^\omega\,dk\right]$
Havrda and Charvát	Havrda and Charvát [27]	$HC_\omega(\theta)$	$(1/2^{1-\omega}-1)\left[\int_{-\infty}^{\infty} f(k;\theta)^\omega\,dk - 1\right]$
Arimoto	Arimoto [28]	$A_\omega(\theta)$	$(\omega/1-\omega)\left\{\left[\int_{-\infty}^{\infty} f(k;\theta)^\omega\,dk\right]^{1/\omega} - 1\right\}$
Tsallis	Tsallis [29]	$T_\omega(\theta)$	$(1/\omega - 1)\left[1 - \int_{-\infty}^{\infty} f(k;\theta)^\omega\,dk\right]$

TABLE 3: Numerical values of the entropy measures of the EGFG distribution $\eta = 2$, $\delta = 3$, $\tau = 0.8$, and $\phi = 2$.

η	κ	δ	τ	ϕ	ω	$R_\omega(\theta)$	$HC_\omega(\theta)$	$A_\omega(\theta)$	$T_\omega(\theta)$
	3	3	0.8	2	0.5	0.391	1.374	1.462	1.138
2	2.9					0.406	1.441	1.549	1.193
	2.5					0.477	1.762	1.997	1.462
	3	3	0.8	2	1.5	0.120	0.442	0.265	0.259
2	2.9					0.132	0.480	0.288	0.281
	2.5					0.182	0.646	0.391	0.378
	3	3	0.8	2	2	0.077	0.326	0.170	0.163
2	2.9					0.088	0.368	0.193	0.184
	2.5					0.137	0.542	0.292	0.271

$$
\begin{aligned}
A_\omega(\theta) &= \frac{\omega}{1-\omega}\left[I_\omega(\theta)^{1/\omega} - 1\right], \\
&= \frac{\omega}{1-\omega}\left[\left\{\frac{1}{\phi}\left((\omega+k)^{(1/\phi)}\eta\right)^{-\omega(\phi+1)+1}Y_{mkji}\Gamma\left(\frac{1}{\phi}\{\omega(\phi+1)-1\}\right)\right\}^{1/\omega} - 1\right].
\end{aligned}
\tag{54}
$$

4.2.4. Tsallis Entropy. Based on Table 2, equation (1), and Proposition 6, the Tsallis entropy of the EGFG distribution can be presented as

$$
\begin{aligned}
T_\omega(\theta) &= \frac{1}{\omega-1}\left[1 - I_\omega(\theta)\right], \\
&= \frac{1}{\omega-1}\left[1 - \frac{1}{\phi}\left((\omega+k)^{(1/\phi)}\eta\right)^{-\omega(\phi+1)+1}Y_{mkji}\Gamma\left(\frac{1}{\phi}\{\omega(\phi+1)-1\}\right)\right].
\end{aligned}
\tag{55}
$$

TABLE 4: Numerical values of the entropy measures of the EGFG distribution $\eta = 2.5$, $\kappa = 3$, $\tau = 0.9$, and $\phi = 2.5$.

η	κ	δ	τ	ϕ	ω	$R_\omega(\theta)$	$HC_\omega(\theta)$	$A_\omega(\theta)$	$T_\omega(\theta)$
	3	1.2	0.9	2.5	0.5	0.284	0.932	0.921	0.772
2.5		2.2				0.304	1.012	1.014	0.838
		3.2				0.316	1.058	1.068	0.876
	3	1.2	0.9	2.5	1.5	0.024	0.095	0.056	0.055
2.5		2.2				0.043	0.164	0.097	0.096
		3.2				0.052	0.200	0.118	0.117
	3	1.2	0.9	2.5	2.5	−0.046	−0.265	−0.109	−0.114
2.5		2.2				−0.028	−0.154	−0.065	−0.067
		3.2				−0.018	−0.100	−0.042	−0.043

TABLE 5: Numerical values of the entropy measures of the EGFG distribution $\eta = 3$, $\kappa = 3$, $\delta = 1.2$, and $\phi = 2$.

η	κ	δ	τ	ϕ	ω	$R_\omega(\theta)$	$HC_\omega(\theta)$	$A_\omega(\theta)$	$T_\omega(\theta)$
	3	1.2	0.5	2	0.5	0.620	2.514	3.166	2.082
3			0.6			0.595	2.375	2.935	1.967
			0.8			0.516	1.958	2.279	1.622
	3	1.2	0.5	2	1.5	0.376	1.199	0.752	0.702
3			0.6			0.345	1.119	0.698	0.655
			0.8			0.248	0.847	0.519	0.496
	3	1.2	0.5	2	2.5	0.310	1.016	0.580	0.483
3			0.6			0.277	0.954	0.531	0.411
			0.8			0.176	0.706	0.360	0.304

TABLE 6: Numerical values of the entropy measures of the EGFG distribution $\eta = 3.5$, $\delta = 3.9$, $\delta = 1.5$, and $\tau = 0.7$.

η	κ	δ	τ	ϕ	ω	$R_\omega(\theta)$	$HC_\omega(\theta)$	$A_\omega(\theta)$	$T_\omega(\theta)$
	3.9	1.5	0.7	1.2	0.5	0.724	3.145	4.302	2.605
3.5				2.2		0.511	1.935	2.245	1.603
				3.2		0.374	1.298	1.364	1.075
	3.9	1.5	0.7	1.2	1.5	0.418	1.305	0.824	0.764
3.5				2.2		0.289	0.968	0.598	0.567
				3.2		0.176	0.626	0.379	0.367
	3.9	1.5	0.7	1.2	2.5	0.342	1.073	0.628	0.462
3.5				2.2		0.225	0.837	0.446	0.361
				3.2		0.116	0.510	0.246	0.220

TABLE 7: Entropies of the EGFG for different parameter combinations.

η	κ	δ	τ	ϕ	ω	$R_\omega(\theta)$	$HC_\omega(\theta)$	$A_\omega(\theta)$	$T_\omega(\theta)$
2.5	3	3.2	0.85	2.5	1.6	0.093	0.354	0.205	0.201
2.2	2.9	3	0.8	2.3	1.5	0.123	0.451	0.270	0.264
1.3	2.5	2.7	0.5	2	1.49	0.124	0.454	0.273	0.267
1.25	2.2	2.5	0.45	1.8	1.45	0.217	0.752	0.463	0.448
1.2	2.1	1.7	0.3	1.5	0.5	0.652	2.699	3.485	2.236
1.0	1.9	1.5	0.1	1.3	0.5	0.798	3.638	5.284	3.013
1.07	1.9	1.5	0.09	1.3	0.5	0.8	3.653	5.313	3.026
0.8	1.7	1.5	0.09	1.3	0.5	0.818	3.779	5.581	3.131
0.7	1.55	1.35	0.087	1.25	0.47	0.987	5.259	10.614	4.405

4.3. Numerical Results. In this section, the idea of following Al-Babtain et al.'s [30] numerical values for the four different entropy measures of the EGFG distribution is calculated. The findings of all considered entropy measures are presented in Tables 3–7.

Tables 3–7 show the numerical values of the entropy measures for the different sets of the parameters. It can be noticed that,

(i) Rényi, Havrda and Charvát, Arimoto, and Tsallis entropy measures are increasing when κ and ω are increasing.

(ii) Rényi, Havrda and Charvát, Arimoto, and Tsallis entropy measures are increasing when δ and ω are increasing.

(iii) Rényi, Havrda and Charvát, Arimoto, and Tsallis entropy measures are decreasing when τ and ω are increasing.

(iv) Rényi, Havrda and Charvát, Arimoto, and Tsallis entropy measures are decreasing when ϕ and ω are increasing.

(v) Rényi, Havrda and Charvát, Arimoto, and Tsallis entropy measures are increasing when all parameter values are decreasing.

5. Conclusion

In this article, the characterization results for the Exponentiated Generalized Fréchet Geometric distribution through five approaches are presented. In the previous section, the analytical expressions of four entropy measures for the EGFG distribution are investigated. All entropy measures are compared numerically by considering the various combination of the parametric values. We hope these expressions of entropies' measures by various techniques may be helpful in uncertainty measures of a random variable of related fields.

Data Availability

The data is generated by using the idea of Al-Babtain et al. [30].

Conflicts of Interest

The authors declare that they have no conflicts of interest.

References

[1] W. Glänzel, "A characterization theorem based on truncated moments and its application to some distribution families," in *Mathematical Statistics and Probability Theory*, pp. 75–84, Springer, Berlin, Germany, 1987.

[2] W. Glänzel, "A characterization of the normal distribution," *Studia Scientiarum Mathematicarum Hungarica*, vol. 23, no. 1, pp. 89–91, 1988.

[3] G. Hamedani, "Characterizations of cauchy, normal, and uniform distributions," *Studia Scientiarum Mathematicarum Hungarica*, vol. 28, no. 3, pp. 243–248, 1993.

[4] G. Hamedani, "Characterizations of univariate continuous distributions II," *Studia Scientiarum Mathematicarum Hungarica*, vol. 39, no. 3-4, pp. 407–424, 2002.

[5] G. G. Hamedani and G. G. Hamedani, "Characterizations of univariate continuous distributions III," *Studia Scientiarum Mathematicarum Hungarica*, vol. 43, no. 3, pp. 361–385, 2006.

[6] G. Hamedani and M. Ahsanullah, "Characterizations of weibull geometric distribution," *Journal of Statistical Theory and Applications*, vol. 10, no. 4, pp. 581–590, 2011.

[7] D. G. G. Hamedani, "Characterizations of transmuted complementary weibull geometric distribution," *Pakistan Journal of Statistics and Operation Research*, vol. 11, no. 2, pp. 153–157, 2015.

[8] F. A. Bhatti, G. G. Hamedani, W. Sheng, and M. Ahmad, "On extended quadratic hazard rate distribution: development, properties, characterizations and applications," *Stochastics and Quality Control*, vol. 33, no. 1, pp. 45–60, 2018.

[9] A. Rafique and N. Saud, "Some characterizations of unimodal, reserve j-shaped distribution," in *Proceedings of the 18th International Conference on Statistical Sciences (ICCS-18)*, pp. 291–340, Lahore, Pakistan, December 2019.

[10] A. Caneco, J. L. Rocha, and C. Grácio, "Topological entropy in the synchronization of piecewise linear and monotone maps: coupled duffing oscillators," *International Journal of Bifurcation and Chaos*, vol. 19, no. 11, pp. 3855–3868, 2009.

[11] J. L. Rocha and S. M. Aleixo, "An extension of gompertzian growth dynamics: weibull and fréchet models," *Mathematical Biosciences and Engineering*, vol. 10, no. 2, p. 379, 2013.

[12] J. L. Rocha and S. Carvalho, "Information theory, synchronization and topological order in complete dynamical networks of discontinuous maps," *Mathematics and Computers in Simulation*, vol. 182, pp. 340–352, 2021.

[13] C. E. Shannon, "A mathematical theory of communication," *Bell System Technical Journal*, vol. 27, no. 3, pp. 379–423, 1948.

[14] Y. Cho, H. Sun, and K. Lee, "Estimating the entropy of a weibull distribution under generalized progressive hybrid censoring," *Entropy*, vol. 17, no. 1, pp. 102–122, 2015.

[15] S. Dey, S. S. Maiti, and M. Ahmad, "Comparison of different entropy measures," *Pakistan Journal of Statistics (PJS)*, vol. 32, no. 2, pp. 97–108, 2016.

[16] A. Basit, A. Riaz, Z. Iqbal, and M. Ahmad, "On comparison of entropy measures for weighted and truncated weighted exponential distributions," *Advances and Applications in Statistics*, vol. 50, no. 6, pp. 477–495, 2017.

[17] A. Namdari and Z. Li, "A review of entropy measures for uncertainty quantification of stochastic processes," *Advances in Mechanical Engineering*, vol. 11, no. 6, Article ID 1687814019857350, 2019.

[18] M. Ijaz, S. Naji AL-Aziz, S. Muhammad Asim, J. G. Dar, and A.-A. H. Abd El-Bagoury, "Comparison of different entropy measures using the relative loss approach for the lomax distribution," *Information Sciences Letters*, vol. 10, no. 3, p. 18, 2021.

[19] A. Rafique and N. Saud, "Exponentiated generalized frechet geometric distribution," in *15th Islamic Countries Conference on Statistical Sciences*, pp. 189–198, ICCS-15), 2019.

[20] F. A. Bhatti and M. Ahmad, "On a new family of kies burr iii distribution: development, properties, characterizations, and applications," *Scientia Iranica*, vol. 27, no. 5, pp. 2555–2571, 2020.

[21] W. Glanzel, "Some consequences of a characterization theorem based on truncated moments," *Statistics*, vol. 21, no. 4, pp. 613–618, 1990.

[22] Z. Liang, Y. Wang, X. Sun et al., "Eeg entropy measures in anesthesia," *Frontiers in Computational Neuroscience*, vol. 9, p. 16, 2015.

[23] Z. Chen, Y. Li, H. Liang, and J. Yu, "Improved permutation entropy for measuring complexity of time series under noisy condition," *Complexity*, vol. 2019, Article ID 1403829, 12 pages, 2019.

[24] Y. Yin and P. Shang, "Weighted permutation entropy based on different symbolic approaches for financial time series," *Physica A: Statistical Mechanics and Its Applications*, vol. 443, pp. 137–148, 2016.

[25] E. E. Solís-Montufar, G. Gálvez-Coyt, and A. Muñoz-Diosdado, "Entropy analysis of rr-time series from stress tests," *Frontiers in Physiology*, vol. 11, p. 981, 2020.

[26] A. Rényi, "On measures of entropy and information," in *Proceedings of the Fourth Berkeley Symposium on Mathematical Statistics and Probability, Volume 1: Contributions to the Theory of Statistics*, pp. 547–561, University of California Press, Berkeley, CA, USA, July 1960.

[27] J. Havrda and F. Charvát, "Quantification method of classification processes: concept of structural a-entropy," *Kybernetika*, vol. 3, no. 1, pp. 30–35, 1967.

[28] S. Arimoto, "Information-theoretical considerations on estimation problems," *Information and Control*, vol. 19, no. 3, pp. 181–194, 1971.

[29] C. Tsallis, "Possible generalization of boltzmann-gibbs statistics," *Journal of Statistical Physics*, vol. 52, no. 1, pp. 479–487, 1988.

[30] A. A. Al-Babtain, I. Elbatal, C. Chesneau, and M. Elgarhy, "Estimation of different types of entropies for the kumaraswamy distribution," *PLoS One*, vol. 16, no. 3, Article ID e0249027, 2021.

Research Article

Multiperson Target Dynamic Tracking Method for Athlete Training Based on Wireless Body Area Network

Diandian Du (ID)

Department of Public Education, Changde Vocational and Technical College, Changde, 415000 Hunan, China

Correspondence should be addressed to Diandian Du; 161105222@stu.cuz.edu.cn

Aiming at the problems of large tracking error and long tracking time in traditional multiperson target dynamic tracking methods, a new method based on wireless body area network for athlete training multiperson target dynamic tracking is proposed. First, the microinertial sensor in the wireless body area network is used to collect the multiperson image data of the athlete training, and the sparse representation is performed after processing, which improves the reliability of the data and reduces the tracking error. Secondly, the multiperson target dynamic tracking method based on the adaptive search box is used, combined with target isolation and occlusion detection, to judge the athlete's training target. Finally, the nearest neighbor algorithm is used to construct an adaptive search box to achieve dynamic tracking of multiple targets. Experimental results show that this method can accurately measure the similarity of target features, with small tracking error and short tracking time. The minimum tracking error is only 0.11 frame.

1. Introduction

In modern life, sports competitions have been deeply loved by the majority of the audience. With the improvement of people's quality of life and the progress and development of science and technology, sports competitions, training videos, and images can no longer meet the requirements of all aspects of society [1]. For example, in the process of athlete training, many people are usually trained in a group, and many coaches guide on site. Therefore, when observing training videos and images, it is necessary to identify multiple or single targets from multiple targets [2].

Multiperson target detection and tracking technology for athlete training is the main content of many disciplines such as digital image processing, computer vision, and artificial intelligence. It has broad application prospects and important research value in many fields such as human-computer interaction, video image monitoring, and food retrieval [3–5]. Generally, the video image scene is composed of background and foreground target. The foreground target is an important part of the image sequence, is the research area of interest, and contains important information. Therefore,

how to quickly segment the multiperson target object and effectively locate and track it is the focus of the research.

Zheng et al. [6] proposed a multiperson target dynamic tracking method based on multifeature fusion, trained the filter model by using directional gradient histogram and color feature, and fused the feature results collected by the filter according to the peak sidelobe ratio and weighting ratio of different feature response diagrams. According to the peak sidelobe ratio of the final target position response map of each frame, judge whether the target is occluded. When occlusion occurs, the model will not be updated, and the current model will continue to be used for tracking in the next frame. However, this method has the problem of low accuracy of feature similarity measurement. Yikun et al. [7] proposed a multiperson target dynamic tracking method based on TLD and fdst. In order to strengthen the tracking accuracy of fdst algorithm in the case of rapid target movement, rapid deformation, and target disappearance, detectors and learners were added on the basis of fdst algorithm to modify and learn the tracking results; the positive and negative samples of the detector and the learner are used to evaluate the confidence of the tracking results, so as to

complete the dynamic tracking of the target. However, the tracking error of this method is large, which makes the needs of practical application difficult to meet. Jianqiang and Zhibing [8] proposed a multiperson target dynamic tracking method based on the fusion of mean shift and particle filter. Using the fast convergence of mean shift algorithm, the particle set is iteratively calculated, and the particles with the first 15% of weight are retained to form a new particle set, reducing the calculation cycle. The heavy particles are obtained by resampling, and the particle set is updated to improve the target positioning accuracy. However, the calculation of this method takes a long time.

In view of the poor effect of the existing multiperson target detection and tracking methods in the dynamic scene, taking the dynamic tracking of athlete training as the research object, based on the existing research theory, the multiperson images of athlete training are accurately collected by wireless body area network, and the collected images are sparse represented. Based on this, the adaptive search box is used to complete the dynamic tracking of athlete training multitarget.

The research contributions of the thesis include the following points:

(1) The paper proposes a new method for athlete's training multiperson target dynamic tracking based on wireless body area network

(2) The microinertial sensor in the wireless body area network is used to collect the multiperson image data of the athlete's training, and the sparse representation is performed after processing, which improves the reliability of the data and reduces the tracking error

(3) The paper adopts a multiperson target dynamic tracking method based on an adaptive search box, combined with target isolation and occlusion detection, to judge the athlete's training target

2. Multiperson Target Dynamic Tracking of Athlete Training Based on Wireless Body Area Network

2.1. Athlete Training Data Acquisition Based on Wireless Body Area Network. Wireless body area network is a wireless network constructed by portable, wearable, or implantable sensor nodes that can perceive a variety of human physiological parameters. Wireless body area network provides a new means for human health monitoring and has great application significance and demand in the fields of disease monitoring, health recovery, special population monitoring, and so on [9]. Through the microinertial sensor worn on the body, the body area network can collect human motion signals and is widely used in human motion monitoring. It can realize the purposes of human motion recognition, abnormal motion detection, gait recognition and analysis, motion energy consumption analysis, and so on.

The research field of wireless body area network is shown in Figure 1.

Figure 1 summarizes the research fields involved in the existing wireless body area network. From the existing research, data fusion technology, situation awareness technology, and WBSN energy control are the technical research hotspots of WBSN, and the research of WBSN for multitarget dynamic tracking in athlete training accounts for a large proportion [10].

When the wireless body area network is used for multitarget dynamic tracking of athlete training, the microinertial sensor in the wireless body area network needs to be used to identify the movement information of multitarget of athlete training [11]. The multiperson target movement information recognition of athlete training based on microinertial sensor is a series of image sampling sequences arranged in a chronological order, including all the movement information of athlete training.

The field of athlete training multiperson target dynamic tracking based on microinertial sensors is a new field. Its essential content is to first obtain the motion signal generated during athlete training through one or more inertial sensors and then sparse represent the sampled image, so as to facilitate the follow-up athlete training multiperson target dynamic tracking [12]. The specific processing process is shown in Figure 2.

Generally, the sample image collected by inertial sensor contains not only the motion signal generated by athlete training but also various noises. Therefore, the collected sample image must be preprocessed first. Preprocessing methods generally include smoothing and denoising, normalization, resampling, windowing, and tilt correction.

Smoothing and denoising are often used in the image processing of human motion samples based on inertial sensors. Therefore, in the process of sample image acquisition, the noise generated by the jitter of athletes' training and the measurement noise of sensors will be included in the collected images, so these interference noises should be removed first [13].

In addition, normalization and resampling are also technologies often used in preprocessing. In multiperson target dynamic detection, because the action amplitude of athletes is not fixed and different athletes are doing different actions, the influence of signal amplitude on sampling results must be eliminated. Normalization can usually be used to adjust the amplitude difference of signals [14].

After the preprocessing of the sampled image, the sparse representation model of the sampled image is constructed. In the multiperson target detection process of athlete training based on inertial sensor, the acceleration values of three axes in the athlete training process can be collected through inertial sensor, and (x, y, z) represents the acceleration values measured by inertial sensor in x, y, and z directions, respectively, so the once collected sample of a target dynamic detection is the time sequence of acceleration data. The sampling value of the sensor at time t is

$$s(t) = (x(t), y(t), z(t)). \tag{1}$$

Then, the l-time sampling value obtained corresponding to a complete athlete's training posture for a short period of
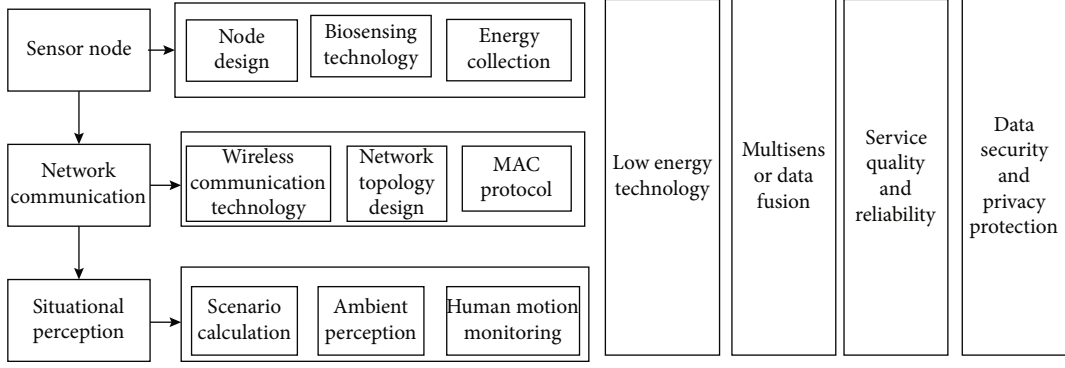
Figure 1: Research area of wireless body area network.
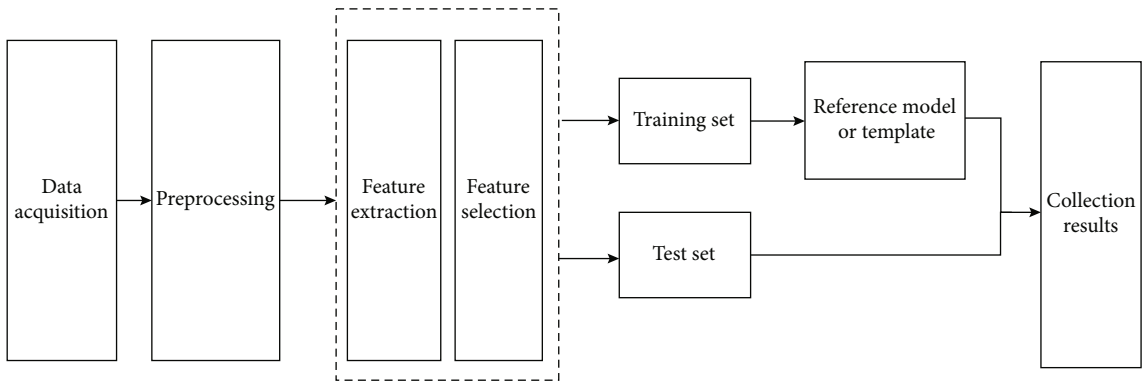
Figure 2: Multiperson target image sampling process of athlete training based on microinertial sensor.

time can be represented by a one-dimensional vector, which is recorded as

$$g = \left(s(1), s(2), \cdots, s(l)\right)^{\mathrm{T}}. \tag{2}$$

From a geometric point of view, many data classes to be detected can be characterized by specific subspaces, and each subspace represents a data category [15]. It is assumed that the spatial distribution of a variety of different motion trajectory data satisfies the mixed subspace model, and different motion trajectory data are approximately distributed in different subspaces. For the collection of dynamic trajectory data, as long as the appropriate dynamic trajectory is selected to meet the mixed subspace model and each subspace represents a trajectory data category, the motion trajectory recognition problem can be transformed into a sparse representation classification model.

The problem of motion trajectory data acquisition is to judge the motion category of a motion trajectory vector $g_{k,\text{test}}$ to be collected given the training set of class C motion target samples. The acquisition based on sparse representation mainly has two steps: sparse coding and sparse representation. Using the super complete dictionary atom composed of training samples, the motion trajectory vector to be collected is expressed as the linear combination of these atoms, so the motion trajectory acquisition problem

is transformed into the acquisition problem of multiple linear regression models.

Assuming that the class i training sample contains n_i motion tracks, the training sample is transformed into a column vector, and the column vector $g_{i,j} \in R^m$ is used to represent the j motion track of class i, where m is the dimension of the motion track vector; then, all one-dimensional motion directions in the training set corresponding to the class i motion track constitute a motion track subspace, which is recorded as

$$G_i = \left[g_{i,1}, g_{i,2}, \cdots, g_{i,n_i}\right] \in R^{m \times n_i}. \tag{3}$$

According to the principle of linear subspace, if the motion trajectory vector $g_{k,\text{test}}$ to be collected belongs to class k motion, the motion trajectory vector can be represented by the linear combination of trajectory vectors of all training motions in the subspace, that is

$$g_{k,\text{test}} = \alpha_{k,1} g_{k,1}, \alpha_{k,2} g_{k,2}, \cdots, \alpha_{k,n_k} g_{k,n_k}. \tag{4}$$

In the formula, $\alpha_{i,j}, j = 1, 2, \cdots, n_k$, is the sparse representation coefficient.

All the training samples of all C kinds of motion tracks in the whole training sample set are formed into redundant

dictionary matrix G. Each base vector in the dictionary represents one training sample, as follows:

$$G = [G_1, G_2, \cdots, G_k] = \left[g_{1,1}, g_{1,2}, \cdots, g_{c,n_c}\right] R^{m \times n}. \quad (5)$$

In the formula, $n = n_1 + n_2 + \cdots + n_c$, and the number of columns in dictionary G is greater than the number of rows. Such a dictionary is called an overcomplete dictionary.

Considering that some errors will inevitably be included in the actual calculation process, when the redundant dictionary G is used to represent the motion trajectory vector $g_{k,\text{test}}$ to be measured, it can be expressed by the following formula:

$$g_{k,\text{test}} = G\alpha + e \quad \in R^m. \quad (6)$$

In the formula, $\alpha = [0, \ldots 0, \alpha_{k,1}, \alpha_{k,2}, \cdots, \alpha_{k,n_i}, 0, \cdots, 0]^{\mathrm{T}} \in R^n$ represents the coefficient vector, $e \in R^m$ represents the observation noise, and the noise tolerance is $\|e\|_2 < \varepsilon$. Ideally, the samples to be collected should only be linearly represented by the training samples from the same category in the dictionary; that is, in the coefficient vector α, only the representation coefficients of the training samples belonging to the same category as the samples to be collected are not 0, and the rest are 0; then, when the number of categories is enough, compared with the whole dictionary, this representation will show the characteristics of sparsity. Therefore, based on the prior knowledge that the super complete dictionary has sparsity in the representation of test samples, the most sparse linear combination in the super complete dictionary is found to represent test samples.

α is a coefficient vector with $1/C$ sparsity. When the number of categories C reaches a certain degree, the solution of the equations has enough coefficients. According to the compressed sensing theory, α can be solved by minimizing the l_1 norm under quadratic constraints. The specific calculation formula is

$$\begin{aligned} \widehat{\alpha} &= \arg \min \|\alpha\|_1 \\ \text{s.t.} \quad &\left\|g_{k,\text{test}} - G\alpha\right\|_2 \leq \varepsilon. \end{aligned} \quad (7)$$

Ideally, the non-0 elements in the sparse coefficient vector $\widehat{x}$ obtained by formula (7) will only appear in the position corresponding to the samples of the same class as the motion trajectory vector $g_{k,\text{test}}$ to be collected, so the category of the test sample can be determined according to the distribution of these non-0 elements. However, due to the existence of noise, in practice, non-0 elements may also appear in the corresponding positions of other categories. Then, calculate the linear weighted difference between the motion vector to be collected and all motion vectors in each category, and the calculation formula is

$$r_i(g_{k,\text{test}}) = \left\|g_{k,\text{test}} - G\delta_i(\widehat{\alpha})\right\|_2, \quad i = 1, 2, \cdots, C. \quad (8)$$

In the formula, $\delta_i(\widehat{\alpha})$ means to extract the coefficients corresponding to all motion vectors of class i in sparse representation coefficient $\widehat{\alpha}$, and the other coefficients are 0. Select the category of $r_i(g_{k,\text{test}})$ with the smallest difference, and record it as the final acquisition result.

Through the above calculation, the multitarget motion data is collected according to the microinertial sensor in the wireless body area network, which lays the foundation for the subsequent multitarget dynamic tracking of multiplayer training.

2.2. Multiperson Target Dynamic Tracking. The multiperson target dynamic tracking method using an adaptive search box uses the separation processing of target isolation and target occlusion, extracts target features through an efficient multiperson target detection algorithm, and maintains a real-time updated tracking area search box. When each target is in an isolated motion state, the nearest neighbor algorithm based on the search box is adopted. When the target is occluded, a feature matching algorithm based on the central area is used to dynamically track the target. The block diagram of multiperson target dynamic tracking is shown in Figure 3.

It can be seen from the multiperson target tracking block diagram flow shown in Figure 3 that this method is a multiperson target dynamic tracking method based on detection. This method maintains a good search box and target feature information base by implementing accurate multitarget detection. Multiperson target detection and marking technology, data association technology, and feature matching technology are adopted. Taking whether the target is occluded as the branch point, the hybrid algorithm is used to deal with target tracking in time-sharing.

It should be noted that when several measurements appear in the target search box, that is, there are several targets in a search box, switch the tracking algorithm immediately and switch from the nearest neighbor algorithm to the feature matching algorithm. This usually occurs in the separation process after the target is blocked. When a target suddenly stops after being blocked and another target crosses, at this time, the target breaks away from the occlusion state and enters the isolated motion of the target. At this time, the nearest neighbor algorithm will inevitably lead to the wrong tracking of the target.

In the actual athlete training scene, the state between targets in multiperson target tracking is the basis of preanalysis and the premise of the realization of tracking method. According to the actual situation of multitarget movement, the multitarget movement state mainly includes four situations: the emergence of new targets, occlusion between targets, mutual occlusion, separation of multitarget, and disappearance of old targets. Among them, the occlusion between multiple human targets is divided into partial occlusion and severe occlusion. Whether the target occlusion is serious or not is judged according to the accuracy of the algorithm. When the tracking algorithm cannot effectively realize the independent tracking of occluded targets, the occluded multiple human targets are combined. Otherwise, some non-severely occluded targets are tracked independently.
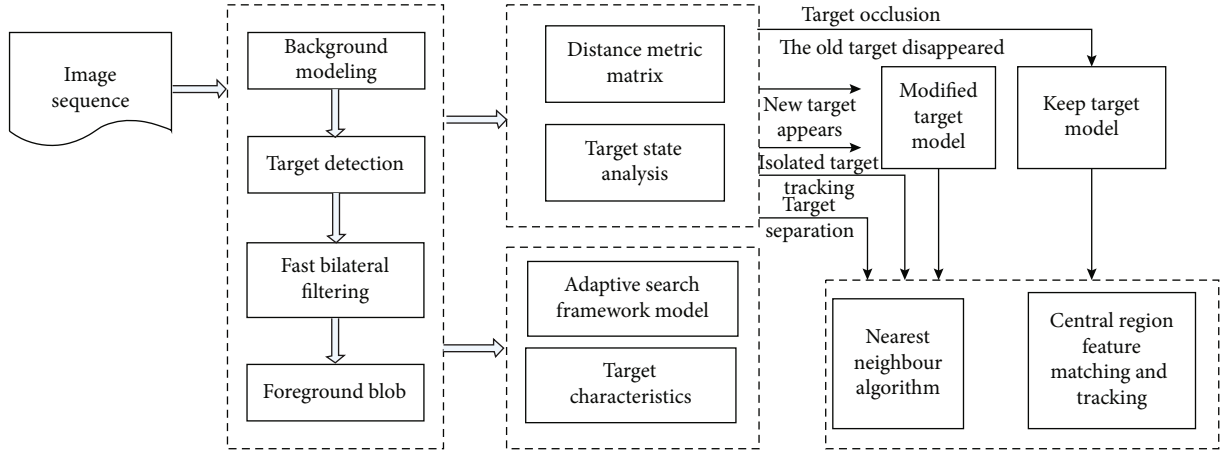
FIGURE 3: Multiperson target dynamic tracking block diagram.

In general, the position change of the moving target on the two adjacent frames of images is very small relative to the image space distance. Therefore, set a distance threshold r. When a target position is in a circle whose origin is the target centroid of the current frame and radius is r, it is judged as the same target, and the circle is defined as the nearest neighbor circle. Therefore, a distance measurement matrix P is proposed, P is $M \times N$ matrix, M represents the number of targets detected in $t - 1$ frame, N represents the number of blobs segmented in $t - 1$ frame, and the multitarget state is determined according to the number of targets in two adjacent frames in a nearest neighbor circle:

$$P(m, n) = \begin{cases} 1, & \text{if } |o_t^n(x, y) - o_{t-1}^m(x, y)| < r, \\ 0, & \text{else.} \end{cases} \tag{9}$$

In the formula, $o_t^n(x, y)$ represents the centroid position of the nth blob detected in the t frame image, and $o_{t-1}^m(x, y)$ represents the centroid position of the mth target in the $t - 1$ frame image.

According to the matrix definition, we can get

$$P_m = \sum_{n=1}^{N} P(m, n),$$

$$P_n = \sum_{m=1}^{M} P(m, n). \tag{10}$$

In the above formula, P_m represents the number of foreground blocks matched with the mth target, and P_n represents the number of targets matched with the nth foreground block.

(1) When a new target enters the scene (including target splitting), $P_m = 0$, that is, the nth blob detected in the current frame fails to find a matching target in the $t - 1$ frame. In order to judge whether the target is new or split, it is necessary to extract the color data-base information for matching. If it is a new target, number the target; record the static characteristic parameters such as centroid, minimum circumscribed rectangle, and color information of the new target; and obtain the dynamic characteristic parameters such as motion speed and direction from the second frame

(2) When the old target leaves the scene (including severe occlusion of the target). At this time, $P_m = 0$, that is, when the mth target in frame $t - 1$ fails to find a matching blob in the current frame. When the mth target is at the boundary of the video scene, it is judged that the old target disappears; delete the mth target, and refresh the target chain; otherwise, judge that the target is seriously occluded, ensure the mth target message, and record the target state at time $t - 1$, so as to realize effective tracking of the target when the target is split

(3) Target occlusion judgment. As shown in Figure 4, r_1 is the minimum inscribed circle radius centered on the centroid of the target contour, and r_2 is the maximum circumscribed circle radius centered on the centroid of the target contour. Considering the shape characteristics of human body, when the centroid distance $d_{i,j}$ of two or more adjacent targets meets $d_{i,j} < r_1^i + r_1^j$, where $i, j \in [1, m]$ and $i \neq j$, judge that the targets block each other and stop updating their characteristic parameters; when $P_n > 1$, that is, when the number of targets matched with the nth block is greater than 1, it is judged that multiple targets block each other. Tracking the smallest outer circumscribed rectangle and the inside and outside circles is shown in Figure 4

As can be seen from Figure 4, the adaptive search frame is based on the extraction of target motion information and makes full use of the target area detected in the previous frame to predict the target search range in the next frame. When the new target enters the image, the minimum
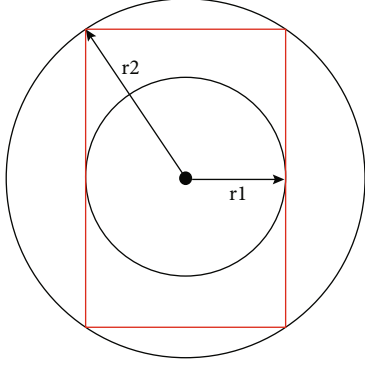
FIGURE 4: Tracking the smallest outer circumscribed rectangle and the inside and outside circles.

FIGURE 5: The calculation principle of target movement direction θ.

circumscribed rectangle of the target is obtained through the target detection and state evaluation algorithm, that is, the length and width of the target, the centroid, and other static parameters. The centroid of multiperson moving target is obtained through the marked target blob. The centroid calculation formula is as follows:

$$X(i) = \frac{\sum f(x, y)x}{\sum f(x, y)},$$

$$Y(i) = \frac{\sum f(x, y)y}{\sum f(x, y)}. \tag{11}$$

In the formula, $f(x, y)$ represents the value of the blob (0 or 1), x and y represent the index positions of the image pixels, and $X(i)$ and $Y(i)$ represent the centroid of the ith target in the Kth frame of the image. In the same way, the length and width of the target can also be obtained through the connected domain of the target.

The dynamic parameters of the target are acquired from the second frame when the target is detected, which mainly include the movement speed and the movement direction. The calculation principle of the target movement direction θ is shown in Figure 5.

As shown in Figure 5, the motion direction is obtained by the centroid position of the current frame and the previous frame. According to the position information of the moving target, the following calculation formula can be obtained:

$$\theta = \arctan\left(\frac{x_t^n - x_{t-1}^n}{y_t^n - y_t^{n-1}}\right), \tag{12}$$

$$\theta \in [0, 360).$$

It is easy to know that when θ is at four special angles of 0, 90, 180, and 270, it is necessary to decompose the movement in the direction of the target centroid (x, y). When $x_t^n = x_{t-1}^n$ and $y_t^n > y_t^{n-1}$, judge $\theta = 0$; similarly, $y_t^n = y_t^{n-1}$ and $x_t^n > x_{t-1}^n$, then $\theta = 90$; $y_t^n = y_t^{n-1}$ and $x_t^n > x_{t-1}^n$, then $\theta = 180$; and $y_t^n = y_t^{n-1}$ and $x_t^n < x_{t-1}^n$, then $\theta = 270$. In order to reduce the computational complexity and improve the

FIGURE 6: Multihuman target dynamic search model.

motion efficiency of the algorithm, according to the principle of computer operation, consider removing the arcsine calculation and converting the θ unit accordingly.

The multitarget dynamic search model is shown in Figure 6.

As shown in Figure 6, build a search box model for each moving target. The establishment of the search box starts from the acquisition of target motion parameters. When a new target appears, initialize its search box from the second frame to complete the dynamic tracking of multiperson targets.

3. Experimental Verification

In order to verify the proposed multiperson target dynamic tracking method for athlete training based on wireless body area network, simulation and comparative verification experiments are carried out.

The environment used in the experiment is the Matlab environment, and the test sequence used is the image sequence. The athlete training wireless body area network multiperson target image data used in the experiment is stored in the PETS-ECCV database, the image
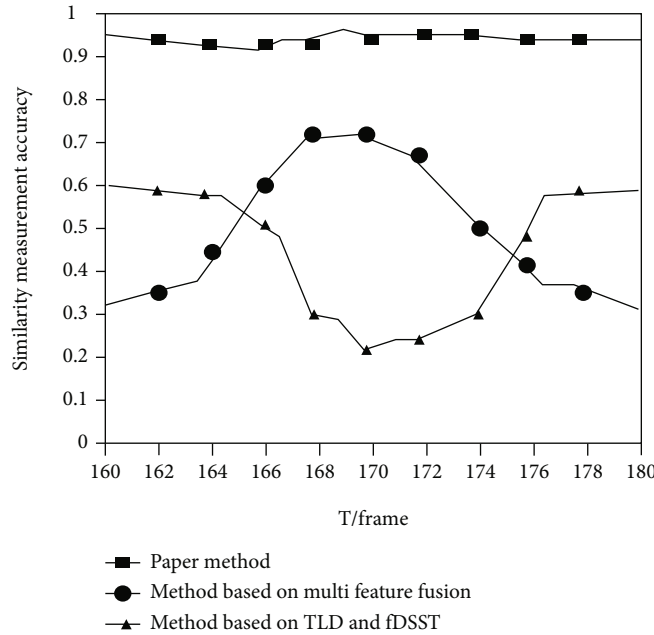
FIGURE 7: Comparison results of feature similarity measurement accuracy.

size is 320×240, the number of images is 500, and the total number of image frames is 180.

The experimental scheme is as follows: taking the accuracy of feature similarity measurement, tracking time, and tracking error as experimental comparison indexes, this method is compared with the multifeature fusion method proposed in reference [6] and the TLD and fdst methods proposed in reference [7]. The specific experimental results are as follows.

3.1. Accuracy of Feature Similarity Measurement. In the process of multiperson target dynamic tracking, it is necessary to dynamically track the training characteristics of different athletes, so it is necessary to judge the characteristics of different athletes. Feature similarity measurement has become an important means of feature judgment. Therefore, taking the accuracy of feature similarity measurement as the experimental comparison index, this method is compared with two traditional methods [16]. The comparison results of feature similarity measurement accuracy of the three methods are shown in Figure 7.

From the comparison results of the feature similarity measurement accuracy shown in Figure 7, it can be seen that the accuracy of the three methods of similarity measurement shows a distinct trend when the test frame sequence continues to increase. The measurement accuracy of the method in this paper is always maintaining a high level, basically above 0.9. The multifeature fusion method started to rise from the beginning of the experiment, but when the frame sequence reached 168, it began to gradually decrease and finally even reached 0.3. The measurement accuracy based on the TLD and fDSST method shows a trend of first decline and then rise, but the highest measurement accuracy of this method does not exceed 0.7. Therefore, it is explained that the method in this paper accurately measures the similarity
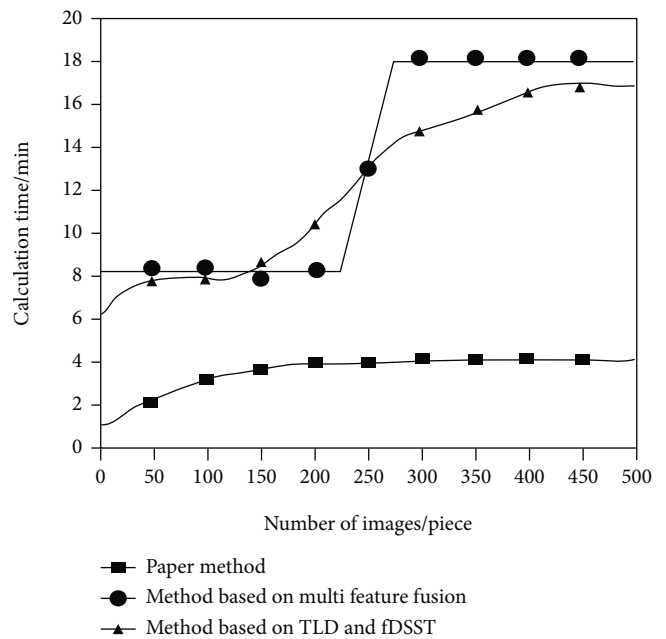
FIGURE 8: Comparison results of tracking time.

of multiperson target features to improve the reliability of tracking [17].

3.2. Tracking Time. Tracking time is one of the key indicators to judge the overall performance of the tracking method. The shorter the tracking time is, the stronger the tracking performance of the method is [18]. The tracking time comparison results of the three methods are shown in Figure 8.

TABLE 1: Comparison of tracking errors.

| Number of iterations | Tracking error/frame | | |
	Paper method	Method based on multifeature fusion	Based on TLD and fDSST method
100	0.13	6.71	4.85
200	0.15	5.67	5.61
300	0.11	5.23	4.56
400	0.12	4.62	5.76
500	0.14	6.32	6.34
600	0.12	4.69	6.47
700	0.12	6.63	4.39
800	0.13	6.16	6.48
900	0.15	5.96	6.31
1000	0.11	7.32	7.45

Observing the tracking time comparison results shown in Figure 8, it can be seen that with the increase of experimental images, the tracking time of the method in this paper shows a slight upward trend, but the maximum time is no more than 5 min. The tracking time of the two literature comparison methods increases seriously, and the maximum time is more than 15 min. Therefore, this method can reduce the tracking time and improve the tracking efficiency [19, 20].

3.3. Tracking Error. Tracking error is used as an index to directly verify the dynamic tracking method, and its results can intuitively show the performance of different tracking methods. The more obvious the tracking error is, the better the tracking performance of the method is. The tracking error comparison results of the three methods are shown in Table 1.

Observing the tracking error comparison results shown in Table 1, we can see that in the process of full iterative verification, the tracking error of the text method is significantly lower than that of the two traditional comparison methods. The minimum tracking error of the method and the method based on TLD and fDSST are 4.62 frames and 4.39 frames, respectively. Therefore, it is proved that the method in this paper can improve the accuracy of tracking.

4. Conclusion and the Future Work

In order to improve the reliability of multiperson target dynamic tracking in athlete training, a wireless body area network-based dynamic tracking method of athlete training multiperson target is proposed, and the performance of the method is verified from both theoretical and experimental aspects. This method has shorter tracking time and lower tracking error when performing multiperson target dynamic tracking during athlete training. Specifically, compared with the method based on multifeature fusion, the tracking time is significantly reduced, and the maximum tracking time is less than 5 minutes; compared with the method based on TLD and fDSST, the tracking error is significantly reduced, and the minimum error is only 0.11 frames. Therefore, it fully shows that the proposed tracking method based on

wireless body area network can better meet the requirements of athlete training multiperson target dynamic tracking. The real-time update of the athlete's status is the current research hotspot. How to capture the athlete's sports data in a shorter time and update their sports status in real time has become the research goal.

Data Availability

The data used to support the findings of this study are available from the corresponding author upon request.

Conflicts of Interest

The author declares that there are no known competing financial interests or personal relationships that could have appeared to influence the work reported in this paper.

References

[1] Y. Shi and Z. Zhao, "Error elimination method in moving target tracking in real-time augmented reality," *Journal of Real-Time Image Processing*, vol. 18, no. 8, pp. 295–305, 2021.

[2] H. Yu, G. J. Yu, B. Yang, and J. Liu, "Motion detection with local linear embedding and its application to indoor device-free human trajectory tracking," *Journal of Information Science and Engineering*, vol. 35, no. 6, pp. 1193–1208, 2019.

[3] M. Zhou, "Feature extraction of human motion video based on virtual reality technology," *IEEE Access*, vol. 8, no. 9, pp. 155563–155575, 2020.

[4] B. Fazzinga, S. Flesca, F. Furfaro, and F. Parisi, "Interpreting RFID tracking data for simultaneously moving objects: an off-line sampling-based approach," *Expert Systems with Applications*, vol. 152, no. 2, article 113368, 2020.

[5] X. Jiang, "Human tracking of track and field athletes based on FPGA and computer vision," *Microprocessors and Microsystems*, vol. 83, no. 4, article 104020, 2021.

[6] Y. Zheng, Z. Ma, S. Zhenhong, L. Hui, and L. Runxin, "Moving target tracking method based on multi-feature fusion," *Instrument Technique and Sensor*, vol. 44, no. 11, pp. 99–103+108, 2019.

[7] W. Li Yikun, D. S. Qingxian, and H. Kun, "A long-term tracking algorithm based on TLD and fDSST," *Electronics Optics & Control*, vol. 26, no. 4, pp. 48–52+74, 2019.

[8] H. Jianqiang and S. Zhibing, "Research on target tracking algorithm based on mean shift and particle filter fusion," *Chinese Journal of Electron Devices*, vol. 42, no. 3, pp. 706–711, 2019.

[9] A. Rohan, M. Rabah, and S. H. Kim, "Real-time implementation of object detection and target tracking for unmanned aerial vehicles based on convolutional neural network," in *2019 IEEE 17th World Symposium on Applied Machine Intelligence and Informatics (SAMI)*, pp. 311–316, United States, 2019.

[10] C. Ma, F. Yang, Y. Li, H. Jia, X. Xie, and W. Gao, "Deep human-interaction and association by graph-based learning for multiple object tracking in the wild," *International Journal of Computer Vision*, vol. 129, no. 6, pp. 1993–2010, 2021.

[11] L. C. Chang, S. Pare, M. S. Meena et al., "An intelligent automatic human detection and tracking system based on weighted resampling particle filtering," *Big Data and Cognitive Computing*, vol. 4, no. 4, pp. 27–35, 2020.

[12] M. Safeea and P. Neto, "Minimum distance calculation using laser scanner and IMUs for safe human-robot interaction," *Robotics and Computer-Integrated Manufacturing*, vol. 58, no. 13, pp. 33–42, 2019.

[13] R. Sarath, J. T. Varghese, and F. Pandya, "Unmanned aerial vehicle for human tracking using face recognition system," in *2019 Advances in Science and Engineering Technology International Conferences (ASET)*, pp. 1–5, United Kingdom, 2019.

[14] L. Chen and S. Li, "Human motion target posture detection algorithm using semi-supervised learning in internet of things," *IEEE Access*, vol. 9, no. 9, pp. 90529–90538, 2021.

[15] L. Xi, Z. Peng, L. Jiao, and B. M. Chen, "Smooth quadrotor trajectory generation for tracking a moving target in cluttered environments," *SCIENCE CHINA Information Sciences*, vol. 64, no. 7, pp. 1–16, 2021.

[16] Q. Zhang, C. Zhou, Y. C. Tian, Y. Qin, and B. Hu, "A fuzzy probability Bayesian network approach for dynamic cybersecurity risk assessment in industrial control systems," *IEEE Transactions on Industrial Informatics*, vol. 14, no. 6, pp. 2497–2506, 2018.

[17] W. Fang, X. Yao, X. Zhao, and J. Yin, "A stochastic control approach to maximize profit on service provisioning for mobile cloudlet platforms," *IEEE Transactions on Systems, Man, and Cybernetics: Systems*, vol. 48, no. 4, pp. 522–534, 2018.

[18] M. Wu, L. Tan, and N. Xiong, "A structure fidelity approach for big data collection in wireless sensor networks," *Sensors*, vol. 15, no. 1, pp. 248–273, 2015.

[19] Y. Qu and N. Xiong, "RFH: a resilient, fault-tolerant and high-efficient replication algorithm for distributed cloud storage," in *2012 41st International Conference on Parallel Processing*, pp. 520–529, France, 2012.

[20] S. Huang, A. Liu, S. Zhang, and T. Wang, "BD-VTE: a novel baseline data based verifiable trust evaluation scheme for smart network systems," *IEEE Transactions on Network Science and Engineering*, vol. 8, no. 3, pp. 2087–2105, 2021.

Research Article

Research on Spectrum Feature Identification of Indoor Multimodal Communication Signal

Yunfei Chen [ID],[1,2] **Yang Liu** [ID],[1,2] **and Xintao Fan**[1,2]

[1]*School of Electrical Engineering, Hebei Vocational University of Technology and Engineering, Xingtai 054035, China*
[2]*School of Electrical Engineering, Xingtai Polytechnic College, Xingtai 054035, China*

Correspondence should be addressed to Yang Liu; yl20210519@163.com

In order to solve the problem of large signal acquisition error caused by radio wave multipath effect in indoor environment, firstly, the signal source carried on the motion platform is collected for spectrum signal, and the signal processed by wavelet threshold denoising algorithms extracted and stored for spectrum feature extraction. Then, after data training and identification, the signal source is input into the system in random mode for identification. The experimental results show that the improved fuzzy clustering algorithm (FCA) is 12.7% higher than the spectrum envelope extraction method (SEEM) in the recognition rate of spectrum characteristics of different modes of signal source.

1. Introduction

In indoor positioning of motion platform, communication signal mode plays a key role in information exchange. Due to the characteristic of indoor radio wave transmission [1] of different modes of communication signal, the working mode can be automatically changed to adjust the channel when the communication [2] is not smooth. The positioning access point AP can identify the signal source on the sports platform to strengthen the positioning and tracking. The spectrum feature identification method is very important for the identification of wave signal is very important. The traditional envelope spectrum feature extraction method [3] can optimize the selection of signal source spectrum features [4] and effectively improve the signal detection accuracy of signal source. However, the feature extraction of the SEEM algorithm is easily limited by the experimental environment. When the indoor environment changes greatly, the error of feature data extracted by the SEEM algorithm is large.

The FCA is a clustering algorithm based on the fuzzy system theory [5]. Bezdek proposed the FCA [6] as early as 1973, which originated from the improved early K-means clustering algorithm. The objective function constructed by the FCA can achieve the maximum similarity of samples

belonging to the same cluster and the minimum correlation of samples between different clusters in the division process. However, the randomness of the FCA clustering center is large, which easily leads to local extremum [7]. At the same time, when the attributes of test samples are close to each other, it is difficult to classify them. All these need to guide the classification. The improved FCA based on pairwise regression fusion can be combined with the FCA in fuzzy classification, so as to improve the classification efficiency.

2. Related Work

The method of analyzing the signal characteristics by using the spectrum of the space wave signal received by the spectrum analyzer receiver has been successfully applied in many fields. At present, some scholars have studied the spectrum characteristics of outdoor GPS satellite signal [8], radar signal, and radio signal. However, there are few studies on the spectrum characteristics of indoor interference signal source. In Reference [9], the distortion of the emitter modulator and the nonlinear characteristics of the power amplifier are introduced into the classifier construction model, and the test results show that the spectrum distortion of the emitter signal exists. In Reference [10], the transient sparse feature

of signal is used as the basis of evaluation mode to realize the identification of emitter signal feature. In Reference [11], the relevant features are extracted by analyzing the time-frequency characteristics of the emitter signal to realize the identification of transient characteristics. The above research results are significant, but none of them is involved in the research of indoor positioning signal source spectrum characteristics.

3. Methodology

3.1. Building Models. In order to solve the problem of large signal acquisition error caused by the multipath effect of indoor signal source, firstly, the spectrum of the radio signal is collected and processed on the indoor platform, and then, the random signal is input to the system to identify the large-scale signal. At last, the construction of signal acquisition and identification system is shown in Figure 1.

The known communication signal source is collected and input into the spectrum identification system by the SA44B spectrum analyzer. According to the four common communication modes of GSM, CDMA, DCS, and PHS, the corresponding spectrum features are extracted and stored in the database after signal detection feature extraction and identification. Then, after learning and training, a higher frequency spectrum feature recognition rate is achieved. In the online identification stage, the signal source with unknown working mode is input into the identification system, and the working mode of the output signal source is determined after identification.

3.2. Signal Acquisition and Processing. This section is to distinguish the source signal of the target for positioning; the four modes of spectrum signals of the signal source carried by the indoor sports platform are collected indoors. The spectrum of CDMA signal source has the characteristics of smooth waveform and obvious peak, as shown in Figure 2. The spectrum of signal source in GSM mode is coarser than that in CDMA mode, but it has clear peak, as shown in Figure 3. The spectrum of DCS working mode is the most disordered among the four kinds of spectrum collected, as shown in Figure 4. In PHS mode, the peak to peak distance of communication signal spectrum is larger, so the characteristics are more obvious, as shown in Figure 5.

Obviously, the characteristics of the four modes of spectrum signals are complex, the optimal characteristic parameters of the spectrum are not easy to select, and there are many clutters in the spectrum, which affect the indoor positioning of the signal source.

In order to prevent the edge information from blurring, a nonlinear filter is introduced, in which the median filter can keep the sharp edge well. The signal processed by median filter still contains noise, and the wavelet denoising method is better for reducing Gaussian white noise in radio wave signal. The wavelet denoising method [12] includes the modulus extremum denoising method, wavelet correlation denoising method, and wavelet threshold denoising method. The traditional wavelet hard thresholding function [13] and the soft thresholding method [14] models are shown in

$$\widehat{W}_{j,k} = \begin{cases} \text{sgn}\,(W_{j,k}) \cdot (|W_{j,k}| - \lambda), & |W_{j,k}| \geq \lambda, \\ 0, |W_{j,k}| < \lambda, \end{cases}$$

$$\widehat{W}_{j,k} = \begin{cases} W_{j,k}, |W_{j,k}| \geq \lambda, \\ 0, |W_{j,k}| < \lambda. \end{cases} \tag{1}$$

The traditional wavelet hard thresholding function is easy to produce Gibbs oscillation [15], while the soft thresholding method is easy to produce "over smooth" distortion due to the constant difference of wavelet coefficients [16].

$$\widehat{W}_{j,k} = \begin{cases} aW_{j,k} + (1-a)\,\text{sgn}\,(W_{j,k}) \cdot \left(|W_{j,k}| - \dfrac{\lambda}{\exp\,(|W_{j,k}| - \lambda)^{\delta}}\right), & |W_{j,k}| \geq \lambda, \\ 0, |W_{j,k}| < \lambda. \end{cases} \tag{2}$$

As shown in formula (2), the threshold adjustment parameter a is $a = 1 - e^{-\alpha(|W_{j,k}| - \lambda)^2}$, W' is the mean value of neighborhood wavelet coefficients, and δ is a positive number. When $e\,|W_{j,k}| \longrightarrow \pm\lambda$ is $\widehat{W}_{j,k} \longrightarrow 0$, the threshold value $W_{j,k} = \pm\lambda$ function is continuous, which can overcome the signal oscillation problem caused by the discontinuity of hard threshold; when $W_{j,k} \longrightarrow \pm\infty$ is $\widehat{W}_{j,k}/W_{j,k} \longrightarrow 1$, the new threshold function conforms to the characteristics of hard threshold function, which can overcome the hard threshold, so as to overcome the distortion caused by the constant difference of wavelet coefficients.

When the threshold adjustment parameters $\alpha \longrightarrow 0$ and $\delta \longrightarrow 0$, the new wavelet threshold function is a soft threshold function; when the threshold adjustment parameters $\alpha \longrightarrow +\infty$ and $\delta \longrightarrow 1$, the new wavelet threshold function is a hard threshold function. By adjusting the parameters a and δ, we can obtain the signal processing results of different modes of the interference signal source. After denoising the spectrum of the four modes, we can normalize the Z-score [17], as shown in Figure 6.

3.3. Spectrum Feature of Signal Extraction. The signal spectrum parameters are selected to extract the peak value, corresponding frequency, signal spectrum bandwidth, and kurtosis [18] of the signal transmitted by different mode signal sources as the characteristic parameters of the corresponding mode of the radio wave signal. The feature parameters of different modes of CDMA, GSM, DCS, and PHS of signal source are extracted step by step to construct the vector sequence required for the feature recognition model of radio wave signal. As shown in Table 1, the four modes of CDMA, GSM, DCS, and PHS are, respectively, marked as $C = 1 \sim 4$.

3.4. Analysis of Category Characteristics. Let the length of eigenvectors in feature set $X = \{x_1, x_2, \cdots, x_n\}$ be l, and the number of eigenvectors be n; then, feature set $\mathbf{X}$ is divided into c fuzzy groups. In order to represent the degree to which
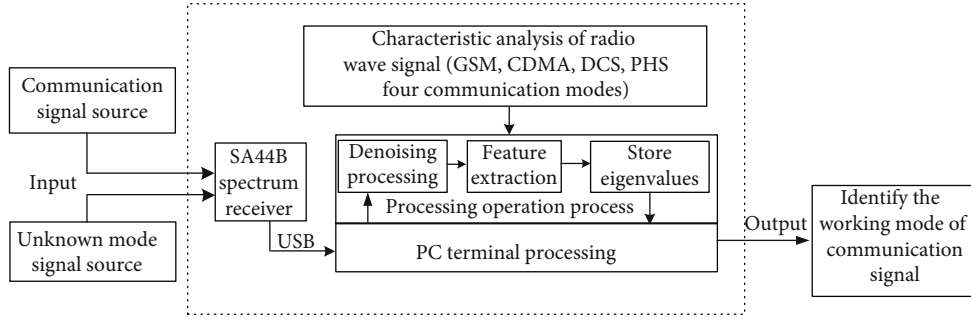
Figure 1: Structure diagram of signal acquisition and identification system.
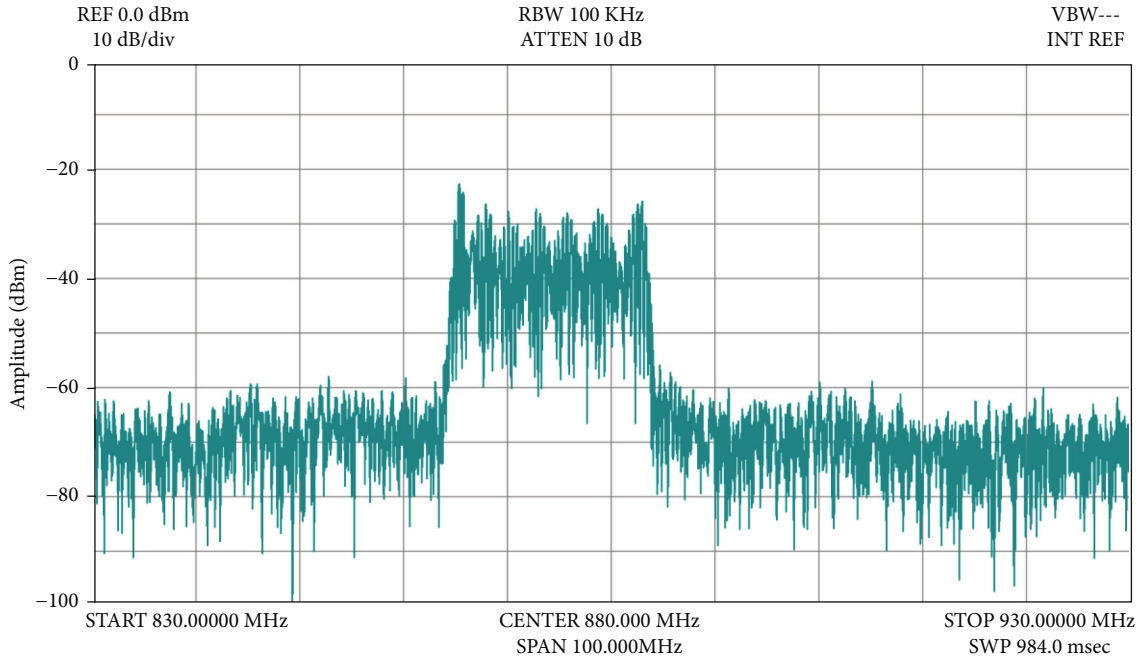
Figure 2: Spectrum of CDMA mode.

each eigenvector belongs to c independent classes, the algorithm returns c clustering center matrix and membership matrix $U_{c \times n} = \{u_{ij}\}$, where each element u_{ij} indicates that x_i of $\mathbf{X}$ belongs to c_j membership. The objective function is constructed as follows:

$$F_{fcm}(u, c) = \sum_{j=1}^{n} \sum_{i=1}^{c} u_{ij}^m \quad d_{ij}^2(x_j, c_i),$$

$$\text{s.t} \sum_{i=1}^{c} u_{ij} = 1, \quad \forall j = 1, \cdots, n. \tag{3}$$

Taking each row of feature set in Table 1 as the corresponding feature vector, the feature vector matrix of $M \times N = 4 \times 8$ can be constructed, and $\mathbf{X}$ is the input matrix of the fuzzy clustering algorithm. The number of clusters is set as $c = 4$, the fuzzy weight parameter is $m = 2$, the number

of iterations is 500, and the iteration stop threshold parameter is $\varepsilon = 1.0 \times 10^{-5}$ by four modes. The cluster center set C and membership matrix U of four kinds of eigenvectors can be obtained by operation.

As shown in formula (3), C is the cluster center set, c_i is the cluster center of class i, m is the fuzzy weight parameter, D is the initial number of clusters in fuzzy clustering, $m = 2$ according to experience, and $d_l(x_i, c_i) = \sqrt{\sum_{i}^{n}(x_i - c_i)^2}$ is the Euclidean distance from feature vector x_i to class center c_i. Through iterative calculation, the data is close to the optimal clustering center $C = \{c_i\}$.

$$C = \begin{bmatrix} 3.7853 & 0.4924 & 1.2582 & 1.3613 \\ 6.3072 & 0.5661 & 1.3713 & 1.8426 \\ 3.6519 & 0.6368 & 1.0911 & 1.1998 \\ 4.8730 & 0.6689 & 1.3461 & 1.3791 \end{bmatrix},$$
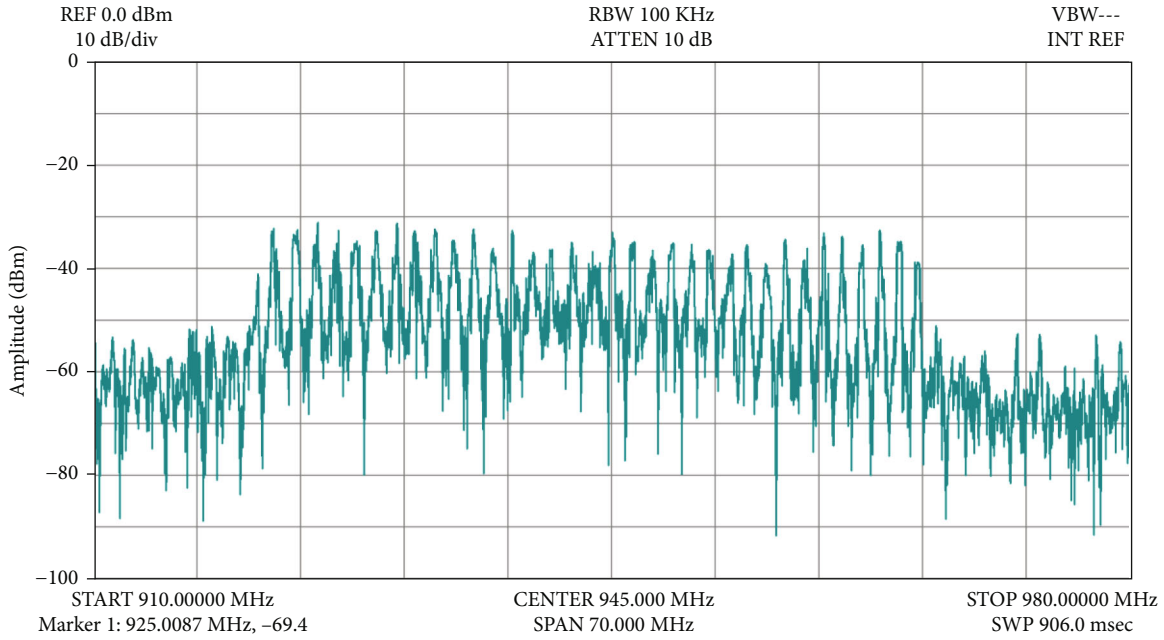
FIGURE 3: Spectrum of GSM mode.
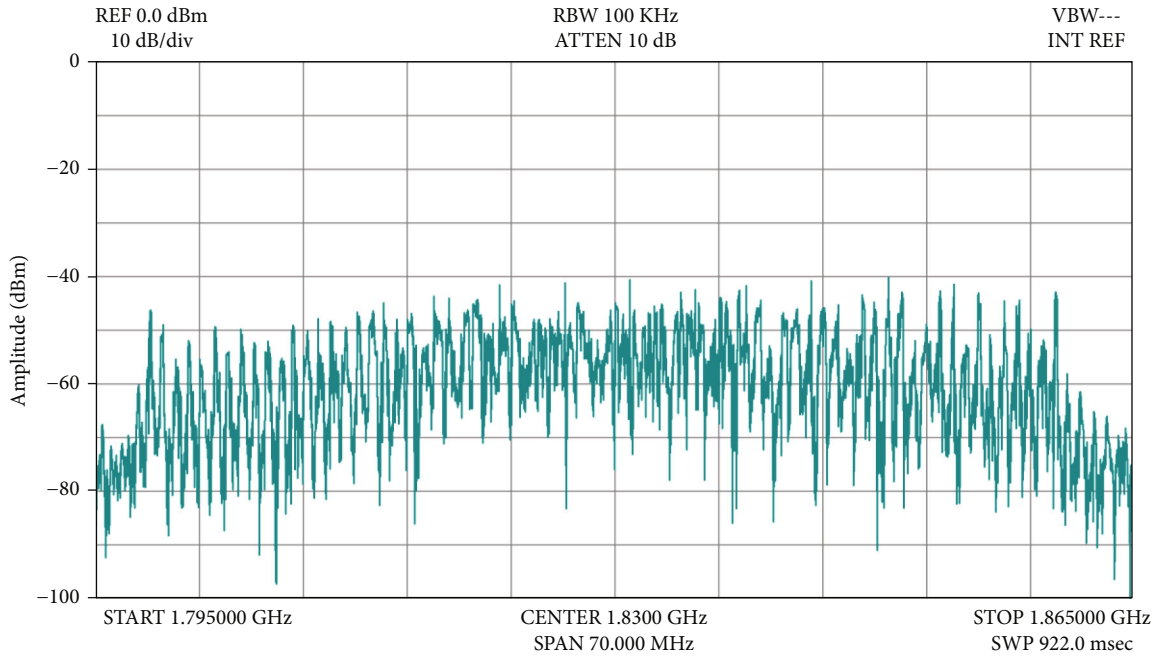
FIGURE 4: Spectrum of DCS mode.

$$
U = \begin{bmatrix}
0.9861 & 0.9994 & 0.0065 & 0.0296 & 0.0001 & 0.0127 & 0.0074 & 0.0090 & 0.0000 \\
0.0018 & 0.0000 & 0.9713 & 0.8936 & 0.0002 & 0.0115 & 0.0097 & 0.0007 & 0.0001 \\
0.0082 & 0.0002 & 0.0032 & 0.0172 & 0.0000 & 0.0060 & 0.0025 & 0.9802 & 0.9999 \\
0.0074 & 0.0003 & 0.0268 & 0.0726 & 0.9997 & 0.9707 & 0.9834 & 0.0020 & 0.0000
\end{bmatrix}.
$$

(4)

From the data in the membership matrix U, we can find the row number to which the eigenvector belongs, that is,

the membership degree of the class label. The row code corresponding to the maximum value in each column of data is the category number to which the eigenvector belongs. According to matrix U, the maximum data values calculated in columns $1 \sim 2$ appear in the first row, so the characteristic data in columns $1 \sim 2$ in Table 1 are classified into the same category. Approximately, according to the maximum membership value of the characteristic data in columns $3 \sim 4$, $5 \sim 6$, and $7 \sim 8$, the state class label can be determined.

REF 0.0 dBm RBW 100 KHz VBW---
10 dB/div ATTEN 10 dB INT REF
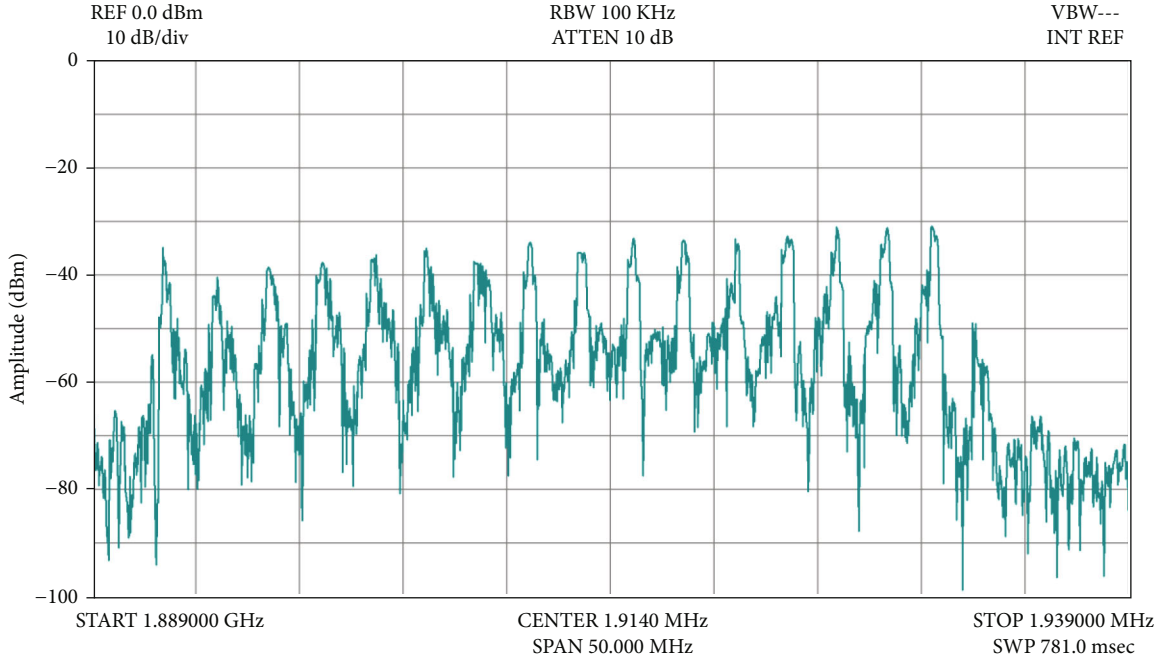
FIGURE 5: Spectrum of PHS mode.

It can be seen that the above-extracted feature data has obvious category features, which can correctly distinguish the four mode state features of signal source, but the resolution is not clear enough, and more detailed classifiers need to be built to distinguish.

3.5. The Establishment of Classifier.

The traditional FCA is influenced by kernel function, and fuzzy selection is not of probability significance. At the same time, it is hard to classify nonlinear samples. Therefore, for known feature set $\{x_i\}_{i=1}^n$, category tag sequence is $\{lable_i\}_{i=1}^n$, $i \in (1, 2, \cdots, n)$, and ω_i is the weight parameter. The function of the soft interval classification optimization model of FCA is improved and constructed as follows:

$$\min_{\omega, b} \frac{1}{2} \|\omega\|^2 + K \sum_{i=1}^n \ell_{\log}\left(y_i\left(\omega^T x_i + b\right) - 1\right). \quad (5)$$

As shown in formula (5), where $K > 0$ is a constant and $\ell_{\log}(y_i(\omega^T x_i + b) - 1)$ is the logistic loss function, that is, $\ell_{\log}(z) = \log(1 + \exp(-z))$. The introduction of the pair rate regression model has the advantage of output prediction marker and probability parameter, which is suitable for multiclassification problems in application.

Therefore, it is equivalent to using the maximum likelihood method to solve the inner layer maximization in the Bayesian framework [19], as shown in

$$\max \ell(\omega, b) = \sum_{i=1}^n \log p(y_i|x_i; \omega, b). \quad (6)$$

Let $\beta = (\omega, b)$, $\widehat{x} = (x; 1)$, formula (7) can be transformed into

$$\min \ell(\beta) = \sum_{i=1}^n \left(-y_i \beta^T \widehat{x}_i + \log\left(1 + e^{\beta^T \widehat{x}_i}\right)\right). \quad (7)$$

As shown in formula (7), it is a high-order continuous convex function of A. according to the Newton iterative method in convex optimization theory, the optimal solution $\beta^* = \underset{\beta}{\arg\min} \ell(\beta)$ can be obtained, and then, the weights ω and b can be obtained. Furthermore, it is assumed that $P(y_i|\omega)$ follows Bernoulli distribution and ω follows Gauss prior distribution. In order to eliminate irrelevant noise component σ^2, the likelihood estimation probability model is obtained, as shown in

$$P(y_i|\omega) = \prod_{i=1}^n \sigma\{y(x_i; \omega)\}^{x_i}[1 - \sigma\{y(x_i; \omega)\}]^{1-x_i}. \quad (8)$$

In order to reduce the learning degree of the model, a penalty parameter $\mathbb{R}(\omega_i|0, \mu_i^{-1})$ is introduced for each weight to get the probability evaluation model.

$$P(\omega|\mu) = \prod_{i=0}^n \mathbb{R}\left(\omega_i|0, \mu_i^{-1}\right). \quad (9)$$

As shown in formula (9), $\mu = (\mu_0, \mu_1, \cdots, \mu_n)^T$ is a sparse probability model constructed by $n + 1$ dimensional hyperparameters. It can be seen that the improved FCA based on pairwise regression fusion has the advantage of estimating the output prediction marker and adding probability parameters at the same time.
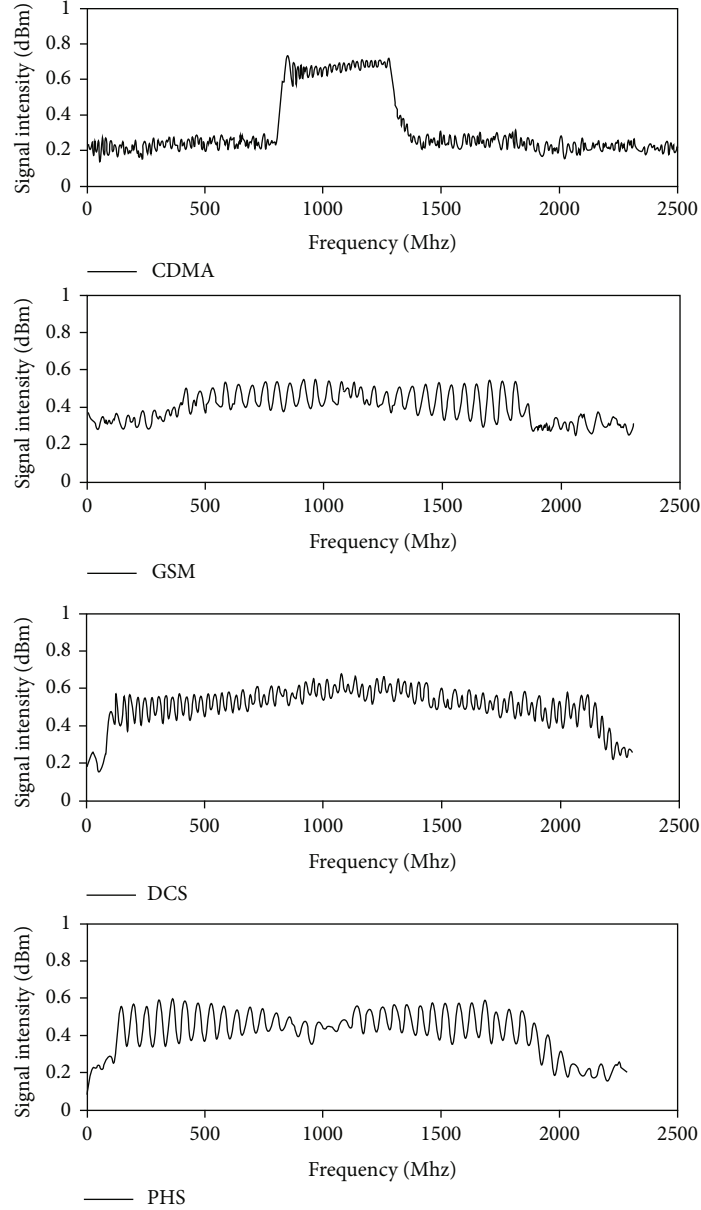
FIGURE 6: Spectrum normalization of four interference modes.

TABLE 1: Partial experimental characteristic data.

RSSI$_M$ (dBm)	f_M (10^3 MHz)	f_{band} (10^3 MHz)	ψ	C
-29.32	0.867	0.028	57.231	1
-30.51	0.873	0.027	56.538	1
-41.65	1.806	0.062	51.267	2
-40.37	1.847	0.058	50..324	2
-39.13	1.930	0.042	27.225	3
-38.42	1.923	0.045	26.881	3
-58.65	1.841	0.002	62.447	4
-60.31	1.831	0.001	63.617	4
…	…	…	…	

3.6. *Optimization of Classification Processing.* Because the soft interval FCA classification model has high prediction cost, in order to reduce the overfitting risk of model training error, The SA algorithm is used to accelerate the convergence of FCA training process. The SA algorithm is easy to global optimization and to avoid local extremum, so it can achieve better global convergence.

Step 1. Initialization program, in which the initial temperature T_0, initial solution vector ψ_0, step size $L_0 = 1$, solution space vector dimension 3, the number of iterations 200, and termination threshold $\xi = 1.0 \times 10^{-3}$.

Step 2. The FCA model is used to calculate the initial solution ω_i, and the SA algorithm is called with ω_i as the initial point to generate a new point $\omega_i' = \omega_i + \gamma L_0$ randomly, where $\gamma \in (0, 1)$ is a random number and $P(\boldsymbol{\omega}_i | \mu)$ is calculated.

Step 3. The fitness $\varphi_{(\omega,b)}$ is calculated by K-fold cross-validation, where the fold number K is set to 5, and the global optimal value is updated according to $\varphi_{(\omega,b)}$. If $\varphi_{(\omega,b)} \leq 0$, it has got the new solution is accepted. Otherwise, the new solution is accepted by probability $p = \exp^{-\Delta\varphi_{(\omega,b)}^2(i)/T}$, where T is the current temperature control parameter. The annealing function is used to control the iteration speed $T_n = \alpha T_{n-1}$, and the annealing smoothing coefficient is set to $\alpha = 0.8$.

Step 4. When the iteration satisfies criterion $T < \xi$ or the number of iterations reaches, the program exits, and the fine classification of samples is obtained.

3.7. Train and Test. In order to verify the resolution and generalization ability of the above models, the "reserve method" is also used to identify and verify the samples collected from different mode signal sources. Each mode state is sampled in 30 groups, and a total of 120 groups of experimental data are collected, and their characteristic parameters are extracted. In order to prevent data overtraining, 100 groups of each group of signal feature set are randomly selected for model training. Using 20 groups of feature samples as verification set for classifier test, the iteration number is 500, then stop threshold $\varepsilon = 1.0 \times 10^{-5}$, and model classification calculation to get confusion state matrix; according to the test results of confusion state matrix, the correct samples can be classified as table diagonal cumulative sum, a total of 18; the overall correct recognition rate can reach 90%, which can effectively identify the signals of four working modes.

Among them, the mode signal with identification error is DCS. The reason is that the spectrum characteristics of the signal source in this frequency band are close to that of the adjacent signal frequency band. When the signal strength of the detection signal source is close to that of the adjacent frequency band, there will be misjudgment, but the misjudgment rate is low. The confusion state matrix calculated from the model classification is shown in Table 2, which shows that the system can get enough accurate results for the specified signal source signal pattern identification.

4. Experimental Results and Analysis

4.1. The Comparison of Identification Rate. Through the SA44B spectrum receiver, the four modes of spectrum signals of the signal source carried by the indoor sports platform are collected indoors. Quantitative test experiments are carried out to verify the accuracy of feature selection of the SEEM algorithm and SA-FCA. The recognition rate is measured by extracting the percentage of correct samples in the unit number of features. The number of samples collected per unit is set to 200, and the proportion of correct eigenvalues and total eigenvalues is calculated, as shown in Figure 7. When the number of spectrum increases to 300, the highest recognition rate can reach 93.1%. Then, the feature selection ability of the SEEM algorithm decreases with the increase of the number of features. When the number of features increases to 400, extracted by SA-FCA, the maximum feature recognition rate reaches 96%. From the com-

TABLE 2: Disturbance source signal characteristic identification results.

Test status	The identification experiment results				
	CDMA	DCS	PHS	Mobile	Accuracy rate (%)
CDMA	5	0	0	0	100
DCS	0	4	0	1	90
PHS	0	0	5	0	100
Mobile	0	0	1	4	90
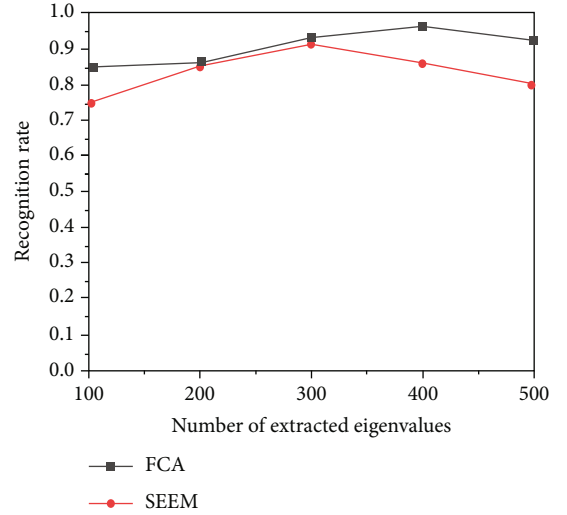
FIGURE 7: Comparison of SEEM and FCA identification rates.

parison chart of recognition rate, it can be seen that the larger the number of selected features is not the better, and the number of features shows a downward trend when the number of features reaches 400.

4.2. Location Accuracy Analysis of Optimal Features. Furthermore, the optimized spectrum eigenvalues of the signal source are used for positioning experiments to verify the influence of the optimization algorithm on the positioning accuracy. Traditional NN algorithm, KNN algorithm [20], SEEM algorithm, and improved FCA algorithm are compared in indoor positioning experiments, as shown in Figure 8. The improved FCA feature selection method can achieve 78% in the positioning error of 1.3 m, which is 13% higher than the SEEM algorithm. The improved FCA feature selection method can achieve 83% in the positioning error of 1.5 m, which is 8% higher than the SEEM algorithm.

5. Discussion

The classification analysis of eigenvalues extracted from radio wave signals is the basis of illegal signal identification. FCA model clustering is widely used as an unsupervised learning algorithm of the "hardening score" method. By adjusting the membership criterion, the individual feature vectors in the feature set are classified into subcategories of a cluster center one by one, and the similarity between
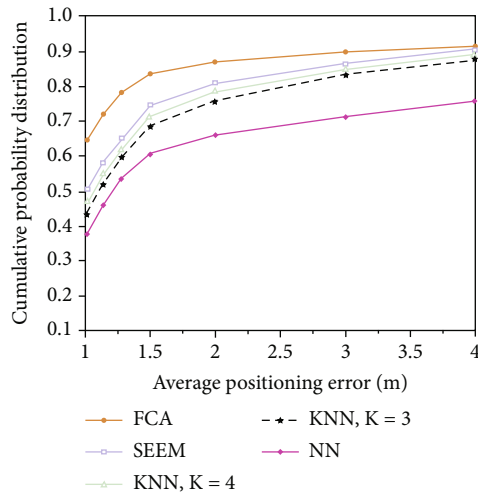
FIGURE 8: Cumulative error distribution of SEEM algorithm and FCA.

different categories is the smallest. According to this, through the fuzzy clustering identification of the characteristics of CDMA, GSM, DCS, and PHS four different mode signals, a small amount of sample data is used to test the effectiveness of extracting the categories of the eigenvalues of radio wave signals.

The FCA is a common classifier suitable for small sample sets and can also be extended to the field of multiclassification. Its core idea is to build a hyperplane model to classify the sample data in the feature space and remove the specific values. The difficulty is to separate the hyperplane close range samples with high confidence rate and maximum interval.

6. Conclusions and Future Work

Aiming at the problem of large positioning error caused by the working mode transformation of the signal source carried by the indoor sports platform, this paper first expounds the feature identification of the interference signal source from the new perspective of the spectrum detection and feature identification of the radio wave signal and studies the spectrum characteristics of the radio wave signal, after the denoising processing of the wavelet threshold method. Then, through the improved FCA model classification training and identification, the effect is better than the envelope method. Finally, the spectrum eigenvalues extracted from the identification are used for positioning. Indoor positioning experiments are carried out by traditional NN algorithm, KNN algorithm, seem algorithm, and improved FCA. The recognition rate of the collected samples is relatively ideal, and the positioning effect based on the feature data is better. In addition, there are other types of signal sources to be further studied, which require a large number of collected data to enrich the identification database, which need to be improved in the follow-up experiments.

References

[1] M. M. Harsha, R. H. Mulangi, and H. Kumar, "Analysis of bus travel time variability using automatic vehicle location data," *Transportation Research Procedia*, vol. 48, pp. 3283–3298, 2020.

[2] S. Dewi and S. Sahriman, "Pemodelan statistical downscaling dengan regresi modifikasi jackknife ridge dummy Berbasis K-means untuk pendugaan curah hujan," *ESTIMASI Journal of Statistics and Its Application*, vol. 1, no. 12, pp. 19–28, 2021.

[3] J. Park, H. Kim, J. Yoon, H. Kim, C. Park, and D. Hong, "Development of an ultrasound technology-based indoor-location monitoring service system for worker safety in shipbuilding and offshore industry," *Processes*, vol. 9, no. 2, p. 304, 2021.

[4] S. Q. Zhang, Y. L. Dong, L. G. Zhang, B. Yan, and P. He, "Feature frequency extraction method based on mean envelope ITD and spectral kurtosis," *Jiliang Xuebao/Acta Metrologica Sinica*, vol. 38, no. 5, pp. 598–601, 2017.

[5] K. Nonalinsavath, L. E. Nugroho, W. Widyawan, and K. Hamamoto, "Indoor location tracking system based on android application using bluetooth low energy beacons for ubiquitous computing environment," *Journal of Communications*, vol. 1, no. 1, pp. 572–576, 2020.

[6] L. Dong, W. Wu, Q. Guo, M. N. Satpute, T. Znati, and D. Z. Du, "Reliability-aware offloading and allocation in multilevel edge computing system," *IEEE Transactions on Reliability*, vol. 70, no. 1, pp. 200–211, 2021.

[7] Q. Yue and L. Zhang, "Two-sided matching for hesitant fuzzy numbers in smart intelligent technique transfer," *Mechanical Systems and Signal Processing*, vol. 139, article 106643, 2020.

[8] M. K. Mishra, R. Renju, N. Mathew, C. Suresh Raju, M. R. Sujimol, and K. Shahana, "Characterization of GSAT-14 satellite Ka-band microwave signal attenuation due to precipitation over a tropical coastal station in the southern peninsular region of the indian subcontinent," *Radio Science*, vol. 55, no. 2, 2020.

[9] S. Cao, X. Chen, X. Zhang, and X. Chen, "Combined weighted method for TDOA-based localization," *IEEE Transactions on Instrumentation and Measurement*, vol. 69, no. 5, pp. 1962–1971, 2020.

[10] W. van Woensel, P. C. Roy, S. S. R. Abidi, and S. R. Abidi, "Indoor location identification of patients for directing virtual care: an AI approach using machine learning and knowledge-based methods," *Artificial Intelligence in Medicine*, vol. 108, article 101931, 2020.

[11] Y. L. Chen, Y. C. Chang, and Y. L. Zeng, "An opportunistic large array concentric geographic routing algorithm with a relay node in wireless sensor networks," *Applied Mechanics & Materials*, vol. 764-765, pp. 838–842, 2015.

[12] M. K. Khan, M. Shiraz, K. Zrar Ghafoor, S. Khan, A. Safaa Sadiq, and G. Ahmed, "EE-MRP: energy-efficient multistage routing protocol for wireless sensor networks," *Wireless Communications & Mobile Computing*, vol. 2018, article 6839671, pp. 1–13, 2018.

[13] J. H. Choi, E. B. Cho, Z. Ghassemlooy, S. Kim, and C. G. Lee, "Visible light communications employing PPM and PWM formats for simultaneous data transmission and dimming," *Optical & Quantum Electronics*, vol. 47, no. 3, pp. 561–574, 2015.

[14] H. el-Sayed, S. Sankar, M. Prasad et al., "Edge of things: the big picture on the integration of edge, IoT and the cloud in a distributed computing environment," *IEEE Access*, vol. 6, pp. 1706–1717, 2018.

[15] E. Berriochoa, A. Cachafeiro, and J. M. García Amor, "Gibbs-Wilbraham oscillation related to an Hermite interpolation problem on the unit circle," *Journal of computational and applied mathematics*, vol. 344, pp. 657–675, 2018.

[16] Y. Gao and Y. Chen, "Spectrum sensing exploiting the maximum value of power spectrum density in wireless sensor network," *Wireless Networks*, vol. 25, no. 4, pp. 1949–1964, 2019.

[17] N. Shahid, I. H. Naqvi, and S. B. Qaisar, "Characteristics and classification of outlier detection techniques for wireless sensor networks in harsh environments: a survey," *Artificial Intelligence Review*, vol. 43, no. 2, pp. 193–228, 2015.

[18] H. A. Chowdhury and M. S. Rahman, "Formant estimation from speech signal using the magnitude spectrum modified with group delay spectrum," *Acoustical Science and Technology*, vol. 42, no. 2, pp. 93–102, 2021.

[19] H. Hunt, "Lightning location system detections as evidence: a unique bayesian framework," *IEEE Transactions on Geoscience and Remote Sensing*, vol. 59, no. 3, pp. 1848–1858, 2021.

[20] J. Zhang, H. You, and R. Jia, "Reliability hazard characterization of wafer-level spatial metrology parameters based on LOF-KNN method," *Microelectronics Reliability*, vol. 107, article 113599, 2020.

Research Article

ECG Signal Detection and Classification of Heart Rhythm Diseases Based on ResNet and LSTM

Qiyang Xie,[1,2] Xingrui Wang,[1] Hongyu Sun,[1] Yongtao Zhang,[3] and Xiang Lu [1]

[1]*College of Electronic and Information Engineering, Shandong University of Science and Technology, Qingdao 266590, China*
[2]*School of Information and Communication Engineering, University of Electronic Science and Technology of China, Chengdu 610054, China*
[3]*Department of Cardiology, Affiliated Hospital of Qingdao University, Qingdao, 266000 Shandong, China*

Correspondence should be addressed to Xiang Lu; sdustlx@sdust.edu.cn

Arrhythmia is one of the most threatening diseases in all kinds of cardiovascular diseases. It is important to achieve efficient and accurate automatic detection of arrhythmias for clinical diagnosis and treatment of cardiovascular diseases. Based on previous research on electrocardiogram (ECG) automatic detection and classification algorithm, this paper uses the ResNet34 network to learn the morphological characteristics of ECG signals and get the significant information of signals, then passes into a three-layer stacked long-term and short-term memory network to get the context dependency of the features. Finally, four classification tasks are implemented on the PhysioNet Challenge 2017 test dataset by using the softmax function. The activation function is changed from the ReLu function to the mish function in this model. Negative information of ECG signals is considered in the training process, which makes the model have more stable and accurate classification ability. In addition, this paper calculates and compares the average information entropy of correctly classified samples and incorrectly classified samples in the test set. Moreover, it eliminates the impact of obvious signal abnormalities (redundancy or loss) on the model classification results, to more comprehensively and accurately explain the classification effect and performance of the model. After eliminating the possibility of abnormal signal, the ResNet34-LSTM3 model obtained an average F1 score of 0.861 and an average area under the receiver operating characteristic curve (ROC) of 0.972 on the test dataset, which indicates that the model can effectively extract the characteristics of ECG signals and diagnose arrhythmia diseases. Comparing the results of the ResNet34 model and ResNet-18 model on the same test dataset, we can see that the improved model in this paper has a better classification and recognition effect on ECG signals as a whole, which can identify atrial fibrillation diseases more effectively.

1. Introduction

With the increasing pressure on people's lives and work, cardiovascular disease has gradually become one of the important diseases threatening human life and health. According to the report of the World Health Organization, the mortality of cardiovascular disease ranks first among all kinds of diseases, accounting for 33.3% of other diseases. Arrhythmia is a kind of cardiovascular disease with a high incidence rate and high risk in all cardiovascular diseases. Atrial fibrillation (AF) is the most common arrhythmia disease. The clinical manifestations of patients are atrial arrhythmia or ineffective contractions. These diseases often occur in the elderly population and have a high incidence rate and long course. It is easy to cause heart failure, stroke, and other complications, which pose a serious threat to the safety of patients. Therefore, early and accurate detection of this kind of arrhythmia is an important challenge in clinical work. At present, the main tool for arrhythmia diagnosis is the electrocardiogram (ECG). By analyzing the ECG signal of patients, medical workers can make an accurate diagnosis of different types of arrhythmias. However, this kind of manual detection method relying on the clinical experience and a lot of professional knowledge of medical workers is often prone to make mistakes [1], and it also needs to invest a lot of manpower and energy. With the continuous development and maturity

of computer technology and electronic information technology, the task of using a computer to analyze ECG signals to realize automatic detection of arrhythmia has become a research hotspot at this stage, which can provide a more effective and reliable diagnosis basis for medical workers, thereby alleviating the investment in human resources [2].

The existing ECG classification algorithms usually include signal preprocessing, such as wavelet transform and manual feature extraction, but the amount of computation will increase the delay of the real-time classification system. In recent years, deep learning algorithm with their advantages of automatic learning features is increasingly used in the field of health care, such as medical image recognition and segmentation, time series data monitoring, and analysis. At present, the outstanding algorithm can establish an end-to-end DNN network to learn the characteristics of ECG records by using the extensive digital characteristics of ECG data, which saves a lot of signal preprocessing steps. Because the performance of DNN increases with the amount of training data, this method can make good use of the extensive digitization of ECG data.

The rest of this paper is organized as follows. The second section reviews the related research. Datasets and methods are described in the third section. The fourth section introduces and analyzes the experimental results. The fifth section summarizes the advantages and disadvantages of this method and puts forward the prospects.

2. Related Work

The common classification task of automatic detection of ECG signals usually has three steps, which are preprocessing, signal, feature extraction, and identification classification [3]. Since ECG signals are acquired using an ECG acquisition recorder, the original signal would be mixed with several noise and invalid signals. In general, low-pass filters, wavelet transform, and other relatively classical denoising methods are used in the preprocessing step. After signal preprocessing, feature extraction of the signal is performed. The traditional feature extraction methods use the discrete Fourier transform or wavelet transform to extract the morphological features of time series signals [4, 5], such as slope, amplitude, peaks, interval, and other characteristic information, and compose the feature vector addition to all types of traditional machine learning algorithms, such as principal component analysis and independent component analysis. More efficient, reliable, and compact eigenvectors can be obtained from ECG signals. These traditional feature extraction algorithms need to provide hand-crafted or feature-specific implications. However, the selection and combination of features often require expertise, and the selection process is time consuming [6]. With the development of deep learning theory, researchers worldwide began to use deep learning algorithms to automatically extract features of interest from data.

In a deep learning-based arrhythmia detection study, Kiranyaz et al. [7] developed a convolutional neural network (CNN) classification algorithm based on one-dimensional convolution for the corresponding disease class of ECG, which can accomplish the basic classification tasks but has low sensitivity for arrhythmia classification of sveb type. Rajpurkar et al. [8] proposed a convolutional neural network algorithm with residual structure, which utilized the electro-cardiographic signal collected from a single-lead wearable device for the detection of arrhythmia information [9] and used the AlexNet network as input bispectral spectrum of ECG signal, and the experiment finally got an average accuracy of 91.3%.Mostayed et al. [10] proposed a recurrent neural network algorithm; they trained the 12 lead ECG signal inputs into a model composed of two bidirectional long short-term memory (LSTM) networks to detect pathologies in the signal. Yildirim [11] used wavelet transform to decompose the ECG signal into a wavelet sequence, then entered into a two-way LSTM model for training and classification, and obtained a recognition accuracy of 99.39% under ideal conditions. Subsequently, Saadatnejad et al. [12] proposed a lightweight feature automatic extraction method combining wavelet transform with LSTM network, which could realize continuous real-time classification of electrocardiographic signals. Feng et al. [13] proposed a 16-layer convolutional neural network and combined it with a long-term memory network to realize multichannel classification, which achieved 95.4% accuracy in classifying myocardial infarction disease in the PTB database.

In addition to the above deep learning algorithms that directly utilize the one-dimensional ECG data for training, literature [14] transformed three adjacent beats in the ECG signal into a two-dimensional coupling matrix, and this matrix obtained the correlation between signal beat and morphological information [15, 16] Jun et al. [17] converted each beat in the signal into a two-dimensional gray-scale image, which was then taken as input to a 2D convolutional neural network. Then, such 2D methods need to convert 1D cardioelectrical signals into 2D information, which also occupies harder disk space while increasing the computational cost. In conclusion, many existing algorithms suffer from complicated preprocessing processes [18, 19] and high time costs [17].

3. ECG Dataset Introduction and Resnet34-LSTM3 Classification and Detection Method

Based on the end-to-end network characteristics, this study tries to combine a 34-layer ResNet network (ResNet34) with three stacked LSTM networks (LSTM-3) in combination with previous experience. Moreover, this model does not need too complex procedures such as signal preprocessing and manual feature extraction, and it uses the ResNet34 network to learn the morphological features of electrocardiographic signals and acquire significant information of the signal (the features extracted by the network are mainly the deep-level abnormal waveform feature information contained in the F wave, P wave, and QRS complex in the ECG signal). The context dependence of features was then acquired utilizing a three-layer stacked LSTM network. Finally, a multiclassification task on the PhysioNet challenge 2017 (https://physionet.org/challenge/2017/) test dataset was implemented through the softmax function. This model

utilizes the max pooling layer, dropout layer, and batch normalization layer several times to optimize the calculations and improve the classification accuracy. At the same time, it is intended to change the activation function from the ReLu function to the Mish function so that the model takes into account the negative value information of the ECG signal in the training process, while making the model more stable. In addition, this paper uses the model to classify ECG signals and calculates and compares the average information entropy of correctly classified samples and incorrectly classified samples. It eliminates the impact of obvious signal abnormalities (redundancy or loss) on the model classification results later, to more comprehensively and accurately explain the classification effect and performance of the model.

3.1. Introduction to ECG Datasets. The dataset used in the experiment is from the PhysioNet Challenge 2017 Short Single-Lead ECG AF Classification Competition website. The training set contains 8528 single-lead ECG signal sampling records, ranging from 9 seconds to slightly more than 60 seconds; each ECG sample has a sampling frequency of 300 Hz and has been band-pass filtered by the AliveCor device. Each sample contains a mat file of the corresponding ECG and a hea file containing waveform information, while all ECG samples are classified by human cardiologists into four categories: normal (N), atrial fibrillation (A), other rhythm (O), and noise (~).

The data division of training set and test set is shown in Figure 1, wherein there are 8528 data in the training set and 852 data in the test set. More details of the training set are shown in Table 1, where SD stands for standard deviation and med stands for median. Figure 2 shows examples of ECG waveforms in four categories (lasting 20 seconds) from top to bottom, with normal rhythm-like normal (N), atrial fibrillation (A), other rhythm (O), and noise (~) from left to right.

3.2. ECG Data Preprocessing. To train the built deep learning model more efficiently, the sequence length of each input network needs to be fixed. For this reason, this study first traversed all ECG signal samples in the dataset, finding the largest sequence length and defined as max_length. On the other hand, because the majority of ECG signal sample points in the dataset are around 9000 (the sampling time is about 30 seconds), and a considerable number of samples are about 18000, so for samples with sampling points close to max_length/2, if the number of sample points is larger than 9000, only the first 9000 sample points of this sample will be taken. If the number of sample points for this sample is less than 9000, then the sample is null-filled so that its sequence length reaches 9000. Similarly, for samples with sampling points close to max_length, if the number of sampling points of this sample is greater than 18000, only the first 18000 sampling points of this sample will be taken. If the number of sampling points of this sample is less than 18000, then the sample will be zero-filled so that its sequence length reaches 18000. The ECG signal samples processed above are later referred to as normalized samples, and the process is shown in Figure 3.
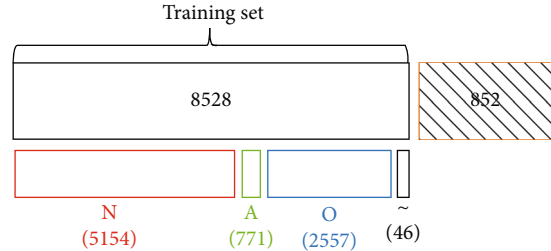
FIGURE 1: Data set composition diagram.

TABLE 1: Data table for the training set.

Type	Number	Mean	SD	Max	Med	Min
			Time length (s)			
Normal (N)	5154	31.9	10.0	61.0	30	9.0
AF (A)	771	31.6	12.5	60	30	10.0
Other (O)	2557	34.1	11.8	60.9	30	9.1
Noisy (~)	46	27.1	9.0	60	30	10.2
Total	8528	32.5	10.9	61.0	30	9.0

Category vectors currently contain four different labels, namely N, A, O, and ~, and each ECG sample corresponds to a label identified by a human cardiologist. In this study, each normalized sample was divided into trunc_samp input sequences of the same length. The label specification of each input sequence is consistent with that of the original sample [20], where trunc_samp is defined as

$$trunc\_samp = int\ (max\_length/step). \qquad (1)$$

In the experiment, the step is set to 256 and int is an integer operation.

The shape of the final input matrix is (normalized number of samples) × trunc_samp, step, 1), where 1 indicates that a single input sequence is one-dimensional and the final output matrix shape is (normalized number of samples) × trunc_samp, 4), of which 4 represents the four types of labels.

3.3. ResNet34-LSTM3 Classification and Detection Method

3.3.1. ResNet34-LSTM3 Model Structure. The ResNet34-LSTM3 network model consists of ResNet34 and LSTM-3. The ResNet34 network is used to extract the feature information of different levels of ECG signals, and the skip structure in the network is used to avoid network degradation such as gradient disappearance and training accuracy degradation due to too large network depth. LSTM-3 stacked network has the feature of capturing information related to the sequence in time. Therefore, the context dependencies of the features can be extracted by the input eigenvector of the ResNet34 network and output to the LSTM-3 network. Several maximum pooling layers, batch normalization layers, and dropout layer are arranged in the network to optimize the calculation and improve the classification accuracy. Considering the negative information of ECG signals, the Mish function is used as the activation function in the
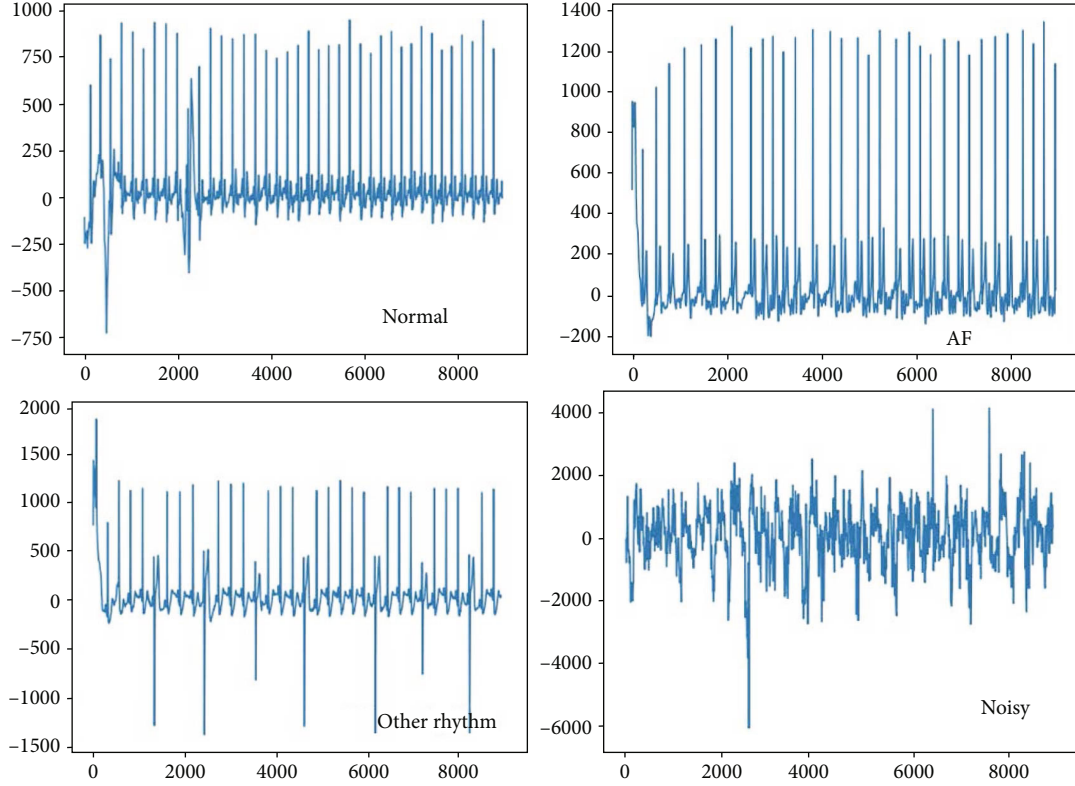
FIGURE 2: Examples of ECG waveforms.
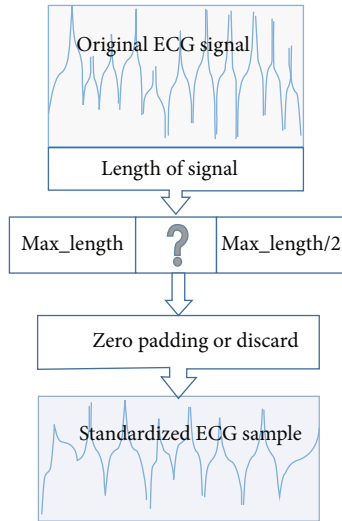
FIGURE 3: Normalized ECG sample generation diagram.

model. The network structure diagram of the ResNet34-LSTM3 model is shown in Figure 4.

3.3.2. ResNet34 Network Architecture. A general deep convolution network is one that stacks more network layers to better extract spatial features at different levels from the signal sequence or image provided. However, it has been found that deep CNN models are difficult to train. Because with the increase of network depth, the training accuracy will first rise and reach saturation and then continue to increase; the

network depth will lead to a decrease in accuracy, that is, the network begins to degenerate [21]. To overcome the degeneration problem, the deep residual network is used in this study to stabilize the training accuracy of the model while increasing the network depth. Compared with other types of deep CNN models such as VGGs and AlexNet, the deep residual network solves the network degradation problem by adding a skip structure, as shown in Figure 5.

The problem of deep network degradation is due to the existence of the nonlinear activation function ReLu, which causes a lot of important information loss for each activation layer from input to output, making this process almost irreversible [22]. The purpose of the residual structure is to enable the deep convolution network to have an equal mapping capability. In this way, when the network is deepened, at least the performance of the deep convolution network and the shallow network are balanced. It is difficult for existing neural networks to fit the potential identity mapping function $H(x) = x$, but if the network is designed as $H(x) = F(x) + x$ (as shown in Figure 5), that is, the identity mapping is directly part of the network in the residual structure, and the network is directly fitted to the residual function $F(x) = H(x) - x$, $F(x) = 0$, the identity mapping $H(x) = x$ can be obtained more quickly, thus solving the degeneration problem of deep convolution network [22].

At the same time, the output function of the residual structure is $H(x) = F(x) + x$, and the constant 1 in the derivative results of x from $(dH(x)/dx = dF(x)/dx) + 1$ and $H(x)$ can also alleviate the possible disappearance of gradients in the deep network when reverse propagation occurs.
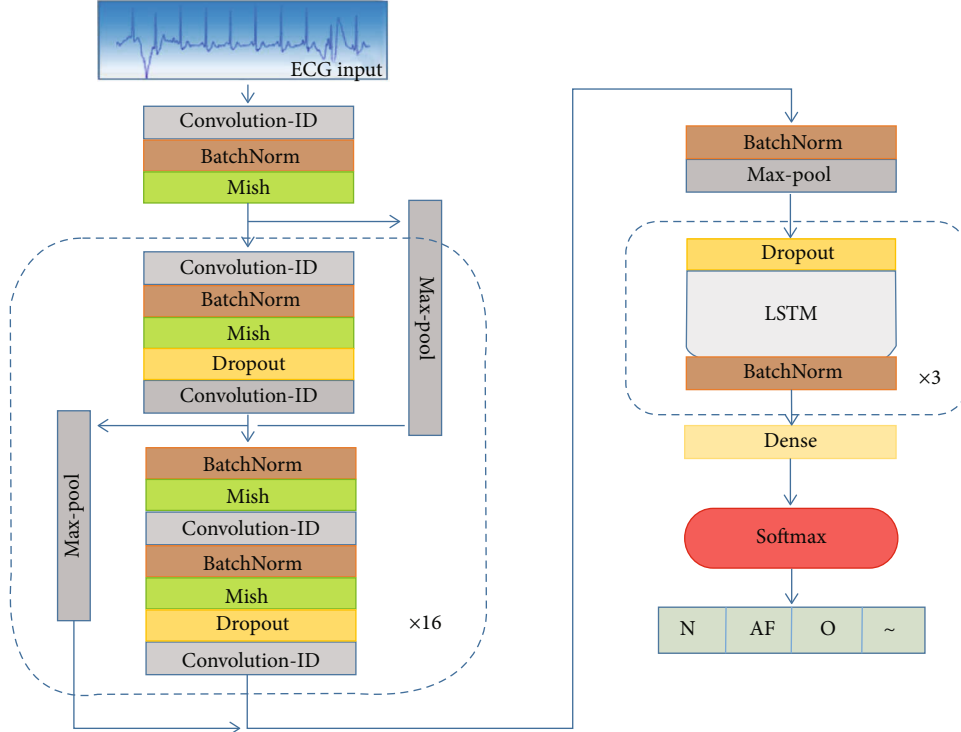
FIGURE 4: ResNet34-LSTM3 network structure diagram.
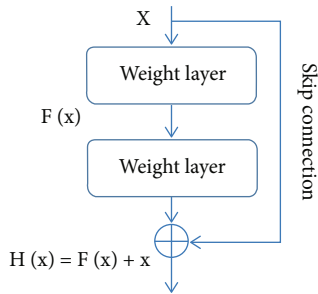
FIGURE 5: Residual structure diagram.

This study uses ResNet34 to extract the characteristics of different levels of input ECG signals. As shown in Figure 4, the ResNet34 network is composed of the signal input layer, one-dimensional convolution layer, BN layer (batch normalization unit), activation layer, dropout layer, and maximum pooling layer as a whole. The convolution layer has the characteristics of weight sharing and local connectivity, which can be used to extract the local characteristics of ECG signals. The formula for calculating one-dimensional convolution is as follows:

$$c^l = \sum_{i=0}^{m} \left(w_i^l x_i^l \right) + b^l. \tag{2}$$

w^l and b^l are the weight and offset of l layer and m is the convolution kernel size.

The batch normalization layer normalizes the distribution of data features at each level, which guarantees that the input feature distribution has the same mean and variance and makes the change of model loss values and gradients more stable [23]. The BN calculation formulas are as follows:

$$\text{Input} : \beta = \{x_{1\cdots m}\},$$

$$\mu_\beta = \frac{1}{m} \sum_{i=1}^{m} x_i,$$

$$\sigma_\beta^2 = \frac{1}{m} \sum_{i=1}^{m} \left(x_i - \mu_\beta \right)^2,$$

$$\widehat{x_i} = \frac{x_i - \mu_\beta}{\sqrt{\sigma_\beta^2 + \varepsilon}},$$

$$y_i = \gamma \widehat{x_i} + \beta \overset{\text{def}}{=} BN_{\gamma,\beta}(x_i),$$

$$\text{Output} : \{y_i = BN_{\gamma,\beta}(x_i)\}. \tag{3}$$

From the above formulas, the BN layer first calculates the mean μ_β and variance σ_β^2 of each minibatch data, then normalizes the data to mean 0 and variance 1 (where ε is to prevent variance from being zero). Finally, two parameters that can be learned (scaling parameter γ and offset parameter β) as output are used for linear change. According to that, some useful feature information is lost after the data is normalized. Therefore, the introduction of linear change will restore the model to a certain extent.

The activation layer can make the model fit nonlinearly and have the ability to classify. Many previous studies have used the Relu function (formula (4)) as the activation function. However, using the Relu function will lose negative information of ECG signals, resulting in a poor classification effect. Therefore, this paper flexibly uses functions as the Mish activation function (formula (5)). The two activation function curves are shown in Figure 6. From Figure 6, it is clear that the function has similar nonlinear ability as the Relu function, while retaining a small amount of negative information in the ECG signal, so that the classification performance of the network is better.

$$\text{ReLu} = \begin{cases} x, x > 0, \\ 0, x \leq 0, \end{cases} \tag{4}$$

$$\text{Mish} = x \times \tan h(\ln (1 + e^x)). \tag{5}$$

To preserve the significant information of each layer of ECG signals and reduce the complexity of network calculation, a maximum pooled layer with a step of 1 and a core size of 2 is added to the network. In addition, the dropout layer is added to the network to randomly discard part of the information to prevent the model training from overfitting.

3.4. LSTM-3 Network Structure. A LSTM network is a time series model that can extract time domain characteristics from any sequence data [24]. Compared with recursive neural networks, LSTM can solve the problem of gradient disappearance in long-term sequence learning, thus improving the learning ability of models. The structure of the LSTM unit is shown in Figure 7.

The equations for calculating the internal parameters of LSTM cells are as follows:

$$f_t = \sigma(w_{fx}x_t + w_{fh}h_{t-1} + b_f), \tag{6}$$

$$i_t = \sigma(w_{ix}x_t + w_{ih}h_{t-1} + b_i), \tag{7}$$

$$o_t = \sigma(w_{ox}x_t + w_{oh}h_{t-1} + b_o), \tag{8}$$

$$c_t = f_t \times c_{t-1} + i_t \times \tan h(w_{cx}x_t + w_{ch}h_{t-1} + b_c), \tag{9}$$

$$h_t = o_t \times \tan h(c_t). \tag{10}$$

In Equations (6)–(10), w is the weight parameter, b is the deviation, σ is the Sigmoid function, h_t is the hidden state of the current unit, and the subscripts of w and b represent the weights and deviations of three different gates, respectively. i_t, f_t, c_t, and o_t are input gates, forgetting gates, cell states, and output gates, respectively. The $\tan h$ is a hyperbolic tangent function.

As shown in Equation (6), the forgetting door controls the input of information from the previous unit. It determines how much information needs to be retained or transmitted to the next unit. The input door controls the input of new information from the outside. It determines how much new information should be used. The current unit state can be obtained by combining the output of the updated forgetting door with the input door as shown in Equation (9). The
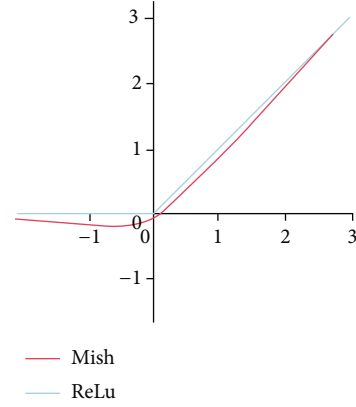
Figure 6: Mish function and ReLu function graph.

hidden state of the current cell is calculated from the cell output and the latest cell state.

Based on the time series advantages of LSTM networks, this study uses a three-layer stacked LSTM network after the ResNet34 network to extract context dependencies in ECG signal characteristics. Each LSTM network contains the same number of LSTM units, which is set to 256 in this paper. The schematic diagram of the single-layer LSTM network structure is shown in Figure 8.

In the LSTM-3 network, the output sequence of the previous LSTM network constitutes the input sequence of the next LSTM network, with one BN layer and dropout layer added between each two LSTM networks. Assuming the eigenvector of the output of the ResNet34 network is a, the learning process of the LSTM-3 network can be represented by the following:

$$h_t^1, c_t^1 = LSTM^1(h_{t-1}^1, c_{t-1}^1, a_t),$$
$$h_t^2, c_t^2 = LSTM^2(h_{t-1}^2, c_{t-1}^2, h_t^1), \tag{11}$$
$$h_t^3, c_t^3 = LSTM^3(h_{t-1}^3, c_{t-1}^3, h_t^2).$$

In the above formulas, LSTM represents an operation function of the LSTM layer, which is used to process the feature sequence, the sequence number $\{1, 2, 3\}$, representing the sequence number of three successively connected LSTM layers, and H and C are the hidden state and layer state components of the corresponding LSTM layer.

3.5. Network Output Layer Design. After the output of the LSTM-3 network, a fully connected layer with 1024 neurons is connected. Finally, the four classifications of the input ECG signal are implemented by the softmax function. The softmax formula is as follows:

$$P(x_i) = \frac{e^{x_i}}{\sum_{j=1}^{4} e^{x_j}}. \tag{12}$$

$P(x_i)$ is the predicted probability distribution of x_i belonging to all possible classes. j is an accumulative variable, ranging from 1 to 4 (total number of categories).
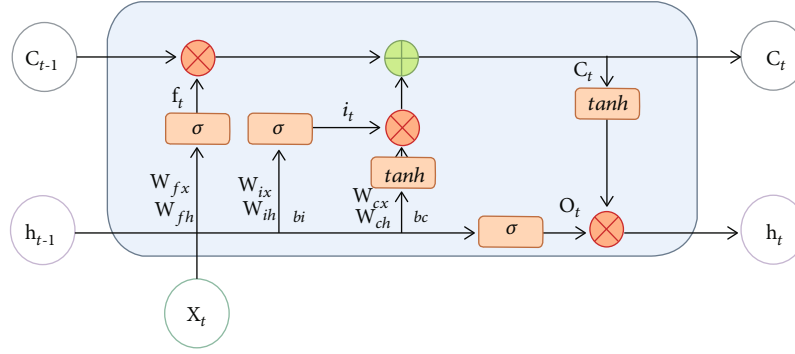
Figure 7: LSTM unit structure diagram.
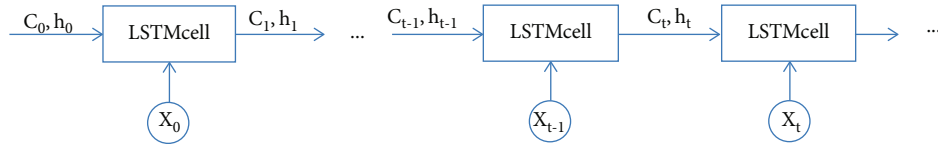
Figure 8: Schematic diagram of single-layer LSTM network structure.

3.6. Information Entropy Verification.

The concept of information entropy is used to describe the uncertainty of an information source. Shannon, the father of information theory, proposed in his paper that "any information has redundancy, and the size of redundancy is related to the occurrence probability or uncertainty of each symbol in the information." Shannon, with the help of the concept of thermodynamics, called the average amount of information after eliminating the redundancy in information as "information entropy." In the experiment, the sampling value of each ECG sample is uncertain, which can be measured according to its occurrence probability. If the probability of sampling value is large, the uncertainty is small and the amount of information provided is small; on the contrary, the uncertainty is large.

In the calculation of the average information entropy of ECG samples, it is assumed that n sampling values can appear in a certain ECG sample to transmit information: $U_1 \cdots U_i \cdots U_n$, The corresponding probability is $P_1 \cdots P_i \cdots P_n$. And generally, it can be considered that the occurrence of various sampling values is independent of each other. At this time, the uncertainty of the single sampling value of ECG signal sample is $-\log (P_i)$, and its average information entropy is E. The calculation formula is as follows:

$$H(U) = E[-\log (P_i)] = -\sum_{i=1}^{n} P_i \log (P_i). \tag{13}$$

After the trained Resnet34-LSTM3 model completes the classification task on the test set, this paper calculates the average information entropy of the correctly classified sample signal and the incorrectly classified sample signal, respectively. Then, the average information entropy of the two kinds of samples is compared. If the average information entropy of the correctly classified sample signals is

Table 2: Hardware equipment.

Hardware type	Hardware name
CPU	AMD Ryzen 5 5600 H with Radeon graphics
Memory	16.0 GB
GPU 0	NVIDIA GeForce RTX 3050Ti Laptop GPU
GPU 1	AMD Radeon (TM) graphics

significantly higher or lower than the latter, it shows that the misclassification of signal samples by the model may be caused by the anomaly of these sample signals themselves. If the average information entropy of the two types of sample signals is the same, it shows that the misclassification of signal samples by the model is caused by the factors of the model itself.

This paper calculates and compares the average information entropy of sample signals, which can eliminate the impact of obvious signal anomalies (redundancy or loss) on the classification results of the model, to more comprehensively and accurately explain the classification effect and performance of the model.

4. Training and Results

The model was trained and evaluated using the training and test datasets provided by the official website of the PhysioNet Challenge 2017 Short Single-Lead ECG AF Classification Competition.

The development IDE used in this study was the PyCharm Professional Edition, and the compilation environment was Python 3.6. The models were trained and tested using the Kerns 2.3.1 framework with TensorFlow 2.0.0 backend. The hardware equipment based on the whole experiment process is shown in Table 2.
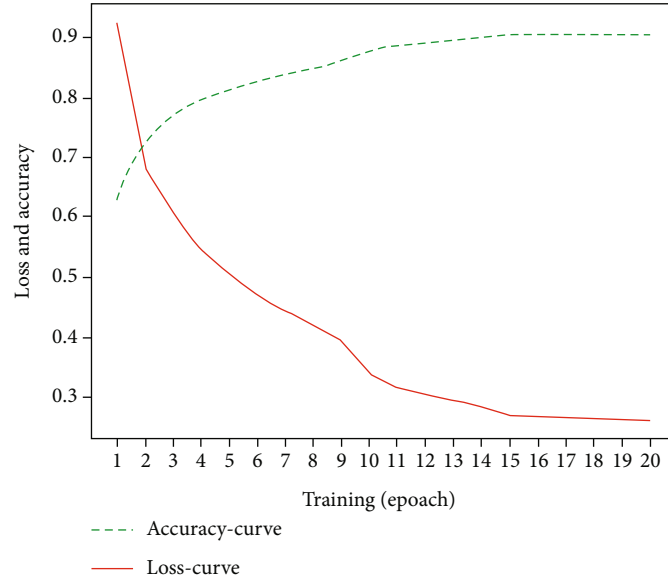
FIGURE 9: Loss curve and accuracy curve of model training.

4.1. Model Training. The maximum epoch of network training is set to 50, and the batch size is 32. Using the Adam optimizer to update the network weight, the initial learning rate is set to 0.001. In the training process, if the accuracy of the model on the verification set is not increased by two consecutive epochs, the learning rate is reduced to 10 times of the original, and the minimum learning rate is set to 10^{-6}. The initial length of the one-dimensional convolution kernel is set to 16, the initial number of convolution kernels in each convolution layer is set to 32, and the number of convolution kernels is doubled after every two convolution layers. The convolution kernel weight is initialized by the normal distribution.

To prevent the model from overfitting in the training process, if the various indicators of the model are not optimized after 8 epochs, the training of the model will be stopped in advance. The loss value curve and accuracy curve of the model in the training process are shown in Figure 9. It can be seen from Figure 9 that the loss value curve and accuracy curve of the model have converged before 20 epochs training.

4.2. Assessment Results. After the model training is completed, the average information entropy of the model was calculated after classification on the test set, as shown in Table 3. The average information entropy of correctly classified sample signal and incorrectly classified sample signal is 8.9088 and 8.9057, respectively. Therefore, the sample signals participating in the model classification test are not obviously abnormal.

After ensuring that there is no obvious abnormality in the sample signal, the overall average precision, recall, F1 score, specificity, and negative predictive value (NPV) of the model on the test set were calculated, as shown in Table 4.

TABLE 3: Average information entropy record table.

Average information entropy of correctly classified sample signals	Average information entropy of incorrectly classified sample signals
8.9088	8.9057

TABLE 4: Classification index score table.

	Precision	Recall	F1 score	Specificity	NPV	Support
A	0.839	0.739	0.786	0.994	0.988	72
N	0.909	0.873	0.890	0.962	0.945	486
O	0.776	0.805	0.790	0.952	0.960	259
~	0.967	0.989	0.978	0.968	0.990	35
Average	0.873	0.852	0.861	0.969	0.971	

It can be seen from the table that the overall average precision, recall, F1 score, specificity, and NPV of ResNet34-LSTM3 classification detection method in the test set are 87.3%, 85.2%, 86.1%, 96.9%, and 97.1%, respectively.

The F1 score values of the model for noise (~), normal rhythm (N), atrial fibrillation (A), and other rhythm (O) are 0.978, 0.890, 0.786, and 0.790, respectively. It shows that the model can recognize the noise signals in the test set well and eliminate the interference of noise in the sample under the training data set with very limited sample size. At the same time, it also has a good classification effect for normal rhythm (N), atrial fibrillation (A), and other rhythm (O). In addition, the specificity scores of the model for all kinds of samples are higher than 0.95, which indicates that the model has good recognition ability for negative cases.

To better evaluate the classification ability of the model for ECG signals, the ResNet34-LSTM3 model in this paper is compared with the ResNet34 model and ResNet18 model,
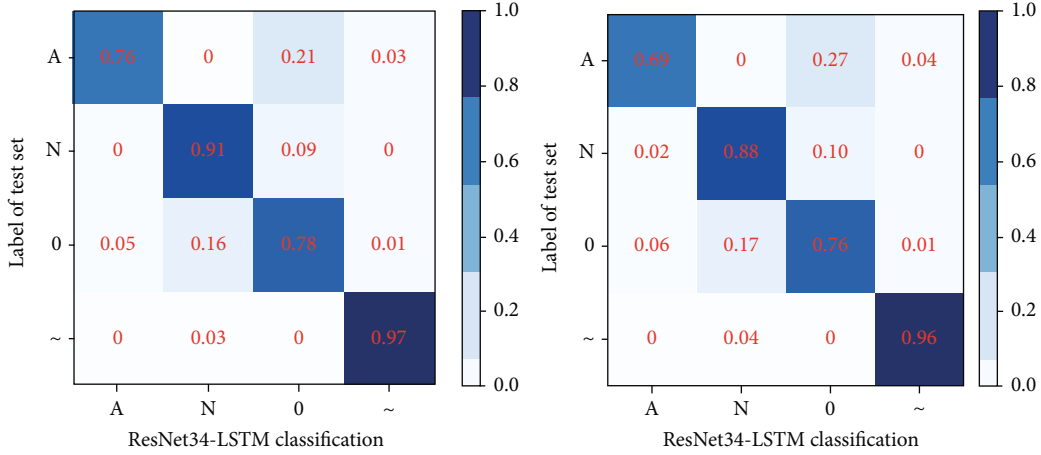
FIGURE 10: Comparison of the ResNet34-LSTM3 and ResNet34 confusion matrix.
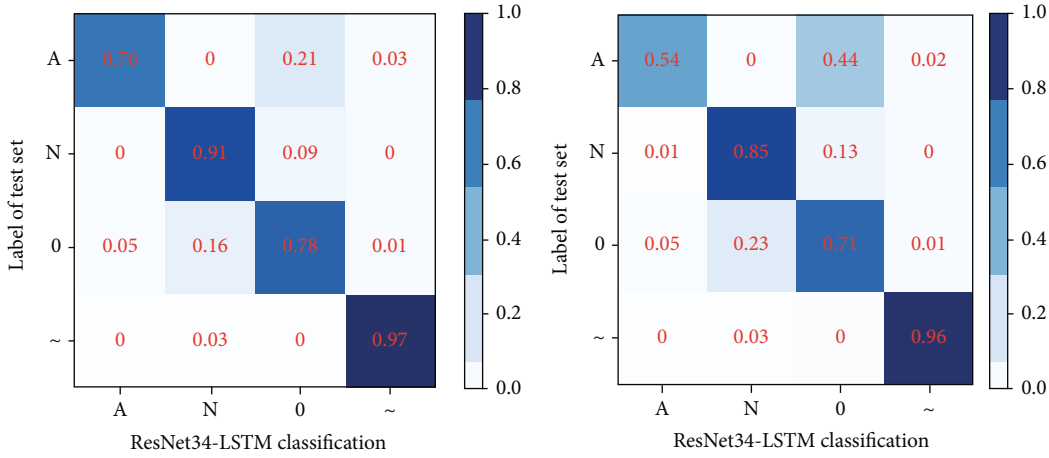
FIGURE 11: Comparison of the ResNet34-LSTM3 and ResNet18 confusion matrix.

which has better classification ability for ECG signals. The confusion matrix comparison of three different models is obtained as shown in Figures 10 and 11. At the same time, the F1 score and AUC value of the three models for four kinds of heart rate classification are obtained as shown in Tables 5 and 6. The experimental data obtained in the two tables are based on the test data set provided by the Physi-oNet Challenge 2017 Short Single-Lead ECG AF classification competition official website.

According to the data in Tables 5 and 6, the overall F1 score average and AUC average of ResNet34-LSTM3 model in the test set are 0.861 and 0.972, respectively, both of which are higher than the other two classification models. Therefore, it can be shown that the ResNet34-LSTM3 model has better classification and recognition effect on ECG signals as a whole. The F1 score and AUC value of the ResNet34-LSTM3 model for atrial fibrillation (A) were 0.786 and 0.967, respectively, which are higher than those of ResNet34 model (0.777 and 0.959), indicating that the improved model can better identify atrial fibrillation (A) diseases.

TABLE 5: F1 scores of three models.

Type	F1 (ResNet34-LSTM3)	F1 (ResNet34)	F1 (ResNet18)
A	0.786	0.777	0.713
N	0.890	0.892	0.885
O	0.790	0.789	0.753
~	0.978	0.978	0.982
Average	0.861	0.859	0.833

The F1 scores and AUC values of the ResNet34-LSTM3 model and ResNet34 model for normal rhythm (N), other rhythm (O), and noise (~) are the same, which indicates that the improved model can still recognize other rhythm signal samples well, and there is no decline in classification ability. The overall F1 score and AUC of ResNet34-LSTM3 model in the test set are significantly higher than those of the ResNet18 model, which shows that the ResNet34-LSTM3 model in this paper is significantly better than the ResNet18 model in the classification ability of ECG signal.

TABLE 6: AUC scores of the three models.

Type	AUC (ResNet34-LSTM3)	AUC (ResNet34)	AUC (ResNet18)
A	0.967 (0.962-0.972)	0.959 (0.954-0.965)	0.954 (0.949-0.959)
N	0.979 (0.978-0.981)	0.979 (0.978-0.981)	0.965 (0.963-0.967)
O	0.945 (0.942-0.949)	0.946 (0.943-0.949)	0.887 (0.883-0.892)
~	0.998 (0.998-0.999)	0.999 (0.998-0.999)	0.998 (0.997-0.998)
Average	0.972	0.971	0.951

5. Conclusions

In this paper, based on the ResNet34 network, a three-layer stacked long-term and short-term memory networks are added, and the Mish function is used as the activation function. The final improved model can obtain the context dependence of the feature and retain the negative information in the ECG signal. The average F1 score of 0.861 and the average AUC value of 0.972 are obtained by the improved ResNet34-LSTM3 model on the PhysioNet challenge 2017 test dataset, which shows that the model can effectively extract the characteristics of ECG signals and diagnose arrhythmia diseases. Comparing the evaluation results of the previous ResNet34 model and ResNet18 model on the same test dataset, it can be seen that the improved model has a better classification and recognition effect on ECG signals as a whole, and it can more effectively identify arrhythmias such as atrial fibrillation, which will provide a more effective and reliable diagnostic basis for medical workers.

There are some important limitations in this study. The input dataset of the experiment is PhysioNet challenge 2017 Short Single-Lead ECG signal, which provides a limited signal compared with the standard 12 lead ECG signal. Therefore, whether the ResNet34-LSTM3 model classification performance is better in the 12 lead ECG signals remains to be determined. In addition, when the algorithm is used clinically, it may be limited by the duration of ECG signals, and the application of all kinds of algorithms, including the one presented algorithm, must eventually tailor specific ECG signal pretreatment methods for the target clinical application. Therefore, in the next stage of the study, we consider segmenting the signal to supplement the signal segment by copying other electrocardiogram signals in the same category in order to maximize the use of information. In the future, we will conduct experiments with more types of ECG data to prove the performance of our model.

In a word, the ResNet34-LSTM3 network model in this paper can distinguish the signals with different concentric laws in Short Single-Lead ECG signals, and its classification performance is also better than that of the predecessors in partial scores. If more tests are carried out in the clinical environment, this method may help medical workers improve the efficiency and accuracy of ECG clinical interpretation.

Data Availability

The data used to support the findings of this study are included within the article.

Conflicts of Interest

The authors declare that there is no conflict of interest regarding the publication of this paper.

Acknowledgments

References

[1] Z. Golrizkhatami and A. Acan, "ECG classification using three-level fusion of different feature descriptors," *Expert Systems with Applications*, vol. 114, pp. 54–64, 2018.

[2] C. Chen, Z. Hua, R. Zhang, G. Liu, and W. Wen, "Automated arrhythmia classification based on a combination network of CNN and LSTM," *Biomedical Signal Processing and Control*, vol. 57, article 101819, 2020.

[3] J. S. Huang, B. Q. Chen, N. Y. Zeng, X. C. Cao, and Y. Li, "Accurate classification of ECG arrhythmia using MOWPT enhanced fast compression deep learning networks," *Journal of Ambient Intelligence and Humanized Computing*, vol. 2, 2020.

[4] O. T. Inan, L. Giovangrandi, and G. Kovacs, "Robust neural-network-based classification of premature ventricular contractions using wavelet transform and timing interval features," *IEEE Transactions on Bio-Medical Engineering*, vol. 53, no. 12, pp. 2507–2515, 2006.

[5] Tran Hoai Linh, S. Osowski, and M. Stodolski, "On-line heart beat recognition using Hermite polynomials and neuro-fuzzy network," *IEEE Transactions on Instrumentation and Measurement*, vol. 52, no. 4, pp. 1224–1231, 2003.

[6] F. Murat, O. Yildirim, M. Talo, U. Baloglu, Y. Demir, and U. R. Acharya, "Application of deep learning techniques for heartbeats detection using ECG signals-analysis and review," *Computers in Biology and Medicine*, vol. 120, article 103726, 2020.

[7] S. Kiranyaz, T. Ince, and M. Gabbouj, "Real-time patient-specific ECG classification by 1-D convolutional neural networks," *IEEE Transactions on Biomedical Engineering*, vol. 63, no. 3, pp. 664–675, 2016.

[8] P. Rajpurkar, A. Y. Hannun, M. Haghpanahi, C. Bourn, and A. Y. Ng, "Cardiologist-level arrhythmia detection with convolutional neural networks," 2017, https://arxiv.org/abs/1707.01836.

[9] H. Alquran, A. M. Alqudah, I. Abu-Qasmieh, A. al-Badarneh, and S. Almashaqbeh, "ECG classification using higher order spectral estimation and deep learning techniques," *Neural Network World*, vol. 29, no. 4, pp. 207–219, 2019.

[10] A. Mostayed, J. Luo, X. Shu, and W. Wee, "Classification of 12-lead ECG signals with bi-directional LSTM network," 2018, https://arxiv.org/abs/1811.02090.

[11] Z. Yildirim, "A novel wavelet sequence based on deep bidirectional LSTM network model for ECG signal classification," *Computers in Biology & Medicine*, vol. 96, pp. 189–202, 2018.

[12] S. Saadatnejad, M. Oveisi, and M. Hashemi, "LSTM-based ECG classification for continuous monitoring on personal wearable devices," *IEEE Journal of Biomedical & Health Informatics*, vol. 24, no. 2, pp. 515–523, 2020.

[13] K. Feng, X. Pi, H. Liu, and K. Sun, "Myocardial infarction classification based on convolutional neural network and recurrent neural network," *Applied Sciences*, vol. 9, no. 9, p. 1879, 2019.

[14] X. Zhai and C. Tin, "Automated ECG classification using dual heartbeat coupling based on convolutional neural network," *IEEE Access*, vol. 6, pp. 27465–27472, 2018.

[15] H. Li, J. Liu, R. Liu, N. Xiong, K. Wu, and T. H. Kim, "A dimensionality reduction-based multi-step clustering method for robust vessel trajectory analysis," *Sensors*, vol. 17, no. 8, article 1792, 2017.

[16] H. Li, J. Liu, K. Wu, Z. Yang, R. W. Liu, and N. Xiong, "Spatio-temporal vessel trajectory clustering based on data mapping and density," *IEEE Access*, vol. 6, pp. 58939–58954, 2018.

[17] T. J. Jun, H. M. Nguyen, D. Kang, D. Kim, D. Kim, and Y.-H. Kim, "ECG arrhythmia classification using a 2-D convolutional neural network," 2018, https://arxiv.org/abs/1804.06812.

[18] L. Dan, J. Zhang, Z. Qiang, and X. Wei, "Classification of ECG signals based on 1D convolution neural network," in *2017 IEEE 19th International Conference on e-Health Networking, Applications and Services (Healthcom)*, Dalian, China, 2017.

[19] M. Jangra, S. K. Dhull, and K. K. Singh, "ECG arrhythmia classification using modified visual geometry group network (mVGGNet)," *Journal of Intelligent and Fuzzy Systems*, vol. 38, no. 3, pp. 3151–3165, 2020.

[20] A. Krizhevsky, I. Sutskever, and G. E. Hinton, "Imagenet classification with deep convolutional neural networks," *Advances in neural information processing systems.*, vol. 60, pp. 84–90, 2017.

[21] K. He, X. Zhang, S. Ren, and J. Sun, "Deep residual learning for image recognition," in *Proceedings of the IEEE Conference on Computer Vision and Pattern Recognition (CVPR)*, pp. 770–778, Las Vegas, NV, USA, 2016.

[22] M. Sandler, A. Howard, M. Zhu, A. Zhmoginov, and L.-C. Chen, "MobileNetV2: inverted residuals and linear bottlenecks," in *Proceedings of the IEEE Conference on Computer Vision and Pattern Recognition (CVPR)*, pp. 4510–4520, Salt Lake City, UT, USA, 2018.

[23] Y. Li, N. Wang, J. Shi, X. Hou, and J. Liu, "Adaptive batch normalization for practical domain adaptation," *Pattern Recognition*, vol. 80, pp. 109–117, 2018.

[24] S. Hochreiter and J. Schmidhuber, "Long short-term memory," *Neural Computation*, vol. 9, no. 8, pp. 1735–1780, 1997.

Research Article

Asymptotic Behavior of Solution for Functional Evolution Equations with Stepanov Forcing Terms

Zhong-Hua Wu [ID]

Faculty of Information Technology, Macau University of Science and Technology, Macau 999078, China

Correspondence should be addressed to Zhong-Hua Wu; w3z3h3@163.com

Through the use of the measure theory, evolution family, "Acquistapace–Terreni" condition, and Hölder inequality, the core objective of this work is to seek to analyze whether there is unique μ-pseudo almost periodic solution to a functional evolution equation with Stepanov forcing terms in a Banach space. Certain adequate conditions are derived guaranteeing there is unique μ-pseudo almost periodic solution to the equation by Lipschitz condition and contraction mapping principle. Finally, an example is used to demonstrate our theoretical findings.

1. Introduction

Periodicity is a common phenomenon in the natural and social sciences that varies over time. Periodicity can be caused by business and economic activities, and it differs from trend changes in that it is not a gradual development in one direction, but rather a series of rising and falling oscillations. Sunrise and sunset, the cycle of the seasons, and the moon changing from deficit to surplus are all cyclical phenomena. In epidemiology, the cycle refers to the frequency of disease according to a certain interval of time, the regular ups and downs of fluctuations; every several years, there is an epidemic peak phenomenon. In physics, it refers to the reciprocal motion of a mass in simple harmonic motion, which is always cyclic, with each cycle taking the same amount of time and being strictly periodic. In mathematics, a function whose output value repeats periodically is called a periodic function. The motion of the planets is not regular and elliptical, because it can be influenced by other stars; the transmission of radio waves can also be disturbed. Thus, the periodicity will no longer be maintained. In such a case, the almost period would better reflect the variation of the above phenomenon with time. In mathematics, the almost periodic function is a class of functions with approximately periodic properties, which is the extension of the continuous periodic function. Different periodic functions have different periods,

and their sums, differences, or products are not necessarily periodic functions anymore, although the almost periodic function may not have strict periodicity, but can have some better properties than the periodic function. In theory, all periodic functions in any paradigm do not constitute a Banach space, while the probable periodic functions in the upper bound paradigm constitute a Banach space. This also shows that the probable periodic function will be more widely used than the periodic function, and it is more practical to discuss the probable periodic solution of the equation.

In fact, strict periodic changes are difficult to appear in nature. In real life, there are not many strict periodic phenomena such as seven days a week. On the contrary, almost periodic changes are more likely to accurately describe the change law of nature. Almost periodic phenomena are more common than periodic phenomena, and almost periodic phenomena are closer to reality than periodic phenomena. In reality, almost periodic phenomena are more likely to occur.

Almost periodic function can better reflect the change law of things in real life and explain the phenomena in real life. It is a phenomenon easier to see in natural science and social science. Almost periodic results are more common than periodic results. Almost periodic function has many other good properties, and its practical application is more and more widely in real life. The almost periodic property

of the solution of the equation has attracted the attention of many scholars. Discussing the almost periodic property of the solution of the equation has more extensive practical significance and practical application value. Therefore, it has become an important topic in mathematical research.

In 1992, Zhang proposed the idea of pseudo almost periodic functions in the academic paper [1]. After that, in 2006, the idea of weighted pseudo almost periodic functions was presented by Diagana in the literature [2]. As an extension of the concept of pseudo almost periodic functions and weighted pseudo almost periodic functions, Blot et al. presented the idea of μ-pseudo almost functions in 2013 [3]. Since then, many scholars have conducted extensive research on the properties of such functions and made advantage of these properties to set up the existence of μ-pseudo almost periodic solutions for partial functional non-autonomous equation [4, 5], partial functional differential equations [6, 7], partial differential equation [8], nonautonomous integrodifferential equations [9], and semilinear fractional integrodifferential equations [10]. In 2007, Diagana proposed the conception of the Stepanov pseudo almost periodic function in the literature [11]. Then, in 2010, Diagana et al. presented the conception of weighted Stepanov-like pseudo almost periodic function in the literature [12], as the generalization of Stepanov pseudo almost periodic functions. In the literature [13], the authors Es-sebbar and Ezzinbi proposed the notion of Stepanov μ-pseudo almost periodic function. In [14], the authors studied whether there is unique μ-pseudo almost periodic solution for a parabolic evolution equation and the equation's forced terms are assumed to be μ-Stepanov pseudo almost periodic. In [15], the authors established the convolution and composition theorems of the μ-Stepanov pseudo almost periodic functions and verified whether there is unique μ-pseudo almost periodic mild solution of fractional integrodifferential equation.

Inspired by the above, in this work, let $(K, \|\cdot\|)$ be a Banach space and $1 < p < \infty$; by the measure theory, we mostly prove whether there is unique μ-pseudo almost periodic solution to a functional evolution equation

$$\frac{d}{dt}\left[z(t) - \psi\left(t, \widetilde{C_1}(t)z(t)\right)\right] = A(t)\left[z(t) - \psi\left(t, \widetilde{C_1}(t)z(t)\right)\right] + g\left(t, z(t), \widetilde{C_2}(t)z(t)\right), \tag{1}$$

for $t \in \mathbb{R}$, where $\{A(t)\}_{t \in \mathbb{R}}$ fulfills the Acquistapace–Terreni condition, which is exponentially stable, and $Q(t, s)$ created by $A(t)$ and $\psi : \mathbb{R} \times K \longrightarrow K$, is μ-pseudo almost periodic and $g : \mathbb{R} \times K \times K \longrightarrow K$ is Stepanov-like μ-pseudo almost periodic functions; $\widetilde{C_1}(t), \widetilde{C_2}(t)(t \in \mathbb{R})$ are families of (perhaps unbounded) linear operators. The topic about whether there is unique μ-pseudo almost periodic solution to functional evolution equation with Stepanov forcing terms of (1) is untreated in the past work, which is one of the crucial incentives of this study.

The following is an outline for this work. Section 2 introduces some essential concepts and basic properties. Section 3 is dedicated to demonstrating whether there are unique μ-pseudo almost periodic solutions of (1). To give you an illustration, in the last part, we provide a case supporting our conclusion.

2. Preliminaries

Throughout the course of this project, $(K, \|\cdot\|)$ and $(\mathbb{H}, \|\cdot\|_{\mathbb{H}})$ are two Banach spaces. $BC(\mathbb{R}, K)$ (respectively, $BC(\mathbb{R} \times \mathbb{H}, K)$) is the Banach space of bounded continuous functions from $\mathbb{R}$ into K (respectively, jointly bounded continuous functions $\psi : \mathbb{R} \times \mathbb{H} \longrightarrow K$) as a result of its norm by

$$\|\psi\|_{\infty} = \sup_{t \in \mathbb{R}} \|\psi(t)\|. \tag{2}$$

We signify by $\mathcal{D}$ the Lebesgue $\widehat{D}$-field of $\mathbb{R}$ and by $\mathcal{N}$ the set of all positive measures μ on $\mathcal{D}$ such that $\mu(\mathbb{R}) = +\infty$ and $\mu([c, d]) < +\infty$ for all $c, d \in \mathbb{R} (c \leq d)$.

From $\mu \in \mathcal{N}$, the following assumptions are assumed.

(H1) For all c, d, and $e \in \mathbb{R}$, such that $0 \leq c < d \leq e$, there exist $\widehat{\nu}_0 \geq 0$ and $\alpha_0 \geq 0$ satisfying $|\widehat{\nu}| \geq \widehat{\nu}_0 \Rightarrow \mu((c + \widehat{\nu}, d + \widehat{\nu})) \geq \alpha_0 \mu([\widehat{\nu}, e + \widehat{\nu}])$.

(H2) For all $\widehat{\nu} \in \mathbb{R}$, there exist $\tilde{\alpha} > 0$ and a bounded interval I satisfying

$$\mu(\{c + \widehat{\nu} : c \in B\}) \leq \tilde{\alpha}\mu(B), \quad \text{if } B \in \mathcal{D} \text{ such that } B \cap I = \varnothing. \tag{3}$$

Definition 1 (see [16]). Let $\psi(t) \in C(\mathbb{R}, K), \psi(t)$ be referred to as almost periodic if, for any $\varepsilon > 0$, the set $E(\psi, \varepsilon) = \{\widehat{\kappa} : \|\psi(t + \widehat{\kappa}) - \psi(t)\| \text{ for all } t \in \mathbb{R}\}$ is relatively dense; that is, for any $\varepsilon > 0$, it is possible to locate a real number $l = l(\varepsilon) > 0$; for any interval with length $l(\varepsilon)$, there exists a number $\widehat{\kappa} = \widehat{\kappa}(\varepsilon)$ in this interval satisfying $\|\psi(t + \widehat{\kappa}) - \psi(t)\|$ for all $t \in \mathbb{R}$. We denote the space of all such functions by $AP(\mathbb{R}, X)$.

Consider the function F, which is equal to

$$F(x) = \sin(x) + \sin\left(\sqrt{2}x\right). \tag{4}$$

F is an almost periodic function, while F is not periodic. See almost periodic function F below in Figure 1.

Definition 2 (see [17]). A continuous function $\psi : \mathbb{R} \times \mathbb{H} \longrightarrow K$ is regarded as almost periodic in t uniformly in relation to $\tilde{u}$ in $\mathbb{H}$, if for any compact subset $K \subset \mathbb{H}$ and every $\epsilon > 0$, there exists $l > 0$ such that every interval of length l, it is possible to find a number $\widehat{\nu}$ in this interval with the feature that

$$\|\psi(t + \widehat{\nu}, \tilde{u}) - \psi(t, \tilde{u})\| < \epsilon, \quad \text{for } (t, \tilde{u}) \in \mathbb{R} \times K. \tag{5}$$

The union of such functions will be referred to as $APU(\mathbb{R} \times \mathbb{H}; K)$.
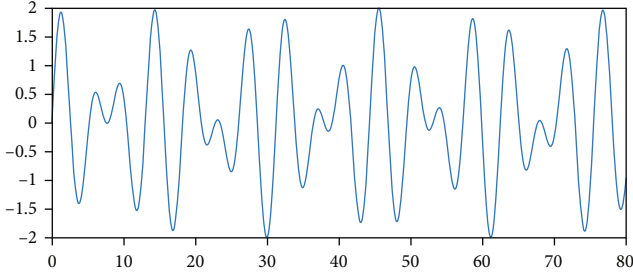
FIGURE 1: Almost periodic function F.

Proposition 3 (see [16]). *If ψ, ψ_1 and $\psi_2 \in AP(K)$, then*

$$\psi_1 + \psi_2 \in AP(K). \tag{6}$$

(i) *$\lambda\psi \in AP(K)$ for any scalar λ*

(ii) *$\psi_\alpha \in AP(K)$ where ψ_α is the right translation function of $\psi(\psi_\alpha: \mathbb{R} \longrightarrow K$ is characterised by $\psi_\alpha(\cdot) = \psi(\cdot + \alpha))$*

(iii) *The range $\mathcal{R}_\psi := \{\psi(t): t \in \mathbb{R}\}$ is a little package in K; thus, ψ is bounded in norm*

(iv) *If $\psi_n \longrightarrow \psi$ uniformly on $\mathbb{R}$ where each $\psi_n \in AP(K)$, then $\psi \in AP(K)$ too*

Definition 4 (see [3]). Let $\mu \in \mathcal{N}$. A continuous bounded function $\psi : \mathbb{R} \longrightarrow K$ is regarded as μ-ergodic if

$$\lim_{\omega \longrightarrow +\infty} \frac{1}{\mu(\widehat{\omega})} \int_{\widehat{\omega}} \|\psi(t)\| d\mu(t) = 0, \tag{7}$$

where $\widehat{\omega} := [-\omega, \omega]$. All of these functions' space is denoted by $\mathcal{E}(\mathbb{R}; K, \mu)$.

Definition 5 (see [3]). Let $\mu \in \mathcal{N}$. A continuous function $\psi : \mathbb{R} \times K \longrightarrow \mathbb{H}$ is regarded as μ-ergodic in $t \in \mathbb{R}$uniformly in relation to $x \in K$, if the two following statements are satisfied:

(i) For all $x \in K$, $\psi(.,x) \in \mathcal{E}(\mathbb{R}; K, \mu)$

(ii) ψ is uniformly continuous on every compact set K in K in terms of the second variable x

The union of such functions will be referred to as $\mathcal{E}U(\mathbb{R} \times K; \mathbb{H}, \mu)$.

Proposition 6 (see [13]). *If a sequence $(\psi_n)_n$ of μ-ergodic functions uniformly converges to a function ψ, then ψ is also μ-ergodic.*

Theorem 7 (see [3]). *Let $\mu \in \mathcal{N}$. Then, $(\mathcal{E}(\mathbb{R}; K, \mu), \|\cdot\|_\infty)$ is a Banach space.*

Definition 8 (see [3]). Let $\mu \in \mathcal{N}$. A continuous function $\psi : \mathbb{R} \longrightarrow K$ is called μ-pseudo almost periodic if it is able to create it as

$$\psi = \psi_1 + \psi_2, \tag{8}$$

where $\psi_1 \in AP(\mathbb{R}; K)$ and $\psi_2 \in \mathcal{E}(\mathbb{R}; K, \mu)$. Indicate with $PAP(\mathbb{R}; K, \mu)$ the area occupied by such functions.

Definition 9 (see [3]). Let $\mu \in \mathcal{N}$. A continuous function $\psi : \mathbb{R} \times K \longrightarrow \mathbb{H}$ is called μ-pseudo almost periodic in $t \in \mathbb{R}$ uniformly in relation to $x \in K$, if it is possible to write it in the form

$$\psi = \psi_1 + \psi_2, \tag{9}$$

where $\psi_1 \in APU(\mathbb{R} \times K; \mathbb{H})$ and $\psi_2 \in \mathcal{E}U(\mathbb{R} \times K; \mathbb{H}, \mu)$. The set of such functions is represented by the symbol $PAPU(\mathbb{R} \times K; \mathbb{H}, \mu)$.

Theorem 10 (see [3]). *Let $\mu \in \mathcal{N}$, $\psi \in PAPU(\mathbb{R} \times \mathbb{H}; K, \mu)$, and $u \in PAP(\mathbb{R}; \mathbb{H}, \mu)$. Assume for all bounded subset B of $\mathbb{H}$, f is bounded on $\mathbb{R} \times B$. Then, the function*

$$[t \mapsto \psi(t, u(t))] \in PAP(\mathbb{R}; K, \mu). \tag{10}$$

Definition 11 (see [12]). Let $1 \leq p < \infty$. The space $BS^p(\mathbb{R}; K)$ of all Stepanov bounded functions, in conjunction with the exponent p, all measurable functions are included in this category f on $\mathbb{R}$ in regard to value K such that $\psi^b \in L^\infty(\mathbb{R}, L^p(0, 1); K)$.$BS^p(\mathbb{R}; K)$. This is a Banach space when the norm is followed

$$\|\psi\|_{S^p} = \left\|\psi^b\right\|_{L^\infty(\mathbb{R},L^p)} = \sup_{t \in \mathbb{R}} \left(\int_t^{t+1} \|\psi(\varrho)\|^p d\varrho \right)^{1/p} < \infty. \tag{11}$$

A function $\psi \in L^p_{\text{loc}}(\mathbb{R}; K)$ is Stepanov bounded (S^p-bounded) if $\|\psi\|_{S^p} < \infty$. It goes without saying that $L^p(\mathbb{R}; K) \subset BS^p(\mathbb{R}; K) \subset L^p_{\text{loc}}(\mathbb{R}; K)$.

Definition 12 (see [12]). A function $\psi \in BS^p(\mathbb{R}; K)$ is called almost periodic in the sense of Stepanov (S^p-almost periodic) if for each $\epsilon > 0$. There is such a thing as a positive number l as a result each length l interval includes a number c; there exists $\widehat{v} \in [c, c + l_\varepsilon]$ satisfying

$$\left(\int_{[t,t+1]} \|\psi(\varrho + v\wedge) - \psi(\varrho)\|^p d\varrho \right)^{1/p} < \varepsilon, t \in \mathbb{R}. \tag{12}$$

Let $AP^p(\mathbb{R}; K)(S^p - AP(\mathbb{R}; K))$ be the collection of all S^p-almost periodic functions.

Definition 13 (see [13]). Let $\mu \in \mathcal{N}$. A function $\psi \in BS^p(\mathbb{R}; K)$ is referred to as S^p-μ-ergodic if

$$\lim_{\omega \longrightarrow +\infty} \frac{1}{\mu(\widehat{\omega})} \int_{\widehat{\omega}} \left(\int_t^{t+1} \|\psi(\varrho)\|^p d\varrho \right)^{1/p} d\mu(t) = 0. \qquad (13)$$

We mean by $\mathcal{E}^p(\mathbb{R}; K, \mu)$ the functions.

Definition 14 (see [13]). Let $\mu \in \mathcal{N}$. A function $\psi \in BS^p(\mathbb{R}; K)$ is called a S^p-μ-pseudo almost periodic (or Stepanov μ-pseudo almost periodic) if it can be stated in this way $\psi = \psi_1 + \psi_2$, where $\psi_1 \in AP^p(\mathbb{R}; K)$ and $\psi_2 \in \mathcal{E}^p(\mathbb{R}; K, \mu)$. $PAP^p(\mathbb{R}; K, \mu)$ or $S^p - PAP(\mathbb{R}; K, \mu)$ denotes a group of functions that are analogous.

Definition 15 (see [14]). Let $\mu \in \mathcal{N}$ A function $\psi : \mathbb{R} \times \mathbb{H} \longrightarrow \mathbb{K}$ with $\psi(.,y) \in L_{loc}^p(\mathbb{R}; K)$ for each $y \in \mathbb{H}$ is called S^p-μ-pseudo almost periodic in $y \in \mathbb{H}$ uniformly in $t \in \mathbb{R}$ if it may be presented as $\psi = \psi_1 + \psi_2$, where $\psi_1 \in AP^p(\mathbb{R} \times \mathbb{H}; K)$ and $\psi_2 \in \mathcal{E}^p(\mathbb{R} \times \mathbb{H}; K, \mu)$. The space occupied by such functions will be indicated by $PAPU^p(\mathbb{R} \times \mathbb{H}; K, \mu)$ or $S^p - PAP(\mathbb{R} \times \mathbb{H}; K, \mu)$.

Theorem 16 (see [14]). *Let $\mu \in \mathcal{N}$ satisfy (H2), if $\psi \in PAP$ $(\mathbb{R}; K, \mu)$ then $f \in PAP^p(\mathbb{R}; K, \mu)$.*

Theorem 17 (see [18]). *Assume that $\psi \in BS^p(\mathbb{R}, K)$. Then, $\psi \in \mathcal{E}^p(\mathbb{R}, K, \mu)$ if and only if, for whatever reason $\epsilon > 0$*

$$\lim_{\omega \longrightarrow +\infty} \frac{\mu \left\{ t \in \widehat{\omega} \, ; \left(\int_t^{t+1} \|\psi(\varrho)\|^p d\varrho \right)^{1/p} > \epsilon \right\}}{\mu(\widehat{\omega})} = 0. \qquad (14)$$

Then, by Propositions 3 and 6, as a consequence, we arrive to the following conclusion.

Proposition 18. *Let $\{\psi_n\}_{n \in \mathbb{N}} \subset PAP(\mathbb{R}; K, \mu)$ be a sequence of functions. If ψ_n uniformly converges to some ψ, then $\psi \in PAP(\mathbb{R}; K, \mu)$.*

3. Main Results

In the next, we are devoted whether there is unique μ-pseudo almost periodic mild solution to (1). Throughout the remainder of this paper, the following hypotheses will be required.

(H3) There exist constants $\mu_0 \geq 0$, $\vartheta \in (\pi/2, \pi)$, $L_1, L_2 \geq 0$, and $\alpha_1, \beta_1 \in (0, 1]$ with $\alpha_1 + \beta_1 > 1$ such that

$$\Sigma_\vartheta \cup \{0\} \subset \rho(A(x) - \mu_0), \|R(\lambda, A(x) - \mu_0)\| \leq \frac{L_2}{1 + |\lambda|},$$

$$\begin{aligned} &\|(A(x) - \mu_0)R(\lambda, A(x) - \mu_0)[R(\mu_0, A(x)) - R(\mu_0, A(y))]\| \\ &\leq L_1 |x - y|^{\alpha_1} |\lambda|^{-\beta_1}, \end{aligned} \qquad (15)$$

for $x, y \in \mathbf{R}$, $\lambda \in \Sigma_\vartheta := \{\lambda \in \mathbf{C} - \{0\} : |\arg \lambda| \leq \vartheta\}$.

(H4) The evolution family $Q(x, \widehat{\kappa})$ produced by $A(x)$ is exponentially stable, namely, there are constants $K_0, \widehat{\beta} > 0$ in order for

$$\|Q(x, \widehat{\kappa})\| \leq K_0 e^{-\beta \wedge (x - \kappa \wedge)}, \qquad (16)$$

for all $x \geq \widehat{\kappa}$. And the function $\mathbb{R} \times \mathbb{R} \mapsto K$, $(x, \widehat{\kappa}) \mapsto Q(x, \widehat{\kappa})$ $s \in AP(\mathbb{R} \times \mathbb{R}, K)$ uniformly for all s in any bounded subset of K.

(H5) The linear operators $\widetilde{C_1}(t), \widetilde{C_2}(t) : K \longrightarrow K$ satisfy

$$t \mapsto \widetilde{C_1}(t) \text{ and } t \mapsto \widetilde{C_2}(t) \in AP(\mathbb{R}, B(K, K)). \qquad (17)$$

Let

$$\omega := \max \left(\sup_{t \in \mathbb{R}} \left\| \widetilde{C_1}(t) \right\|_{B(K,K)}, \sup_{t \in \mathbb{R}} \left\| \widetilde{C_2}(t) \right\|_{B(K,K)} \right). \qquad (18)$$

(H6) The function $\psi \in PAPU(\mathbb{R} \times \mathbb{H}; \mathbb{H}, \mu)$ and there exists $L_\psi > 0$ which satisfies

$$\|\psi(t, s_1) - \psi(t, s_2)\| \leq L_\psi \|s_1 - s_2\|, \qquad (19)$$

for all $t \in \mathbb{R}$ and for each $s_1, s_2 \in \mathbb{H}$.

(H7) The function $g \in PAPU^p(\mathbb{R} \times K \times K; K, \mu)$ and there exists $L_3 > 0$ that satisfies $\|g(t, m_1, n_1) - g(t, m_2, n_2)\| \leq L_3 (\|m_1 - m_2\| + \|n_1 - n_2\|)$, for all $t \in \mathbb{R}$ and for $(m_1, n_1), (m_2, n_2) \in K \times K$.

Definition 19. A continuous function $z : \mathbb{R} \longrightarrow K$ is referred to as a μ-pseudo almost periodic mild solution of (1), if for each $t \geq t_0$ and $t_0 \in \mathbb{R}$,

$$\begin{aligned} z(t) - \psi\left(t, \widetilde{C_1}(t)z(t)\right) &= Q(t, t_0) \left[z(t_0) - \psi\left(t_0, \widetilde{C_1}(t_0)z(t_0)\right) \right] \\ &+ \int_{t_0}^t Q(t, \varrho)g\left(\varrho, z(\varrho), \widetilde{C_2}(\varrho)z(\varrho)\right) d\varrho, \quad t \in \mathbb{R}. \end{aligned} \qquad (20)$$

It can be shown that a function z is a mild solution of (1) for each $t \in \mathbb{R}$ and by the expression

$$z(t) = \psi\left(t, \widetilde{C_1}(t)z(t)\right) + \int_{-\infty}^t Q(t, \varrho)g\left(\varrho, z(\varrho), \widetilde{C_2}(\varrho)z(\varrho)\right) d\varrho, \qquad (21)$$

since

$$z(t_0) = \psi\left(t_0, \widetilde{C_1}(t_0)z(t_0)\right) + \int_{-\infty}^{t_0} Q(t_0, \varrho) g\left(\varrho, z(\varrho), \widetilde{C_2}(\varrho)z(\varrho)\right) d\varrho,$$

$$Q(t, t_0)z(t_0) = Q(t, t_0)\psi\left(t_0, \widetilde{C_1}(t_0)z(t_0)\right) + \int_{-\infty}^{t_0} Q(t, \varrho) g\left(\varrho, z(\varrho), \widetilde{C_2}(\varrho)z(\varrho)\right) d\varrho$$

$$= Q(t, t_0)\psi\left(t_0, \widetilde{C_1}(t_0)z(t_0)\right) + \int_{-\infty}^{t} Q(t, \varrho) g\left(\varrho, z(\varrho), \widetilde{C_2}(\varrho)z(\varrho)\right) d\varrho$$

$$- \int_{t_0}^{t} Q(t, \varrho) g\left(\varrho, z(\varrho), \widetilde{C_2}(\varrho)z(\varrho)\right) d\varrho$$

$$= Q(t, t_0)\psi\left(t_0, \widetilde{C_1}(t_0)z(t_0)\right) + z(t) - \psi\left(t, \widetilde{C_1}(t)z(t)\right)$$

$$- \int_{t_0}^{t} Q(t, \varrho) g\left(\varrho, z(\varrho), \widetilde{C_2}(\varrho)z(\varrho)\right) d\varrho.$$

$$(22)$$

It follows that

$$z(t) = \psi\left(t, \widetilde{C_1}(t)z(t)\right) + \int_{-\infty}^{t} Q(t, \varrho) g\left(\varrho, z(\varrho), \widetilde{C_2}(\varrho)z(\varrho)\right) d\varrho.$$

$$(23)$$

Theorem 20. *Let $\mu \in \mathcal{N}$. If $g \in PAPU^p(\mathbb{R} \times W \times K; K, \mu)$ satisfies the following condition*

$$\|g(t, m_1, r_1) - g(t, m_2, r_2)\|_X \le L_3\left(\|m_1 - m_2\|_W + \|r_1 - r_2\|_X\right),$$

$$(24)$$

for all $t \in \mathbb{R}$ and $m_1, m_2 \in W$ and $r_1, r_2 \in K$. If $\varphi \in PAP(\mathbb{R}; K, \mu)$ moreover $\phi \in PAP(\mathbb{R}; W, \mu)$, then $g(., \phi(.), \varphi(.)) \in PAP^p(\mathbb{R}; K, \mu)$.

Proof. Since $g \in PAPU^p(\mathbb{R} \times K, K, \mu)$, then $g = \zeta + h$ and $\phi = u + v, \varphi = x + y$, where $\zeta \in APU^p(\mathbb{R} \times K \times K, K), h \in \mathscr{E}^p(\mathbb{R} \times K \times K, K, \mu), u, x \in AP(\mathbb{R}, K)$ and $v, y \in \mathscr{E}(\mathbb{R}, K, \mu)$. Decompose g as follows:

$$\Psi(t) = \zeta(t, u(t), x(t)) + g(t, \phi(t), \varphi(t)) - \zeta(t, u(t), x(t))$$

$$= \zeta(t, u(t), x(t)) + g(t, \phi(t), \varphi(t)) - g(t, u(t), x(t))$$

$$+ h(t, u(t), x(t)).$$

$$(25)$$

Let us rewrite $\Psi(t) = F(t) + \Phi(t) + \Delta(t)$, where

$$F(t) = \zeta(t, u(t), x(t)),$$

$$\Phi(t) = g(t, \phi(t), \varphi(t)) - g(t, u(t), x(t)), \qquad (26)$$

$$\Delta(t) = h(t, u(t), x(t)).$$

We have $F(t) \in AP^p(\mathbb{R}, X)$ through the composition of S^p-almost periodic functions in [19]. So it can be proved $\Phi(t)$ and $\Delta(t)$ belong to $\mathscr{E}^p(\mathbb{R} \times K, K, \mu)$. Obviously, $\Phi(t) \in BS^p(\mathbb{R}, X)$. Actually, we get

$$\left(\int_{[t,t+1]} \|\Phi(\varrho)\|^p d\varrho\right)^{1/p}$$

$$\le \left(\int_{[t,t+1]} (L_3(\|\phi(\varrho) - u(\varrho)\| + \|\varphi(\varrho) - x(\varrho)\|))^p d\varrho\right)^{1/p}$$

$$\le L_3\left(\left(\int_{[t,t+1]} \|v(\varrho)\|^p d\varrho\right)^{1/p} + \left(\int_{[t,t+1]} \|y(\varrho)\|^p d\varrho\right)^{\frac{1}{p}}\right), \quad \text{for any } t \in \mathbb{R}.$$

$$(27)$$

Since v, y is bounded, then $\Phi(t) \in BS^p(\mathbb{R} \times X, X)$. Let $A_{\widehat{\omega}}^{\epsilon}$ and $M_{\widehat{\omega}, \epsilon}$ be denoted by

$$A_{\widehat{\omega}}^{\epsilon} = \left\{ t \in \widehat{\omega} ; \left(\int_{[t,t+1]} \|\Phi(\varrho)\|^p d\varrho\right)^{1/p} > \epsilon \right\},$$

$$M_{\widehat{\omega}, \epsilon} = \left\{ t \in \widehat{\omega} ; \left(\int_{[t,t+1]} \|v(\varrho)\|^p d\varrho\right)^{1/p} + \left(\int_{[t,t+1]} \|y(\varrho)\|^p d\varrho\right)^{1/p} > 2\epsilon \right\}.$$

$$(28)$$

From (27), we obtain $M_{\widehat{\omega}, \widehat{\beta}} \subset A_{\widehat{\omega}}^{\epsilon}$ and $\mu(M_{\widehat{\omega}, \widehat{\beta}}) \le \mu(A_{\widehat{\omega}}^{\epsilon})$ infers that

$$\frac{\mu\left(\left\{ t \in \widehat{\omega} ; \left(\int_{[t,t+1]} \|\Phi(\varrho)\|^p d\varrho\right)^{1/p} > \epsilon \right\}\right)}{\mu(\widehat{\omega})}$$

$$\le \frac{\mu\left(\left\{ t \in \widehat{\omega} ; \left(\int_{[t,t+1]} \|v(\varrho)\|^p d\varrho\right)^{1/p} > \epsilon \right\}\right)}{\mu(\widehat{\omega})} \qquad (29)$$

$$+ \frac{\mu\left(\left\{ t \in \widehat{\omega} ; \left(\int_{[t,t+1]} \|y(\varrho)\|^p d\varrho\right)^{1/p} > \epsilon \right\}\right)}{\mu(\widehat{\omega})}.$$

From Theorem 16, we get $v, y \in \mathscr{E}^p(\mathbb{R}, K, \mu)$. Since $v, y \in \mathscr{E}^p(\mathbb{R}, K, \mu)$ and Theorem 17, we derive that

$$\lim_{\omega \to +\infty} \frac{\mu\left(\left\{ t \in \widehat{\omega} ; \left(\int_{[t,t+1]} \|v(\varrho)\|^p d\varrho\right)^{1/p} > \epsilon \right\}\right)}{\mu(\widehat{\omega})}$$

$$= \lim_{\omega \to +\infty} \frac{\mu\left(\left\{ t \in \widehat{\omega} ; \left(\int_{[t,t+1]} \|y(\varrho)\|^p d\varrho\right)^{1/p} > \epsilon \right\}\right)}{\mu(\widehat{\omega})} = 0,$$

$$(30)$$

which deduces that

$$\lim_{\omega \to +\infty} \frac{\mu\left(\left\{ t \in \widehat{\omega} ; \left(\int_{[t,t+1]} \|\Phi(\varrho)\|^p d\varrho\right)^{1/p} > \epsilon \right\}\right)}{\mu(\widehat{\omega})} = 0. \quad (31)$$

This deduces from Theorem 17 that $\Phi(t) \in \mathscr{E}^p(\mathbb{R} \times K, K, \mu)$. Now, we show that $\Delta(t) \in \mathscr{E}^p(\mathbb{R}, K, \mu)$. From $u, x \in$

$AP(\mathbb{R}, K)$ then $\overline{u(\mathbb{R})}, \overline{x(\mathbb{R})}$ is compact; moreover, ζ^b is uniformly continuous with respect to $\mathbb{R} \times [0,1] \times \overline{u(\mathbb{R})}$ (or $\overline{x(\mathbb{R})}$). We infer that h^b is uniformly continuous with respect to $\mathbb{R} \times [0,1] \times \overline{u(\mathbb{R})}$ (or $\overline{x(\mathbb{R})}$), namely, for $\epsilon > 0$, let $\widehat{\beta} > 0$ such that for $(a_1, b_1), (a_2, b_2) \in \overline{u(\mathbb{R})} \times \overline{x(\mathbb{R})}$ with $\|a_1 - a_2\| + \|b_1 - b_2\| < \widehat{\beta}$ we get

$$\left(\int_{[t,t+1]} \|h(\varrho, a_1, b_1) - h(\varrho, a_2, b_2)\|^p d\varrho \right)^{1/p} < \frac{\varepsilon}{2}, \quad \text{for any } t \in \mathbb{R}. \tag{32}$$

Because $\overline{u(\mathbb{R})} \times \overline{x(\mathbb{R})}$ is compact, there exist finite balls O_θ with center $(\beta_\theta, \gamma_\theta) \in u(\mathbb{R}) \times x(\mathbb{R}), \theta = 1, 2 \cdots n$ such that for any $(a_2, b_2) \in \overline{u(\mathbb{R})} \times \overline{x(\mathbb{R})}$ we get $\|\beta_\theta - a_2\| + \|\gamma_\theta - b_2\| < \widehat{\beta}$ for $1 \leq \theta \leq n$. Let

$$\mathfrak{B}_\theta = \left\{ t \in \mathbb{R}, \|u(t) - \beta_\theta\| + \|x(t) - \gamma_\theta\| < \widehat{\beta} \right\}, \quad \theta = 1, 2, 3, \cdots, n,$$
$$\mathfrak{D}_1 = \mathfrak{B}_1,$$
$$\mathfrak{D}_\theta = \frac{\mathfrak{B}_\theta}{\left(\cup_{i=1}^{\theta-1} \mathfrak{B}_i \right)}, \quad \theta = 1, 2, 3, \cdots, n. \tag{33}$$

Thus,

$$\mathbb{R} = \bigcup_{\theta=1}^{n} \mathfrak{B}_\theta,$$
$$\mathbb{R} = \bigcup_{\theta=1}^{n} \mathfrak{D}_\theta, \tag{34}$$
$$\mathfrak{D}_i \cap \mathfrak{D}_j = \varnothing (i \neq j).$$

Define function $e_1, e_2 : \mathbb{R} \longrightarrow K$ by $e_1(t) = \beta_\theta, e_2(t) = \gamma_\theta$ for $t \in B_\theta$ and $\theta = 1, 2, 3, \cdots, n$. So $\|u(t) - e_1(t)\| + \|x(t) - e_2(t)\| < \widehat{\beta}$ for $t \in \mathbb{R}$. Therefore, we have

$$\left(\int_{[t,t+1]} \|h(\varrho, u(\varrho), x(\varrho)) - h(\varrho, e_1(\varrho), e_2(\varrho))\|^p d\varrho \right)^{1/p} \leq 4 \times 2^{1/p} \epsilon. \tag{35}$$

Since $h \in \mathscr{E}^p(\mathbb{R} \times K, K, \mu)$, then there exists $\varpi_0 > 0$ such that for $\varpi > \varpi_0$: for every $\theta = 1, 2, 3, \cdots, n$

$$\frac{1}{\mu(\widehat{\varpi})} \int_{\widehat{\varpi}} \left(\int_{[t,t+1] \cap \mathfrak{D}_\theta} \|h(\varrho, \beta_\theta, \gamma_\theta)\|^p d\varrho \right)^{1/p} d\mu(t) \leq 4 \times 2^{1/p} n^{1/p} \epsilon. \tag{36}$$

Then,

$$\frac{1}{\mu(\widehat{\varpi})} \int_{\widehat{\varpi}} \left(\int_{[t,t+1]} \|h(\varrho, u(\varrho), x(\varrho))\|^p d\varrho \right)^{1/p} d\mu(t) = \frac{1}{\mu(\widehat{\varpi})} \int_{\widehat{\varpi}}$$
$$\cdot \left(\sum_{\theta=1}^{n} \int_{[t,t+1] \cap \mathfrak{D}_\theta} \|h(\varrho, u(\varrho), x(\varrho)) - h(\varrho, \beta_\theta, \gamma_\theta) + h(\varrho, \beta_\theta, \gamma_\theta)\|^p d\varrho \right)^{1/p} d\mu(t)$$
$$\leq \frac{2^{1+(1/p)}}{\mu(\widehat{\varpi})} \int_{\widehat{\varpi}} \left(\sum_{\theta=1}^{n} \int_{[t,t+1] \cap \mathfrak{D}_\theta} \|h(\varrho, u(\varrho), x(\varrho)) - h(\varrho, \beta_\theta, \gamma_\theta)\|^p d\varrho \right)^{\frac{1}{p}} d\mu(t)$$
$$+ \frac{2^{1+(1/p)}}{\mu(\widehat{\varpi})} \int_{\widehat{\varpi}} \left(\sum_{\theta=1}^{n} \int_{[t,t+1] \cap \mathfrak{D}_\theta} \|h(\varrho, \beta_\theta, \gamma_\theta)\|^p d\varrho \right)^{1/p} d\mu(t)$$
$$\leq \frac{2^{1+(1/p)}}{\mu(\widehat{\varpi})} \int_{\widehat{\varpi}} \left(\int_{[t,t+1]} \|h(\varrho, u(\varrho), x(\varrho)) - h(\varrho, e_1(\varrho), e_2(\varrho))\|^p d\varrho \right)^{1/p} d\mu(t)$$
$$+ \frac{2^{1+(1/p)}}{\mu(\widehat{\varpi})} \int_{\widehat{\varpi}} \left(\sum_{\theta=1}^{n} \int_{[t,t+1] \cap \mathfrak{D}_\theta} \|h(\varrho, \beta_\theta, \gamma_\theta)\|^p d\varrho \right)^{1/p} d\mu(t) \leq \epsilon. \tag{37}$$

It follows that $\Delta(t) \in \mathscr{E}^p(\mathbb{R}, K, \mu)$. The proof is completed. □

Lemma 21. *Let $\mu \in \mathcal{N}$. Assume that $(H3) - (H4)$ hold. If Φ is an S^p-μ-pseudo almost periodic function, then*

$$(\Gamma\Phi)(t) = \int_{-\infty}^{t} Q(t, \varrho)\Phi(\varrho) d\varrho, \quad t \in \mathbb{R} \tag{38}$$

is a μ-pseudo almost periodic function.

Proof. Since $\Phi \in S^p PAP(\mathbb{R}; K, \mu)$, then we have the following decomposition $\Phi = \Phi_1 + \Phi_2$ where $\Phi_1 \in S^p AP(\mathbb{R}; K)$ and $\Phi_2 \in \mathscr{E}^p(\mathbb{R}; K, \mu)$. We define

$$(\Gamma\Phi_1)(t) = \int_{-\infty}^{t} Q(t, \varrho)\Phi_1(\varrho) d\varrho, (\Gamma\Phi_2)(t)$$
$$= \int_{-\infty}^{t} Q(t, \varrho)\Phi_2(\varrho) d\varrho, \quad t \in \mathbb{R}. \tag{39}$$

Since there exist $(1/p) + (1/q) = 1$, where $p > 1$, the proof is as follows. Let us show that $(\Gamma\Phi_1)(t) \in AP(\mathbb{R}; K)$.
We define

$$(\Gamma\Phi_1)_\theta(t) = \int_{t-\theta}^{t-\theta+1} Q(t, \varrho)\Phi_1(\varrho) d\varrho, \theta \in \mathbb{N}, \quad t \in \mathbb{R}. \tag{40}$$

By virtue of the Hölder inequality and formula (16), we get

$$\left\| (\Gamma\Phi_1)_\theta(t) \right\| = \left\| \int_{t-\theta}^{t-\theta+1} Q(t, \varrho)\Phi_1(\varrho) d\varrho \right\|$$
$$\leq \int_{t-\theta}^{t-\theta+1} \|Q(t, \varrho)\| \|\Phi_1(\varrho)\| d\varrho$$
$$\leq K_0 \left[\int_{t-\theta}^{t-\theta+1} e^{-q\beta\wedge(t-\varrho)} d\varrho \right]^{1/q} \left[\int_{t-\theta}^{t-\theta+1} \|\Phi_1(\varrho)\|^p d\varrho \right]^{1/p}$$
$$\leq \frac{K_0 \left(e^{q\beta\wedge} - 1 \right)}{\sqrt[q]{q\widehat{\beta}}} e^{-\theta\beta\wedge} \|\Phi_1\|_{S^p}. \tag{41}$$

Since $\sum_{\theta=1}^{\infty} e^{-\beta\wedge\theta}$ is convergent, so take advantage of the Weierstrass theorem, we obtain that the sequence of functions $\sum_{\theta=1}^{\infty}(\Gamma\Phi_1)_\theta(t)$ is convergent uniformly on $\mathbb{R}$; moreover, $\sum_{\theta=1}^{\infty}(\Gamma\Phi_1)_\theta(t) = (\Gamma\Phi_1)(t)$ then $(\Gamma\Phi_1)(.)$ is continuous and

$$\begin{aligned}
\|(\Gamma\Phi_1)(t)\| &\le \sum_{\theta=1}^{\infty}\|(\Gamma\Phi_1)_\theta(t)\| \\
&\le \frac{K_0(e^{q\beta\wedge}-1)}{\sqrt[q]{q\widehat{\beta}}}\|\Phi_1\|_{S^p}\sum_{\theta=1}^{\infty}e^{-\beta\wedge\theta}, \quad \text{for all } t \in \mathbb{R}.
\end{aligned} \tag{42}$$

Next, we can demonstrate that $(\Gamma\Phi_1)(.) \in AP(\mathbb{R};K)$. Since $\Phi_1 \in S^pAP(\mathbb{R};K)$, let $\epsilon > 0$; afterwards, there is $l(\epsilon) > 0$ such that each length interval $l(\epsilon)$ contains $\widehat{\nu}$ based on the estimate

$$\sup_{t\in\mathbb{R}}\left[\int_t^{t+1}\|\Phi_1(\varrho+\nu\wedge)-\Phi_1(\varrho)\|^p d\varrho^{1/p}\right] < \epsilon_1\epsilon, \tag{43}$$

where $\epsilon_1 = \sqrt[q]{q\widehat{\beta}}(e^{\beta\wedge}-1)/(K_0(e^{q\beta\wedge}-1))$,

$$\begin{aligned}
&\|(\Gamma\Phi_1)_\theta(t+\widehat{\nu})-(\Gamma\Phi_1)_\theta(t)\| \\
&= \left\|\int_{t+\widehat{\nu}-\theta}^{t+\widehat{\nu}-\theta+1}Q(t+\widehat{\nu},\varrho)\Phi_1(\varrho)d\varrho - \int_{t-\theta}^{t-\theta+1}Q(t,\varrho)\Phi_1(\varrho)d\varrho\right\| \\
&\le \int_{t-\theta}^{t-\theta+1}\|Q(t,\varrho)\|\|\Phi_1(\varrho+\widehat{\nu})-\Phi_1(\varrho)\|d\varrho \\
&\le K_0\left[\int_{t-\theta}^{t-\theta+1}e^{-q\beta\wedge(t-\varrho)}d\varrho\right]^{1/q}\left[\int_{t-\theta}^{t-\theta+1}\|\Phi_1(\varrho+\nu\wedge)-\Phi_1(\varrho)\|^p d\varrho\right]^{1/p} \\
&\le \frac{K_0(e^{q\beta\wedge}-1)}{\sqrt[q]{q\widehat{\beta}}}e^{-\theta\beta\wedge}\epsilon_1\epsilon.
\end{aligned} \tag{44}$$

Hence,

$$\sum_{\theta=1}^{\infty}\|(\Gamma\Phi_1)_\theta(t+\widehat{\nu})-(\Gamma\Phi_1)_\theta(t)\| < \epsilon\epsilon_1\frac{K_0(e^{q\beta\wedge}-1)}{\sqrt[q]{q\widehat{\beta}}}\sum_{\theta=1}^{\infty}e^{-\theta\beta\wedge} = \epsilon. \tag{45}$$

Therefore, $\sum_{\theta=1}^{\infty}(\Gamma\Phi_1)_\theta(.) \in AP(\mathbb{R},K)$ for all $\theta \in \mathbb{N}$ and $(\Gamma\Phi_1)(.) \in AP(\mathbb{R};K)$.

Next, we show that $(\Gamma\Phi_2)(.) \in \mathscr{E}(\mathbb{R};K,\mu)$.

Let $\widehat{\omega} > 0$, $\Phi_2 \in \mathscr{E}^p(\mathbb{R};K,\mu)$; we get that

$$\lim_{\widehat{\omega}\longrightarrow+\infty}\frac{1}{\mu(\widehat{\omega})}\int_{\widehat{\omega}}\left(\int_\varrho^{\varrho+1}\|\Phi_2(\sigma)\|^p d\sigma\right)^{1/p}d\mu(\varrho) = 0. \tag{46}$$

First, we prove that $\Gamma\Phi_2 \in BC(\mathbb{R};K)$. As a matter of fact, it is similar to above work of $\Gamma\Phi_1$. Then, we demonstrate that $\Gamma\Phi_2 \in \mathscr{E}(\mathbb{R};K,\mu)$. We observe

$$(\Gamma\Phi_2)_\theta(t) = \int_{t-\theta}^{t-\theta+1}Q(t,\varrho)\Phi_2(\varrho)d\varrho, \theta \in \mathbb{N}, \quad t \in \mathbb{R}. \tag{47}$$

Taking advantage of the Hölder inequality and applying formula (16), considering that

$$\begin{aligned}
\|(\Gamma\Phi_2)_\theta(t)\| &= \left\|\int_{t-\theta}^{t-\theta+1}Q(t,\varrho)\Phi_2(\varrho)d\varrho\right\| \\
&\le \int_{t-\theta}^{t-\theta+1}\|Q(t,\varrho)\|\|\Phi_2(\varrho)\|d\varrho \\
&\le K_0\left[\int_{t-\theta}^{t-\theta+1}e^{-q\beta\wedge(t-\varrho)}d\varrho\right]^{1/q}\left[\int_{t-\theta}^{t-\theta+1}\|\Phi_2(\varrho)\|^p d\varrho\right]^{1/p} \\
&\le \frac{K_0(e^{q\beta\wedge}-1)}{\sqrt[q]{q\widehat{\beta}}}e^{-\theta\beta\wedge}\|\Phi_2\|_{S^p},
\end{aligned} \tag{48}$$

it follows that

$$\begin{aligned}
\frac{1}{\mu(\widehat{\omega})}\int_{\widehat{\omega}}\|(\Gamma\Phi_2)_\theta(t)\|d\mu(t) &\le \frac{K_0(e^{q\beta\wedge}-1)}{\sqrt[q]{q\widehat{\beta}}}e^{-\theta\beta\wedge}\frac{1}{\mu(\widehat{\omega})}\int_{\widehat{\omega}} \\
&\quad \cdot \|\Phi_2(t)\|_{S^p}d\mu(t),
\end{aligned}$$

$$\begin{aligned}
&\lim_{\widehat{\omega}\longrightarrow+\infty}\frac{1}{\mu(\widehat{\omega})}\int_{\widehat{\omega}}\|(\Gamma\Phi_2)_\theta(t)\|d\mu(t) \\
&\le \frac{K_0(e^{q\beta\wedge}-1)}{\sqrt[q]{q\widehat{\beta}}}e^{-\theta\beta\wedge}\cdot\lim_{\widehat{\omega}\longrightarrow+\infty}\frac{1}{\mu(\widehat{\omega})}\int_{\widehat{\omega}}\|\Phi_2(t)\|_{S^p}d\mu(t) = 0.
\end{aligned} \tag{49}$$

Hence, $(\Gamma\Phi_2)_\theta \in \mathscr{E}(\mathbb{R},K,\mu)$. For another, since $\sum_{\theta=1}^{\infty}e^{-\beta\wedge\theta}$ is convergent, so applying the Weierstrass theorem, then the series, as a result, $\sum_{\theta=1}^{\infty}(\Gamma\Phi_2)_\theta(t)$ is convergent uniformly on $\mathbb{R}$.

What is more, $\sum_{\theta=1}^{\infty}(\Gamma\Phi_2)_\theta(t) = (\Gamma\Phi_2)(t)$; therefore, $\sum_{\theta=1}^{\infty}(\Gamma\Phi_2)_\theta(t) \in \mathscr{E}(\mathbb{R},K,\mu)$, so $(\Gamma\Phi_2)(t) \in \mathscr{E}(\mathbb{R},K,\mu)$ from Proposition 18. □

Theorem 22. *Let $\mu \in \mathcal{N}$ and suppose that (H3)–(H7) hold. If $L_\psi\omega + (2K_0L_3/\widehat{\beta})(1+\omega) < 1$, then equation (1) has a unique μ-pseudo almost periodic mild solution.*

Proof. Define the operator Π as follows:

$$(\Pi z)(t) = \psi\left(t,\widetilde{C_1}(t)z(t)\right)+\int_{-\infty}^{t}Q(t,\varrho)g\left(\varrho,z(\varrho),\widetilde{C_2}(\varrho)z(\varrho)\right)d\varrho. \tag{50}$$

For $z(t) \in PAP(\mathbb{R};K,\mu)$, by Lemma 21 in [5], we get that $\widetilde{C_1}(t)z(t)$ is μ-pseudo almost periodic; by (H6) and Theorem 10, it is simple to demonstrate that $\psi(t,\widetilde{C_1}(t)z(t))$ is part of $PAP(\mathbb{R};K,\mu)$. We will demonstrate this now that $\int_{-\infty}^{t}Q(t,\varrho)g(\varrho,z(\varrho),\widetilde{C_2}(\varrho)z(\varrho))d\varrho$ is part of $PAP(\mathbb{R};K,\mu)$;

by using Theorem 20 and hypothesis (H7), we can easily deduce that $g(\varrho, z(\varrho), \widetilde{C_2}(\varrho)z(\varrho))$ is part of $PAP^p(\mathbb{R}; K, \mu)$. Thus, Π is mapping from $PAP(\mathbb{R}; K, \mu)$ into itself.

Let $z, v \in PAP(\mathbb{R}; K, \mu)$. We deduce that

$$
\begin{aligned}
\|(\Pi z)(t) - (\Pi v)(t)\| &\leq \left\| \psi\left(t, \widetilde{C_1}(t)z(t)\right) - \psi\left(t, \widetilde{C_1}(t)v(t)\right)\right\| + \int_{-\infty}^{t} \|Q(t,\varrho)\| \\
&\quad \cdot \left\| g\left(\varrho, z(\varrho), \widetilde{C_2}(\varrho)z(\varrho)\right) - g\left(\varrho, v(\varrho), \widetilde{C_2}(\varrho)v(\varrho)\right)\right\| d\varrho \\
&\leq L_\psi \left\| \widetilde{C_1}(t)z(t) - \widetilde{C_1}(t)v(t)\right\| + K_0 L_3 \int_{-\infty}^{t} e^{-\beta\wedge(t-\varrho)} \\
&\quad \cdot \left(\left(1 + \left\|\widetilde{C_2}(\varrho)\right\|\right)\|z(\varrho) - v(\varrho)\|\right) d\varrho \\
&\leq L_\psi \left\| \widetilde{C_1}(t)\right\| \|z - v\|_\infty + 2K_0 L_3 \\
&\quad \cdot \left(1 + \left\|\widetilde{C_2}(\varrho)\|\right)\left(\int_{-\infty}^{t} e^{-\beta\wedge(t-\varrho)} d\varrho\right)\|z - v\|_\infty \\
&\leq \left(L_\psi \omega + \frac{2K_0}{\widehat{\beta}}(1+\omega)L_3\right)\|z - v\|_\infty.
\end{aligned}
\tag{51}
$$

Thus,

$$
\|\Pi z - \Pi v\|_\infty \leq \left(L_\psi \omega + \frac{2K_0}{\widehat{\beta}}(1+\omega)L_3\right)\|z - v\|_\infty. \tag{52}
$$

As a result, this establishes that Π is a contraction map. We may infer that Π has a single fixed point in $PAP(\mathbb{R}; K, \mu)$ such that $\Pi z = z$. Consequently, (1) has a unique μ-pseudo almost periodic mild solution. □

4. Example

As an example, take a look at the differential equations listed below.

$$
\begin{aligned}
&\frac{d}{dz}[u(z,x) - \psi(z, c_1(z,x)u(z,x))] \\
&= \frac{d^2}{dx^2}[u(z,x) - \psi(z, c_1(z,x)u(z,x))] \\
&\quad + (-3 + \sin(mz) + \sin(nz))[u(z,x) - \psi(z, c_1(z,x)u(z,x))] \\
&\quad + g(z, u(z,x), c_2(z,x)u(z,x)), \quad z \in \mathbb{R}, \; x \in [0,1],
\end{aligned}
\tag{53}
$$

$$
\begin{aligned}
u(z,0) - \psi(z, c_1(z,0)u(z,0)) &= u(z,1) - \psi(z, c_1(z,1)u(z,1)) \\
&= 0, \quad z \in \mathbb{R},
\end{aligned}
\tag{54}
$$

where $m, n \in \mathbb{R}$ and $m/n \notin \mathbb{Q}, \psi, g : \mathbb{R} \times K \mapsto K$, and $c_1, c_2 : \mathbb{R} \times [0,1] \mapsto \mathbb{R}$ are continuous functions. So as to rephrase this equation in form (1.1), we set the spaces $K = L^2([0,1])$ provided with the norm $\|\cdot\|_2$. The operator $A : D(A) \subset K \longrightarrow K$ is defined by

$$
Au = u'' \quad u \in D(A). \tag{55}
$$

Furthermore, A is the infinitesimally small generator C_0-semigroup $\{T(z)\}_{z\geq 0}$ with $\|T(z)\| \leq e^{-z}$ $(K = \widehat{\beta} = 1)$ for $z \geq 0$.

We consider the operator $A(z)$ given by

$$
\begin{cases}
D(A(z)) = D(A), \\
A(z)v = (A - 3 + \sin(mz) + \sin(nz))v, \quad \text{for all } v \in D(A).
\end{cases}
\tag{56}
$$

Thus, $D(A(z)) = D(A)$. Furthermore,

$$
\begin{aligned}
\|A(z) - A(s)\| &= \|(\sin(mz) - \sin(ms) + \sin(nz) - \sin(ns))\| \\
&\leq (|m| + |n|)|z - s|,
\end{aligned}
\tag{57}
$$

for every $s, z \in \mathbb{R}$, and hence, (H3) holds. Then, an evolution family $Q(z,s)_{z\geq s}$ generated by $A(z)$ with

$$
Q(z,s)v = T(z-s) \exp\left(\int_s^z (-3 + \sin(m\widehat{v}) + \sin(n\widehat{v}))d\widehat{v}\right)v. \tag{58}
$$

Since $\|Q(z,s)\| \leq e^{-(z-s)}$, then it is very clear to know that $A(z)$ fulfill the hypothesis (H4) with $K_0 = 1, \widehat{\beta} = 1$. At the same time, we define

$$
\begin{aligned}
\widetilde{C_1}(z)u &= c_1(z,x)u, \quad \text{for all } z \in \mathbb{R}, \\
\widetilde{C_2}(z)u &= c_2(z,x)u, \quad \text{for all } z \in \mathbb{R}.
\end{aligned}
\tag{59}
$$

$c_1(z,.), c_2(z,.): \mathbb{R} \times [0,1] \mapsto \mathbb{R}$ are continuous and almost periodic in $z \in \mathbb{R}$ uniformly in $x \in [0,1]$. Then, Equation (53) can be represented as the abstract equation (1).

Study the measure μ with respect to its Radon-Nikodym derivative of

$$
\rho(z) = \begin{cases}
e^z, & \text{if } z \leq 0, \\
1, & \text{if } z > 0.
\end{cases}
\tag{60}
$$

Then, $\mu \in \mathcal{N}$ satisfy (H1) and (H2). If we take the assumption that ψ, g satisfy (H6) and (H7), therefore, all assumptions of Theorem 22 are fulfilled; thus, the evolution equation (53) has a unique μ-pseudo almost periodic solution if L_ψ, L_3 is sufficiently small.

5. Conclusions and the Future Work

The primary objective of this research is to find out whether there is unique μ-pseudo almost periodic solution to a functional evolution equation with Stepanov forcing components in a Banach space using measure theory, evolution family, and Hölder inequality. The Lipschitz condition and the contraction mapping theory are used to develop certain suitable conditions that guarantee whether there is unique μ-pseudo almost periodic solutions to the problem. As a future work, we intend to study whether there is unique Stepanov-like

pseudo almost periodic solution of neural network and discrete equation. We will also use the Hölder inequality to consider whether there is a unique Stepanov-like pseudo almost periodic solution of discrete equation. Almost periodic problems play a very important basic role in engineering applications and mathematical research.

Data Availability

The data used to support the findings of this study are included in the article.

Conflicts of Interest

The author states that the publishing of this paper does not include any conflicts of interest.

Acknowledgments

References

[1] C. Zhang, *Pseudo Almost Periodic Functions and Their Applications*, ProQuest LLC, Ann Arbor, MI, Canada, 1992.

[2] T. Diagana, "Weighted pseudo almost periodic functions and applications," *Comptes Rendus Mathematique*, vol. 343, no. 10, pp. 643–646, 2006.

[3] J. Blot, P. Cieutat, and K. Ezzinbi, "New approach for weighted pseudo-almost periodic functions under the light of measure theory, basic results and applications," *Applicable Analysis*, vol. 92, no. 3, pp. 493–526, 2013.

[4] C. Jendoubi, "μ-Pseudo almost periodic solutions for delayed partial functional differential equations in admissible spaces," *Applicable Analysis*, pp. 1–19, 2021.

[5] M. Miraoui, "Existence of μ-pseudo almost periodic solutions to some evolution equations," *Mathematical Methods in the Applied Sciences*, vol. 40, no. 13, pp. 4716–4726, 2017.

[6] M. Adimy, K. Ezzinbi, and C. Marquet, "Ergodic and weighted pseudo-almost periodic solutions for partial functional differential equations in fading memory spaces," *Journal of Applied Mathematics and Computing*, vol. 44, no. 1–2, pp. 147–165, 2014.

[7] K. Ezzinbi and M. Miraoui, "μ-Pseudo almost periodic and automorphic solutions in the α-norm for some partial functional differential equations," *Numerical Functional Analysis and Optimization*, vol. 36, no. 8, pp. 991–1012, 2015.

[8] K. Ezzinbi, M. Miraoui, and A. Rebey, "Measure pseudo-almost periodic solutions in the α-norm to some neutral partial differential equations with delay," *Mediterranean Journal of Mathematics*, vol. 13, no. 5, pp. 3417–3431, 2016.

[9] Z. Xia, "Pseudo asymptotic behavior of mild solution for non-autonomous integrodifferential equations with nondense domain," *Journal of Applied Mathematics*, vol. 2014, Article ID 419103, 10 pages, 2014.

[10] Z. Xia, "Pseudo asymptotic behavior of mild solution for semi-linear fractional integro-differential equations," *Miskolc Mathematical Notes*, vol. 16, no. 1, pp. 553–563, 2015.

[11] T. Diagana, "Stepanov-like pseudo almost periodic functions and their applications to differential equations," *Communications in Mathematical Analysis*, vol. 3, no. 1, 2007.

[12] T. Diagana, G. M. Mophou, and G. M. N'Guérékata, "Existence of weighted pseudo-almost periodic solutions to some classes of differential equations with Sp-weighted pseudo-almost periodic coefficients," *Nonlinear Analysis Theory, Methods and Applications*, vol. 72, no. 1, pp. 430–438, 2010.

[13] B. Es-Sebbar and K. Ezzinbi, "Stepanov ergodic perturbations for some neutral partial functional differential equations," *Mathematical Methods in the Applied Sciences*, vol. 39, no. 8, pp. 1945–1963, 2016.

[14] M. Baroun, K. Ezzinbi, K. Khalil, and L. Maniar, "Pseudo almost periodic solutions for some parabolic evolution equations with Stepanov-like pseudo almost periodic forcing terms," *Journal of Mathematical Analysis and Applications*, vol. 462, no. 1, pp. 233–262, 2018.

[15] E. Alvarez, "Composition and convolution theorems for μ-Stepanov pseudo almost periodic functions and applications to fractional integro-differential equations," *Electronic Journal of Differential Equations*, vol. 2018, no. 27, pp. 1–15, 2018.

[16] C. Corduneanu, *Almost Periodic Functions*, Interscience Publishers, Chelsea Pub Co, 1989.

[17] T. Yoshizawa, *Stability Theory and the Existence of Periodic Solutions and Almost Periodic Solutions*, vol. 14, Springer Science & Business Media, 2012.

[18] A.-N. Akdad, B. Essebbar, and K. Ezzinbi, "Composition theorems of Stepanov μ-pseudo almost automorphic functions and applications to nonautonomous neutral evolution equations," *Differential Equations and Dynamical Systems*, vol. 25, no. 3, pp. 397–416, 2017.

[19] T. Diagana, "Stepanov-like pseudo-almost periodicity and its applications to some nonautonomous differential equations," *Nonlinear Analysis, Theory, Methods and Applications*, vol. 69, no. 12, pp. 4277–4285, 2008.

Research Article

The Statistical Analysis of Multidimensional Psychological Characteristics and User Feedback Willingness

Haiying Wang,[1] Yaning Li,[2] Chang Zhou,[3] Haizhe Jin ⓘ,[2] and Lin Wang[4]

[1]*School of Art Design, Zhejiang A&F University, Hangzhou 311300, China*
[2]*Northeastern University, Shenyang 110000, China*
[3]*Faculty of Arts, Design and Architecture, the University of New South Wales, Sydney 4385, Australia*
[4]*Department of Library and Information Science, Incheon National University, Incheon 22012, Republic of Korea*

Correspondence should be addressed to Haizhe Jin; 20190091@zafu.edu.cn

The purpose of this paper is to study the influence of multidimensional psychological characteristics on users' feedback intention by using several statistical analysis methods based on information theory. The feedback process can be described as a communication process based on information theory. The feedback information entropy is associated with the degree of uncertainty elimination of the users who provide feedback information. Many factors are related to this uncertainty, such as information senders often stopped feedback process for some reasons and information senders may have provided fake or spam information. In order to encourage more useful feedback information, a model of a user's willingness to provide feedback was established with personality traits and cognitive styles as independent variables, feedback motivation as intermediary variables, and feedback willingness as the dependent variable. 206 online and offline questionnaires were obtained to be analyzed by correlation analysis, regression analysis, and structural equation analysis. Cronbach's α coefficient was used to test the reliability of the questionnaire, and exploratory factor analysis method was used to verify the validity of the questionnaire. First, correlation analysis was used to explore the correlation between personality traits, cognitive styles, and motivation factors. Second, we further explored the strength of the relationship of the five correlated groups of variables through linear regression analysis. At last, we conducted structure equation analyses to test the hypotheses. The results show that both personality traits and cognitive styles can have a significant impact on feedback motivation factors and also show that self-efficacy may be the only evident feedback motivation to encourage useful feedback information. The results show that the willing users with extraversion trait are more likely be motivated by self-efficacy and thus have evident feedback willingness.

1. Introduction

User feedback (*user review*) refers to the behavior of users to deliver feedback information such as their own experience, feature requests, or bug reports of products or services to providers through feedback platforms [1]. Based on the information theory proposed by Shannon [2], we regarded user feedback as a communication process (Figure 1 shows the feedback process based on information theory). In this communication process, the enterprises can be viewed as the receivers receiving feedback from senders who provide feedback message [3]. Enterprises received feedback information via a variety of media, and entropy needs measurement to estimate its validity. In recent years, the technology of Internet and the Internet of Things have grown rapidly, allowing users to provide feedback information via more platforms, such as feedback module in APP, enterprise WeChat, app stores, forums, customer service center, and micro blogs [4, 5].

The feedback information entropy is associated with the degree of uncertainty elimination of the users who provide feedback information. Many factors are related to this
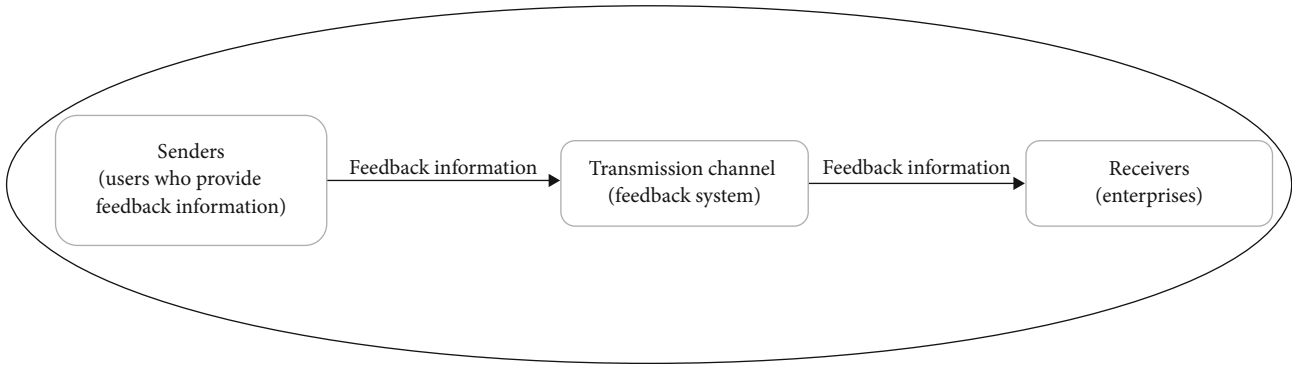
FIGURE 1: Feedback process based on information theory.
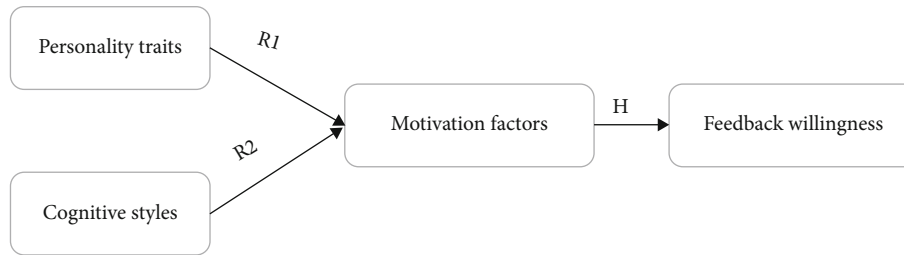
FIGURE 2: Research model.

uncertainty, such as information senders often stopped feedback process for some reasons and information senders may have provided fake or spam information [6–8].

In order to encourage more useful feedback information in various platforms, it is important to find who are willing to post useful information and understand why they do so. As we know, individual differences in behavior and attitude can be determined by the differences in multiple psychological characters, such as personality traits and cognitive styles, mediated by motivation factors [9, 10]. A few papers have studied the effect of personality traits on user feedback behavior without taking the motivation factors into consideration or only consider single motivation factor [11, 12]. Certain researchers have investigated how cognitive styles influence some online behaviors, such as multimedia perception, online information searching, and creative behavior [13–16], but few have directly discussed the influence of cognitive styles on user feedback. There is a lack of research on the influence of MPC on user feedback.

To address this issue, we develop a conceptual model to discuss the influence of multidimensional psychological characteristics (including personality traits and cognitive styles) on user feedback willingness and also mediate effect of motivation factors in this relationship in the Chinese context (Figure 2 shows the research model). We construct user feedback motivation factors based on social cognition theory [17] and the motivations of consumer reviews [18, 19] that are related to but different from user feedback. We study the conceptual model in two steps. First, we assume that different motivation factors have different degrees of effect on user feedback and identify the effective motivation factors that can significantly make the users generate evident feed-

back willingness to post useful feedback information (Hypothesis 1). We then provide evidence that personality traits and cognitive styles can significantly influence evident feedback willingness as well as demonstrate differences between different traits and styles (Research Question 1 and Research Question 2). This will help enterprises find who are willing to provide useful feedback information according to the corresponding personality traits or cognitive styles and to understand the motivations for doing so.

2. Related Works

Many papers have studied the motivations of *consumer review* (*customer review*, *online review*, and *product review*) which refers to the behavior of consumers who post their own experience information on online platforms after purchasing a product or service. User feedback behavior shares many similarities with customer review in that they are both voluntary behaviors of posting information related to the experience of using a product or service on the platform. Some motivation factors of user feedback can be proposed based on the similarities with customer reviews. First, both customer review and user feedback can help others to some extent. User feedback can help enterprise evolution, and consumer review can help other customers make purchasing decisions. Therefore, we retained the "altruism" factor of customer review [20, 21] as one of the factors of user feedback motivation. Second, "rewards" can be a motivator for both [22, 23]. As for the factor of "a desire to share experience" [18, 22], some feedback platforms, such as the feedback module in APP, enterprise WeChat, and customer service, are invisible to others and may only be visible to

enterprises. Therefore, we did not regard it as a motivational factor for users' feedback. And other factors have little to do with user feedback.

We proposed some other factors based on some other related research and the social cognition theory [17]. Firstly, users may wish that the product or service would be better through their useful suggestions, which would also beneficial to them. By referring to the similar research of Wasko and Faraj [24] on the motivation of contributors to obtain long-term benefits in electronic network practice, we simply called this user feedback motivation factor "self-interest." Secondly, if users' suggestions can be accepted by the enterprise, users would feel that they could have some influence on the decision-making and development of the product or service. Referring to the results of Sundaram et al. [25] on the motivation of influence on other consumers in word-of-mouth communication, we simply call this user feedback motivation factor "influence." Thirdly, users may look forward to getting a sense of accomplishment and approval from the provider for the feedback. By referring to the study of Wasko and Faraj [24] on the similar motivation in electronic network practice, we called this motivation "achievability." At last, we added "self-efficacy" factor based on the social cognition theory proposed by Bandura [17]. Self-efficacy indicates a subjective judgment of the knowledge and ability that users must apply in the process of feedback, such as the judgment of the ability to operate software and express feedback information.

Based on the above analyses, we proposed the following hypotheses:

Hypothesis 1. Availability has a positive effect on user feedback willingness.

Hypothesis 2. Self-interest has a positive effect on user feedback willingness.

Hypothesis 3. Influence has a positive effect on user feedback willingness.

Hypothesis 4. Altruism has a positive effect on user feedback willingness.

Hypothesis 5. Reward has a positive effect on user feedback willingness.

Hypothesis 6. Self-efficacy has a positive effect on user feedback willingness.

2.1. The Influence of Personality Traits on User Feedback Motivations.
Allport [26] defined personality traits as the dynamic organization within the individual of those psychophysical systems that determined his unique adjustments to his environment. Personality traits can influence user attitude and behavior [27, 28]. Among the related personality traits' papers, the five-factor model has been recognized by most researchers as the most reasonably individual personality model [29]. The five-factor model was proposed by Gold-berg [30], which included extraversion, neuroticism, openness, agreeableness, and conscientiousness.

Some scholars have discussed the different effects of these five different personalities on behaviors related to user feedback such as information sharing behavior [31, 32] and web service using behavior [33]. Also, some scholars have discussed that users with different personality traits have different degrees of desires for some motivation factors [34, 35]. Some related research showed that extroversion was positively correlated with the willingness to share information [36]. Users with extraversion trait were more likely to engage in comments related to self-actualization and disclosure behavior to help others [37] and were more likely to use web services that were helpful to them [33]. In addition, extroverted individuals had high desires for social recognition, praise, status, and rights [34, 35]. Adaji et al. [11] suggested that extroverted users who posted unhelpful information were susceptible to rewards. Some literature has shown that neuroticism was negatively correlated with personal information sharing, because people with high scores of neuroticism were more likely to be emotional, less likely to trust others, and therefore less willing to contribute their own knowledge [5]. Some researchers found that openness was positively correlated with information sharing behavior. People with high openness were more abstract in thinking and liked to explore new knowledge, and these variables were highly correlated with information sharing [31, 32]. The results of research on conscientiousness and agreeableness were inconclusive, and some research results showed that there was no significant correlation between these two factors and willingness to share [38].

The literature above is about the research on the relationship of personality traits and the motivation factors of some other behaviors related to user feedback. We also wanted to know if the users with five different personality traits would be motivated differently by the feedback motivational factors, so we proposed the following research question.

Research Question 1. Will motivation factors of user feedback be significantly affected by personality traits? Will users with certain personality trait dimension be more likely motivated by some motivation factors?

2.2. The Influence of Cognitive Styles on User Feedback Motivations.
Cognitive styles refer to the individual's consistent and characteristic predispositions of perceiving, remembering, organizing, processing, thinking, and problem solving [39]. The Soloman Learning Style questionnaire proposed by Felder et al. [40] has been widely used to test individual cognitive style in four dimensions (active/reflective, sensing/intuitive, visual/verbal, and sequential/global) and proven to have good reliability and validity after a large number of practical tests.

Some researchers have investigated the effect of cognitive styles on some relevant online behavior [13, 14], but few of them have taken behavior motivation into consideration. For example, Sangari and Zerehsaz [14] examined the relationship between collaborative information seeking motivation and users' cognitive styles. The results showed that the
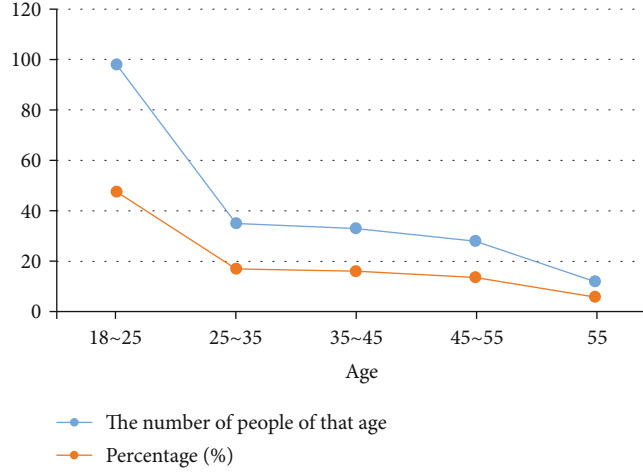
FIGURE 3: Age distribution of the participants.

accommodating style had the highest number of relationships with collaborative information seeking variables. Gulliver et al. [13] showed that cognitive styles can affect information assimilation, self-perceived achievement, and level of self-confidence.

In this paper, we will discuss the relationship between cognitive styles and user feedback motivations. We proposed the following research question.

Research Question 2. Will motivation factors of user feedback be significantly affected by cognitive styles? Will users with certain cognitive style dimension be more likely motivated by some motivation factors?

3. Method

3.1. Participants and Procedure. Online and offline questionnaires were distributed at the same time. Online questionnaires were distributed by sharing the link of Questionnaire Star via project team members' WeChat groups. We sent random WeChat red packet (ranging from *0* yuan to *3* yuan RMB) as online questionnaire reward. And offline questionnaires were distributed on campus and in enterprises in paper form. A part of the offline participants was students from Northeastern University, who were randomly selected in front of the university cafeteria and each received a pen as a reward. In order to better understand the feedback experience of the users who were already working, we selected employees from Hangzhou Chitu Sports Technology Co., Ltd who have a long-term cooperative relationship with us as other offline participants. Each employee participant received a stack of post-it notes as a reward. We obtained ethical approval from all the participants that participation would be anonymous and their responses would be used only for this research. All participants volunteered to take part in this survey and gave informed consent.

We distributed *234* questionnaires in total, and *58* (*24.7%*) online questionnaires, 115 (49.1%) offline university questionnaires, and *61* (*26.1%*) offline enterprise questionnaires were returned. After discarding invalid and incomplete cases, there were 206 valid for further analysis.
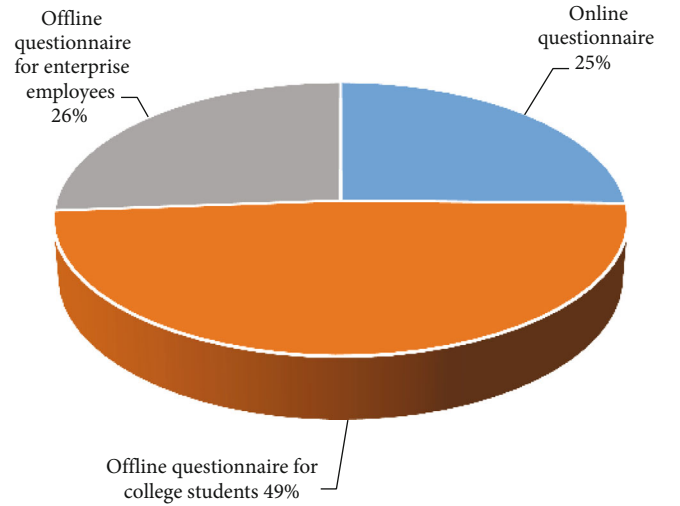
FIGURE 4: Distribution structure of questionnaires.

Among all the participants, 88 (42.7%) were men and *118* (*57.2%*) were women; ages ranged from 18 to 55 years ($M = 29.50$, SD = 5.41) (Figure 3 is the age distribution of the participants; Figure 4 shows the distribution structure of questionnaires).

3.2. Measures. All the measures were presented to the participants in Chinese. Participants rated the items on a *7*-point Likert scale ranging from *1* (completely disagree) to *7* (completely agree). The score of each dimension is the sum of the scores of all items in that dimension. The higher the score, the more prominent the characteristics of the dimension.

Cronbach's α coefficient was used to test the reliability of the questionnaires. The questionnaire data were input into SPSS for analysis. The calculation formula of Cronbach's α is shown in

$$\alpha = \frac{K}{K-1}\left(1 - \frac{\sum_{i=1}^{k}\sigma_i^2}{\sigma_T^2}\right), \tag{1}$$

TABLE 1: The items of motivation factors.

Variables	Number	Items
Achievability	AA1	I look forward to getting a sense of accomplishment from the feedback.
	AA2	I look forward to getting approval from the company for the feedback.
Self-interest	AB1	I give feedback so I can use it more easily in the future.
	AB2	I give feedback to solve my own problems.
Altruism	AC1	I hope that my feedback will prevent other users from experiencing the same problems.
	AC2	I hope that my feedback will improve the experience of other users.
	AC3	I hope the feedback information will be valuable for stakeholder's improvement.
	AC4	I hope the feedback information will be helpful for the product.
Influence	AD1	I want to have some influence on the company decision-making.
	AD2	I hope the product will better meet my expectations.
Rewards	AE1	I look forward to hearing from them after feedback.
	AE2	I expect to get some material reward after feedback.
	AE3	I expect to get some reputation after feedback.
Self-efficacy	BA1	I am confident in my ability to spot problems.
	BA2	I am confident in my ability to express my opinions.
	BA3	I am confident in my ability to operate the feedback system.
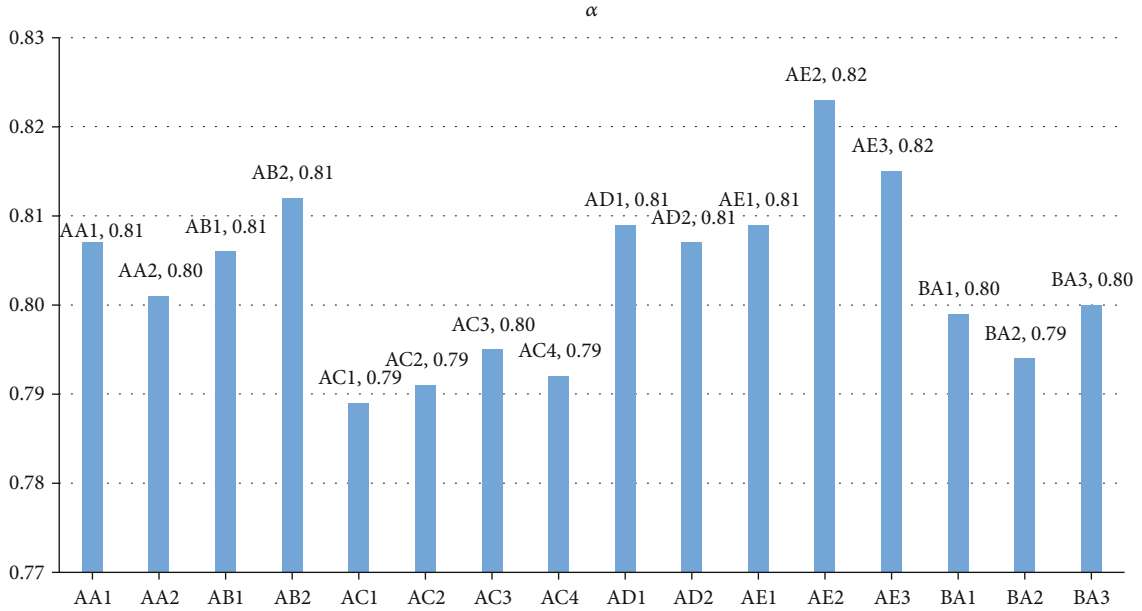
FIGURE 5: Cronbach's α coefficient of each item of motivation factor scale.

where K is the total number of items in the scale, σ_i^2 is the in-question variance of the score of item i, and σ_T^2 is the variance of the total score of all items.

Similarly, the questionnaire data were input into SPSS to verify the validity of the questionnaire, and the exploratory factor analysis method [41] was used to test the data and the formula is shown in

$$\mathrm{kmo} = \frac{\sum\sum_{i \neq j} r_{ij}^2}{\sum\sum_{i \neq j} r_{ij}^2 + \sum\sum_{i \neq j} r_{ij \cdot 1,2 \cdots k}^2}, \tag{2}$$

where r_{ij} is the simple correlation coefficient between variables.

3.2.1. Personality Traits.
We used the Big Five Personality Inventory (CBF-PI-B) developed by Wang et al. [42] to measure personality traits ($\alpha = 0.871$), which combined the language expression habits of Chinese people; it was adopted due to its good reliability and validity. Sample items include "I often meet with my friend," "I often feel nervous and uneasy," and "I often feel full of energy and vitality."

(a)

(b)

(c)

(d)

(e)

(f)
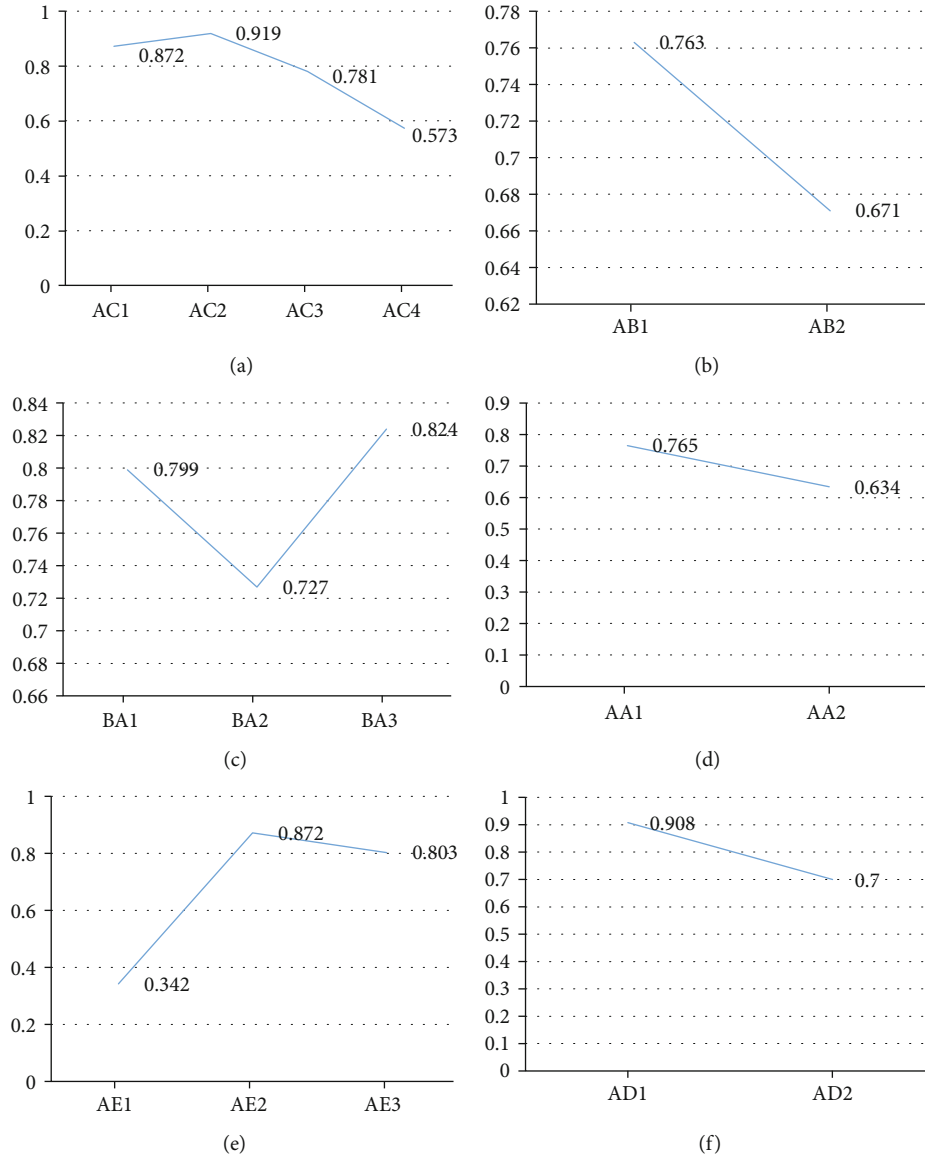
FIGURE 6: Factor load of motivation factors: (a) altruism, (b) self-interest, (c) self-efficacy, (d) achievability, (e) reward, and (f) influence.

3.2.2. Cognitive Styles. Cognitive styles ($\alpha = 0.865$) were measured using Soloman Learning Style questionnaire [40] in this study. Sample items for cognitive styles are "When things happen, I tend to react quickly on instinct and don't want to think too much," "When I recall done before, is mostly a mental picture in my mind," and "I tend to understand the details of things but not the overall structure."

3.2.3. Motivation Factors. The motivation factors were measured according to a number of relevant papers; the items are listed in Table 1. And the Cronbach α coefficient of each item is shown in Figure 5. The comprehensive Cronbach α coefficient was 0.788, which indicated a good reliability. Also, the questionnaire data were input into SPSS to verify the validity of the questionnaire, and the exploratory factor analysis method was used to test the data. The exploratory factors of each factor are shown in Figure 6. The KOM was 0.779, Sig was less than 0.01, and the cumulative inter-

pretation variance of the six factors reached *74.768%*. With the exception of some measurement errors, the sample validity can thus be considered to be good.

3.2.4. Feedback Willingness. Feedback willingness was measured according to Bhattacherjee [43]. Items include "I am willing to give feedback" and "I am going to give feedback in the future." The questionnaire used a 1-7 Likert scale, with 1 indicating very reluctant to give feedback and 7 indicating very willing to give feedback.

4. Results

4.1. Correlation Analysis. Correlation analysis [44, 45] was used to explore the correlation between personality traits, cognitive styles, and motivation factors. The correlation analysis formula used to calculate the correlation coefficient between any two variables is shown in Formula (3). The

Table 2: Descriptive statistics and correlations of study variables.

	M	SD	1	2	3	4	5	6	7	8	9	10	11
(1) Gender													
(2) Age	24.50	5.41	0.05										
(3) Neuroticism	27.33	7.65	0.16	0.09									
(4) Conscientiousness	34.89	5.24	0.13	0.16	0.05								
(5) Agreeableness	34.52	5.83	0.42*	-0.09	0.16	0.09							
(6) Openness	34.96	5.32	0.06	0.13	0.13	0.16	0.08						
(7) Extraversion	30.42	6.22	-0.05	0.18	0.12	0.09	0.03	0.13					
(8) Active/reflective	-1.88	4.33	0.18	0.12	0.06	0.13	0.11	0.09	0.24				
(9) Sensing/intuitive	2.97	4.28	-0.12	-0.10	-0.05	0.18	0.21	0.13	0.12	0.16			
(10) Visual/verbal	4.65	3.36	0.16	0.09	0.18	0.12	-0.11	0.14	0.21	0.03	0.07		
(11) Sequential/global	0.89	4.85	-0.08	0.12	0.12	-0.10	0.05	0.11	0.01	-0.04	0.12	0.13	
(12) Achievability	4.13	1.55	-0.05	0.18	0.16	0.09	0.12	0.12	0.23**	0.01	-0.03	-0.06	0.03
(13) Self-interest	5.88	0.92	0.53*	-0.15	-0.08	0.12	0.02	-0.03	0.08	-0.06	0.24**	0.03	0.13
(14) Altruism	4.56	1.23	0.49*	-0.10	-0.05	0.18	0.12	0.13	0.22**	0.23**	-0.16	0.11	0.03
(15) Influence	4.96	1.24	-0.31	0.11	0.10	0.10	-0.03	-0.10	0.12	0.08	0.04	0.06	0.12
(16) Rewards	4.98	1.13	0.05	0.07	0.12	-0.10	-0.11	0.11	0.01	-0.04	0.09	-0.06	-0.16
(17) Self-efficacy	4.99	1.54	0.16	0.09	-0.30**	0.10	0.08	0.11	0.44**	0.18	-0.00	0.13	0.10

Note. $N = 206$. $^*p < 0.05$. $^{**}p < 0.01$.

Table 3: The results of linear regression analysis.

Variables	Achievability	Altruism		Self-interest	Self-efficacy
Model	1	2	3	4	5
Intercept	2.69**	4.34**	3.33**	5.65**	3.64**
Extraversion	0.05*		0.04*		0.06**
Neuroticism					-0.02
Sensing/intuitive				0.06*	
Active/reflective		0.07*			

Note. $N = 206$. $^*p < 0.05$. $^{**}p < 0.01$.

questionnaire data were imported into SPSS for correlation analysis using the Pearson correlation coefficient [46–48]. Table 2 shows means, standard deviations, and correlations for the study variables.

$$r = \frac{\sum XY - (((\sum X)(\sum Y))/n)}{\sqrt{\left(\sum X^2 - ((\sum X)^2/n)\right)\left(\sum Y^2 - ((\sum Y)^2/n)\right)}}$$
$$= \frac{E(XY) - E(X)E(Y)}{\sqrt{D(X)}\sqrt{D(Y)}}, \quad (3)$$

where X and Y are variables and n is the number of the variables.

Through the correlation analysis, the five groups of variables were correlated, which were neuroticism, extraversion on self-efficacy, extraversion on achievability, extraversion on altruism, sensing/intuitive on self-interest, and active/reflective on altruism.

4.2. Regression Analysis. We further explored the strength of the relationship of the five correlated groups of variables through linear regression analysis [49, 50]. The calculation formula of linear regression analysis is shown in Formula (4) [51, 52]. Table 3 shows the results of linear regression analysis. The data from Table 3 can answer questions 1 and 2. We can infer that the users with extraversion personality trait may be more likely to be positively motivated by self-efficacy, altruism, and achievability. The users with neuroticism personality trait may be more likely to be negatively motivated by self-efficacy. The users with sensing/intuitive cognitive style may be more likely to be positively motivated by self-interest.

$$y = \beta_0 + \beta_1 x_1 + \beta_2 x_2 + \cdots + \beta_p x_p + \varepsilon, \quad (4)$$

where y is the variable being interpreted, x is the explanatory variable, ε is constant, and β is the coefficient.
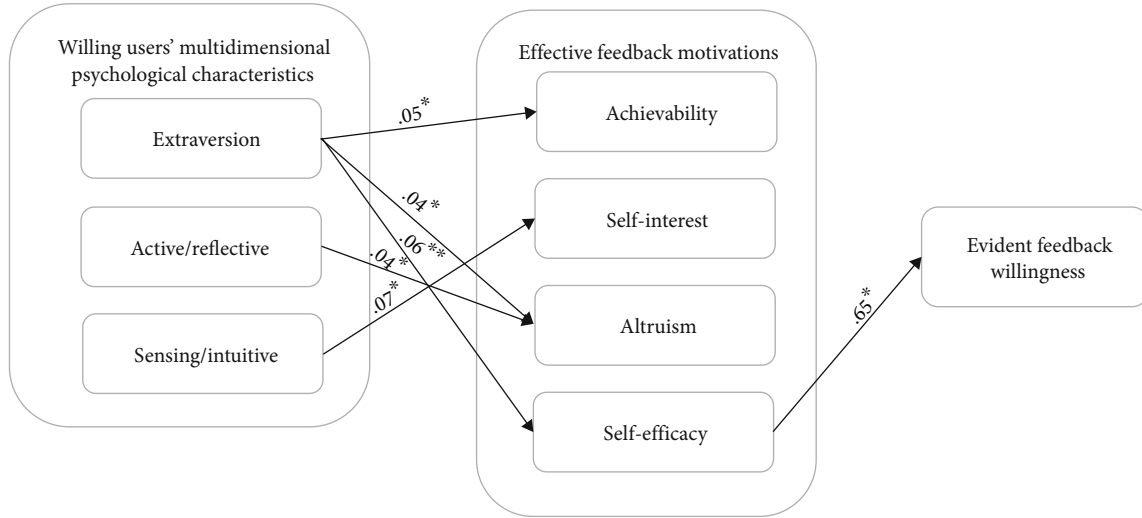
FIGURE 7: The final model. Note: $^*p < 0.05$; $^{**}p < 0.01$.

4.3. Relationship between Motivation Factors and Feedback Willingness. We conducted structure equation analyses to test Hypotheses 1–6 [41, 53]. The data were imported into AMOS 22.0 for analysis [54, 55]. According to the analysis results, CMIN/DF was *2.06* which met the required standard (ranging from *1* to *5*), GFI > 0.9 (the calculation can be seen in Formula (5)) [56], AGFI > 0.8, RMSEA < 0.08, and CFI > 0.9 [51]. We can see that all the absolute fitting indexes of the model met the required standard [57, 58], indicating that the model has a good fitting degree.

$$\text{GFI} = 1 - \frac{F}{F_b}, \tag{5}$$

where y is the F is the value of the fitting function and F_b is the value of the fitting function obtained when $\Sigma = 0$.

The results of structure equation analyses showed that only the path from self-efficacy to feedback willingness (estimate = 0.65, $p = 0.004 < 0.05$) meets the required standard [41, 59]. Therefore, Hypothesis 6 was supported.

4.4. The Final Model of User Feedback Willingness. Based on the results of correlation analyses, regression analyses, and structural equation analyses, the final model was obtained. Figure 7 demonstrates the path from "willing users' multidimensional psychological characteristics" to "effective feedback motivations" to "evident feedback willingness" with all the supported hypotheses. The loading factors of variables in the final model were marked on each arrow.

As we can see from Figure 7, the only one critical path was obtained, namely, "extraversion"–"self-efficacy"–"evident feedback willingness," which indicates that users with extroverted trait are more likely motivated by self-efficacy and thus have evident feedback willingness.

5. Discussion

In this study, we aimed to provide evidence concerning the influence of multidimensional psychological characteristics

(including personality traits and cognitive styles) on feedback willingness, by examining motivation factor as a mediator of this relationship. We separately investigated the influence of psychological characteristics on motivation factors and which motivators can produce evident feedback willingness. The results show that both personality traits and cognitive styles can have a significant impact on feedback motivation factors, and there are differences among different traits and styles.

The results also show that self-efficacy may be the only evident feedback motivation to encourage useful feedback information. Hypothesis 6 is supported. At last, the critical path from "extraversion" to "self-efficacy" to "evident feedback willingness" is obtained, which indicates that the willing users with extraversion trait are more likely motivated by self-efficacy and thus have evident feedback willingness.

5.1. Theoretical Implications. We have contributed to the literature in several ways. First, we have systematically investigated the effect of personality traits on user feedback willingness by considering as many motivation factors as possible, which is in contrast with previous research that did not consider motivation factors [11] or only consider single motivation factor [12]. Our research discovered the personality traits of the willing users and evident feedback motivation factors, which provided theoretical support for the establishment of an effective feedback platform. The effective incentives of feedback platforms can be designed based on evident feedback motivation factors; the preference of the feedback interaction can be designed based on the personality traits of willing users. The results of our research showed that the willing users with extraversion trait were more likely to post useful feedback information, which is consistent with the research results on the influence of personality on information sharing behavior. Related research indicated that extroverts were more likely to express themselves and talk to their supervisors [44], or extroverts were more likely to engage in online activities related to comments and retweets [37].

Second, we extended the research of the influence of cognitive styles on behavior motivations. Previous researchers have studied the effect of cognitive styles on some online behaviors, such as multimedia perception [13], online information searching [14], and creative behavior [15], but few studied the effect on behavior motivations. The results of our research showed that the cognitive styles can influence the motivation factors and there are differences between different styles in the field of user feedback. Our research showed that sensing/intuitive style is more likely motivated by self-interest factor and active/reflective style is more likely motivated by altruism factor.

5.2. Practical Implications. These results can provide some practical guidance for enterprises. Our results showed that the users with extraversion trait are more willing to post useful feedback information, so enterprises can focus on extroverts to participate in online or offline user survey when they want to improve their products or service. For example, they can invite extroverts to be participants for interview, focus groups, questionnaires, etc. Enterprises also can send online feedback questionnaire links and feedback request emails to export-oriented users. In contrast to previous extensive and random user surveys, which invited a large number of users who were not willing to provide useful feedback, such a screening of users can save costs and ensure the effectiveness of the information obtained. Our results also showed that what motivated extroverts to post useful feedback information was self-efficacy, and then, enterprises can pay more attention to establish incentives based on self-efficacy.

5.3. Limitations and Directions for Future Research. There are two main limitations in this study. First, as we used a cross-sectional research design, we cannot infer causality between the study variables. Second, our research only concluded that the users with extraversion trait are more likely motivated by self-efficacy, while for enterprises, they may do not know how to find the extraverts and how to establish incentives based on self-efficacy. Therefore, we will study how to identify the personality traits of users based on big data technology and discuss how to establish effective incentives based on self-efficacy motivation factor in user feedback platforms.

Data Availability

The simulation experiment data used to support the findings of this study are available from the corresponding author upon request.

Conflicts of Interest

The authors declare that there are no conflicts of interest regarding the publication of this paper.

Acknowledgments

References

[1] M. R. Itzel, P. Anna, and S. S. Renata, "An ontology of online user feedback in software engineering," *Applied Ontology*, vol. 10, no. 3-4, pp. 297–330, 2015.

[2] C. E. Shannon, "A mathematical theory of communication," *The Bell system technical journal.*, vol. 27, no. 3, pp. 379–423, 1948.

[3] J. Hu, H. Zhang, L. Liu, X. Zhu, C. Zhao, and Q. Pan, "Convergent multiagent formation control with collision avoidance," *IEEE Transactions on Robotics*, vol. 36, no. 6, pp. 1805–1818, 2020.

[4] Y. Zhao, M. Peng, and Z. Dan, "Research on public opinion feedback mechanism under "Internet plus" – a case study of Fuxin City," *Economic Outlook the Bohai Sea*, vol. 11, pp. 127-128, 2018.

[5] E. Goodman, M. Kuniavsky, and A. Moed, *Observing the User Experience: A Practitioner's Guide to User Research*, Tsinghua University Press, Beijing, 2nd Edition edition, 2015.

[6] D. Martens and W. Maalej, "Towards understanding and detecting fake reviews in app stores," *Empirical Software Engineering*, vol. 24, no. 6, pp. 3316–3355, 2019.

[7] L. Dong, M. N. Satpute, W. Wu, and D.-Z. Du, "Two-phase multidocument summarization through content attention-based subtopic detection," *IEEE Transactions on Computational Social Systems*, pp. 1–14, 2021.

[8] S. Bajaj, N. Garg, and S. K. Singh, "A novel user-based spam review detection," *Procedia Computer Science*, vol. 122, pp. 1009–1015, 2017.

[9] S. J. Motowidlo, W. C. Borman, and M. J. Schmit, "A theory of individual differences in task and contextual performance," *Human Performance*, vol. 10, no. 2, pp. 71–83, 1997.

[10] S. J. Bas and A. B. Whinston, "Research commentary, introducing a third dimension in information systems design—the case for incentive alignment," *Information System Research*, vol. 12, no. 3, pp. 225–239, 2001.

[11] I. Adaji, K. Oyibo, and J. Vassileva, *Understanding Low Review Ratings in Online Communities: A Personality Based Approach*, pp. 34–42, 2018.

[12] M. Yasin, L. Porcu, M. T. Abusharbeh, and F. Liébana-Cabanillas, "The impact of customer personality and online brand community engagement on intention to forward company and users generated content: Palestinian banking industry a case," *Economic Research*, vol. 33, no. 1, pp. 1985–2006, 2020.

[13] S. R. Gulliver and G. Ghinea, "Cognitive style and personality: impact on multimedia perception," *Online Information Review*, vol. 34, no. 1, pp. 39–58, 2013.

[14] M. Sangari and M. Zerehsaz, "Collaborative information seeking in digital libraries, learning styles, users' experience, and task complexity," *Journal of Information Science Theory and Practice*, vol. 8, no. 4, pp. 55–66, 2020.

[15] L. M. Tonetto, P. G. Brust-Renck, S. Ruecker, F. S. Fogliatto, and D. A. Pacheco, "Differences in thinking styles across professionals with different academic backgrounds when developing a product," *Architectural Engineering and Design Management*, vol. 17, no. 1-2, pp. 3–16, 2021.

[16] S. Yasmeen, I. Batool, and R. S. Bajwa, "Learning styles and employee creative behavior; an exploration through cognitive styles," *Journal of Business and Social Review in Emerging Economies*, vol. 6, no. 1, pp. 43–54, 2020.

[17] A. Bandura, "Self-efficacy mechanism in human agency," *American psychologist*, vol. 37, no. 2, p. 122, 1982.

[18] F. M. Shipman and C. C. Marshall, "Are user-contributed reviews community property? Exploring the beliefs and practices of reviewers," in *In Proceedings of the 5th annual acm web science conference*, pp. 386–395, New York, May 2013.

[19] C. Dellarocas, G. Gao, and R. Narayan, "Are consumers more likely to contribute online reviews for hit or niche products?," *System*, vol. 27, no. 2, pp. 127–158, 2010.

[20] P. Pai and H. T. Tsai, "Reciprocity norms and information-sharing behavior in online consumption communities: an empirical investigation of antecedents and moderators," *Information and Management*, vol. 53, no. 1, pp. 38–52, 2016.

[21] R. Jiang, Z. Fei Ma, and J. Yang, "An assessment model for cloud service security risk based on entropy and support vector machine," *Concurrency and Computation-Practice & Experience*, 2021.

[22] Y. Tong, X. Wang, C. H. Tan, and H. H. Teo, "An empirical study of information contribution to online feedback systems: a motivation perspective," *Information and Management*, vol. 50, no. 7, pp. 562–570, 2013.

[23] D. H. Zhu, Z. J. Zhang, Y. P. Chang, and S. Liang, "Good discounts earn good reviews in return? Effects of price promotion on online restaurant reviews," *International Journal of Hospitality Management*, vol. 77, pp. 178–186, 2019.

[24] M. M. Wasko and S. Faraj, "Why should I share? Examining social capital and knowledge contribution in electronic networks of practice," *MIS Quarterly*, vol. 29, no. 1, pp. 35–57, 2005.

[25] D. S. Sundaram, K. Mitra, and C. Webster, "Word-of-mouth communications, a motivational analysis," *Association for Consumer Research (U.S.)*, vol. 25, no. 1, pp. 527–540, 1998.

[26] G. W. Allport, "Personality: a psychological interpretation," *American Journal of Sociology*, vol. 45, no. 1, pp. 48–50, 1937.

[27] C. Ju, Q. Gu, Y. Fang, and F. Bao, "Research on user influence model integrating personality traits under strong connection," *Sustainability*, vol. 12, no. 6, p. 2217, 2020.

[28] F. Wang, J. Zhang, S. Wang, S. Li, and W. Hou, "Analysis of driving behavior based on dynamic changes of personality states," *International Journal of Environmental Research and Public Health*, vol. 17, no. 430, 2020.

[29] R. R. McCrae and O. P. John, "An introduction to the five-factor model and its applications," *Journal of Personality*, vol. 60, no. 2, pp. 175–215, 1992.

[30] L. R. Goldberg, "An alternative "description of personality", the big-five factor structure," *Journal of Personality & Social Psychology*, vol. 59, no. 6, pp. 1216–1229, 1990.

[31] N. Cabrera, W. C. Collins, and J. F. Salgado, "Determinants of individual engagement in knowledge sharing," *The International Journal of Human Resource Management*, vol. 17, no. 2, pp. 245–264, 2006.

[32] B. Gupta, "Role of personality in knowledge sharing and knowledge acquisition behavior," *Journal of the Indian Academy of Applied Psychology*, vol. 34, no. 1, pp. 143–149, 2008.

[33] T. Amiel and S. L. Sargent, "Individual differences in Internet usage motives," *Computers in Human Behavior*, vol. 20, no. 6, pp. 711–726, 2004.

[34] J. Alexander and M. A. Tate, *Web Wisdom: How to Evaluate and Create Information on the Web*, Erlbaum, Mahwah, NJ, 1999.

[35] H. G. Chen, *Principles of Management*, East China University of Science and Technology Press, Shanghai, 2013.

[36] X. S. Li, N. Xu, J. X. Zhang, and M. J. Zhou, "The relationship between localized personality and knowledge sharing behavior: the mediating role of self-efficacy and social value," *Psychological Exploration*, vol. 35, no. 2, pp. 153–157, 2015.

[37] E. E. Hollenbaugh and A. L. Ferris, "Facebook self-disclosure: examining the role of traits, social cohesion, and motives," *Computers in Human Behavior*, vol. 30, no. 1, pp. 50–58, 2014.

[38] P. M. Caligiuri, "The big five personality characteristics as predictors of expatriate's desire to terminate the assignment and supervisor-rated performance," *Personnel Psychology*, vol. 53, no. 1, pp. 67–88, 2010.

[39] Y. Liu and D. Ginther, "Cognitive styles and distance education," *Online Journal of Distance Learning Administration*, vol. 2, no. 3, pp. 1556–3847, 1999.

[40] R. M. Felder and L. K. Silverman, "Learning and teaching styles in engineering education," *Engineering Education*, vol. 78, no. 7, pp. 674–681, 1988.

[41] J. Yin, W. Lo, S. Deng, Y. Li, Z. Wu, and N. Xiong, "Colbar: a collaborative location-based regularization framework for QoS prediction," *Information Sciences*, vol. 265, pp. 68–84, 2014.

[42] M. C. Wang, X. Y. Dai, and S. Q. Yao, "China's big five personality questionnaire preliminary establishment III: short form and test reliability and validity of version," *Chinese Journal of clinical psychology*, vol. 19, no. 4, pp. 454–457, 2011.

[43] A. Bhattacherjee, "Understanding information systems continuance: an expectation-confirmation model," *MIS quarterly*, pp. 351–370, 2001.

[44] J. Y. Wei, J. T. Yu, and L. Lu, "Research on the influence of extroverted personality traits on upward knowledge and skill sharing," *Science and technology management research*, vol. 34, no. 2, pp. 84–92, 2014.

[45] Y. Jing, H. Hu, S. Guo, X. Wang, and F. Chen, "Short-term prediction of urban rail transit passenger flow in external passenger transport hub based on LSTM-LGB-DRS," *IEEE Transactions on Intelligent Transportation Systems*, vol. 22, no. 7, pp. 4611–4621, 2021.

[46] W. Shu, K. Cai, and N. Xiong, "Research on strong agile response task scheduling optimization enhancement with optimal resource usage in green cloud computing," *Future Generation Computer Systems*, vol. 124, pp. 12–20, 2021.

[47] W. Fang, X. Yao, X. Zhao, J. Yin, and N. Xiong, "A stochastic control approach to maximize profit on service provisioning for mobile cloudlet platforms," *IEEE Transactions on Systems, Man, and Cybernetics: Systems*, vol. 48, no. 4, pp. 522–534, 2018.

[48] W. Wei, X. Xia, W. Marcin, X. Fan, and R. Damasevicius, "Multi-sink distributed power control algorithm for cyber-physical-systems in coal mine tunnels," *Computer Networks*, vol. 161, pp. 210–219, 2019.

[49] J. Hu, H. Zhang, Z. Li, C. Zhao, Z. Xu, and Q. Pan, "Object traversing by monocular UAV in outdoor environment," *Asian Journal of Control*, 2020.

[50] Z. Yang, P. Xu, W. Wei, G. Gao, N. Zhou, and G. Wu, "Influence of the crosswind on the pantograph arcing dynamics," *IEEE Transactions on Plasma Science*, vol. 48, no. 8, pp. 2822–2830.

[51] B. Li, Y. Liu, A. Zhang, W. Wang, and S. Wan, "A survey on blocking technology of entity resolution," *Journal of Computer Science and Technology*, vol. 35, no. 4, pp. 769–793, 2020.

[52] B. Lin, F. Zhu, J. Zhang et al., "A time-driven data placement strategy for a scientific workflow combining edge computing

and cloud computing," *IEEE Transactions on Industrial Informatics*, vol. 15, no. 7, pp. 4254–4265, 2019.

[53] J. Yang, N. Xiong, A. V. Vasilakos et al., "A fingerprint recognition scheme based on assembling invariant moments for cloud computing communications," *IEEE Systems Journal*, vol. 5, no. 4, pp. 574–583, 2011.

[54] N. Xiong, A. V. Vasilakos, J. Wu et al., "A self-tuning failure detection scheme for cloud computing service," in *2012 IEEE 26th International Parallel and Distributed Processing Symposium*, Shanghai, China, May 2012.

[55] Y. Zeng, N. Xiong, J. H. Park, and G. Zheng, "An emergency-adaptive routing scheme for wireless sensor networks for building fire hazard monitoring," *Sensors*, vol. 10, no. 6, pp. 6128–6148, 2010.

[56] H. Li, J. Liu, R. W. Liu, N. Xiong, K. Wu, and T. Kim, "A dimensionality reduction-based multi-step clustering method for robust vessel trajectory analysis," *Sensors*, vol. 17, no. 8, p. 2017, 2017.

[57] Y. Qu and N. Xiong, "RFH: a resilient, fault-tolerant and high-efficient replication algorithm for distributed cloud storage," in *RFH: A Resilient, Fault-Tolerant and High-Efficient Replication Algorithm for Distributed Cloud Storage*, pp. 520–529, Pittsburgh, PA, USA, September 2012.

[58] M. Wu, L. Tan, and N. Xiong, "A structure fidelity approach for big data collection in wireless sensor networks," *Sensors*, vol. 15, no. 1, pp. 248–273, 2015.

[59] Q. Zhang, C. Zhou, Y. C. Tian, N. Xiong, Y. Qin, and B. Hu, "A fuzzy probability Bayesian network approach for dynamic cybersecurity risk assessment in industrial control systems," *IEEE Transactions on Industrial Informatics*, vol. 14, no. 6, pp. 2497–2506, 2018.

Research Article

Study on Announcement Effect of Stock Repurchase from the Perspective of Configuration Analysis

Hong Bing Wang [ID],[1] **Ai Hua Jin** [ID],[2] **and Hai Yun Yu** [ID][3]

[1]*Business College, Wuxi Vocational College of Science and Technology, Wuxi 214101, China*
[2]*Business College, Jiangsu Vocational College Information Technology, Wuxi 214153, China*
[3]*Business College, Jiangnan University, Wuxi 214122, China*

Correspondence should be addressed to Ai Hua Jin; 100498@jsit.edu.cn

This paper takes the stock repurchase cases in 2018-2019 after the promulgation of the New Company Law as the research object. Using the qualitative comparative analysis method and PSO-ICA-GARCH model, we analyze the influencing factors of the stock repurchase announcement market reaction. Through the analysis of the degree of premium (DP), repurchase ratio (RR), natural logarithm of total assets (LAS), return on net assets (ROE), top 10 shareholder equity ratio (CR10), and executive shareholding ratio (MSL), it is found that the paths of high CAR stock repurchase effect include repurchase clause-oriented type and centralization-proportional matching type; the path of nonhigh CAR stock repurchase effect includes size-premium limit type, profit-proportion limit type, and repurchase clause limit type. Compared with GARCH model, it has higher separation accuracy and more accurate model prediction effect.

1. Introduction

At present, stock repurchase has gradually become a tool and means for listed companies to manage market value and safeguard the interests of shareholders. The stock repurchase announcement represents a listed company's recognition of the value of its own stock and is also a "commitment" to market investors [1]. Whether stock repurchase can achieve the stability of stock prices and promote the return of undervalued stock prices to value is a question worthy of study [2, 3].

The main multivariate volatility models include the BEKK model and constant value condition correlation number (CCC-GARCH) model [4] and dynamic condition correlation coefficient (DCC-GARCH) model [5]. A new GICA-GARCH model is proposed, which combines ICA and the multivariate GARCH (MGARCH) model [6].

This paper uses the method of qualitative comparative analysis to study 240 stock repurchase cases in China's Shanghai and Shenzhen markets from 2018 to 2019 from the perspective of configuration analysis and explores the interaction and mutual matching relationship between the

influence factors of the stock repurchase announcement effect. Through the configuration analysis of the effect of high and nonhigh cumulative excess return (CAR) stock repurchase announcements, it provides a basis and reference for the behavior selection of securities regulatory authorities, listed companies, and investors.

The rest of this paper is organized as follows: Section 2 discusses the effect analysis of the stock repurchases announcements. The research on the stock repurchase announcement from the perspective of configuration analysis is discussed in Section 3. Section 4 shows the data analysis, and Section 5 concludes the paper with summary and future research directions.

2. Effect Analysis of the Stock Repurchases Announcements

Since the launch of stock trading, the legal system and operating mechanism of the Chinese securities market have been continuously improved and improved [7]. Looking back at the history of the securities market, the development of the stock repurchase market can be divided into three stages

TABLE 1: The development of stock repurchase of listed companies.

Development stage	Basic features
Before the split share reform (1992-2004)	Exception management is implemented, repurchase is limited to nontradable shares, and only "write-off repurchase for the purpose of reducing the company's share capital" and "company merger repurchase" are allowed. Only agreement repurchase is allowed. A total of 15 share repurchases occurred during the period [8].
In the split share reform (2005-2007)	The repurchase has expanded from nontradable shares to tradable shares, and the scope of implementation has been expanded to four situations such as capital reduction, merger, share awards, and division objections. The repurchase agreement is mainly based on repurchase agreements, and there are fewer centralized auction repurchases in the open market. A total of 41 share repurchases occurred during the period.
After the split share reform (2008—)	Further relax the restrictions on repurchase, especially after the revision of the company law in 2018, promote the marketization of share repurchase, regulate information disclosure, and increase transparency. Stock repurchases are mainly based on centralized bidding in the open market, with less agreement repurchase. A total of 141 share repurchases occurred during the period from 2008 to 2017, and a total of 755 share repurchases occurred during the period from 2018 to 2019.

before, during, and after the equity division reform. The basic characteristics and performance of each stage are shown in Table 1.

China's stock repurchase still has the following shortcomings: (1) The market adaptability of existing research is insufficient. After the completion of the share-trading reform in China, the marketization process of stock repurchase has continued to advance [9]. Especially in recent years, with the construction of relevant legal systems, market mechanisms have been continuously improved, and stock repurchase is in a new historical stage. Most of the existing stock repurchase studies are based on nontradable share repurchase, and they are case studies of agreement repurchase, which are sporadic and scattered [10]. (2) There is insufficient innovation in research methods. In addition to qualitative analysis and research, it mainly uses traditional regression analysis methods to carry out quantitative empirical research [11]. Based on the "net effect" thinking, it is assumed that the impact of each variable is "linear and additive" to calculate each independent variable. There are non-overlapping contributions to the variation of the dependent variable; however, estimation techniques designed for linear additive models often have shortcomings in estimating complex interaction effects [12]. In fact, the announcement effect of stock repurchase must be an economic phenomenon in which multiple variables are synergistic and combined.

The main reasons for the stock repurchase of listed companies include the following: (1) prevent the control from falling; (2) carry out earnings management; (3) adjust the capital structure; and (4) signal transmission [13]. Generally speaking, the announcement of a stock repurchase by a listed company can promote a significant increase in the company's stock price and bring a positive market response [14].

The factors that affect the effect of stock repurchase announcements can be summarized into three categories: (1) corporate governance: the main research variables are equity concentration, senior management's shareholding ratio, management equity pledge [15], etc.; (2) financial status: the main research variables include company size, book value, debt ratio, price-earnings ratio, and capital expenditures [16]; and (3) repurchase terms: the main research variables are repurchase ratio, premium rate, etc. For example, based on the stock repurchase data in the United States, Canada, and other markets [17], it is found that the repurchase ratio, the repurchase premium ratio, the degree of change in the asset-liability ratio, the management shareholding ratio, and the cumulative excess return are positively correlated. Research from China's Shanghai and Shenzhen markets found that executive shareholding ratio, proposed repurchase ratio, management equity pledge ratio, equity concentration, and growth ability all have a positive relationship with the repurchase effect [18].

3. Research on the Stock Repurchase Announcement from the Perspective of Configuration Analysis

3.1. The Framework Design of the Stock Repurchases Announcements Effect. This article intends to integrate factors such as corporate governance, financial status, and repurchase terms and explore the multiple concurrent path factors and causal complex mechanisms of the difference in the effect of different companies' stock repurchase announcements, that is, how to link the various antecedent conditional variables and how to match the stock repurchase, the purchase announcement effect.

The framework of the stock repurchases announcements effect is shown in Figure 1. We analyze the effect of announcements by synergizing the size of the company, profitability, premium level, governance structure, repurchase ratio, and equity concentration.

According to the public company's repurchase announcement, the purpose of stock repurchase is to promote stock prices to rise above the market. This article chooses "cumulative excess return (CAR)" as the measurement indicator of the announcement effect, that is, the explained outcome variable. This article also selects the degree of premium (DP), repurchase ratio (RR), natural logarithm of total assets (LAS), return on net assets (ROE), top 10 shareholder equity ratio (CR10), and executive shareholding ratio (MSL) as statistical data [19].
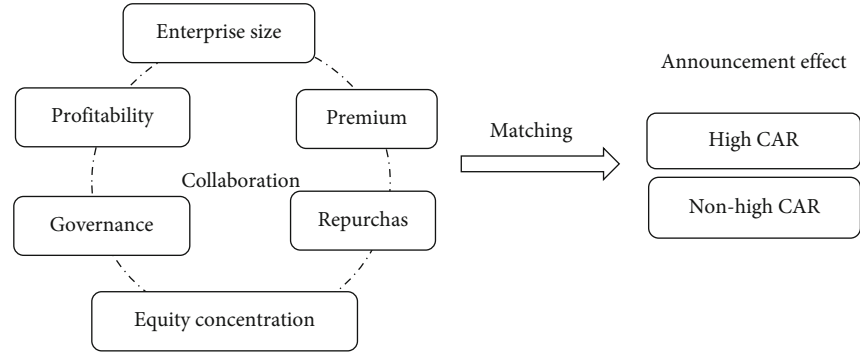
FIGURE 1: The framework design of the stock repurchases announcements effect.

The formulas for the degree of premium (DP) and repurchase ratio (RR) are as follows:

$$DP = \frac{P_n}{P_q} \times 100\%, \tag{1}$$

$$RR = \frac{S_n}{S_q} \times 100\%, \tag{2}$$

in which P_n is the proposed repurchase price (maximum price), P_q is the closing price on the trading day before the announcement, S_n is the proposed repurchase quantity (upper limit), and S_q is the total share capital, for the Buyback Clause. For such variables, indicators that have a substantial impact on repurchase should be selected. There are many terms in the announcement of the stock repurchase of listed companies, including the purpose and purpose of the share repurchase, the type, quantity and proportion of the shares to be repurchased, price (total amount or pricing principle), time limit, the method of repurchasing shares, the source of funds, and whether the relevant shareholders have plans to reduce their holdings. The proposed repurchase price and the proposed repurchase quantity are the key terms, which are substantively influential terms, and are also the core differences between the terms of the stock repurchase announcements of different listed companies.

3.1.1. Natural Logarithm of Total Assets (LAS) and Return on Net Assets (ROE).
For financial position variables, indicators can usually be selected from two aspects of enterprise size and profitability. Financial status is directly expressed as the level and structure of a company's assets, liabilities, and owner's equity. It is also indirectly affected by the company's asset quality and profitability. It is a combination of static asset scale and dynamic profitability.

3.1.2. Top 10 Shareholder Equity Ratio (CR10).
For corporate governance variables, you can usually choose indicators from two aspects: equity concentration and governance structure. The reasons are as follows: Modern corporate governance is based on the separation of ownership and management rights. Based on the classic principal-agent theory, equity concentration and governance structure are the core reflections of corporate governance.

3.1.3. Senior Management's Shareholding Ratio (MSL).
Senior management's shareholding ratio includes the following: whether the major shareholders are substantively participating in the company's operation and management and the way they participate, whether the company's directors, supervisors, senior managers, etc. hold shares, the size of the shareholding ratio, and the "separation of the two rights." The coordination method of the organization and operation of the subordinate company has a significant impact and is the main aspect of the corporate governance structure.

3.2. PSO-ICA-GARCH Model.
The GARCH model is a regression model for financial data, expressed as

$$r_t = c_1 + \sum_{i=1}^{R} \varnothing_i r_{t-i} + \sum_{j=1}^{M} \varnothing_j \epsilon_{t-j} + \epsilon_t, \tag{3}$$

$$\epsilon_t = u_t \sqrt{h_t}, \tag{4}$$

$$h_t = k + \sum_{i=1}^{q} G_i h_{t-i} + \sum_{i=1}^{p} A_i \epsilon_{t-i}^2, \tag{5}$$

in which h_t is the conditional variance, u_t is an independent and identically distributed random variable, h_t and u_t are independent of each other, and u_t is a standard normal distribution [20].

The GARCH model has certain problems. Some scholars have proposed the O-GARCH model and the ICA-GARCH model. When modeling the multivariate volatility of stock returns, the O-GARCH model assumes that the main components are weakly correlated. In empirical analysis, the problem of inconsistency between the forecasting effect and the actual situation will often arise. The ICA algorithm in the ICA-GARCH model has low convergence accuracy and is easy to fall into the problem of local optimization. Combining the PSO-ICA algorithm with the GARCH model to construct the PSO-ICA-GARCH model can effectively overcome the above problems.

The PSO-ICA-GARCH model first uses the PSO-ICA algorithm to decompose the stock return sequence into mutually independent components, that is, if there is a matrix and a d-dimensional vector $s_t = (s_{1t}, s_{2t}, \cdots\cdots, s_{dt})$, for each moment t, s_{it} and $s_{jt} (i \neq j)$ are all independent of
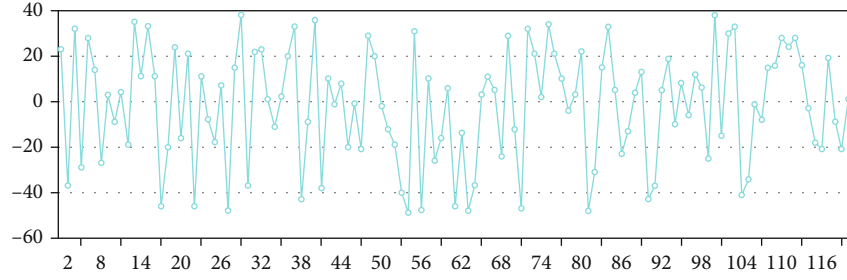
Figure 2: CAR value of 120 samples (%).

each other, so that Equation (6) holds. Then, s_t is said to be d-independent components of r_t. At this time, the conditional covariance matrix V_t is a diagonal matrix, and the PSO-ICA algorithm assumes that the independent components follow a non-Gaussian distribution, which is more in line with the characteristics of the financial time return sequence data, then performs unit GARCH modeling on each independent component s_{it}, and finally obtains the conditional covariance matrix H_t of the return sequence r_t. The PSO-ICA-GARCH model is as follows:

$$r_t = As_t, \tag{6}$$

$$s_{it} = v_{it}\alpha_{it}, \tag{7}$$

$$v_{it}^2 = \omega + \alpha s_{i,t-1}^2 + \beta v_{i,t-1}^2, \tag{8}$$

in which, A is the mixing matrix, $\{s_{it}\}$ is the independent component, and v_{it} is the variance of the independent component $\{s_{it}\}$.

Qualitative comparative analysis (QCA) is based on technical methods such as set and Boolean algebra and combines the advantages of qualitative and quantitative research methods to explore how the interaction between antecedent conditions.

Traditional regression analysis adopts the "net effect" thinking, which believes that each variable has the autonomous or independent ability to affect the level, intensity, or probability of the dependent variable. But when independent variables are correlated with each other, the unique effect of a single variable may be masked by the correlated variable. In fact, the antecedent conditions of social phenomena are generally interdependent and nonindependent, and cause and effect are asymmetry. Therefore, to explain the causes of social phenomena, we need to adopt a holistic and combined approach. Qualitative comparative analysis can find the configuration relationship between multiple factors and the same goal by different routes.

From a configuration perspective, factors such as repurchase conditions, financial status, and corporate governance have no independent influence on the stock price of listed companies that implement repurchase, but they play a role in linkage and matching. Various factors may strengthen or offset each other. It is more practical and exploratory to test the "joint effect" of different conditional factors on the realization of stock repurchases goals, that is, what we need

to care about is the collective relationship between different configurations and result effects.

4. Data Analysis

4.1. Data Source and Data Calibration. This article uses the fsQCA3.0 software for data processing. Using python software, we collected and sorted out 755 stock repurchase announcements in 2018 and 2019 from the website (http://www.eastmoney.com). Because stock repurchase must be a stock case where all the processes have been completed, the following samples should be excluded: (1) those who have not completed the repurchase (including the suspension of implementation) cases; (2) repurchase cases that are only at the stage of the board of directors plan or passed at the general meeting of shareholders but did not formally initiate repurchase; (3) repurchase cases in nonpublic market such as agreements; and (4) repurchase cases announced before the promulgation of the new "Company Law." Finally, this paper obtains 240 public market stock repurchases that have been implemented.

This article takes the announcement date as the origin and adds up the daily excess returns for a total of 16 days from 5 trading days before the origin to 10 trading days after the origin to get the cumulative excess return "$CAR_{[-5,10]}$."

Basic data such as daily excess return rate, total assets, return on net assets, top 10 shareholder equity ratios, and senior management shareholding ratios are taken from the Xenophon database and processed manually according to research requirements. The data on the degree of premium and the repurchase ratio are calculated based on the repurchase announcement.

Qualitative comparative analysis methods need to calibrate different research variables, that is, the process of assigning collective membership to cases on the basis of considering the differences between cases. The three anchor points (or critical values) of full affiliation, no affiliation, and crossover point of calibration need to be determined according to the basic theory and actual knowledge of the research. The case set processed by the calibration function is between 0 and 1 to determine the data basis for subsequent analysis.

Through the measurement of 120 sample data, the CAR value, DP value, LAS value, and ROE value are shown in Figures 2–5. The range of CAR value is between -60 and 40; the range of DP value is between 50 and 380; the range of CAR value is between -60 and 40; the range of LAS value
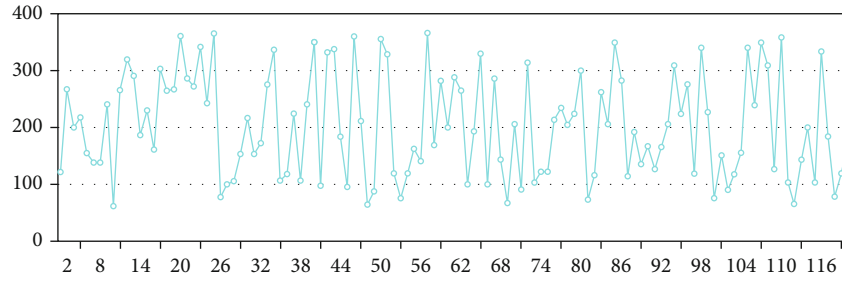
FIGURE 3: DP value of 120 samples (%).
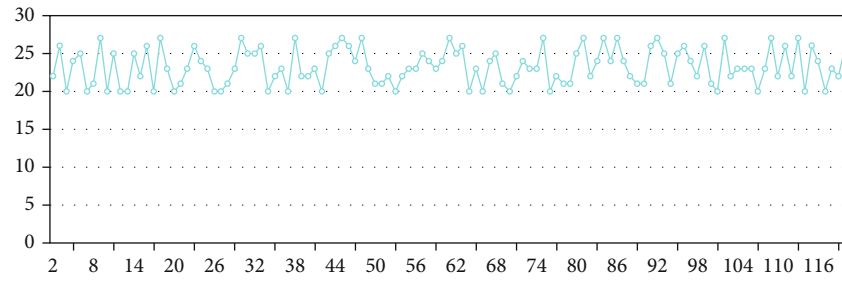
FIGURE 4: LAS value of 120 samples (Yuan).
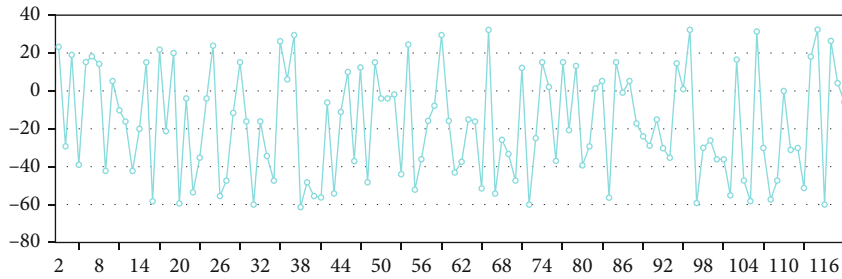
FIGURE 5: ROE value of 120 samples (%).

TABLE 2: The outcome variables and condition variables.

Variable	Average value	Standard deviation	Minimum	Max	Calibration		
					Fully affiliated	Intersection	Not affiliated at all
CAR (%)	2.9506	10.0727	-50.1	38.28	8.955	3.2913	-2.373
DP (%)	150.4426	35.4733	56.9110	366.75	161.797	144.8179	127.8387
RR (%)	2.4365	2.0224	0.01	14	3	2.0575	1.115
LAS (Yuan)	22.5388	1.2901	19.964	27.293	23.3053	22.5139	21.7224
ROE (%)	8.7528	7.9406	-61.782	31.471	11.9721	8.6682	5.3644
CR10 (%)	56.2520	19.2112	9.7426	88.5	69.365	57.7888	46.2124
MSL (%)	17.8728	10.2887	0	73.49	14.9919	7.5624	0.1329

is between 10 and 30; and the range of ROE value is between -60 and 40.

The descriptive statistics of the result variables and condition variables involved and the value of the calibration anchor points are shown in Table 2. It can be seen from Table 2 that the maximum value of CAR of 240 sample cases is 38.28%, the minimum value is -50.1%, the mean is 2.9506%, and the standard deviation is 10.0727%. The cases with CAR greater than or equal to 8.955% are classified as "fully subordinate," less than or equal to -2.373% of the cases

were classified as "completely nonaffiliated," and the CAR value of the "cross-point" cases was set to 3.2913%.

4.2. Necessity Analysis of Single Factor. Qualitative comparative analysis requires that each condition must be individually tested for necessity before performing condition configuration analysis. If a certain condition always exists when the result occurs, the condition is considered a necessary condition of the result (that is, the condition is a superset of the combination of results). The judgment is based on
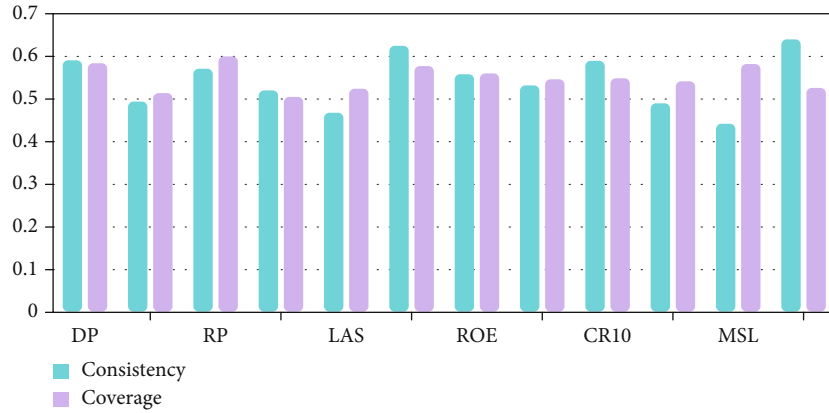
FIGURE 6: Analysis of $CAR_{[-5,10]}$.
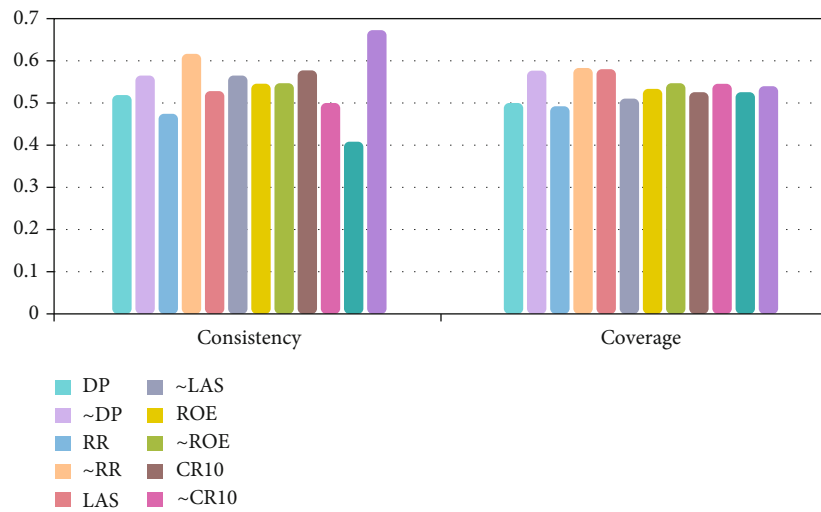
FIGURE 7: Analysis of $\sim CAR_{[-5,10]}$.

TABLE 3: Necessity analysis of single factor.

Conditions tested		$CAR_{[-5,10]}$		$\sim CAR_{[-5,10]}$	
		Consistency	Coverage	Consistency	Coverage
Buy-back Clause	DP	0.591421	0.583211	0.520037	0.500406
	~DP	0.493373	0.513012	0.566861	0.575158
	RR	0.568618	0.602810	0.474648	0.491011
	~RR	0.519881	0.503508	0.616047	0.582204
Financial position	LAS	0.466205	0.523721	0.527967	0.578748
	~LAS	0.625010	0.575718	0.565511	0.508303
	ROE	0.559315	0.558304	0.546106	0.531925
	~roe	0.531077	0.545262	0.546528	0.547544
Corporate governance	CR10	0.588540	0.548026	0.577153	0.524415
	~CR10	0.489256	0.542492	0.502573	0.543770
	MSL	0.440849	0.580739	0.408757	0.525430
	~MSL	0.639746	0.525814	0.673837	0.540429

the consistency level higher than 0.9. The analysis of $CAR_{[-5,10]}$ is shown in Figure 6, the analysis of $\sim CAR_{[-5,10]}$ is shown in Figure 7, and the specific data is shown in Table 3.

From Figures 6 and 7 and Table 3, it can be seen that the consistency index of a single antecedent condition that affects the high CAR or nonhigh CAR announcement effect

TABLE 4: Configuration of the announcement effect of stock repurchases.

| Configure | High CAR | | Nonhigh CAR | | | | |
| | Repurchase condition | Centralized cooperation | Scale-premium limited | Profit-proportionally | | Repurchase condition | |
	C1	C2	N1	N2a	N2b	N3a	N3b
DP	●	⊗	⊗	●		⊗	⊗
RR	●	●		⊗	⊗	⊗	⊗
LAS	⊗	⊗	⊗		●	●	
ROE	⊗	⊗	●	⊗	⊗	●	⊗
CR10	⊗	●	●		●	⊗	●
MSL	⊗	●		⊗		●	⊗
Consistency	0.8174	0.8094	0.8505	0.8359	0.8202	0.8411	0.8012
Raw coverage	0.0752	0.0654	0.0648	0.1293	0.1012	0.0612	0.0792
Unique coverage	0.0593	0.0495	0.0375	0.0510	0.0151	0.0305	0.0478
Solution consistency	0.8140			0.8206			
Solution coverage	0.1246			0.2843			

ranges from 0.4 to 0.7, with a minimum value of 0.408757 and a maximum value of 0.673837, all of which do not exceed 0.9. It means that each individual antecedent condition has an impact on the high or nonhigh CAR stock repurchase announcement effect. The explanatory power is weak, and a single antecedent condition does not constitute a necessary condition for the result. Therefore, it is necessary to consider all antecedents and explore different configurations that produce high and nonhigh CARs, respectively.

4.3. Sufficiency Analysis of Conditional Configuration. The purpose of the sufficiency analysis of conditional configuration is to try to find whether the configuration of multiple condition variables is the sufficiency condition of the result, that is, to analyze whether the configuration of multiple antecedent conditions in different combinations constitutes a result set (high, nonhigh CAR announcement effect).

We use the fsQCA3.0 software to construct a traditional Boolean algebra truth table based on the calibrated 240 sample case data, perform standardized analysis to obtain the conditional configuration, and use it to explain the complexity of cause and effect. This article has 6 conditional variables. The initial truth table has 64 rows. It is necessary to set the consistency threshold and the frequency threshold to simplify.

Setting the consistency threshold is to eliminate the combination of factors in the sample case whose consistency level with the set logical relationship is lower than the threshold. According to the general setting method of the consistency level threshold, the consistency level threshold is set to 0.8. Setting the frequency threshold is to eliminate the combination of factors whose frequency of occurrence is lower than the threshold. The frequency threshold usually depends on the sample size. In principle, the conditional configuration is required to cover at least 75% of the samples. This article sets the frequency threshold to 2. Based on this, this paper obtains two conditional configurations of high CAR announcement effect (C1, C2), and five condi-

tional configurations of nonhigh CAR announcement effect (N1, N2a, N2b, N3a, N3b). The specific condition configuration is shown in Table 4. The original coverage indicates the influence of the factors in each configuration solution on the result. The unique coverage indicates the possibility of the configuration solution being able to achieve high innovation investment.

It can be seen from Table 4 that the consistency indexes of the path solutions that produce high and nonhigh CAR announcement effect results are 0.8140 and 0.8206, respectively, which are both greater than or equal to 0.8, indicating sufficient conditions for the corresponding high and nonhigh CAR announcement effect results. The solution coverage indicators are 0.1246 and 0.2843, respectively, indicating that the corresponding configuration conditions can explain 12.46% and 28.43% of the stock repurchase cases with high and nonhigh CAR announcement effects, respectively, specifically the following:

(1) Repurchase condition-oriented type (C1): without resorting to other conditions, the superior conditions of high repurchase premium and high repurchase ratio can achieve the announcement effect of high CAR stock repurchase, which can be defined as the repurchase condition-oriented type. This path can explain 7.52% of the high CAR stock repurchases announcement effect cases, and 5.93% of the high CAR stock repurchases announcement effect cases can only be explained by this path

(2) Centralization-proportionally coordinated type (C2): the high degree of equity concentration and the proportion of senior management's shareholding reflect a higher degree of centralization of corporate governance, and the high repurchase ratio is more consistent with the interests of senior management holding shares. This realization of high CAR stock repurchase announcement effect can be defined as a centralized-proportional coordination type. This path can explain

6.54% of high CAR stock repurchases announcement effect cases, and 4.95% of high CAR stock repurchases announcement effect cases can only be explained by this path

(3) Scale-premium restriction type (N1): in the case of a small company, even if the listed company has strong profitability and high equity concentration (auxiliary conditions), if there is no attractive high repurchase premium condition, then we cannot realize the high CAR stock repurchase announcement effect, which can be defined as a scale-premium restriction type. This path can explain 6.48% of nonhigh CAR stock repurchase announcement effect cases, and 3.75% of nonhigh CAR stock repurchase announcement effect cases can only be explained by this path

(4) Profit-proportionally restricted type (N2a, N2b): the common core conditions of the two paths of N2a and N2b are ~RR and ~ROE, that is, in the absence of a high repurchase ratio and high level of profitability, they will show noncompliance. The effect of high CAR stock repurchase announcements is that N2a is also supplemented by low executive shareholding ratio, which can be defined as a profit-proportion restricted type. The two paths can explain 12.93% and 10.12% of the nonhigh CAR stock repurchase announcement effect cases, respectively. The 5.1% and 1.51% of the nonhigh CAR stock repurchase announcement effect cases can only be explained by the two paths

(5) Repurchase condition restricted type (N3a, N3b): the common core conditions of the two paths of N3a and N3b are ~RR and ~DP, that is, in the absence of a high repurchase ratio and high repurchase premium, supplemented by low equity concentration (N3a) or low profitability and low executive shareholding ratio (N3b) will show the effect of nonhigh CAR stock repurchase announcements, which can be defined as restricted by repurchase conditions. The two paths can explain 6.12% and 7.92% of the nonhigh CAR stock repurchase announcement effect cases, respectively. The 3.05% and 4.78% of the nonhigh CAR stock repurchase announcement effect cases can only be explained by the two paths.

Based on the comparison and analysis of the above configurations, the potential substitution relationship between the following configurations can be found:

(1) High CAR announcement effect condition configuration. There is a potential substitution relationship between the repurchase condition-oriented (C1) and centralization-proportional coordination (C2) configurations, that is, under the same high repurchase ratio, the combination of high controlling rights and high-level management shares high repurchase premiums can be substituted for each other to achieve a high CAR announcement effect

(2) Nonhigh CAR announcement effect condition configuration. First, there is a potential substitution relationship between the profit-proportion restricted type (N2a, N2b) and the repurchase condition restricted type (N3a, N3b), that is, under the premise that the repurchase ratio is also limited (low repurchase ratio), low repurchase premium and low profitability can be substituted for each other to achieve nonhigh CAR announcement effects. Second, there is a potential substitution relationship between the scale-premium restricted type (N1) and the repurchase condition restricted type (N3a, N3b), that is, under the premise of low repurchase premium, low asset scale and low repurchase ratio can replace each other to achieve nonhigh CAR announcement effect.

5. Conclusion

This article uses qualitative comparative analysis methods and the PSO-ICA-GARCH model to analyze 240 stock repurchase cases in the Chinese securities market from 2018 to 2019, and through the study of five types of 7 paths of high and nonhigh CAR stock repurchase announcement effects. We have the following findings: (1) Superior repurchase conditions are the most direct way to achieve high CAR stock repurchase announcement effects. (2) With high equity concentration and senior management's shareholding in the case of proportion, a high repurchase ratio can also achieve a high CAR stock repurchase announcement effect. (3) Under the premise of limited repurchase premium and repurchase ratio, the company's size, profitability, equity concentration (only as an auxiliary condition), and senior management shareholding ratio (only as an auxiliary condition) will restrict the high realization of the announcement effect of CAR stock repurchase. The next step is to further optimize the model to make the analysis more accurate and effective.

Data Availability

The data used to support the findings of this study are included in the article.

Conflicts of Interest

The authors declare that they have no conflicts of interest.

Acknowledgments

References

[1] R. K. Chou, Y.-C. Wang, and J. Jimmy Yang, "Share pledging, payout policy, and the value of cash holdings," *Journal of Empirical Finance*, vol. 61, no. 8, pp. 18–33, 2021.

[2] Y.-T. Hsu and C.-W. Huang, "Why do stock repurchases change over time," *European Financial Management*, vol. 26, no. 4, pp. 938–957, 2020.

[3] D. Bendig, D. Willmann, S. Strese, and M. Brettel, "Share repurchases and myopia: implications on the stock and consumer markets," *Journal of Marketing*, vol. 82, no. 2, pp. 19–41, 2018.

[4] P. Kumar, N. Langberg, J. Oded, and K. Sivaramakrishnan, "Voluntary disclosure and strategic stock repurchases," *Journal of Accounting and Economics*, vol. 63, no. 2-3, pp. 207–230, 2017.

[5] Y. Sun, C. Xu, G. Li et al., "Intelligent human computer interaction based on non redundant EMG signal," *Alexandria Engineering Journal*, vol. 59, no. 3, pp. 1149–1157, 2020.

[6] G. Li, L. Zhang, Y. Sun, and J. Kong, "Towards the sEMG hand: internet of things sensors and haptic feedback application," *Multimedia Tools and Applications*, vol. 78, no. 21, pp. 29765–29782, 2019.

[7] D. Jiang, G. Li, Y. Sun, J. Hu, J. Yun, and Y. Liu, "Manipulator grabbing position detection with information fusion of color image and depth image using deep learning," *Journal of Ambient Intelligence and Humanized Computing*, vol. 1, no. 3, pp. 1–14, 2021.

[8] G. L. Du Jiang, C. Tan, L. Huang, Y. Sun, and J. Kong, "Semantic segmentation for multiscale target based on object recognition using the improved Faster-RCNN model," *Future Generation Computer Systems*, vol. 123, no. 3, pp. 94–104, 2021.

[9] D. J. Skinner, "The evolving relation between earnings, dividends, and stock repurchases," *Journal of Financial Economics*, vol. 87, no. 3, pp. 582–609, 2008.

[10] S. Chahine, M. J. Zeidan, and H. Dairy, "Corporate governance and the market reaction to stock repurchase announcement," *Journal of Management Governance*, vol. 16, no. 4, pp. 707–726, 2012.

[11] D. Lin and X. Yang, "Analysis on the influencing factors of stock repurchase market response — empirical evidence from China's A-share market," *Journal of Xi'an Jiaotong University*, vol. 29, no. 5, pp. 23–27, 2009.

[12] K. Yang, Y. Wei, S. Li, L. Liu, and L. Wang, "Global financial uncertainties and China's crude oil futures market: evidence from interday and intraday price dynamics," *Energy Economics*, vol. 96, no. 4, pp. 105149–105149, 2021.

[13] Y. Wei, L. Bai, K. Yang, and G. Wei, "Are industry- level indicators more helpful to forecast industrial stock volatility? Evidence from Chinese manufacturing purchasing managers index," *Journal of Forecasting*, vol. 40, no. 1, pp. 17–39, 2021.

[14] L. Bai, Y. Wei, G. Wei, X. Li, and S. Zhang, "Infectious disease pandemic and permanent volatility of international stock markets: a long-term perspective," *Finance Research Letters*, vol. 40, 2021.

[15] C. P. Stephens and M. S. Weisbach, "Actual share reacquisitions in open-market repurchase programs," *The Journal of Finance*, vol. 53, no. 1, pp. 313–333, 1998.

[16] T. Jiang and Y. Wei, "Stock repurchase: benefit transmission under the goal of public governance—analysis of stock repurchase cases in my country's securities market," *Management World*, vol. 12, no. 4, pp. 105–117, 2007.

[17] X. Ca and J. Zhong, "Research on the market effect of stock repurchase of listed companies," *World Economic Situation*, vol. 87, no. 16, pp. 18–21, 2003.

[18] Y. Z. Du and L. D. Jia, "Configuration perspective and qualitative comparative analysis (QCA): a new way of management research," *Management World*, vol. 17, no. 6, pp. 156–167, 2017.

[19] P. C. Fiss, "Building better causal theories: a fuzzy set approach to typologies in organization research," *Academy of Management Journal*, vol. 54, no. 2, pp. 393–420, 2011.

[20] X. Zhang, "PSO-ICA-GARCH model for volatility analysis of stock market," *Journal of Xi'an University of Technology*, 2021, https://kns.cnki.net/kcms/detail/61.1294.n.20210416.1533.002.html.

Research Article

Use Python Data Analysis to Gain Insights from Airbnb Hosts

Zichun Tian (ID)

Olin Business School, Washington University in St. Louis, St. Louis 63130, USA

Correspondence should be addressed to Zichun Tian; t.zichun@wustl.edu

This paper uses Python and its external data processing package to conduct an in-depth analysis machine study of Airbnb review data. Increasingly, travelers are now using Airbnb instead of staying in traditional hotels. However, in such a growing and competitive Airbnb market, many hosts may find it difficult to make their listings attractive among the many. With the development of data science, the author can now analyse large amounts of data to obtain compelling evidence that helps Airbnb hosts find certain patterns in some popular properties. By learning and emulating these patterns, many hosts may be able to increase the popularity of their properties. By using Python to analyse all data from all aspects of Airbnb listings, the author proposes to test and find correlations between certain variables and popular listings. To ensure that the results are representative and general, the author used a database containing many multidimensional details and information about Airbnb listings to date. To obtain the desired results, the author uses the Pandas, NLTK, and matplotlib packages to better process and visualize the data. Finally, the author will make some recommendations to Airbnb hosts based on the evidence generated from the data in many ways. In the future, the author will build on this to further optimize the design.

1. Introduction

Even though Airbnb has gained a lot of popularity since its inception, there is increasingly emerging voice stating that they would rather choose hotels than Airbnb. According to a news report, some reasons include inaccurate descriptions of properties, prices being not cheaper than hotels, and long response time when communicating with hosts [1]. The annual booking times have a decreasing growth rate since 2018, the accumulated listing shows a decreasing growth rate since 2017, and the closest competitor Vrbo has started to occupy the market shares that originally belong to Airbnb [2].

When the time comes to 2020, the outbreak of COVID-19 has brought even more pressure on Airbnb hosts. Due to the uncertainties of the travel plans, Airbnb allowed a more flexible cancel policy when booking a place which will increase the opportunity costs of the hosts [3]. A report says that 70% of guests are fearful to stay at an Airbnb compared to hotels that have more strict and standardized cleaning protocols if they must travel during the pandemic. For the hosts, the cost of accepting guests also increases because of the stricter hygiene procedures [4]. As a result, the hosts

and Airbnb itself are now facing new challenges both from inside and outside. Since the diversified hosts and their properties that are located almost everywhere in the world are the core competitiveness of Airbnb, Airbnb should help them become more appealing through multiple ways to compete with hotels and other rivals.

The author tried to find some specific patterns that are most common among popular properties and apply these patterns to other properties to maximize advantages and attractiveness to guests [5].

To better help understand, the author wants to clarify some terms that are frequently used in the Airbnb system. The hosts mean the property owners who rent guests the places to stay. Guests are people that do not want to live in hotels and rent the hosts' properties to stay. The listings are created when hosts put their properties on the Airbnb system and are available for guests to stay. Listings include all the information that describes the properties like price, description, and location.

The database the author used is downloaded from a website called "Inside Airbnb" which provided all the relative data of Airbnb listings from all locations around the world.

The author used the data from the Los Angeles site which includes three CSV files. The first file is called calendar which includes all the listing details including the maximum and minimum price of every listing in Los Angeles daily [6]. Since each listing is highly likely to be listed more than one day, there will be many repeated data that need to be eliminated when the author processes the data [7]. The second file is called reviews, and it records all the reviews and everything related to that like dates, reviewer names, and unique IDs. These reviews are given by guests that are followed by every stay or transaction [8]. The reviews are very useful because the author can do sentiment analysis to find the most popular words that are valued by the guests to help Airbnb hosts improve. The last file is called listings which has much more data than the previous two files. It contains all the information of every Airbnb listing in Los Angeles. Some valuable information is room types, host response time, review scores of each section from guests, room descriptions, etc.

These three files can be connected through unique IDs, and then, the author can combine all these factors to find all the relations that existed in these data.

2. Current Status of Research

In many fields of scientific research, for the same problem, there are often different scholars using the same or different scientific methods to conduct research and experiments, and the conclusions are not the same. In this case, how can the author synthesize the results of different existing studies to get a more reliable conclusion? Meta-analysis is a statistical method that analyses and generalizes the data collected from multiple studies to provide a quantitative average effect to answer the research question [9]. Its advantage is that it increases the credibility of the conclusions by increasing the sample content and resolves inconsistencies in research findings. It is a quantitative review of the literature, which is a systematic, objective, and quantitative synthesis of the results of multiple independent studies on the same topic, based on a rigorous design, using appropriate statistical methods.

To conduct meta-analysis, the first step is to determine the effect values of the study results, i.e., the statistical quantities that can be used to measure the good or bad results of the study, and usually, correlation coefficients, relative ratios, and standardized relative differences can be used as effect values [10]. Consistent effect values are the basis of meta-analysis, and only when the effect values are unified is it possible and reliable to conduct a comprehensive analysis of the results [11]. In practical research, more than one effect value is often needed to evaluate the results of an experiment or study [12]. For example, in the field of education, to evaluate a student's good or bad performance, one cannot only look at the score of one subject but needs the combination of multiple subjects; in the medical field, to conduct a hypertension drug test, one needs to measure both the blood pressure of the heart during systole and the blood pressure of the heart during diastole; in the financial field, several indicators are reflecting the liquidity risk of an enterprise, such

as current ratio, quick ratio, and short-term cash service multiple [13].

To conduct simulation experiments and eventually analysis, you need to write programs through computer languages to achieve, at this stage, the most used computer language for analysing big data which is mainly two, one is Python and one is R. Among them, Python is more powerful; in addition to data processing, modelling analysis can also be website development, game development, etc., which can be said to be the hottest computer language. It is more suitable for technical people who have some computer theory foundation and aim at engineering development. R was originally developed to help users to do data analysis, statistical modelling, visualization models, etc., in a user-friendly and fast way, and it has a very powerful open-source library. Users can easily call the packages to build their models without programming their implementation, which is easier to implement for researchers who are not very good at computer languages and do not need to spend much time and effort here.

3. Python Methods

3.1. Experimental Method. Since the raw data the author collected is disorderly and chaotic, the author must choose the right method in Python to process and visualize these data [14]. There are many packages and preinstalled programs available to choose from in Python; the author must choose the right one to facilitate our works:

$$I_i = \alpha\theta_i^2 + \beta\theta_i^2 + \chi\theta_i^2. \tag{1}$$

The first method this paper used in Python is the Pandas package. Pandas is a package that has been frequently used when manipulating and analysing data. It allows this paper to import data from various formats and lets the author do some certain manipulation on data as desired [15]:

$$G_j = \frac{\sum_{i,j=1}^{m,n} R_i * U_{ij}^2}{\sum_{i,j=1}^{m,n} E_i * U_{ij}^2}. \tag{2}$$

The Python Pandas package has been frequently used in quantitative finance applications in recent years. In a report that mainly focuses on statistical computing in Python, the author used the Pandas package to reshape the primary data set which contains the stock prices of some certain companies and industries. With the function of easily changing DataFrame to series and removing dummy variables, the Pandas package can save much time used to prepare data:

$$CSV = (H(m_i) + H(n_i)) - \left(H(m_j) + H(n_j)\right), \tag{3}$$

$$M' = \left\{ M' = m - m_c, \ \forall m \in M \right\}, \tag{4}$$

$$M'' = \left\{ M'' \middle| m'' = \frac{m' \times d}{D}, \ \forall m' \in M' \right\}. \tag{5}$$
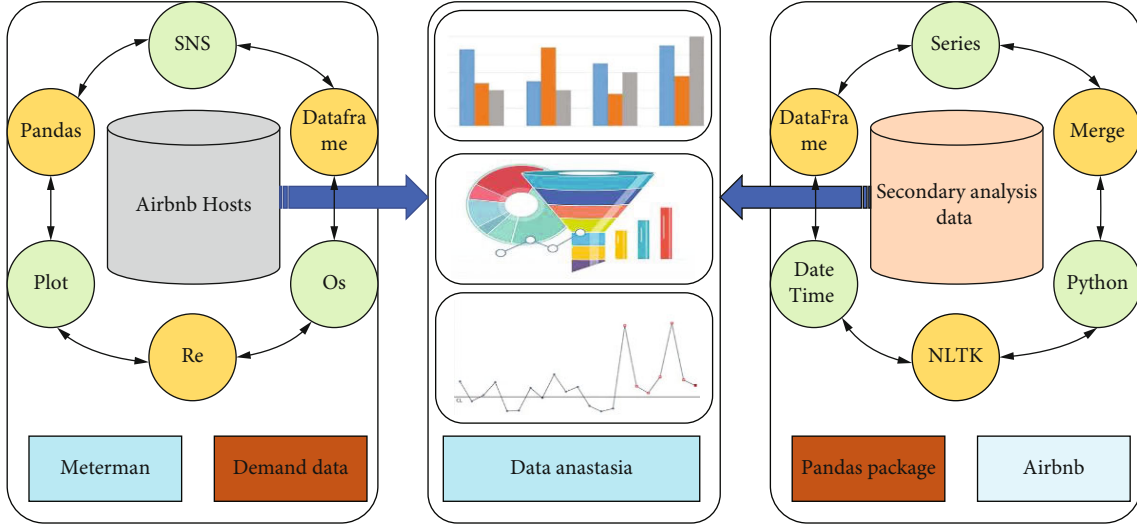
FIGURE 1: Python data analysis framework.

In this case, this paper use Pandas to read all the three CSV files and use series, DataFrame, merge, and DateTime code inside Pandas to help better understand and visualize the results, as shown in Figure 1.

Another method in Python the author used is NLTK which is also called Natural Language Toolkit. Its primary purpose is to let Python programming language work with human language data [16]. As this paper mentioned above, the author planned to do sentiment analysis to figure out the most popular words in the review from the database and thus making NLTK the most suitable tool in this scenario. According to research, sentiment analysis using Python NLTK has been applied to normal business operations to improve performance. They use sentiment analysis to study the customers' behaviour and let their business improve in that direction.

The last method this paper uses in Python is matplotlib which is a plotting library in Python. It is useful when visualizing the results. By drawing the plots, this paper can better understand the comparison from multiple aspects.

3.2. Sentiment Analysis. Sentiment analysis can study the customers' behaviour to some extent and can somewhat replace the time- and money-consuming traditional methods like surveys and focus groups. By just analysing the easily accessible sources of data, sentiment analysis can give the business owners relatively accurate feedbacks to measure the customers' tendencies:

$$P(y_i) = p_i^{y_i}(1 - p_i)^{1-y_i}, \tag{6}$$

$$W_c = \int_R \frac{\varphi^2(w)}{w} \, dw. \tag{7}$$

However, sentiment analysis can be hard to finish and can be easily compromised. To get accurate results, the author must eliminate all the nonvariables and dummy variables to make the dataset clean [17].

Becoming a super host on Airbnb seems an official quality assurance that will bring the hosts more clicks and thus more stays and more revenue. Besides the indirect benefits (increase in the revenue), Airbnb will provide the super hosts more direct benefits like travel coupons, exclusive events, and priority support, as shown in Figure 2.

The criteria to become a super host can be fussy [18]. It asks hosts to be almost perfect in all aspects including but not limited to review scores, response rate, and cancellation rate. As a result, the Airbnb super hosts can be seen as examples for all hosts to learn from [19].

Some traditional positive words like recommend and good cannot fully reflect the guests' thoughts. Many people with ok feelings who are not willing to leave a long talk may use recommend and nice words [20]. As a result, these words can be misleading. So, filtering these reviews before processing is necessary when dealing with the review data [21].

4. Analysis of Results

4.1. Basic Attributes of the Datasets. Before diving deep into the dataset, the author did a basic statistical analysis to calculate the number of unique listings, hosts, and basic perimeter (mean, median, and standard deviation).

Since there are many repeated listings in all these three CSV files, the author used the drop_duplicates() function to make the dataset clean. After that, the author used the len() function to calculate; there are 38481 unique listings and 22274 unique hosts. The mean, median, standard deviation, minimum, and maximum number of listings per host are shown in Figure 3.

As is shown in Figure 3, most hosts only have one listing and some may have more than one listing. The author divided the hosts into super and nonsuper hosts and calculated the same perimeter as above to better understand the difference between each group. The numbers are shown in Figure 4.
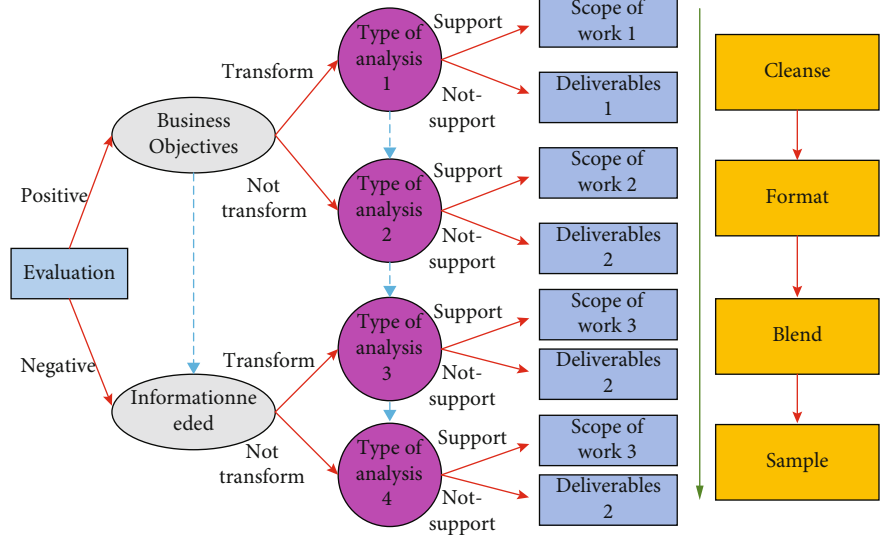
FIGURE 2: Data analysis steps.
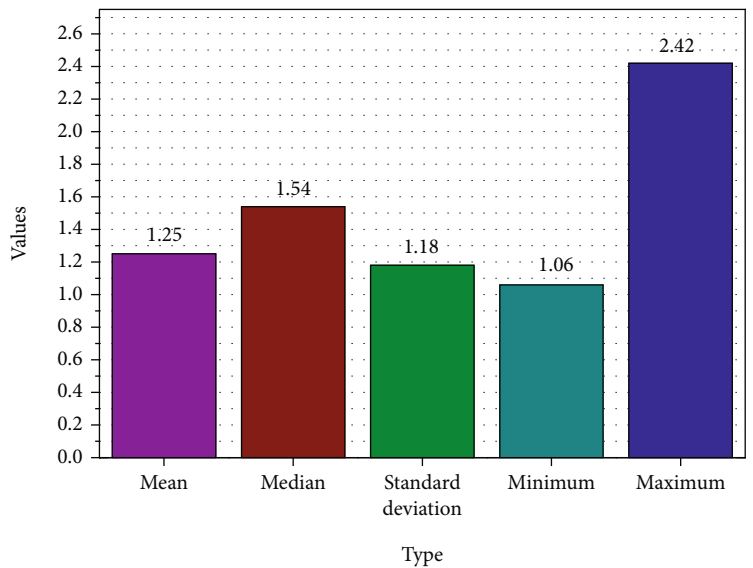
FIGURE 3: Perimeter of number of listings per host.

Then, we want to analyse the datasets in two parts. The first part is to analyse some correlations among all the hosts, and the second part is to make some comparisons between super and nonsuper hosts.

First, the author wants to do a sentiment analysis of reviews among all the hosts. This paper intends to find the most 10 popular words in the reviews of the listings. After that, this paper can have a rough view of what the guests value when staying in an Airbnb, so this paper can let hosts improve towards that direction [22].

To generate the most accurate results, the author eliminate all the stopping words like punctuations and let the next popular words replace some words like "recommend" and "great" that cannot fully reflect the guests' opinion. This paper also made a histogram to visualize the results as shown in Figure 5.

Word "location" is ranked #3 in the most popular 10 words in the reviews. A good location is not just limited to close to attractions and landmarks or convenient transportation but depends on the purpose of the guests. Family travels may favour attractions nearby, but many other types of travelers like business or single travelers may favour quiet neighbourhoods, various selection of restaurants, safe community, etc. As a result, hosts should dig their properties' unique advantages as much as possible and add these words to the titles or descriptions of their listings to attract more guests.

Not surprisingly, "clean" is one of the most popular 10 words in the guests' reviews. Clean is the prerequisite for guests to perceive all other advantages that the hosts provided in properties. A clean property will not add scores but a slight lack of clean will reduce the scores largely.
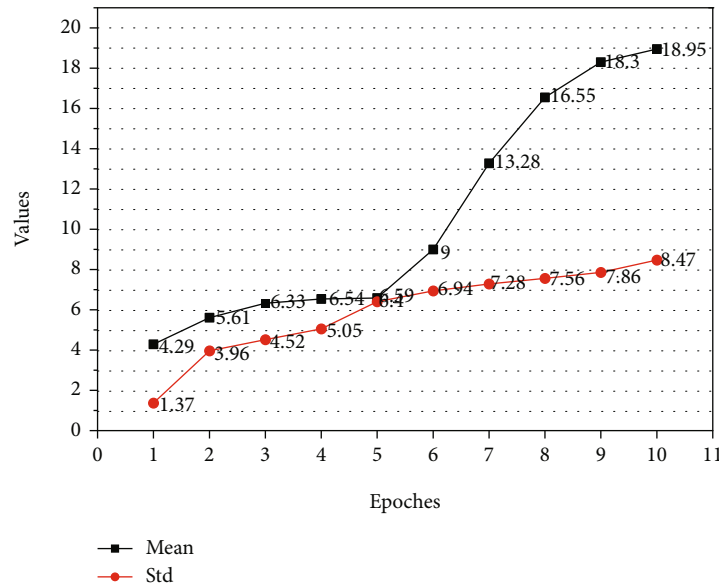
Figure 4: Number of listings per nonsuper hosts.
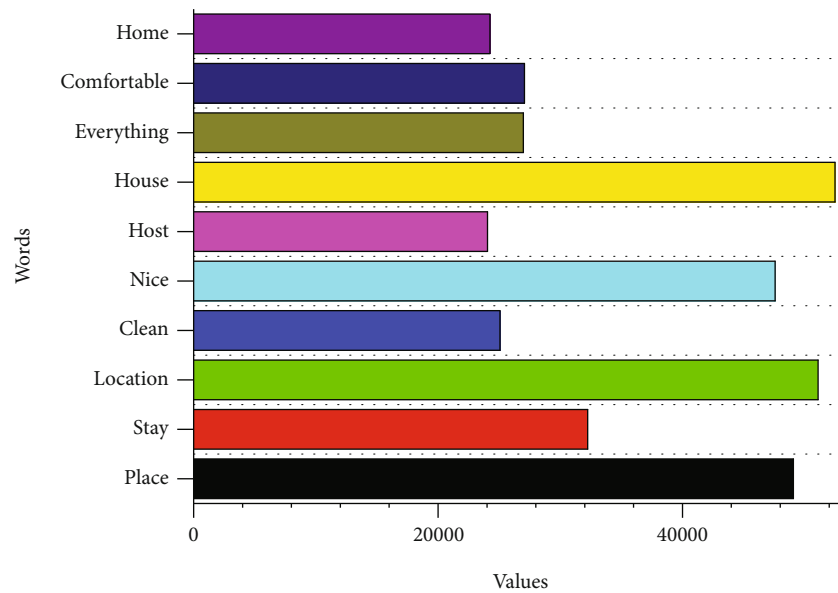
Figure 5: Most popular 10 words in reviews.

Another word "nice host" suggests hosts being polite, honest, and responsive when communicating with potential guests. Sometimes, using strategies like asking guests if they travel for special purposes, for example, anniversary, and preparing some small gifts for them would leave good impressions.

Since guests take "everything" as a criterion to measure properties, hosts should equip the properties with complete home appliances and living essentials. According to a report, some new Airbnb properties are now equipping gaming and cinema equipment like PlayStation, Xbox, and projectors to attract guests.

Second, the author proposed to find the correlation between the room popularity and the time (month of a year)

to suggest hosts and Airbnb system when to fully or part-time engage to operate their properties.

Since there is no such direct column that can imply room popularity, the author planned to count the room_type column in the listing. CSV is an indirect indicator of room popularity. There are four room types in this dataset which are the entire home/apt, private room, shared room, and hotel room. To get corresponding dates, the author merged listing and calendar DataFrame based on listing_id. Besides, an inner merge is appropriate in this case because it can eliminate listings that do not have corresponding dates. A line chart shown in Figure 6 has been made to help understand results.
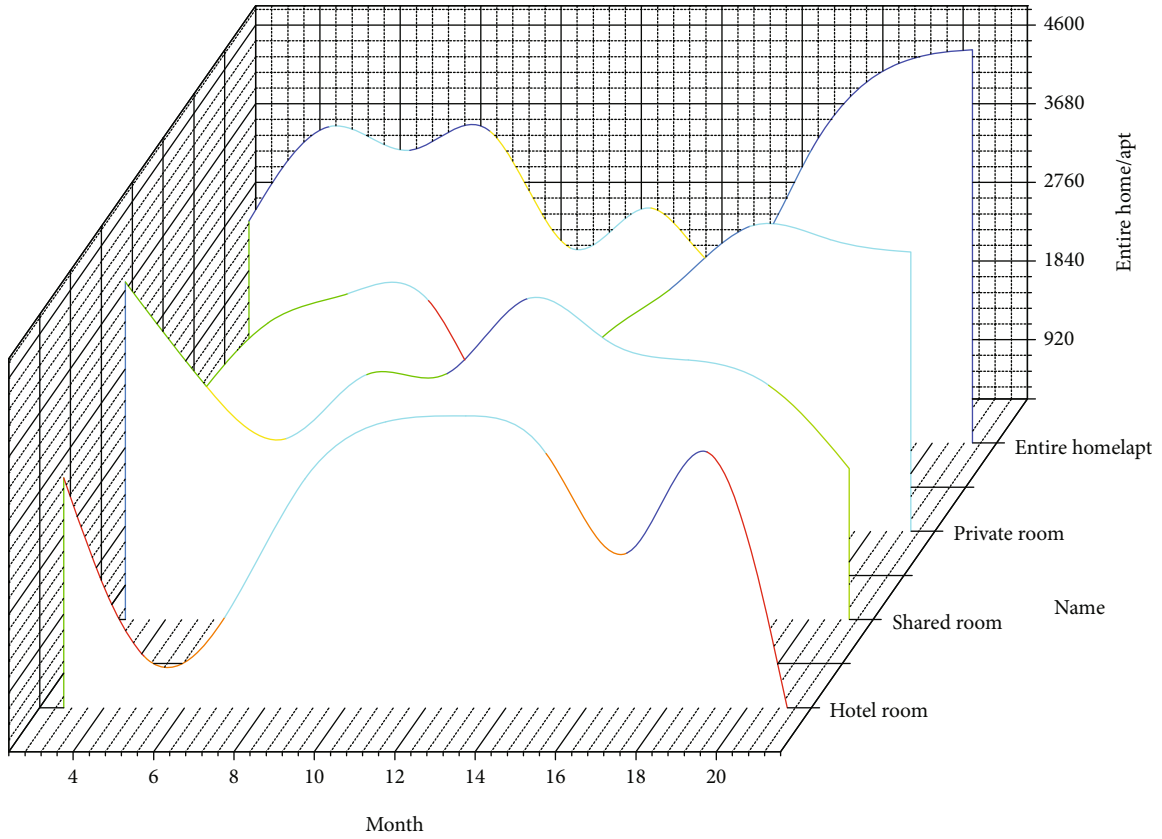
Figure 6: Room popularity correlated with a month.
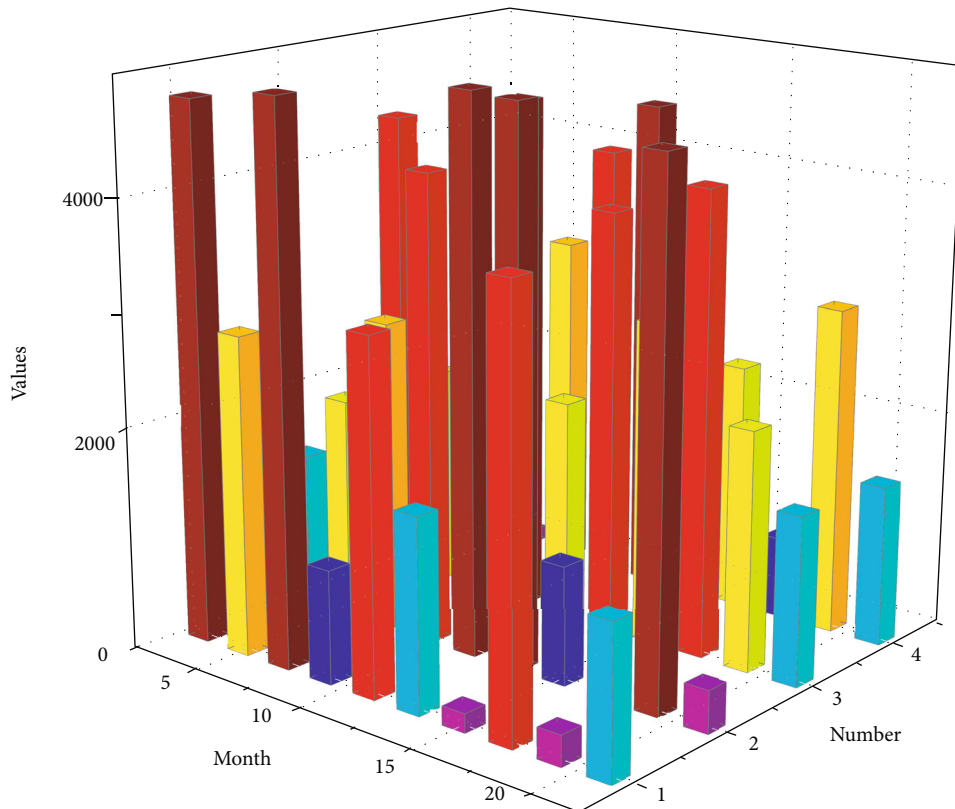
Figure 7: Average monthly price correlated with the month.
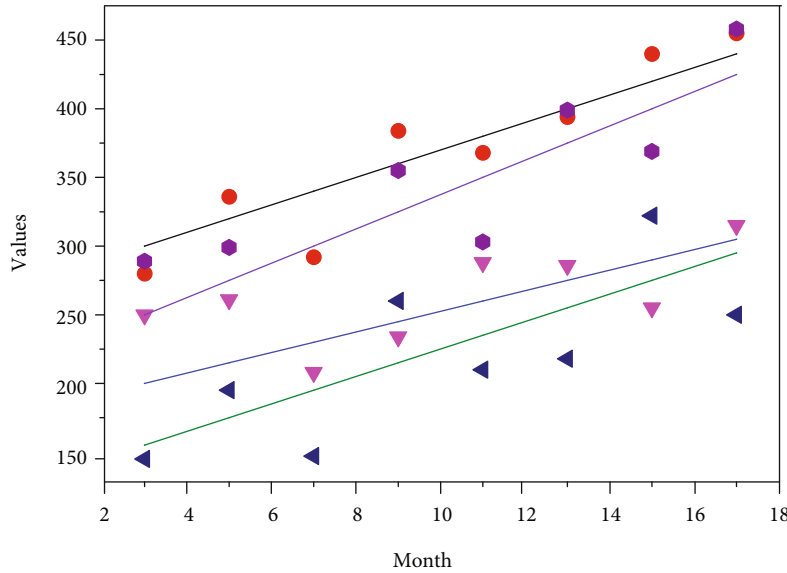
FIGURE 8: Room price correlation with room type.

The difficulty of big data processing lies not only in the huge overall quantity of data but also in the fact that each data contains more features, i.e., the data has a high number of dimensions. This makes it difficult to analyse and understand the data intuitively, and then, the choice of data processing tools or algorithms is also blind, which affects the final data analysis results and reduces work efficiency. KL scatter is a measure of the difference between two different probability distributions p and g, also known as relative entropy. KL scatter calculates not only the spatial difference between two distributions but also the information loss of one distribution compared to the other. To data visualization, the loss of information after mapping data from a high-dimensional space to a low-dimensional space should be as small as possible.

SOM mimics the competitive learning mechanism in the biological brain's nervous system and is therefore also called a self-organizing competitive network. When the brain is stimulated by some input signals, a - number of neurons will start to excite. If these inputs are similar, then they stimulate the same neurons, while other neurons are inhibited by the excited neurons. This process is a competition between different neurons for the opportunity to be stimulated by the input signal. Corresponding to the clustering algorithm, the neurons can be considered clustering centres and the input signals as data.

When designing a new database, the researchers should not only carefully study the business requirements but also examine the existing systems. Most database projects are not built from scratch; usually, there will always be existing systems in the organization that meet specific needs (and may not have automatic calculations). Obviously, the existing system is not perfect; otherwise, the researchers do not have to build a new system. But research on the old system can reveal some subtle issues that you might overlook. It is good for researchers to look at existing systems.
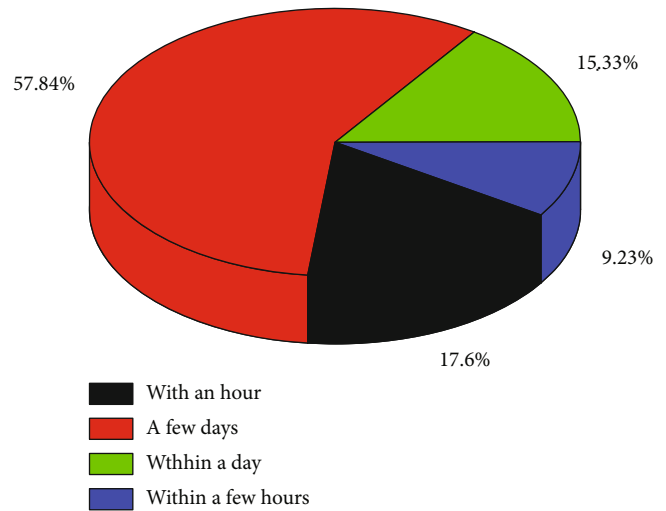
FIGURE 9: Average response time of super hosts.

From the graph above, the author can conclude that all the four types of rooms except hotel rooms (quantity is too small to generate statistical evidence) correlate with time (month of a year). The number of these three types of rooms being booked goes through a large boost around July and a slight increase around November and December. This meets the traditional traveling season which is June to August and before Christmas.

The trend shown in the graph suggests that the Airbnb hosts are well-prepared during the traveling season and Airbnb can advertise more to occupy market shares belonging to hotels.

Last, the author planned to test if there is a relationship between the popularity of each room type and their prices. This can imply whether the host should increase or decrease prices during season/off-season to increase property popularity.

28%

72%

65%

35%

▨ Verified

▨ UnVerified

(a)   (b)
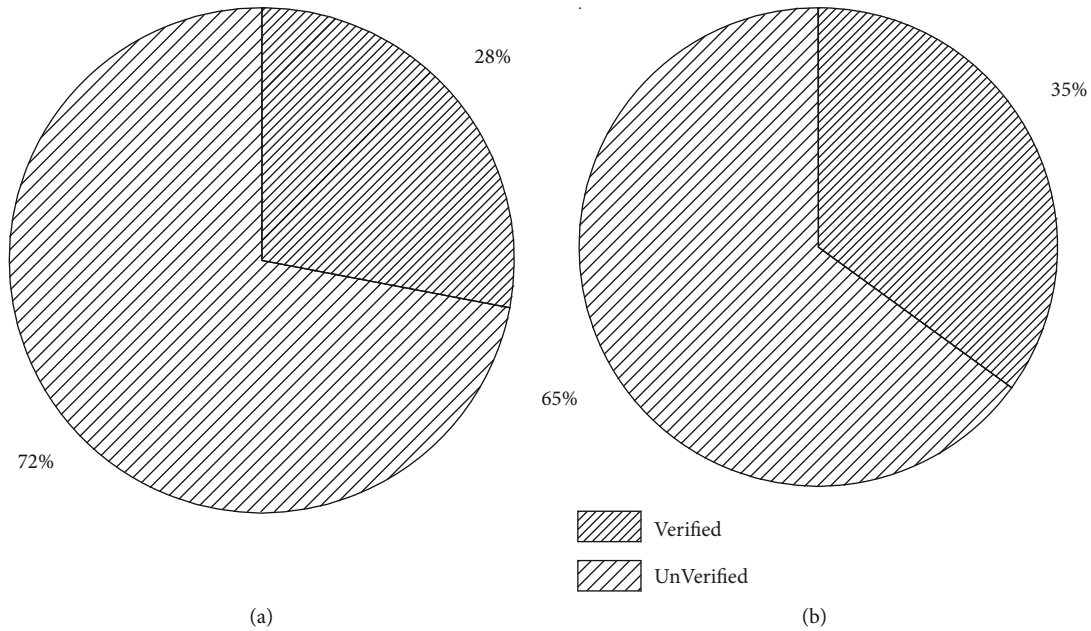
FIGURE 10: Identity-verified distribution between super and nonsuper hosts.

To get results, this paper first calculated the average monthly price for each room type and visualized it with a line chart shown in Figure 7. Then, the author can use a linear regression model to test relations.

With each room type's average monthly price, the author can now generate regression analysis between price and popularity as shown in Figure 8.

From the graph above, the author can hardly conclude that the room popularity is correlated with its prices for all three types of room except hotel room (uncommon on Airbnb as quantity is too small to generate statistical evidence). As a result, an increase or decrease in price cannot generate more popularity, so Airbnb hosts should maintain their prices relatively stable during season/off-season to compete with the hotel industry.

4.2. Comparisons between Super and Nonsuper Host Patterns. As this paper mentioned above, becoming a super host can bring a lot of direct and indirect benefits. According to the Airbnb policies, a host needs to maintain a 90% or higher response rate, 1% or lower cancellation rate, and 4.8 or higher total review scores, as shown in Figure 9.

The author planned to divide all the hosts into nonsuper and super hosts and compare the same features between these two groups. After the author finds some specific patterns among super hosts, this paper will make suggestions for nonsuper hosts to learn from gaining advantages and super host to maintain its advantages.

To find the specific patterns of the super host, the author first examined the average response time of super and nonsuper hosts.

There are four types of response time in this dataset which are "within an hour," "within few hours," "within a day," and "within a few days." The author used SQL language in Python to first filter super hosts from nonsuper hosts then the author group by these four different response

times and finally count the number of each type of response time. A pie chart with the percentage shown in Figure 10 on each section has been made to visualize the results.

As is shown on the pie charts, super hosts are more likely to respond to the messages within an hour. Many potential guests may turn to other options when waiting for hosts' long-time responses which may lead to loss of potential customers. To conclude, nonsuper hosts should increase their communication efficiency to decrease the response time to gain some advantages.

Second, the author proposed to compare identity-verified situations between super and nonsuper hosts. Verified identity is an optional procedure for hosts. Hosts will get badges that say "identified verified" on their homepage if they upload their government-issued photo ID to the Airbnb system. Figure 10 shows the results of the comparison.

As shown from the graphs, super hosts are more likely to get their identity verified. According to research, guests say if all others stay the same; they prefer identity-verified owner's properties because that badge gives a sense of safety. So, hosts need to get their identity verified to gain advantages if Airbnb can stick to the user privacy policies. From the two evaluation criteria of deviation and standard deviation, each of the three models has its advantages and disadvantages. The metamodel without introducing time t performs best in terms of deviation, and the metamodel with introducing time t performs best in terms of standard deviation, but the differences between the three methods in terms of deviation and standard deviation are not large. In terms of martingale distance, the effect of the metamodel with the introduction of time t is much better than that of the metamodel without the introduction of time t.

The effect of the model with the introduction of time t and $t2$ is better than that of the metamodel with the introduction of time t, and the difference between the three models is larger. Therefore, the author believes that
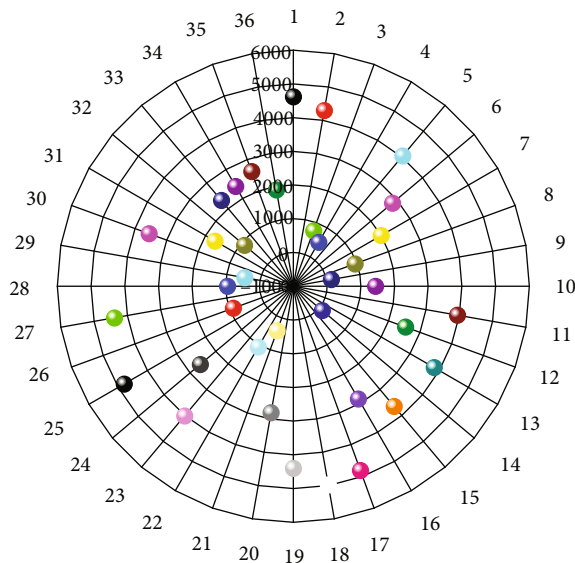
FIGURE 11: Comparison of mean scores of super/nonsuper hosts.

introducing time t and t to build a multivariate metaregression model is better than building a multivariate meta-analysis model in combining the parameter estimates. In summary, when it comes to the need to split the data according to features, and the features have an impact on the parameter estimates of the variables, the quantitative relationship between the features and each parameter estimate can be obtained through the multivariate metaregression model, obtaining a more accurate result of combining the parameter estimates, which is more reasonable and effective than the multivariate meta-analysis model. The basic attributes including the mean value were calculated before, and the median values were 115.2 and 25.1, respectively.

Last, the author intends to compare different review scores between super and nonsuper hosts. There are six different types of scores including accuracy, cleanliness, check-in, communication, location, and value. The guests will submit their evaluations after check-out from hosts, and a large part of an evaluation is to rate the properties from various aspects. These types of scores range from 1 to 10 where 10 is the best and 1 is awful.

To compare, the author calculated the mean of each type of score for super and nonsuper hosts and make all six scores in one histogram as shown in Figure 11 to better understand the differences.

The numbers on the horizontal axis are the mean review scores, and each paired column shown in the histogram is one of six types of scores.

As shown in the histogram, super hosts exceed nonsuper hosts on all types of scores, but super hosts only gain large advantages on three types of scores which are accuracy, cleanliness, and value. Accuracy measures whether the real condition of the properties is compatible with the hosts' description. Hosts can weaken the properties' drawbacks and emphasize the advantages in descriptions, but they need to achieve a balance to avoid being evaluated as false descriptions by guests. Cleanliness is another point that nonsuper

hosts need to improve. Value scores represent the degree of compatibility between what the hosts paid and what they have. The value is most difficult to interpret because it varies from person to people's different perceptions. It is also hard to be defined to a specific single point but goes through the entire procedure; from communicating, booking, staying, and leaving, the value can be defined in every moment in an Airbnb transaction. So, nonsuper hosts should try to make everything perfect in every link.

5. Conclusion

Based on the evidence found through data analysis, the author can now make some suggestions to Airbnb hosts. The first part is for all hosts (super and nonsuper hosts). First, by studying the guests' reviews, the author's recommendations are trying to dig their unique advantages, taking cleanliness as the top priority, and equipping the properties as much as possible. Second, by studying the room popularity changing with time, this paper suggests that Airbnb hosts and themselves should be fully engaged around July and December. Last but not the least, Airbnb hosts should remain their property prices stable to compete with hotels. The second part suggestions are for nonsuper hosts to improve and super hosts to maintain. First, nonsuper hosts should reduce response time when communicating with potential guests. Second, nonsuper hosts should get their identities verified. Last, accuracy, cleanliness, and perceived value are the top three problems that nonsuper hosts need to improve.

Data Availability

The simulation experiment data used to support the findings of this study are available from the corresponding author upon request.

Conflicts of Interest

The author declares that there are no conflicts of interest regarding the publication of this paper.

References

[1] R. Bion, R. Chang, and J. Goodman, "How R helps Airbnb make the most of its data," *The American Statistician*, vol. 72, no. 1, pp. 46–52, 2018.

[2] C. Chang and S. Li, "Study of price determinants of sharing economy-based accommodation services: evidence from Airbnb. com," *Journal of Theoretical and Applied Electronic Commerce Research*, vol. 16, no. 4, pp. 584–601, 2021.

[3] D. Coyle, "Do-it-yourself digital: the production boundary, the productivity puzzle and economic welfare," *Economica*, vol. 86, no. 344, pp. 750–774, 2019.

[4] L. Garay, S. Morales, and J. Wilson, "Tweeting the right to the city: digital protest and resistance surrounding the Airbnb effect," *Scandinavian Journal of Hospitality and Tourism*, vol. 20, no. 3, pp. 246–267, 2020.

[5] S. Jhaver, D. S. Appling, E. Gilbert, and A. Bruckman, "" Did you suspect the post would be removed?" Understanding user

reactions to content removals on Reddit," in *Proceedings of the ACM on human-computer interaction*, vol. 3, pp. 1–33, 2019.

[6] J. Liu, J. Park, K. Xie, H. Song, and W. Chen, "Effect of commercial neighbors on the online popularity of peer-to-peer accommodation-sharing properties," *Journal of Hospitality & Tourism Research*, vol. 44, no. 5, pp. 780–805, 2020.

[7] L. Luo, "Intelligent led lighting centralized control system based on internet of things," *Shenyang Gongye Daxue Xuebao/Journal of Shenyang University of Technology*, vol. 40, no. 4, pp. 453–458, 2018.

[8] S. Ma, H. Gu, D. P. Hampson, and Y. Wang, "Enhancing customer civility in the peer-to-peer economy: empirical evidence from the hospitality sector," *Journal of Business Ethics*, vol. 167, no. 1, pp. 77–95, 2020.

[9] M. M. Mariani and M. Borghi, "Online review helpfulness and firms' financial performance: an empirical study in a service industry," *International Journal of Electronic Commerce*, vol. 24, no. 4, pp. 421–449, 2020.

[10] A. C. Mermet, "Who is benefiting from Airbnb? Assessing the redistributive power of peer-to-peer short-term rentals," *The Professional Geographer*, vol. 73, no. 3, pp. 553–566, 2021.

[11] M. Zhang, F. Conti, H. Le Sourne et al., "A method for the direct assessment of ship collision damage and flooding risk in real conditions," *Ocean Engineering*, vol. 237, p. 109605, 2021.

[12] R. Peng, M. Zhang, C. Guo, J. Cui, and J. Song, "Public bicycle operating system based on space-time security and the internet of things," *Wuhan University Journal of Natural Sciences*, vol. 23, no. 6, pp. 541–548, 2018.

[13] S. Ruiz-Correa, I. Ruiz-Correa, C. Olmos-Carrillo et al., "Mi Casa es su Casa? Examining Airbnb hospitality exchange practices in a developing economy," *ACM Transactions on Social Computing*, vol. 2, no. 1, pp. 1–24, 2019.

[14] L. Rupprecht, J. C. Davis, C. Arnold, Y. Gur, and D. Bhagwat, "Improving reproducibility of data science pipelines through transparent provenance capture," *Proceedings of the VLDB Endowment*, vol. 13, no. 12, pp. 3354–3368, 2020.

[15] S. Xiao, S.-H. Ma, L. Guo, and S. K. Mukhopadhyay, "European option pricing with a fast Fourier transform algorithm for big data analysis," *IEEE Transactions on Industrial Informatics*, vol. 12, no. 3, pp. 1219–1231, 2016.

[16] A. A. Sinha, S. Rajendran, R. P. Nazareth, W. Lee, and S. Ullah, "Improving the service quality of telecommunication companies using online customer and employee review analysis," *Quality Management Journal*, vol. 27, no. 4, pp. 182–199, 2020.

[17] G. Williams, M. Tushev, F. Ebrahimi, and A. Mahmoud, "Modeling user concerns in sharing economy: the case of food delivery apps," *Automated Software Engineering*, vol. 27, no. 3-4, pp. 229–263, 2020.

[18] Y. Yao, J. R. Basdeo, O. R. Mcdonough, and Y. Wang, "Privacy perceptions and designs of bystanders in smart homes," in *Proceedings of the ACM on Human-Computer Interaction*, vol. 3(CSCW), pp. 1–24, New York, NY, USA, 2019.

[19] M. Yaşlıoğlu, "Dynamics of the network economy: a content analysis of the search engine trends and correlate results using word clusters," *International Journal of Data Analysis Techniques and Strategies*, vol. 12, no. 1, pp. 1–29, 2020.

[20] J. Zhang, "Listening to the consumer: exploring review topics on Airbnb and their impact on listing performance," *Journal of Marketing Theory and Practice*, vol. 27, no. 4, pp. 371–389, 2019.

[21] Z. Yong-zhang, P.-x. Lwe, W. A. N. G. Shu-gong, X. I. A. O. Fan, L. Jing-zhe, and G. A. O. Le, "Research progress on big data and intelligent modelling of mineral deposits," *Bulletin of Mineralogy, Petrology and Geochemistry*, vol. 36, no. 2, pp. 327–331, 2017.

[22] Z. Xie, J. Wang, and L. Miao, "Big data and emerging market firms' innovation in an open economy: the diversification strategy perspective," *Technological Forecasting and Social Change*, vol. 173, article 121091, 2021.

Research Article

Anti-Interference Heartbeat Measurement Based on a Miniaturized Doppler Radar Sensor

Lingtong Min, Qinyi Lv, Laisen Nie, and Deyun Zhou

School of Electronics and Information, Northwestern Polytechnical University, Xi'an 710129, China

Correspondence should be addressed to Laisen Nie; nielaisen@nwpu.edu.cn

It is a hot topic to utilize the Doppler radar sensor in noncontact biosignal monitoring nowadays. Unfortunately, most detections are easily affected by interference or strong noise. Even slight body movements can cause serious demodulation distortion. In this paper, we proposed a novel algorithm to solve the sudden and unexpected interference. Firstly, the one-dimensional signal detected by the sensor is divided into segments to form a two-dimensional data matrix. In both the intrasegment and intersegment domains of the data matrix, a robust algorithm is employed to suppress unwanted interference, which significantly improves the robustness of demodulation. Experiments show the effectiveness of the proposed algorithm, based on which weak heartbeat signal hidden in the interference can be well extracted.

1. Introduction

The miniaturized continuous-wave Doppler radar sensors (DRS) have been extensively studied due to its crucial potential in human healthcare and monitoring applications [1, 2]. Admirable progress in past decades has been made to overcome challenges in small-scale motion monitoring. To solve the null point problems in small-angle approximation, quadrature demodulation was introduced [3]. Using arctangent demodulation to recover the accurate phase information was then reported [4]. The Doppler radar systems both based on instruments [5] and integrated on a single CMOS chip [6] have also been come up with to detect respiration and heartbeat. Some demodulation algorithms were also discussed [7–9]. DRS can also be used to detect other motions, such as animal biosignals [10], mechanical vibration measurement [11], gesture recognition [12], and rotation of wind turbine blades [13]. Nowadays, the basic approach of continuous-wave Doppler radar sensor is the demodulation of frequency shift in reflecting waves from the moving target. Since the phase demodulation method is a linear method and can achieve great accuracy, it has become the most popular and advanced demodulation approach [14].

The Doppler radar sensor is easily affected by interferences like random body movements (RBM). Firstly, random body movements occur naturally as far as the human body stands or sitting. When there exists body movement, especially in the strong case, large body movement will conceal the small biosignal and likely result in signal clipping in conventional DRS [9]. Multiple contributions have been done to deal with body movement problems [15–20]. In [15], two antennas are placed to detect from the front and the back of a human body simultaneously. In this way, biosignal can be enhanced because it exists from all sides; while body movement is cancelled by multiplying the signal detected from both sides. Also, circuit saturation is likely to happen in the presence of large body movement [16]. As for injection locking radars array in [17, 18], users have to either sweep the radar's carrier frequency or adjust the subject's position. The hybrid sensing system with both radar and camera is employed in [19]. This system shows good potential to cancel body movement but is still complex in both hardware and signal processing. All of the work presents complicated hardware architecture with high costs, and the detection is limited in the study of relatively small RBM.

What is more, SISO (single-in and single-out) Doppler radar architecture is only limited in one target detection.

In the scene of biosignal detection, if there exist other moving objects like pedestrian or part of moving limbs, mass distortion can be seen in the result. The system with multiple receiving channels can distinguish the multiple targets by the blind separation algorithm [20]. Radar with more complex waveforms can also detect multiple people [21]. But these architectures will also increase system cost and complexity.

In fact, the biosignal includes both heartbeat signal and respiration signal. But the respiration signal is always much stronger and more flat than the heartbeat signal, which makes heartbeat signal detection more difficult. As a consequence, more attention is paid to heartbeat signal detection. In our paper, we mainly focus on heartbeat signal reconstruction by radar.

In this paper, we propose a novel Doppler radar-based adaptive anti-interference algorithm to recover the heartbeat signal. The entire one-dimensional movement can be decomposed into several segments to form a new two-dimensional data matrix for further processing. Every segment in the intrasegment domain and adjacent segments in the intersegment domain are evaluated, respectively, by a well-designed criterion, including changes in signal strength and signal-to-noise ratio (SNR). A miniaturized radar operating at 24 GHz is employed to verify the effectiveness of our method.

The rest of this paper is organized as follows. In Section 2, the theory of Doppler radar is briefly introduced. Then we propose the anti-interference algorithm. To illustrate the effectiveness of the proposed approach, a series of noncontact measurements are performed in Section 3, and the obtained results are presented. Finally, a conclusion is drawn in Section 4.

2. Materials and Methods

2.1. Problem Description. A classical Doppler radar sensor is shown in Figure 1. The basic principle of DRS is the reflection of continuous wave modulated by a moving target, such as the human chest. As for a target at a distance d_0 with time-varying motion given by $x(t)$, the received signal is quadrature demodulated, and I/Q channels of the baseband signals are

$$I(t) = A_I(t) \cos\left[\theta_0 + \frac{4\pi x(t)}{\lambda} + \varphi_0(t)\right] + DC_I(t), \quad (1)$$

$$Q(t) = A_Q(t) \sin\left[\theta_0 + \frac{4\pi x(t)}{\lambda} + \varphi_0(t)\right] + DC_Q(t), \quad (2)$$

where $DC_I(t), DC_Q(t)$ denote the direct current offsets. $A_I(t), A_Q(t)$ denote the alternate current amplitudes, both of the output I/Q signals, respectively. $\varphi_0(t)$ denotes the residual phase noise of the receiver. θ_0 represents the phase shift accumulated due to the initial distance and transceiver system. From Equations (1) and (2), the motion $x(t)$ can be
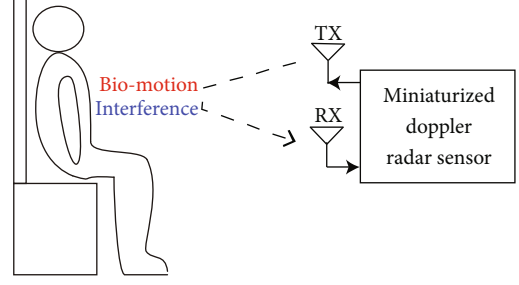
FIGURE 1: A classical radar system for biosignal detection including antennas, RF circuits to transmit and receive signals, and a signal processing unit. Interference is inventible during the detection.

mathematically expressed as

$$x(t) = \frac{\lambda}{4\pi}\left\{\arctan\frac{[Q(t) - DC_Q(t)]/A_Q(t)}{[I(t) - DC_I(t)]/A_I(t)} - \theta_0 - \varphi_0(t)\right\}. \quad (3)$$

From Equation (1), we can conclude that the principal causes of nonlinearity in demodulation are the unknown DC offsets and the imbalance between $A_I(t)$ and $A_Q(t)$. The imbalance is mainly due to hardware architecture, namely the receiver, which can be mostly overcome by advanced digital downconversion [9]. Thus, in this paper, the imbalance is solved, and the amplitude of each channel is the same. $DC_I(t)$ and $DC_Q(t)$ are originally produced by the reflection of background. It is time-varying because the offset could be disturbed by multiple factors, such as limb waving and temperature drift of circuits. It is worth noting that the change of DC offset is usually slow. Given the facts above, the DC offset during the small piece of time, such as 1 or 2 seconds, can be treated as constant. In the following experiment part, 80 sampling points are chosen as the piece length, which is 0.9 second because the sampling rate is 90 Hz.

From another perspective to eliminate trigonometric functions, Equations (1) and (2) are rewritten as

$$\left(\frac{I(t) - DC_I(t)}{A_I(t)}\right)^2 + \left(\frac{Q(t) - DC_Q(t)}{A_Q(t)}\right)^2 = 1. \quad (4)$$

The I/Q signal is obviously forming ellipse, shown in Equation (2). Based on the facts and discussion above, the slow-varying DC offset is assumed as constant ($DC_I[j]$ and $DC_Q[j]$), where the index j represents the jth segment of the whole demodulation. Meanwhile, in the jth short time segment, the imbalance of quadrature signals can be overcome by the digital downconversion receiver [9]. The amplitude then also has be treated as constant in the jth segment, which is $A_I(t) = A_Q(t) = A[j]$. Consequently, the ellipse in Equation (4) is simplified into a circle:

$$(I(t) - DC_I[j])^2 + (Q(t) - DC_Q[j])^2 = A^2[j]. \quad (5)$$

It is seen that after eliminating the imbalance between

(a)

(b)

(c)

(d)
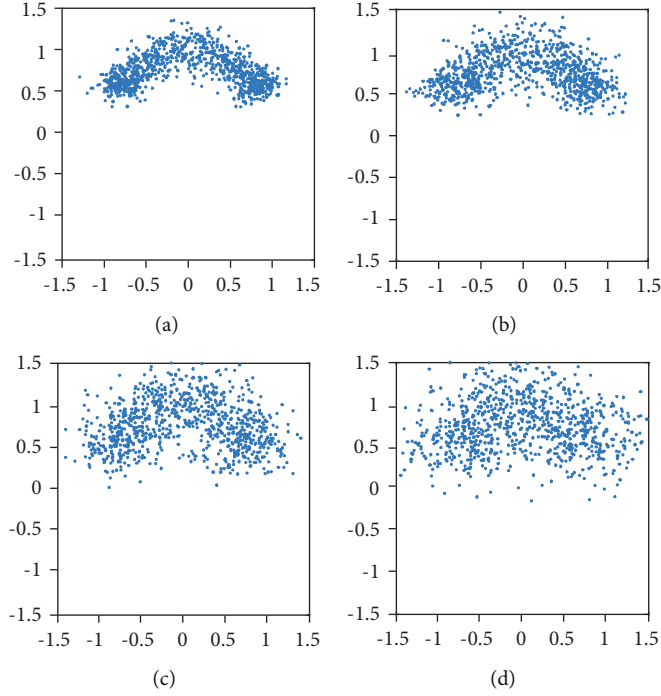
FIGURE 2: The constellations for simulated signal with different SNR: (a) SNR = 13 dB, (b) SNR = 10 dB, (c) SNR = 7 dB, and (d) SNR = 5 dB.

$I(t)$ and $Q(t)$ by digital-IF architecture, the ellipse turns into a circle, where the balanced amplitude is the radius $A[j]$, and the $(DC_I[j], DC_Q[j])$ is the center. In this ideal condition, as long as the circle center can be obtained from $I(t)$ and $Q(t)$, the motion $x(t)$ can be mathematically recovered.

The whole detection has been divided into m segments, and in each segment, the continuous-time variables are sampled into discrete series symbolled by index i. Equation (5) was then changed into

$$\left(I[i][j] - DC_I[j]\right)^2 + \left(Q[i][j] - DC_Q[j]\right)^2 = A^2[j]. \qquad (6)$$

The whole detection sampling data array, containing m times n points and in one dimension, now is rearranged into 2-dimensional m times n matrix for further process. In the first dimension, i represents the sample point index in each segment, ranging from 1 to n. j represents the segment index, ranging from 1 to m.

In traditional pulse radar signal processing, the signal data matrix can be processed from the fast-time dimension and slow-time dimension, in which the range and speed are obtained, respectively. Inspired by this concept, we can analogically name the first dimension in the Doppler radar matrix as an intrasegment dimension, because the vector interval is the reciprocal of the sampling rate. The second dimension is called the intersegment dimension, and the interval is determined by segment length. The calculation based on the matrix is more effective and clearer.

In the following subsections, we will discuss how to arrange the matrix with the size of m times n. Then, in the intersegment domain, the optimization algorithm is developed to get a better result. In the intrasegment domain, the
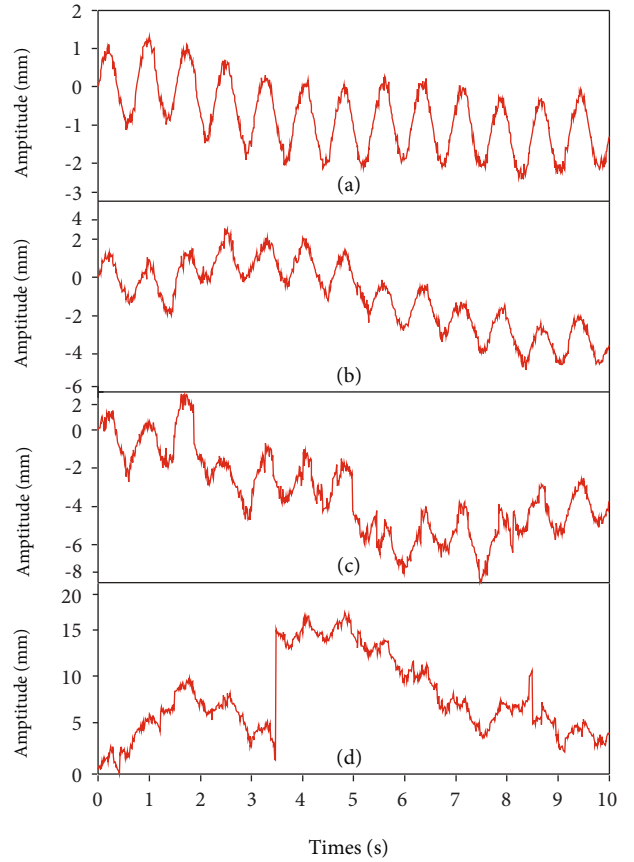
FIGURE 3: The demodulation result in time domain for simulated signal with different SNR: (a) SNR = 13 dB, (b) SNR = 10 dB, (c) SNR = 7 dB, and (d) SNR = 5 dB.
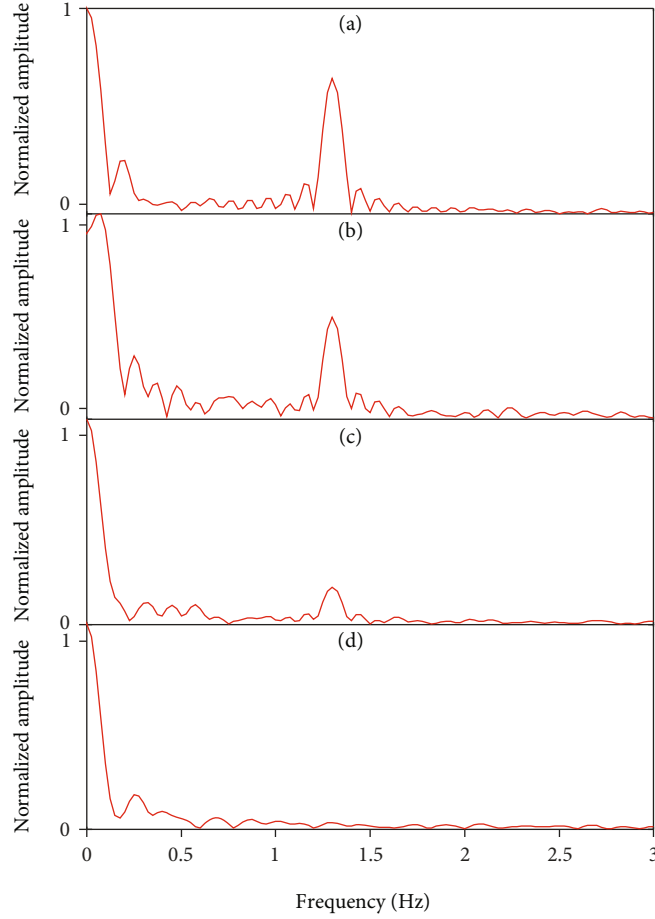
FIGURE 4: The demodulation result in frequency domain for simulated signal with different SNR: (a) SNR = 13 dB, (b) SNR = 10 dB, (c) SNR = 7 dB, and (d) SNR = 5 dB.

parameters produced by each segment in the intersegment domain are combined to access the fitness and adaptively filter out the interference.

2.2. The Demodulation and Optimization in Intrasegment Domain. In the segment j, the sampled I/Q signals can be expressed as a series $(I[1][j], Q[1][j]), (I[2][j], Q[2][j]), \cdots, (I[n][j], Q[n][j])$. The process of optimization can base on circle function. In this case, DC offset and radius are constant in each segment j. $(DC_I[j], DC_Q[j], A[j])$ are adjusted to form a circle and minimize deviation between the sampling series to the boundary of circle. According to (6), we define a loss function under a practical condition with noise

$$F(DC_I[j], DC_Q[j], A[j]) = \sum_{i=1}^{n} \left\{ (I[i][j] - DC_I[j])^2 \right.$$
$$\left. + (Q[i][j] - DC_Q[j])^2 - A[j]^2 \right\}.$$

(7)

The optimization algorithm minimizes the loss function as small as possible through an iterative process. When the loss function $F(DC_I[j], DC_Q[j], A[j])$ reaches its minimum, we take it as the optimal result. The parameters $(DC_I[j],$
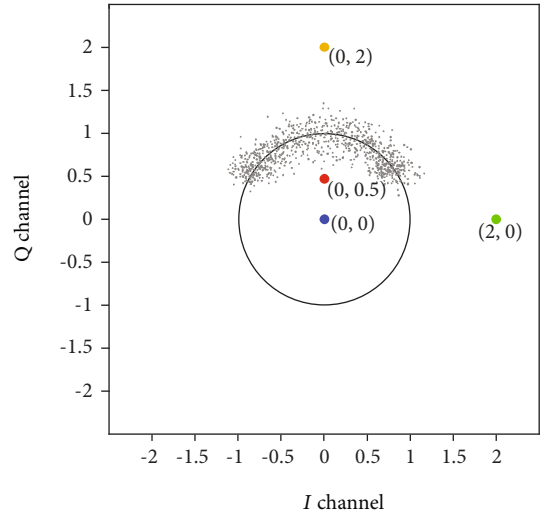
FIGURE 5: The constellation of simulated signal and four points for demodulation as DC offset: DC offset 1 (0, 0); DC offset 2 (0, 0.5); DC offset 3 (0, 2); and DC offset 4 (2, 0).
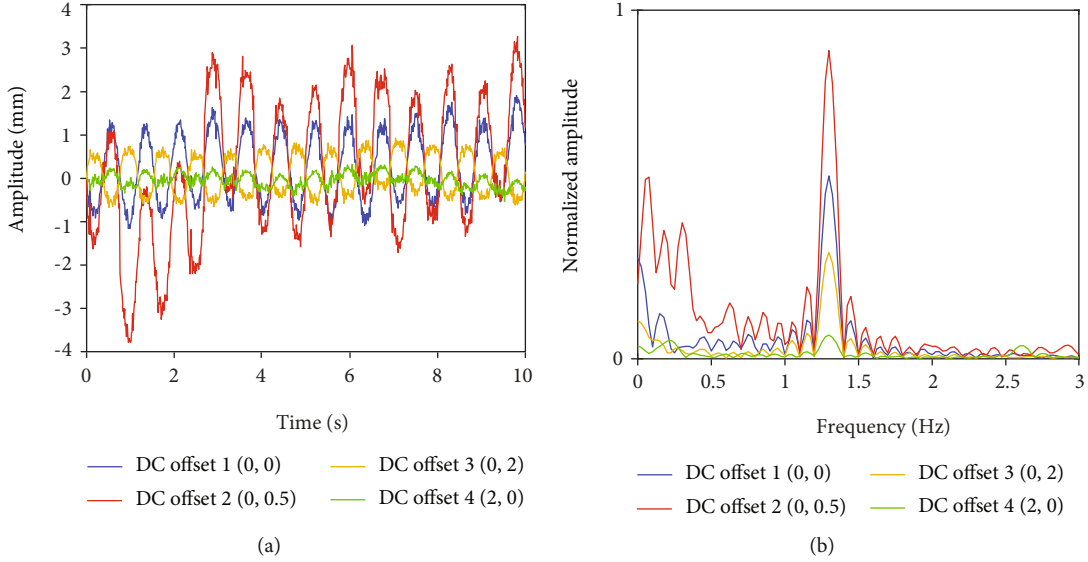
FIGURE 6: The demodulation result when four points are chosen for DC offset. (a) The result in time domain. (b) The result in frequency domain.

$DC_Q[j], A[j]$) will play an important role in evaluation to the degree of interference, which will be discussed in the next subsection.

After that, the extended DACM algorithm can retrieve the phase without phase wrapping problem, i.e.

$$\Phi(t) = \int_0^t \omega(t)dt = \int_0^t \frac{I(t)\dot{Q}(t) - \dot{I}(t)Q(t)}{I(t)^2 + Q(t)^2} dt. \tag{8}$$

Motion recovered by DACM will never encounter signal clipping caused by arctangent codomain. As a result, the instantaneous motion in each time slice can be linearly reconstructed.

2.3. DC Offset in the Demodulation. The recovered motion $x(t)$ in each segment is just an ideal result. Concretely, the motion $x(t)$ is well reconstructed only when there exists one moving target with no strong interference. Next, we will analyze the influence of DC offset to demodulation in case of noises and interference.

The noise is reflected in both amplitude and phase. Correspondingly, in the following simulation, we add white noise to $A_I(t)/A_Q(t)$ and $\varphi_0(t)$ in Equations (1) and (2). The demodulation result with noise $xn(t)$ is expressed as

$$xn(t) = \frac{\lambda}{4\pi} \left\{ \arctan \frac{[Q(t) - DC_Q]/(A + \text{noise1})}{[I(t) - DC_I]/(A + \text{noise2})} - \text{noise3} \right\}, \tag{9}$$

where $A_I(t) = A + \text{noise1}$, $A_Q(t) = A + \text{noise2}$, and $\varphi_0(t) = \text{noise3}$. Here, θ_0 is ignored because we only care about the change of $xn(t)$, not the initial position.

The signal-to-noise ratio (SNR) in baseband is defined as SNR $= A^2/\text{noise\_power}$, where noise power is the square of noise variance. Phase noise has been discussed in reference
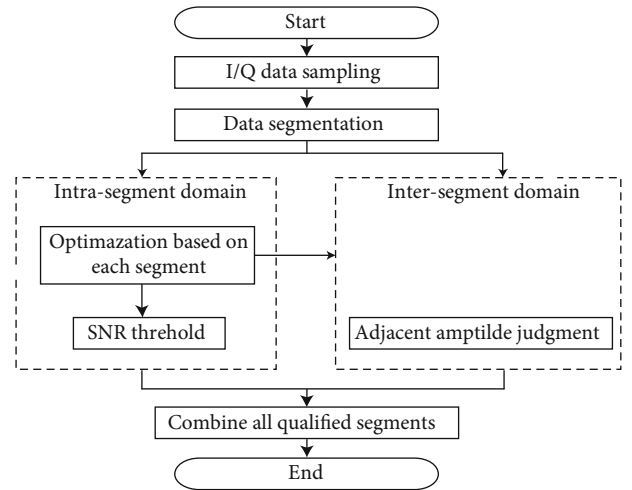
FIGURE 7: The flowchart of adaptive anti-interference algorithm.

[3], where the author concludes that although phase noise does affect the demodulation so much, it can still be neglected in most modern receivers.

To verify the influence of different SNR, we conducted a simulation. The heartbeat is assumed to 1.3 Hz, and four SNR are set as follows: 13 dB, 10 dB, 7 dB, and 5 dB. The DC offsets of each channel are 0. In Figure 2, four constellations can be observed. As the SNR degrading, the arc cannot be identified. But the demodulation still works until the SNR is lower than 7 dB, as shown in Figure 3 in time domain and Figure 4 in frequency domain. In practical detection for heartbeat signal signals, though the output power is limited, the SNR can be guaranteed to be large enough by designing proper antennas with high gain and constraining the measuring distance not to be too far.

In most cases, the phase is the ratio of arc to the radius. If the arc keeps constant, the radius is the inverse ration of

(a)

(b)

FIGURE 8: (a) The enlarged radar circuits viewed from front side and back side; (b) the setup of the experiment, including miniaturized radar, voltage source, laptop, and the subject under detection.

(a)

(b)

(c)
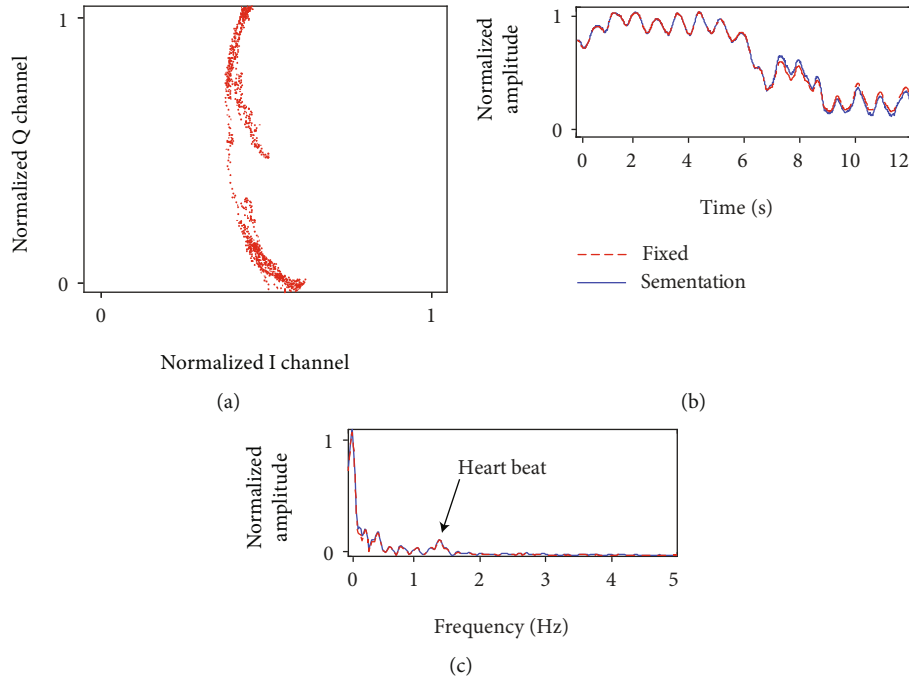
FIGURE 9: (a) I/Q constellation of biosignal when the subject tries to keep still. (b) Demodulation results in time domain by two methods: with segmentation or with fixed DC offset. (c) Demodulation results in frequency domain by two methods: with segmentation or with fixed DC offset.

movement. Following, the simulation is carried out to explore the impact of DC offset.

In the ideal case, if the DC offset is exactly located at the center of one circle, the demodulation of the Doppler signal can be effortlessly retrieved. However, in real cases, the center, which is decided by mathematical algorithms introduced in previous subsection, has the inevitable error. Small and trivial errors likely lead to significant demodulation distortion.

The second simulation is conducted to analyze this phenomenon. The frequency of heartbeat is set as 1.3 Hz like before, and the amplitude of heartbeat is 1 mm. The amplitude of each channel from the received signal is 1, and SNR is 13 dB. The original DC offset (center of the circle) is (0, 0) in ideal, which is named to DC offset 1. Then, we deliberately choose another three points deviated from the center (0, 0) as DC offsets in demodulation. DC offset 2

located at (0, 0.5) is closer to I/Q signal points; DC offset 3 is located at (0, 2), which is in the opposite direction of the real DC offset 1 (0, 0) to sampling points along the Q-channel-axis. DC offset 4 is (2, 0), in the I-channel-axis. All four DC offsets are marked in Figure 5, the constellation of sampling points.

In Figure 6(a), demodulation results in the time domain of four DC offset are shown. Recovered motion based on DC offset 1 (0, 0) is within expectation, and the amplitude of heartbeat is 1 mm. Because the DC offset 2 (0, 0.5) is closer to the sampling point, the demodulated amplitude is larger, near 2 mm. However, the tendency of whole motion is not stable because the noise affects the result more heavily as DC offset gets closer to sampling points. DC offset 3 (0, 2) is out of the circle formed by sampling data, but the heartbeat signal can still be observed from the demodulation result. The phase of the result is flipped 180 degrees. DC

(a)

(b)

(c)

(d)
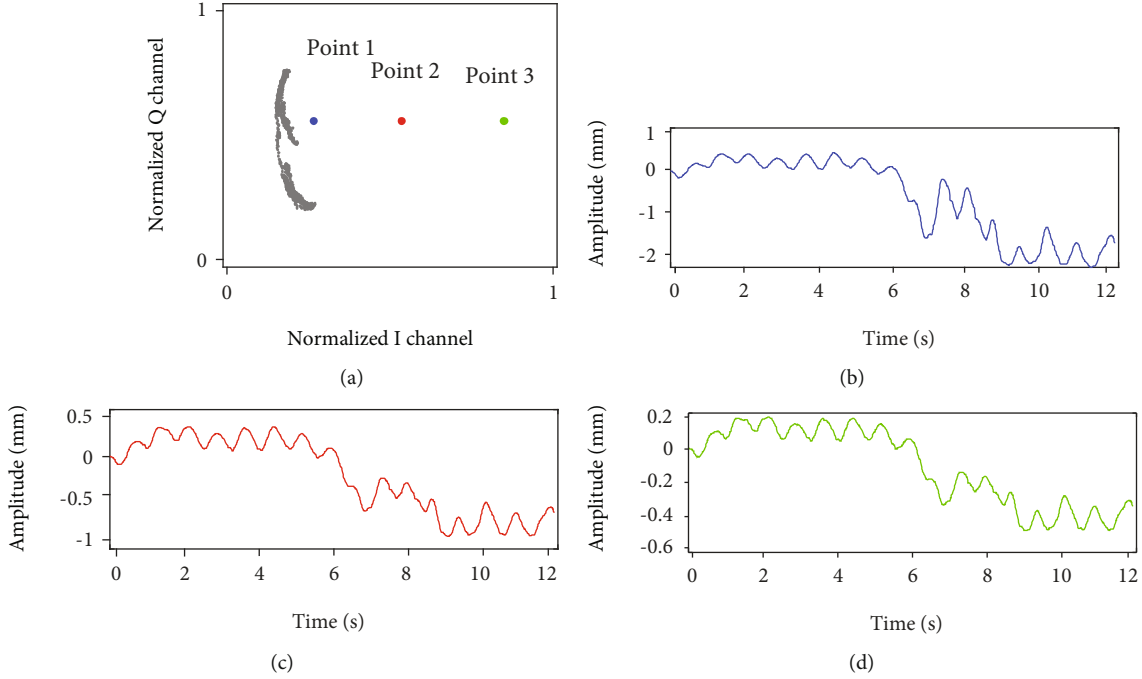
FIGURE 10: (a) I/Q constellation and the 3 points chosen as DC offset for demodulation. (b) Demodulation result when the DC offset is at point 1. (c) Demodulation result when the DC offset is at point 2. (d) Demodulation result when the DC offset is at point 3.

offset 4 is chosen along the I-channel-axis, and the corresponding result is much deteriorated.

In the frequency domain as shown in Figure 6(b), the heartbeat is visible under all the different DC offsets. The low-frequency noise is very obvious under DC offset 2, as we mentioned in time domain because of low SNR. Heartbeat signal is very weak under DC offset 4, and nonnegligible harmonic is located in 2.6 Hz.

In summary, the phase demodulation method is pretty robust for the DC offset with acceptable error. Nevertheless, the recover motion will be distorted when the noise is too strong or DC offset is chosen too far from the real center of sampling points. In other words, the validity of DC offset can be determined by SNR and signal intensity.

2.4. Adaptive Anti-Interference Algorithm.

As discussed above, now we find two parameters of prime importance: SNR and the signal intensity. In the practical measurement, we obtain only I/Q baseband signals. After the optimizations in Equation (6), DC offset $(DC_I[j], DC_Q[j])$ and the amplitude $A[j]$ can be reorganized to present the SNR and the signal intensity.

The noise of sampling points is expressed as a mean square error (MSE). Here the "mean" of sampling points is directly obtained by the optimized amplitude $A[j]$, not the average value of all distances between sampling data and DC offset.

$$MSE = \frac{1}{n} \sum_{i=1}^{n} \left(\sqrt{(I[i][j] - DC_I[j])^2 + (Q[i][j] - DC_Q[j])^2} - A[j] \right)^2.$$

(10)
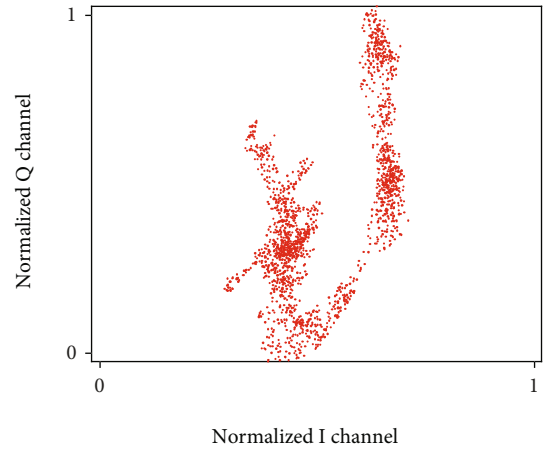
FIGURE 11: The constellation of I/Q signal when the subject under normal condition.

This MES can also be seen as the indicator of circle fitness. SNR is the ratio of signal to noise, which can be expressed as $A[j]^2/MSE^2$.

The signal intensity can be present by the amplitude in the baseband. As shown in Equation (6), the amplitude $A[j]$ in every segment is acquired by optimizing. In normal cases, adjacent $A[j]$ and $A[j-1]$ should not drastically change as the signal power is relatively stable. However, if interference and strong body movements occur, as discussed above, the $A[j]$ will be much bigger or smaller than the previous $A[j-1]$. As a result, we can construct a threshold between segments to determine whether there is strong interference.

(a)

(b)
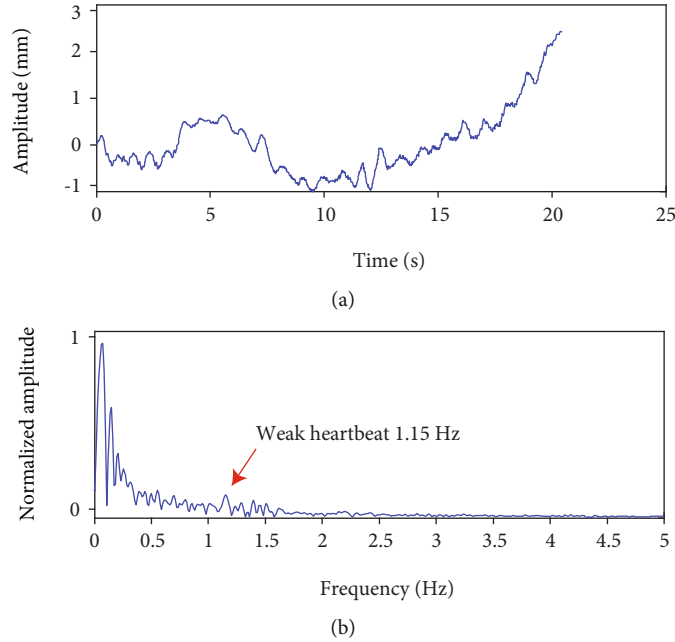
FIGURE 12: The demodulation result when using the fixed DC offset method. (a) In time domain. (b) In frequency domain.

Based on this idea, an adaptive anti-interference algorithm is come up with. This algorithm automatically judges whether there is too strong interference by identifying low SNR within the segment and dramatic change of $A[j]$ between segments. The SNR threshold is set to 7 dB as the first condition to decide whether this is a "bad segment." Another condition for "bad segment" is $A[j] > 3 A [j-1]$ or $A[j] > 3A \, A[j-1]$. If any of the two conditions is satisfied, the segment is determined as "bad segment" and discarded.

Figure 7 shows the flowchart of the adaptive anti-interference algorithm. When the detection starts, the radar samples the I/Q signal by quadrature downconversion. Then, the sampled data are divided into segments, and the data matrix is formed. In the intrasegment domain, every segment is optimized to obtain the best DC offset for demodulation. The process of optimization also gives us two parameters: radius directly and SNR indirectly after calculation. SNR in intrasegment domain is employed to judge whether each segment is qualified for demodulation or seriously interfered. And we also design a threshold based on the radius of adjacent segments in intersegment domain to decide whether this segment can be used for further process. To maintain the length of detection time window, we do not directly delete the "bad segments" with interference. Instead, we replace the "bad segment" with the qualified segment closest to it. At last, the segments that satisfied our standards in both intrasegment and intersegment domains are combined together. Because some "bad segments" are discarded, we also eliminate the discontinuous gap between the newly formed adjacent segments. Consequently, the splicing motion removes the interference and also avoids introducing new noise.

3. Results and Discussion

3.1. Hardware and Experiment Setup. Several experiments of different cases were conducted in order to validate the proposed approach. A 24 GHz miniaturized radar is employed, which is initially designed as digital-IF architecture to detect biosignal under body movement [19]. The system mainly bases on the monolithic millimeter-wave integrated circuit BGT24MTR11 produced by Infineon. The working principle of the circuit is as follows: First, the 24 GHz RF signal generated by the local oscillator (LO) is mixed with the low-IF signal generated by the waveform generator, and the signal is transmitted through the antenna; then, the receiving antenna receives the RF signal containing the motion information of the target to be measured. The signal is down-mixed by the same LO to obtain a low-IF signal, and two orthogonal signals are generated during the quadrature downconversion process; in the next step, the low-IF analog signal is sampled by a 12-bit analog-digital conversion chip to obtain a quadrature digital signal; finally, the digital signal passes through the CPLD and the microprogrammed control unit (MCU) to reduce the data transmission rate to the computer for further processing; here, the MCU is also configured to control the main integrated circuit chips. The entire system is provided by a single crystal oscillator to provide the reference signal source, which ensuring the synchronization of the system and the coherence of the receiving and sending signals. The whole size of the printed circuit board (PCB) with four layers is about 14 cm × 5 cm, as shown in Figure 8(a). The transmitting power is set to 6 dBm, and the gain of the series-fed antenna is around 12 dBi. The sampling rate of analog-to-digital converter is 90 Hz.

(a)

(b)
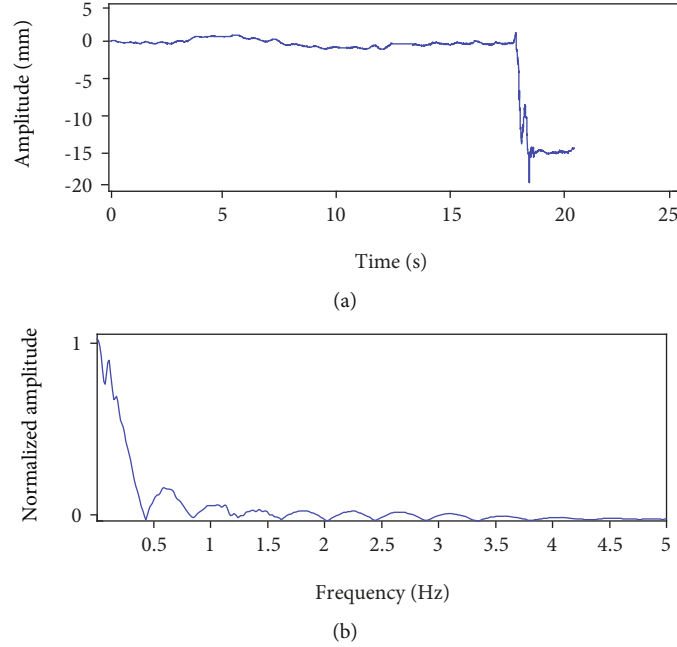
FIGURE 13: The demodulation result when using the multiple segments with different DC offset method. (a) In time domain. (b) In frequency domain.

The setup of experiments is shown in Figure 8(b). The 24 GHz miniaturized radar is placed vertically so that the antenna can transmit microwave signal to the subject. The voltage source is used to drive the circuits. The laptop receives the baseband I/Q signals through the USB port, and then, the data are processed in computer software.

In the biosignal measurement, the distance from the subject to antenna is about 50 cm. A 32-year-old male with 180 cm height is under detection. As discussed in Section 1, the subject always holds his breath to avoid respiration signal, and we only focus on heartbeat signal and interference.

3.2. Measurement on Different DC Offset. Before the measurement for more generalized cases with nonnegligible noise and interference, our first experiment is conducted when the subject tries his best to hold still. As shown in Figure 9(a), part of a circle formed by the I/Q series is clearly observed in the constellation. The fixed DC offset method and segmentation method with multiple DC offsets are, respectively, used to demodulate the motion from the phase. The recover motions in time domain and frequency domain are shown in Figures 9(b) and 9(c). Because, in this experiment, the noise and interference are very weak, no segment is judged as "bad segment" to be discarded, and there is no significant difference between the two methods.

Based on the same data, we also analyze the demodulation result with different DC offsets. In constellation shown in Figure 10(a), three DC offsets are chosen for motion recover: point 1, point 2, and point 3. Point 2 is close to the normal DC offset acquired by optimization. Point 1 is the DC offset very near to the I/Q signal arc, and point 3 is far from signal sampling points adversely. The modulation results in time domain are shown in Figures 10(b)–10(d).

TABLE 1: Main parameters of each segment in the experiment of heartbeat detection with interference.

Segment index j	DCI[j],	DCQ[j],	A[j]	SNR[j]
1	608526	-474756	8215	34
2	613464	-474613	3370	27
3	610951	-474800	5985	33
4	613463	-474421	3474	27
5	611635	-473168	5223	30
6	609639	-473656	7124	34
7	613312	-473079	3486	28
8	612722	-474169	4120	31
9	613108	-474565	3627	29
10	613371	-474731	3408	28
11	614357	-474357	3394	23
12	613495	-474406	3303	18
13	612278	-476394	2662	21
14	612952	-474742	2070	20
15	368166	-478876	246712	59
16	613134	-475000	2189	16
17	614693	-473513	2539	23
18	613542	-474391	2191	28
19	613582	-474346	2110	20
20	613061	-474980	2056	23
21	615021	-475248	190	3
22	613700	-473420	1904	18

All the results show the heartbeat signal obviously and are very similar in tendency. However, the amplitude of each recovered motion remains highly divergent. This corresponds well with the theoretical analysis. So, it is pretty

(a)

(b)
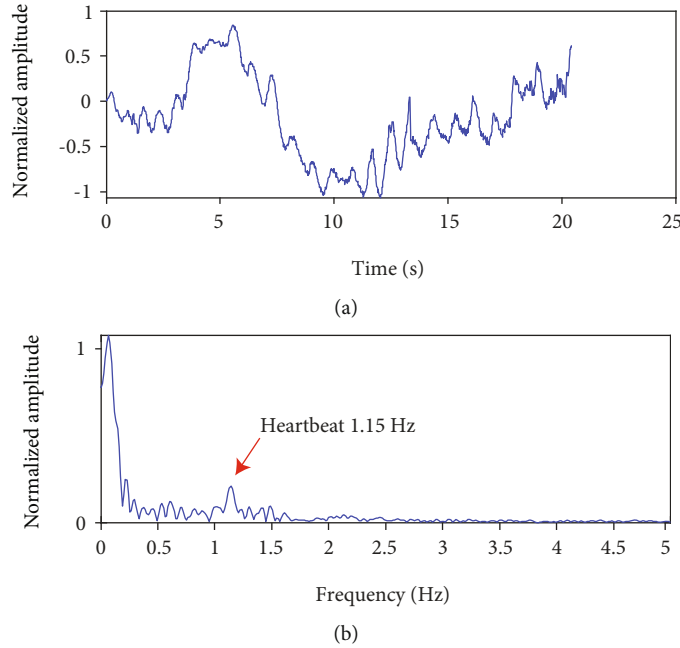
FIGURE 14: The demodulation result when using adaptive anti-interference algorithm. (a) In time domain. (b) In frequency domain.

robust for DC offset optimization to recover the frequency or time domain shape of the heartbeat. What really matters is the case with great interference and strong noise, and in the next subsection, we will solve this problem by the proposed adaptive anti-interference algorithm to filter the "bad segment" and reorganize the sampling series to recover heartbeat signal.

3.3. The Experiment of Heartbeat Detection with Interference. In this subsection, we conduct an experiment under normal conditions, in which there may be interference and strong noise. The subject tries to keep normally sitting, but uncontrolled random body movement (RBM) is inevitable.

The constellation shown in Figure 11 is much noisier than that in Section 3.2. Part of circles is still pretty evident, but not limited to only one circle center. Firstly, we still use the fixed DC offset. The demodulation result is shown in Figure 12. In time domain, the heartbeat signal can be seen, but the body movement is relatively strong, which is about 3.5 cm. In the frequency domain, the heartbeat signal is weak but still exists above noise floor at 1.15 Hz.

In Figure 13, the multiple segments with different DC offsets are used to recover the whole movement. It is obvious that the signal deformed seriously from 17 to 18 seconds. The cause is that the segment at that time encounters strong body movements, and the segment with fewer sampling points is interfered easily. In frequency domain, the heartbeat is totally concealed by the strong interference.

In Table 1, the corresponding parameters $DC_I[j]$, $DC_Q[j]$, $A[j]$ and SNR $[j]$ for each segment j are listed. As stated above, each segment contains 80 sampling point, that is about 0.9 second with 90 Hz sampling rate. It is obvious to notice that segment 15 and segment 21 are abnormal no matter from the perspective of $A[j]$ or SNR$[j]$. The segment

15 and 21 corresponds well with the sudden change occurs in Figure 13(a).

After applying our adaptive anti-interference algorithm, we can filter the "bad segment" which is with low SNR or deviated from the adjacent segment seriously in amplitude. The result is shown in Figure 14. In time domain, the heartbeat is obvious at 1.15 Hz, and the body movement in the whole detection is decreased to about 1.5 cm from 3.5 cm obtained by the demodulation algorithm with fixed DC offset. In frequency domain, the heartbeat signal has much better SNR in Figure 14(a) compared to the result in Figure 12(a). So, a more robust measurement of heartbeat with interference can be implemented.

From all the experiments, we can conclude that by using the proposed adaptive anti-interference algorithm, we can filter out the strong interference in normal detection for heartbeat signals. Better demodulation results can be obtained compared to the traditional method.

This method is effective for sudden and short-term interference as demonstrated above. However, if the interference lasts for a long time such as 30 seconds, this method is likely to fail. Due to the iterative process of the DC offset as shown in Equation (7), the algorithm takes a little longer. This also needs to be overcome to realize real-time measurement.

4. Conclusions

In conclusion, we come up with a novel anti-interference algorithm in the detection of biosignal, applied to scenarios with motion with strong interference or noise, just like the case of random body movement. Specifically, the signal-to-noise ratio threshold in intrasegment domain and signal strength comparison of adjacent segments in the intersegment domain are used as a criterion for determining

whether there is strong interference. The unqualified segments will be automatically replaced by the qualified ones, and all the segments are reorganized together at last. This algorithm can improve the performance of heartbeat detection in both the time domain and frequency domain. After theoretical analyses, simulations and experiments are conducted to validate the proposed method. This novel method makes the application of the Doppler radar in the field of biosignal detection more universal and promising in daily activities.

Data Availability

The data used to support the findings of this study have not been made available because of the potential privacy.

Conflicts of Interest

The authors declare that there is no conflict of interest regarding the publication of this paper.

Authors' Contributions

Lingtong Min and Qinyi Lv are co-first authors.

Acknowledgments

References

[1] C. Li, V. M. Lubecke, O. Boric-Lubecke, and J. Lin, "A review on recent advances in Doppler radar sensors for noncontact healthcare monitoring," *IEEE Transactions on Microwave Theory and Techniques*, vol. 61, no. 5, pp. 2046–2060, 2013.

[2] C. Li, Z. Peng, T. Y. Huang et al., "A review on recent progress of portable short-range noncontact microwave radar systems," *IEEE Transactions on Microwave Theory and Techniques*, vol. 65, no. 5, pp. 1692–1706, 2017.

[3] A. D. Droitcour, O. Boric-Lubecke, V. M. Lubecke, J. Lin, and G. T. A. Kovac, "Range correlation and I/Q performance benefits in single-chip silicon Doppler radars for noncontact cardiopulmonary monitoring," *IEEE Transactions on Microwave Theory and Techniques*, vol. 52, no. 3, pp. 838–848, 2004.

[4] B. K. Park, O. Boric-Lubecke, and V. M. Lubecke, "Arctangent demodulation with DC offset compensation in quadrature Doppler radar receiver systems," *IEEE Transactions on Microwave Theory and Techniques*, vol. 55, no. 5, pp. 1073–1079, 2007.

[5] J. Wang, X. Wang, J. Huangfu, C. Li, and L. Ran, "Noncontact distance and amplitude-independent vibration measurement based on an extended DACM algorithm," *IEEE Transactions on Instrumentation and Measurement*, vol. 63, no. 1, pp. 145–153, 2014.

[6] C. Li, X. Yu, C. Lee, L. Ran, and J. Lin, "High-sensitivity software-configurable 5.8-GHz radar sensor receiver chip in 0.13-μm CMOS for noncontact vital sign detection," *IEEE Transactions on Microwave Theory and Techniques*, vol. 52, no. 5, pp. 1410–1419, 2010.

[7] Q. Lv, D. Ye, S. Qiao et al., "High dynamic-range motion imaging based on linearized Doppler radar sensor," *IEEE Transactions on Microwave Theory and Techniques*, vol. 62, no. 9, pp. 1837–1846, 2014.

[8] T. Fan, C. Ma, Z. Gu et al., "Wireless hand gesture recognition based on continuous-wave Doppler radar sensors," *IEEE Transactions on Microwave Theory and Techniques*, vol. 64, no. 11, pp. 4012–4020, 2016.

[9] J. Wang, X. Wang, Z. Zhu, J. Huangfu, C. Li, and L. Ran, "1-D microwave imaging of human cardiac motion: an ab-initio investigation," *IEEE Transactions on Microwave Theory and Techniques*, vol. 61, no. 5, pp. 2101–2107, 2013.

[10] N. Hafner, J. C. Drazen, and V. M. Lubecke, "Fish heart rate monitoring by body-contact Doppler radar," *IEEE Sensors Journal*, vol. 13, no. 1, pp. 408–414, 2012.

[11] B. Spencer Jr., S. Cho, and S.-H. Sim, "Wireless monitoring of civil infrastructure comes of age," *Structure*, vol. 13, pp. 12–16, 2011.

[12] Y. Zhang, S. Dong, C. Zhu, M. Balle, B. Zhang, and L. Ran, "Hand Gesture Recognition for Smart Devices by Classifying Deterministic Doppler Signals," *IEEE Transactions on Microwave Theory and Techniques*, vol. 69, no. 1, pp. 365–377, 2021.

[13] A. Naqvi, S.-T. Yang, and H. Ling, "Investigation of Doppler features from wind turbine scattering," *IEEE Antennas and Wireless Propagation Letters*, vol. 9, pp. 485–488, 2010.

[14] S. Dong, Y. Zhang, C. Ma et al., "Doppler cardiogram: a remote detection of human heart activities," *IEEE Transactions on Microwave Theory and Techniques*, vol. 68, no. 3, pp. 1132–1141, 2020.

[15] C. Li and J. Lin, "Random body movement cancellation in Doppler radar vital sign detection," *IEEE Transactions on Microwave Theory and Techniques*, vol. 56, no. 12, pp. 3143–3152, 2008.

[16] F. K. Wang, T. S. Horng, K. C. Peng, J. K. Jau, J. Y. Li, and C. C. Chen, "Single-antenna Doppler radars using self and mutual injection locking for vital sign detection with random body movement cancellation," *IEEE Transactions on Microwave Theory and Techniques*, vol. 59, no. 12, pp. 3577–3587, 2011.

[17] M.-C. Tang, C.-Y. Kuo, D.-C. Wun, F.-K. Wang, and T.-S. Horng, "A self- and mutually injection-locked radar system for monitoring vital signs in real time with random body movement cancellation," *IEEE Transactions on Microwave Theory and Techniques*, vol. 64, no. 12, pp. 4812–4822, 2016.

[18] C. Gu, G. Wang, Y. Li, T. Inoue, and C. Li, "A hybrid radar-camera sensing system with phase compensation for random body movement cancellation in Doppler vital sign detection," *IEEE Transactions on Microwave Theory and Techniques*, vol. 61, no. 12, pp. 4678–4688, 2013.

[19] Q. Lv, L. Chen, K. An et al., "Doppler vital signs detection in the presence of large-scale random body movements," *IEEE Transactions on Microwave Theory and Techniques*, vol. 66, no. 9, pp. 4261–4270, 2018.

[20] Z. Gu, T. Fan, Q. Lv et al., "Remote blind motion separation using a single-tone SIMO Doppler radar sensor," *IEEE Transactions on Geoscience and Remote Sensing*, vol. 57, no. 1, pp. 462–472, 2019.

[21] M. Mercuri, I. R. Lorato, Y.-H. Liu, F. Wieringa, C. Van Hoof, and T. Torfs, "Vital-sign monitoring and spatial tracking of multiple people using a contactless radar-based sensor," *Nature Electronics*, vol. 2, no. 6, pp. 252–262, 2019.